# Investigation of flow instabilities in microfluidic devices

Thesis submitted in accordance with the requirements of
the University of Liverpool for the degree of Doctor in Philosophy
by
Allysson Ferreira Domingues
May 2019

# Abstract

Combining and separating fluid streams has many industrial and biomedical applications, such as biomedical devices, mini- or micro-scale mixers, and micro-rheometry. In this work, we have investigated the influence of both purely inertial and purely elastic flow instabilities on different micro-geometries using Newtonian and viscoelastic fluids.

This study has explored numerical and experimental inertial instabilities in a so-called *mixing-separating* cell micro-geometry that contains an internal stagnation point where fluid streams are combined. The geometry consists of two straight square parallel channels with flow from opposite directions and a central gap that allows the streams to interact, mix, or remain separate (often referred to as the *H-geometry*). Under creeping-flow conditions (Reynolds number $[Re \to 0]$), the flow is steady, two-dimensional, and produces a sharp interface between fluid streams entering the geometry from opposite directions. When $Re$ exceeds a critical value, one of two different supercritical, inertial instability appears which leads to significant changes in the flow pattern and an increased level of interaction between the two streams, although the flow remains steady.

In a wide gap geometry ($g = 5H$, where $g$ and $H$ corresponds to the gap size and the channel height respectively), as $Re$ increases, the central vortex divides into two vortices, whereas the flow topology and the form of the instability are different in other gap sizes. The experimental results for one gap size are used to validate our numerical method, which is then applied to a wider range of gap sizes. The exact form of the instability is dependent on the gap size and Reynolds number and we identify two distinct instabilities, one of which appears in devices with large gaps and another which appears in devices with small gaps. At intermediate gap sizes both instabilities can occur in the same device (at different onset Re). The results suggest that gap size is of primary importance in determining the type of instability that occurs. With a judicious choice of gap size, the instabilities can be exploited (or avoided) in scientific, medical or other microfluidic applications.

By varying the angle between the pair of inlet and outlet arms from the so-called 'mixing-separating' (0° angle) to a so-called cross-slot (90° angle), where the inlet and outlet channels are orthogonal (including intermediate geometries between these two extremes), we can firmly establish how the instability relates to both gap size and

impingement angle. The impingement angle and gap size are geometrically dependent upon each other (i.e. if the impingement angle is changed, the gap size is changed as a result of the new angle), and isolating the effect of the impingement angle and gap size is non-trivial.

The creeping flow of a highly viscoelastic fluid through the mixing-separating cell micro-geometry undergoes a series of purely elastic flow transitions from symmetric flow to steady asymmetric flow and eventually to time-dependent flow depending on the Weissenberg number ($Wi$). Our experimental results suggest that the effect observed can be exploited to enhance mixing in biomedical or other applications.

Finally, we have investigated the influence of a purely inertial flow instability on the enhancement of heat transfer in a cross-slot micro-geometry where symmetry is broken but the flow remains steady. The effects of the instability have presented as an effective method of enhancing mixing and heat transfer in the cross-slot device and can be exploited in applications such as lab-on-chip and micro chemical-reaction devices at a low Reynolds number (i.e. $Re < 100$).

**Keywords:** Inertial instability, Mixing-separating device, Cross-Slot, Heat transfer, Steady symmetry-breaking bifurcation, Swirling strength, Elastic instability

# Declaration of Authorship

I, Allysson Domingues, declare that this thesis titled, 'Investigation of flow instabilities in microfluidic devices' and the work presented in it are my own. I confirm that:

- This work was done wholly or mainly while in candidature for a research degree at this University.
- Where any part of this thesis has previously been submitted for a degree or any other qualification at this University or any other institution, this has been clearly stated.
- Where I have consulted the published work of others, this is always clearly attributed.
- Where I have quoted from the work of others, the source is always given. With the exception of such quotations, this thesis is entirely my own work.
- I have acknowledged all main sources of help.
- Where the thesis is based on work done by myself jointly with others, I have made clear exactly what was done by others and what I have contributed myself.

Allysson Domingues
May 2019

# Publications

**Peer-reviewed journals:**

- Abed W., **Domingues, A.**, Poole R. J., and Dennis D., **2017**, Heat transfer enhancement in a cross-slot micro-geometry. *Int. J. Therm. Sci.*, 121, pp.249-265. DOI: https://doi.org/10.1016/j.ijthermalsci.2017.07.017

- **A. Domingues**, Poole R. J., and Dennis D., **2019**, Inertial instabilities in a microfluidic mixing-separating device. *Phys. Fluids*, 31(7), p.074101. DOI: https://doi.org/10.1063/1.5108885

- M. Davoodi, **A. Domingues**, Dennis D., and Poole R. J., **2019**, Delay of symmetry-breaking instability in cross-slot geometries using a passive flow-control mechanism. *J. Fluid Mech.*, 881, 1123-1157. DOI: https://doi.org/10.1017/jfm.2019.781

**Conference proceedings:**

- Abed, W., **Domingues, A.**, Poole, R.J., Dennis, D.,"The enhancement of convective heat transfer in a cross-slot micro-geometry," International Congress on Rheology, Kyoto (Japan), August 2016.

- **Domingues, A.**, Abed, W., Poole, R.J., Dennis, D.,"Heat transfer enhancement in a cross-slot micro-geometry," Bulletin of the American Physical Society, Portland (US), November 2016.

- **Domingues, A.**, Poole, R.J., Dennis, D.,"Inertial instabilities in a mixing-separating microfluidic device," Bulletin of the American Physical Society, Denver (US),November 2017.

- **Domingues, A.**, Davoodi, M., Poole, R.J., Dennis, D.,"Inertial and elastic flow instabilities in a mixing-separating microfluidic devices," Annual European Rheology Conference, Sorrento (Italy), April 2018.

- Davoodi, M., **Domingues, A.**, Poole, R.J., Dennis, D.,"Delay of symmetry-breaking instability in cross-slot geometries using a passive flow control mechanism," Annual European Rheology Conference, Sorrento (Italy), April 2018.

- **Domingues, A.**, Davoodi, M., Poole, R.J., Dennis, D.,"Inertial flow instabilities in microfluidic devices," UK Fluids Conference, Manchester (UK), September 2018.

# Contents

**Abstract** **i**

**Contents** **viii**

**List of Figures** **xxi**

**Acknowledgement** **xxii**

**1 Introduction** **1**

1.1 Motivation . . . . . 1
1.2 Inertial instabilities in microfluidics . . . . . 2
1.3 Elastic instabilities in microfluidics . . . . . 6
1.4 Project aims and objectives . . . . . 7
1.5 Outline of this document . . . . . 8

**2 Background** **10**

2.1 Fluid flow instabilities at micro-scale . . . . . 10
2.2 Mixing in micro-scale flows . . . . . 10
2.3 Reynolds number influence . . . . . 11
2.4 Diffusion dominates the mixing process in the micro-scale . . . . . 12
2.5 Convective flow associated with inertial instabilities in microfluidics . . 13
2.5.1 Serpentine channel . . . . . 15
2.5.2 T-shaped micro-geometry . . . . . 17
2.5.3 Cross-slot device . . . . . 19
2.5.4 Mixing-separating cell . . . . . 25
2.6 Particle separation in microfluidics . . . . . 31
2.7 Heat transfer in micro-flows . . . . . 32
2.7.1 Thermal boundary layer and the Nusselt number influence . . . . 35
2.8 Elastic instabilities . . . . . 37
2.8.1 Weissenberg number and Deborah number . . . . . 38
2.8.2 Purely elastic flow instabilities and Boger fluids . . . . . 39

2.8.3 Instabilities in viscometric flows with curved streamlines . . . . . 40
2.8.4 Elastic instabilities in stagnation point flows . . . . . 41
2.8.5 T-shaped planar channel . . . . . 41
2.8.6 Cross-Slot device . . . . . 41
2.8.7 Mixing-separating cell . . . . . 42
2.9 Summary and guidance . . . . . 43

**3 Experimental methodology and materials 45**
3.1 Introduction . . . . . 45
3.1.1 Flow visualisation . . . . . 45
3.1.2 Pressure drop measurements . . . . . 46
3.1.3 Microfluidic device fabrication . . . . . 47
3.2 Experimental setup - Mixing-separating cell . . . . . 48
3.3 Working fluids . . . . . 52
3.3.1 Newtonian solution . . . . . 53
3.3.2 Polymeric solution . . . . . 54
3.4 The uncertainty of experimental parameters . . . . . 57
3.4.1 Experimental mass flow rate uncertainties . . . . . 58
3.4.2 Flow bulk velocity uncertainties . . . . . 58
3.4.3 Reynolds number uncertainties . . . . . 59
3.4.4 Friction factor uncertainties . . . . . 59
3.4.5 $fRe$ uncertainties . . . . . 60

**4 Numerical methods and techniques 62**
4.1 Governing equations and numerical method . . . . . 62
4.2 Numerical simulations in a mixing-separating cell . . . . . 63
4.2.1 Computational meshes . . . . . 65
4.2.2 Gap and angle variation . . . . . 67
4.2.3 Bifurcation parameters and vortex identification method . . . . . 68
4.3 Numerical simulations in a cross-slot device . . . . . 72
4.3.1 Computational meshes . . . . . 72
4.3.2 Thermal boundary conditions . . . . . 75

**5 Inertial instabilities in a mixing-separating device 78**
5.1 Experiment and simulations using a wide gap ($g = 5H$) . . . . . 78
5.1.1 Friction factor . . . . . 78
5.1.2 Visualisation of the base flow . . . . . 80
5.1.3 Visualisation of the inertial instability . . . . . 81
5.1.4 Characterisation of the instability from experiments . . . . . 83
5.1.5 Characterisation of the instability from simulations . . . . . 84

5.2 Simulations investigating the effect of varying the gap size ($g$) . . . . . 86
5.2.1 Instability onset for different gap sizes . . . . . 87
5.2.2 Results of simulations with $g = 3.86H$ . . . . . 87
5.2.3 Results of simulations with $g = 2.61H$ . . . . . 89
5.2.4 Results of simulations with $g = 2H$ . . . . . 93
5.3 Summary . . . . . 95

**6 Effects of angle variation on the inertial instability 97**
6.1 Geometry selection . . . . . 98
6.2 Instability variation: from subcritical pitchfork to supercritical . . . . . 98
6.3 60° X-shaped geometry compared to a $g = 2H$ mixing-separating . . . . 99
6.4 30° X-shaped geometry compared to a $g = 3.86H$ mixing-separating . . 101
6.4.1 Flow development along the outlet channels . . . . . 102
6.5 Summary . . . . . 105

**7 Elastic instabilities in a mixing-separating cell micro-device 106**
7.1 Flow visualisation on the elastic instability . . . . . 107
7.1.1 Steady states . . . . . 107
7.1.2 Periodic flow . . . . . 108
7.2 Single-sided amplitude spectrum . . . . . 110
7.3 Purely elastic instability: periodic behaviour . . . . . 114
7.4 Supercritical instability: Hopf bifurcation . . . . . 117
7.5 Summary . . . . . 118

**8 Inertial instabilities in a cross-slot micro-geometry 119**
8.1 Experimental procedure . . . . . 120
8.2 Preliminary simulations . . . . . 121
8.2.1 Temperature distribution . . . . . 121
8.2.2 Hysterisis . . . . . 129
8.3 Estimation of the heat transfer enhancement . . . . . 131
8.3.1 Simulations with adiabatic walls . . . . . 131
8.3.2 Simulations with constant temperature walls . . . . . 137
8.4 Summary . . . . . 142

**9 Conclusions and future recommendations 144**
9.1 Inertial instabilities . . . . . 144
9.2 Elastic instabilities . . . . . 147
9.3 Overall conclusions . . . . . 147
9.4 Future Work . . . . . 148

**A Supplemental material 152**

**B Symmetries** **153**

**C Transverse velocity bifurcation parameter $w_{max}/U_b$** **155**

**Bibliography** **168**

# List of Figures


1.1 Schematic diagram of a cross-slot geometry showing the relevant details: two opposing inlets, two outlets, and the stagnation point. . . . . 3

1.2 Spiral instability in a cross-slot geometry: Confocal experimental imaging ((a)–(d)) showing the steady-symmetric flow and the symmetry-breaking bifurcation - spiral vortex structure (right). Newtonian fluid flow in the cross-slot device with aspect ratio 1 ($\alpha = 1$) under the following conditions: (a) $Re = 15.2$; (b) $Re = 42.8$; (c) $Re = 60.6$; and (d) $Re = 91.0$. [from Haward et al. [7]] . . . . . 4

2.1 Pictorial representation of the two types of bifurcations: (a) supercritical and (b) subcritical. [$y$] represents a bifurcation parameter, which is some measure of $y$ that captures the features of the transition. The solid line indicates a stable branch while a dotted line indicates an unstable branch [41, 42]. . . . . 15

2.2 Schematic of a serpentine channel. . . . . 16

2.3 Development and evolution of the flow structure of Newtonian fluid in curved tube shown by numerical simulation. a) Velocity vector in different sections in the elbow showing the Dean type vortices ($L = 20R$ entrance length). b) Three-dimensional flow patterns (helicity iso-surface value) and velocity vectors in different sections after the elbow ($L = 20R$ entrance length). [from Bernad et al. [46]] . . . . . 17

2.4 Secondary flow patterns (Dean vortices) in a rectangular channel. The flow patterns in the channel of aspect ratio 1 (same size for channel width($a$) and height($b$); $a = b$) and curvature ratio 8. With increasing Dean number ($D_e$) two pairs of additional vortices appear at the corners. [from Sugiyama et al. [47]] . . . . . 18

2.5 Schematic of a T-shaped mixer. . . . . 19

2.6 Steady engulfment regime in a three-dimensional T-mixer. (a) Vortical behaviour identified according to the $\lambda_2$-criterion at $Re = 160$ and iso-contours of tracers at different $y$-sections along the outlet channel. Vorticity component in the $y$-direction and in-plane velocity vectors at different sections (b) $y = 1$ and (c) $y = 3$; The thick lines locate the boundary of the vortices. [from Fani et al. [56]] . . . . . 20
2.7 Top views of different T-shaped microfluidic junctions to evaluate mixing performance when varying the angle of the opposing inlet channels. [from Sarkar et al. [60]] . . . . . 21
2.8 Schematic of a cross-slot device. . . . . 22
2.9 Two examples of stagnation point flows: (a) colliding streams and (b) anti-parallel streams. The dashed line shows the initial orientation of a vortex. [from Aryshev et al. [64]] . . . . . 23
2.10 (top) Pictorial representation of the vortex formation in two different colliding flow structures. (bottom) Experimental flow visualisations depicting the vortex formation.[from Aryshev et al. [64]] . . . . . 24
2.11 Vortical patterns in a cross-slot device for a Newtonian fluid when $Re > Re_{crit}$. In (a) and (b), the streamlines at the vertical streamwise plane. (Note: the dotted lines indicate to the location of the transverse section of the outflow channels). (c) Top view showing the flow features when unbalancing the inlet flow rates. [from Kalashnikov and Tsiklauri [37]] . 25
2.12 The cross-shaped micromixer used in the investigation of mixing by Wong et al. [65]. At the outlet channel, the static mixing elements. [from Wong et al. [65]] . . . . . 26
2.13 Particle trajectory distribution of the adaptive-design micromixer at $Re = 20$ from Shih and Chung [66]. In detail the three different mixing units preseting a convection-enhanced mechanism (vortex agitation). [from Shih and Chung [66]] . . . . . 27
2.14 Three dimensional nature of the flow at $Re = 113$. (a) 3D streamlines obtained numerically (in red) showing that the flow is highly three-dimensional. (b) Comparison between the experiments (grey-scale image obtained when Rhodamine is injected) and the numerical streamlines (in red). [from Oliveira et al. [68]] . . . . . 27
2.15 Two-dimensional symmetry breaking in steady flows. (a) The numerical 2D schematic of the cross-slot device from Poole et al. [9]. On the bottom, the break of symmetry on the recirculation zones when $Re > Re_{crit}$: (a) Re = 1500; asymmetric growth of recirculation regions beyond bifurcation: (b) Re = 1540, (c) Re = 1580, and (d) Re = 1600. [from Poole et al. [9]] . . . . . 28

2.16 Symmetry breaking in three-dimensional steady flows. On top, a 3D schematic diagram of the cross-slot device along with 3D rendering of a vortex structure observed for the flow of water at $Re = 75.8$ in a cross slot with aspect ratio 1 ($\alpha = 1$). On the bottom, confocal experimental imaging (($a$)-($d$)) and numerically generated streamlines (($e$)-($h$)) depicting the evolution of flow structures in the $y$-$z$ plane and $x = 0$ for Newtonian fluid flow in the cross-slot device with aspect ratio 1 ($\alpha = 1$) under the following conditions: (a), (e) $Re = 15.2$; (b), (f) $Re = 42.8$; (c), (g) $Re = 60.6$; and (d), (h) $Re = 91.0$. The numerical result shown in (f) is one of two possible solutions at this $Re$ as a symmetric solution can also be obtained [7]. [from Haward et al. [7]] . . . . . 29
2.17 (i) The bifurcation parameter ($\psi_{expt}$) applied to different aspect ratio ($\alpha$) when varying Reynolds number ($Re$) at the experimental cross-slot device. The inset shows experimental and numerical critical Reynolds numbers for the instability transition in different aspect ratio geometries ($\alpha$). (j) The numerical bifurcation parameter ($\psi_{num}$) as a function of the control parameter, $\epsilon$, fitted with a Landau sixth-order polynomial. [from Haward et al. [7]] . . . . . 30
2.18 Schematic of a mixing-separating cell. . . . . 31
2.19 Numerical and experimental studies of flow field within a mixing-separating cell from early 1980s [69]. At $Re = 5$, both cases show a stagnation point at the centre of symmetry for a wide gap size – ($5H = 25$mm) five times the height of the channel. [from Cochrane et al. [69]] . . . . . 32
2.20 Vortical behaviour in the experimental studies within a mixing-separating cell at $Re = 25$. The unavailability of a very refined mechanism for controlling the flow rates limited the experimental conditions. [from Walters and Webster [70]] . . . . . 33
2.21 Numerical studies showing the vortical flow within a wide gap ($g = 5H = 25$mm) mixing-separating cell with varying $Re$. [from Walters and Webster [70]] . . . . . 34
2.22 (a) Typical two-dimensional flow a few seconds after starting motion from rest showing the stagnation point flow present at low $Re$. (b) Side views of vortex formation process at $Re = 500$. Note: Top flow is from left and bottom flow is from right. [from Humphrey and Li [71]] . . . . . 35

2.23 On top, fluid velocity magnitude contour inside a cavity with aspect ratio ($\lambda = 3$) at different Reynolds number. At the bottom, colour online representing the LBM simulations of particle trajectory. (a) $Re = 74$, (b) $Re = 123$, (c) $Re = 230$ and (d) $Re = 243$. The velocity magnitudes are computed on a symmetry plane ($z = 1.73$). The limit cycle orbit at $Re = 123$ and $Re = 230$ is illustrated in the figures. [from Haddadi and Di Carlo [74]] . . . . . 36
2.24 Shear flow generated by sliding one plate on top of another. Shear and normal forces may be supplied to keep the plates at a fixed distance. . . 38

3.1 A schematic of an apparatus for flow visualisation of the cross-slot geometry. (a) Schematic diagram of a cross-slot device. (b) Design of a microfluidic cross-slot device allowing direct observation of the $y-z$ plane at $x = 0$. The device is vertically mounted on an inverted microscope with a long working distance lens, enabling a direct view of the centre of the geometry where the spiral vortex instability forms. (c) A prototype microfluidic cross-slot device fabricated in fused silica. (d) Photograph illustrating the experimental setup with the cross slot mounted on an inverted microscope [from Haward et al. [7]]. . . . . 47
3.2 SEM (Scanning Electron Microscopy) images of the mixing-separating microchannel resulting from the micromachining process. (left) Top view showing measured channel width and wall thickness. (right) Inclined view to show the wall and channel height. . . . . 48
3.3 (a) A scheme illustrating the experimental apparatus of a microfluidic mixing-separating cell device allowed for direct observation of the $x - y$ plane at $z = 0$ and the characteristic channel dimensions ($H = W = 500\mu$m; $g = 5H = 2.5$mm; $a = H/5 = 100\mu$m). The origin is placed at the geometric centre of the device gap ($g$). The rig is mounted on an inverted microscope fitted with a filter cube. A pulsed Nd:YAG laser is used to excite the dyed fluid, and a CCD camera enables to capture the instability formation [notes: 1-not to scale; 2-camera FOV (field of view): 3.2mm x 2.4mm]. (b) The exploded view of the prototype microfluidic device rig. The channels were micro-machined in brass and encased in polyoxymethylene. A 6.5mm thick upper wall fabricated from borosilicate glass to obtain a sealed condition while allowing the flow structure to be visualised. (c) Photograph illustrating the experimental rig set-up assembled. . . . . 50
3.4 Pressure transducer calibration curves. . . . . 51

3.5 Design of the channels micro-machined in brass and encased in polyoxymethylene. A 6.5mm thick upper wall fabricated from borosilicate glass to obtain a sealed condition while allowing the flow structure to be visualised. Note: The immediate availability of the images provides an instantaneous feedback during the experimental setup. . . . . 52
3.6 Schematic showing the different heights for initial and final CaBER plate positions. . . . . 55
3.7 Plot of viscosity as a function of shear rate for the polymer solution. Figure shows three different samples of a single fluid batch in three different days. △ Sample 1: 17/08/17, ◯ Sample 2: 24/08/17, □ Sample 3: 31/08/17 . . . . . 56
3.8 Extensional rheology data (CaBER) showing the time dependence of the normalised diameter of the polymer solution filament. The full red line is an exponential fit within the elasto-capillary range (refer to equation 3.4). The figure shows measurements of the time decay of minimum diameter of the filament for different samples of a single fluid batch in three different days. △ Sample 1: 17/08/17, ◯ Sample 2: 24/08/17, □ Sample 3: 31/08/17 . . . . . 57

4.1 Geometry of the mixing-separating cell used to perform the numerical simulations. . . . . 64
4.2 Schematic of the imposed inlets and outlets in the numerical method. . 64
4.3 Definition of the centre planes $x-y$, $x-z$, and $y-z$. . . . . 65
4.4 Detail of the refinement rate at the central gap of the numerical mesh M4. 65
4.5 Variation of the velocity profile associate to the reverse flow ($v-$velocity component) along the gap size (line along $x$-direction at $y=0$ and $z=0$) for the different meshes at a fixed Reynolds number ($Re=30$). The inset zooms into the region around the maximum value of $v/U_b$. . . . . 66
4.6 Effect of mesh refinement on the maximum value of the $v-$velocity component ($v_{max}/\mathrm{U_b}$) along the gap channel for $Re=30$. M4 shows a low percentage error (0.51%) for a reasonable number of cells (855000). . . . 67
4.7 Variation of the angle ($\alpha$) between inlets and outlets arms of the a mixing-separating cell. (left to right) From the so-called 'mixing-separating' (0° angle) to a so-called cross-slot (90° angle) where the inlet and outlet channels are orthogonal. . . . . 68
4.8 Schematic showing the main variables (angle $\alpha$, height of the central gap $h$, and gap size $g$) when varying the angle between the pair of inlets and outlets of the mixing-separating cell device. . . . . 68

4.9 Schematic of the cross-slot micro-geometry depicting the entrance plane of the outlet arm, and an example of transverse velocity profile ($w$-component) along the centreline of this plane. . . . . 70
4.10 Detail of the refinement rate at the centre of the numerical mesh C4. . . 73
4.11 Effect of mesh refinement on the maximum normalised velocity ($u_{max}/U_b$) at the inlet channel in fully-developed region. . . . . 74
4.12 Evaluation of the transverse maximum velocity ($w_{max}/U_b$) and the normalized root mean square temperature ($T_{RMS}/\bar{T}$) at the inlet plane to the outlet arm when increasing the number of cells. Insets are streamlines showing spiral vortex structure on the centre plane of the cross for meshes C4 and C5. $Re = 100$ and $Pr = 100$ . . . . . 74
4.13 Comparison of Mesh C4 (left) and Mesh C5 (right) at $Re = 50$ (top), and $Re = 100$ (bottom). . . . . 76

5.1 Friction factor-Reynolds number product ($fRe$) function of Reynolds number. The error bars indicate that the measured values of $fRe$ and Darcy's equation are within 3% when $Re > 5$. At the lower range of $Re$ ($Re < 5$), there is a significant amount of scattering due to large relative uncertainties (refer to chapter 3). . . . . 79
5.2 Experimental flow visualisation images with rhodamine-tinted stream (white) and on undyed stream (black) prior the onset of any instability. (a) $Re = 2$ and (b) $Re = 29$. The experimental visualisations are superimposed with streamlines at the centre plane of the geometry from the equivalent simulations. . . . . 80
5.3 (a) The interface between the two fluid streams for different $Re$ obtained using an edge detection, showing an increase in interface angle (with respect to the $x$-axis) with increasing $Re$. Image processing phases identifying edges between the two streams at Re 2: (b) raw figure, (c) binary image, and (d) edge detection. . . . . 81
5.4 Experimental flow visualisation (left-hand side) and numerical streamlines (right-hand side) of the flow in the mixing-separating device at different $Re$. (a) $Re = 29$, before onset of instability; (b) $Re = 30$, single vortex after bifurcation; (c) $Re = 40$, two separate co-rotating vortices; (d) $Re = 60$, the distance between the two vortices has increased. . . . . 82
5.5 Experimental flow visualisation for different $Re$ showing the delimited area of interest (yellow box) for the experimental quantification of stream interaction. . . . . 83
5.6 characterisation of the instability using the mixing parameter, $M$, from the experiments, exhibiting the square-root growth expected of a supercritical instability close to onset. . . . . 84

5.7 The variation of the bifurcation parameter used to analyse the numerical data ($\lambda_{ci,max}H^2/\nu$) with $Re$ for $g = 5H$. The critical Reynolds number is 29 and the inset shows a square-root growth near to the instability onset ($30 < Re < 50$). For $Re$ beyond the region of square-root growth, $50 < Re < 185$, the instability parameter grows linearly (with a gradient $\approx 4.6$). . . . . 85
5.8 The variation of the instability growth parameters $M$ (experimental) and $\lambda_{ci,max}H^2/\nu$ (numerical) with $Re$ for $g = 5H$, showing excellent agreement in the region close to onset ($30 < Re < 45$). . . . . 86
5.9 The change in flow pattern between the base flow (no vortices, $Re = 29$), and the bifurcated flow just after onset (a single large vortex, $Re = 30$) in a mixing-separating device with $g = 5H$. The colormap shows the swirling strength ($\lambda_{ci}H^2/\nu$) and the vectors show the direction of the velocity field. . . . . 87
5.10 The evolution of the vortices with $Re$ in a mixing-separating device ($g = 5H$). From $Re = 32$ to $Re = 50$, the cores of the two vortices gradually alter their positions. In the region $50 < Re < 90$, the vortices do not alter their positions significantly. The vortices merge into a large vortex at $Re = 120$. Rotational symmetry is preserved for all $Re$. Vectors show the direction of the velocity only. . . . . 88
5.11 Variation of the bifurcation parameter for the device with a gap size of $3.86H$. The instability critical $Re$ number is 26. Close to the onset, the bifurcation parameter $\lambda_{ci}$ fits a square root function. Similar to a $5H$ gap, when $Re > 50$, the growth of the instability is linear with a gradient $\approx 4.5$. . . . . 89
5.12 The evolution of the vortices with $Re$ in a mixing-separating device ($g = 3.86H$). Before the instability there are no vortices ($Re = 26$), at onset two vortices appear ($Re = 27$) and then merge as $Re$ is increased ($27 < Re < 50$). One large vortex is formed and persists at higher $Re$ (e.g. $Re = 90$). Rotational symmetry is preserved for all $Re$. Vectors show the direction of the velocity only. . . . . 90
5.13 Variation of the bifurcation parameter for the device with a gap size of $2.61H$. The critical $Re$ number is 23. Close to the onset, the bifurcation parameter fits a square root function. Similar to the $g = 5H$ and $g = 3.86H$ gaps, when $Re > 50$, the growth of the instability is linear with a gradient $\approx 4.3$. At $Re = 84$ the second supercritical instability occurs (seen in the square-root growth of $w_{max}/U_b$) and interrupts the linear growth of $\lambda_{ci}$ parameter until $Re > 100$. . . . . 91

5.14 The evolution of the vortices with $Re$ in a mixing-separating device ($g = 2.61H$). Before the instability there are no vortices ($Re = 23$), at onset two vortices appear ($Re = 24$) and then merge as $Re$ is increased ($Re \approx 50$). One long, slender vortex spanning the channel is formed and persists at higher $Re$ (e.g. $Re > 70$). The onset of the second instability at $Re = 84$ has no significant effect on the vortex in this plane. Rotational symmetry is preserved for all $Re$. Vectors show the direction of the velocity only. . . . . 92

5.15 Streamlines on the $y$-$z$ plane of the $g = 2.61H$ device before and after onset of the $w_{max}/U_b$ instability. At $Re = 84$ the flow is reflectionally symmetric about $z = 0$ and $y = 0$, at $Re = 85$ the symmetry in both these planes is broken and the $w$-component of velocity on the $z = 0$ plane is non-zero. The extent of the asymmetry grows as $Re$ is further increased (e.g. see $Re = 90$) although rotational symmetry is preserved throughout. The streamlines are 3D and coloured by the inlet from which they originate, they therefore leave the plane in this 2D plot. . . . 93

5.16 Variation of the bifurcation parameter for the $g = 2H$ geometry. There is no instability in $\lambda_{ci}$, which is zero for all $Re$. Instead, the first and only instability is similar to the second instability in the $g = 2.61H$ device, where the $w_{max}/U_b$ parameter highlights a supercritical bifurcation, i.e. it fits a square root function near to onset ($Re_c = 51$) and no hysteresis. 94

5.17 Streamlines on the $y$-$z$ plane of the $g = 2H$ device before and after onset of the $w_{max}/U_b$ instability. At $Re = 52$ the reflectional symmetry is broken and the $w$-component of velocity on the $z = 0$ plane is non-zero. This is an engulfment instability, and as $Re$ is further increased (e.g. see $Re = 60$) a large spiral vortex is formed providing significant mixing of the two fluid streams. Rotational symmetry is preserved throughout. The streamlines are 3D and coloured by the inlet from which they originate, they therefore leave the plane in this 2D plot. . . . . 95

6.1 Stagnation point generated when varying the angle between the pair of opposing inlet and outlet channels. From a mixing-separating cell device to a cross-slot device. . . . . 98

6.2 The maximum transverse velocity ($w_{max}/U_b$) along the centreline $y = 0$ on the plane $y$-$z$ (refer to figure 6.3 top right-hand side) with increasing and decreasing Reynolds number on different angle geometries. From 90° angle to 60°, the instability changes from a subcritical pitchfork with hysteresis to a non-hysteretic supercritical. Moreover, the instability growth parameter ($w_{max}/U_b$) is zero for the $Re$ numbers tested ($Re <$ 140) on geometries 30° and 0°. (Note that the data presented here for a 90° angle geometry was extracted from our previous study [40].) . . . . 99

6.3 (a) Numerically-determined streamlines depicting the evolution of the flow structure in the plane $x$-$y$ and $z = 0$ for fluid flow in a 60° angle geometry. Panels (a) show the results for progressively increasing $Re$. (b) The colour scale indicates the dimensionless vorticity ($\omega_x H/U_b$) over the plane $x = 0$, and superimposed velocity vectors exhibit the directionality of the flow in the cross-section. The flow breaks its reflectional symmetry when a nonzero transverse velocity component appears for $Re > Re_c$, although (a) shows a vortical behaviour for $Re < Re_c$. . . . . 100

6.4 Flow development with increasing $Re$ illustrated by numerical streamlines in the plane $x$-$y$ and $z = 0$ for a 30° angle geometry. Panels show with progressively increasing $Re$ a central vortex appears for $Re = 20$. By increasing $Re$, the central vortex splits into a pair of co-rotating vortices, and secondary motions rise at the edge of the corners near to the beginning of the outlet channels. . . . . 102

6.5 Top panels: Numerical streamlines in the plane $x$-$y$ and $z = 0$ and the isosurfaces of vortex core regions at $Re = 90$ for (a) 60° and (b) 30° angle geometry. Bottom panels: The colour scale indicates the dimensionless vorticity ($\omega_x H/U_b$) over the plane over the central cross-section plane of the channel (plane $y$-$z$ plane and $x = 0$) superposed by the velocity vectors showing the directionality of the flow. . . . . 103

6.6 Cross-sectional velocity magnitude (normalised by the bulk flow velocity) on four different planes along the outlet arm with distances of $0H$ (outlet starting plane), $2H$, $4H$, and $8H$ channel heights (or hydraulic diameter) from the entrance of (a) a 60° angle geometry, and (b) 30° angle. The flow cannot restore its parabolic flow profile even after $8H$ distance from the entrance for all $Re$ numbers tested when the angle is 60°. Conversely, for a 30° the flow field is symmetric and can reach the fully developed form for $20 < Re < 90$. . . . . 104

7.1 (a) Experimental Steady flow pattern for $Wi = 0$ using fluorescent dye (average over 50 images at 8Hz) (b) Steady flow for $Wi = 1.9$ (c) onset of flow fluctuations on time: $Wi = 2.0$ . . . . . 108

7.2 (a) Interface between the two fluid streams detected by the edge detection algorithm. (b) The algorithm calculates the area delimited by the red line in detail. . . . . 109
7.3 Temporal variations of the parameter $N$ for flow at $Wi = 2.0$ in the mixing-separating device. . . . . 110
7.4 Single-sided amplitude spectrum of $N$ for flow at $Wi = 2.0$ in the mixing-separating cell. . . . . 111
7.5 (top) Quasi-steady signal of $N(t)$ for $Wi = 1.8$ before the bifurcation ($Wi_c$). (bottom) FFT of the signal showing the high frequencies to be excluded from the periodic states when ($Wi > Wi_c$). . . . . 112
7.6 (a) An example of a Hann window in a rounded waveform, and a proposed mixed window (Hann/Rectangular with $r = 0.15$). Note that The mixed window rapidly attenuates the edges of the signal to zero. (b) Applying the windowing for the same example signal using two different windows from the figure above. (c) FFTs of the example signal with and without applying the detrending and windowing methods. The left represents the FFT applied with a Hann window method and Right the proposed mixed window (Hann/Rectangular with $r = 0.15$). . . . . 113
7.7 Single-sided amplitude spectrum of $N$ for flow at different $Wi$ numbers in the mixing-separating cell. The inset shows the full spectrum ($f < 25$) and the plot shows a zoom at the low frequencies ($f < 5$). . . . . 114
7.8 fluctuations on time of the quantity $N - \bar{N}$ before and after the onset of the instability at $Wi = 2.0$. Clearly, the amplitude of $N$ is higher when far from the onset (for instance, $Wi = 4.2$). . . . . 115
7.9 Experimental flow visualisation in the mixing-separating cell micro-geometry using fluorescent dye (Rhodamine-B) for different Weissenberg numbers ($Wi$). Red box delineating the interface between the two streams for calculations of the $N$ parameter. Figure shows different instants in time of the fluctuations when $Wi > Wi_c$. . . . . 116
7.10 Temporal variations of the parameter $N$ for flow in the mixing-separating device at different Weissenberg numbers ($Wi$). Figure shows the variation of $N$ before and after the bifurcation ($Wi > Wi_c$). . . . . 117
7.11 The $N_{RMS}$ when varying $Wi$ number for data points obtained from our experimental results. The data are fitted with a function of the form $a(Wi - Wi_c)^b$, with $b$ fixed at 0.5 (characteristic of a supercritical instability). . . . . 118

8.1 Schematic of a cross-slot device. . . . . 119
8.2 The relationship between temperature and viscosity fitting a Sutherland viscosity law. . . . . 122

8.3 Symmetric flow and temperature distribution patterns in the cross-slot micro-geometry, at the centre of the cross-slot and $20d$ downstream of the stagnation point in each outlet arm for $Re = 36.6$. (a) Grayscale images illustrating the development of isothermal flow structure (b) Experimental visualisation of the temperature-sensitive dye and (c) Numerical temperature distribution. . . . . 123
8.4 Asymmetric flow and temperature distribution patterns in the cross-slot micro-geometry, at the centre of the cross-slot and $20d$ downstream of the stagnation point in each outlet arm for $Re = 46.3$. (a) Grayscale images illustrating the development of isothermal flow structure (b) Experimental visualisation of the temperature-sensitive dye and (c) Numerical temperature distribution. . . . . 125
8.5 Asymmetric flow and temperature distribution patterns in the cross-slot micro-geometry, at the centre of the cross-slot and $20d$ downstream of the stagnation point in each outlet arm for $Re = 80.6$. (a) Grayscale images illustrating the development of isothermal flow structure (b) Experimental visualisation of the temperature-sensitive dye and (c) Numerical temperature distribution. . . . . 126
8.6 Experimental ([E], in red), simulation with constant viscosity ([SCV], in blue), and simulation with temperature dependent viscosity ([SVV], in purple) probability density function (PDF) for the normalised temperature ($\theta$) in the FOV $20d$ downstream of the cross-slot centre: (a) symmetric flow regime ($Re = 36.6$), (b) asymmetric flow regime ($Re = 46.3$), and (c) asymmetric flow regime ($Re = 80.6$). Right hand side shows temperature distribution, $20d$ downstream of the cross, to highlight data on which PDFs are based. See figures 8.3, 8.4, and 8.5 for colour map values. 128
8.7 Constant viscosity (left) and variable viscosity (right) temperature distributions at $Re = 80.6$ . . . . . 129
8.8 Normalized temperature ($\theta$) variation along the line $x = 0$ for constant and temperature-dependent viscosity at $Re = 80.6$ . . . . . 130
8.9 The maximum transverse velocity ($w_{max}/U_b$) along the centerline ($z = 0$) of the inlet to the outlet arm with increasing and decreasing Reynolds number. The critical Reynolds numbers ($Re_c$) are 39 when increasing $Re$ and 53 when decreasing $Re$. . . . . 131
8.10 Maximum transverse velocity ($w_{max}/U_b$) along the centerline ($z = 0$) with increasing and decreasing Reynolds number. Insets (a, b, c) from figure 8.3 where $Re = 36.6$, (d, e, f) from figure 8.4 where $Re = 46.3$, and (g, h, i) from figure 8.5 where $Re = 80.6$. . . . . 132

8.11 Normalised $T_{RMS}$ (Eq. 4.11) as function of inverted Graetz number, $Gz^{-1} = x/(dRePr)$, for various Reynolds number ($Re$) and $Pr = 1$ Prandtl number. Dashed curves represent symmetric cases; solid curves lines represent asymmetric cases. . . . . 134
8.12 Normalised $T_{RMS}$ as function of inverted Graetz number, $Gz^{-1}$, for various $Re$ and $Pr = 10$. Dashed curves represent symmetric cases; solid curves lines represent asymmetric cases. . . . . 134
8.13 Normalised $T_{RMS}$ as function of inverted Graetz number, $Gz^{-1}$, for various $Re$ and $Pr = 100$. Dashed curves represent symmetric cases; solid curves lines represent asymmetric cases. . . . . 135
8.14 Heat transfer enhancement, representing the $T_{RMS}$ ratio calculated between the asymmetric and symmetric cases for $Re$ and $Pr = 1$. . . . . 135
8.15 Heat transfer enhancement, $T_{RMS}$ ratio between the asymmetric and symmetric cases for $Re$ and $Pr = 10$. . . . . 136
8.16 Heat transfer enhancement, $T_{RMS}$ ratio between the asymmetric and symmetric cases for $Re$ and $Pr = 100$. . . . . 136
8.17 The evolution of the bifurcation parameter, maximum transverse velocity ($w_{max}/U_b$), with varying $Gz^{-1}$ along the outlet channel for $Pr = 10$. . . 137
8.18 Normalised $T_{RMS}$ (Eq. 4.11) as function of the normalised position ($x$) along the outlet channels, $x/d$, for various Reynolds number ($Re$) and $Pr = 1$ Prandtl number. Dashed curves represent symmetric cases; solid curves lines represent asymmetric cases. . . . . 138
8.19 Normalised $T_{RMS}$ as function of the normalised position ($x$) along the outlet channels, $x/d$, for various $Re$ and $Pr = 10$. Dashed curves represent symmetric cases; solid curves lines represent asymmetric cases. . . . 138
8.20 Normalised $T_{RMS}$ as function of the normalised position ($x$) along the outlet channels, $x/d$, for various $Re$ and $Pr = 100$. Dashed curves represent symmetric cases; solid curves lines represent asymmetric cases. 139
8.21 Heat transfer enhancement, representing the $T_{RMS}$ ratio calculated between the asymmetric and symmetric cases for $Re$ and $Pr = 1$ as function of the normalised position ($x$) along the outlet channels, $x/d$. . . . . 139
8.22 Heat transfer enhancement, $T_{RMS}$ ratio between the asymmetric and symmetric cases for $Re$ and $Pr = 10$ as function of the normalised position ($x$) along the outlet channels, $x/d$. . . . . 140
8.23 Heat transfer enhancement, $T_{RMS}$ ratio between the asymmetric and symmetric cases for $Re$ and $Pr = 100$ as function of the normalised position ($x$) along the outlet channels, $x/d$. . . . . 140

8.24 Variation of the ratio between mean Nusselt number for the cross-slot and straight channel for increasing and decreasing Reynolds numbers under constant wall temperature ($CWT$) boundary condition. . . . . 141
8.25 Mean Nusselt number ratio as a function of the product of $Re$ and $Pr^n$. In the correlation shown, $n = 0.084$. . . . . 142

9.1 (a) A scheme illustrating the experimental apparatus of a microfluidic cross-slot device allowed for direct observation of the $x$-$y$ plane at $z = 0$ and the characteristic channel dimensions ($H = W = 500\mu$m; $g = 5H = 2.5$mm; $a = H/5 = 100\mu$m). The origin is placed at the geometric centre of the device gap ($g$). The rig is mounted on an inverted microscope fitted with a filter cube. A pulsed Nd:YAG laser is used to excite the dyed fluid, and a CCD camera enables to capture the instability formation [notes: 1-not to scale; 2-camera FOV (field of view): 3.2mm x 2.4mm]. (b) The exploded view of the prototype microfluidic device rig. The channels were micro-machined in brass and encased in polyoxymethylene. A 6.5mm thick upper wall fabricated from borosilicate glass to obtain a sealed condition while allowing the flow structure to be visualised. (c) Photograph illustrating the experimental rig set-up assembled. . . . . 151

B.1 Symmetry analysis at the $x$-$y$ plane with increasing $Re$. The results show that the inertial effects breaks reflectional symmetry in the flow field. 154
B.2 Normalised velocity magnitude at the $x$-$y$ plane for different Reynolds number. . . . . 154

C.1 The $w_{max}/U_b$ parameter applied at the $x$-$y$ plane for different gaps with increasing $Re$. . . . . 155
C.2 Enlarged schematic diagram of the cross-slot micro-geometry depicting the inlet plane of the outlet arm and the transverse velocity profiles along the centreline of this plane with increasing and decreasing Reynolds number. . . . . 156

# Acknowledgement

*None of what I have accomplished would have been possible without the support of my family;*
***My parents and my sister:*** *for my parents' belief in the value of a good education, I shall be forever grateful. I am truly thankful to have them in my life.*
***My wife:*** *for all her love, strength, and encouragement. Life has given us a beautiful family, a happy home, and love for each other.*

---

I wish to express my gratitude to my supervisors, Dr David Dennis and Professor Robert Poole, without whose guidance this work would not have been possible. I would also like to thank Waleed Abed and Mahdi Davoodi for helping me when I first started my research. Besides, a special thanks to Tiago Henriques for his help and support − an eternal friendship Brazil and Portugal.

It was a privilege to have worked with Rishav Agrawal, Oguzhan Der, Owolabi Bayode, Abdul Ismail, Osama Maklad, Victor Ibezim, Konstantinos Zografos, and Henry Ng, they helped create a stimulating atmosphere for research and contributed immensely to my learning experience. Outside the office, Helio Quintanilha, Jack Carter-Hallam, all mechanical workshop's technicians, and all friends who made my stay in Liverpool enjoyable − specially Guilherme & Carol and Mauricio & Rosi.

# Chapter 1

# Introduction

## 1.1 Motivation

Microfluidic devices are tiny chips that can, for example, sort out disease biomarkers, cells, and other small structures in samples such as blood by using microscopic channels incorporated into the devices [1]. In a fictitious scenario, if a doctor obtains a small finger prick from the patient, the resultant tiny droplet of blood is used to make 50 measurements in about 10 to 15 minutes. Then, the information acquired is instantly added to the patient's digital health record. This measurement capability could become an invaluable asset to help track and improve the patient's health over time. For example, this feature could be used to detect disease processes before they become serious, such as in cancer. During the time in which the disease is still very treatable, this measurement capability could be indispensable for diagnostic and preventive medicine. However, there is one problem with this scenario: this device does not exist, which illustrates a technology lacuna and how it intersects our lives. What we can do with technology is crucially defined by our tools and knowledge; if we want new capabilities and new possibilities, we need to create new tools [1].

Compared to traditional macro-scale mixing methods, microfluidic devices provide a good alternative at a lower cost, improved portability, and shorter operational time. For example, they have the potential to reduce blood-processing time from an hour to a few minutes [2]. However, many problems arise when designing a microfluidic device, and scientists can struggle to find solutions due to the complexity of each problem; to solve such problems without careful consideration and targeting would be unlikely to provide any serious physical insight into the fundamental problems themselves. For example, miniaturised valves have a tendency to stick irreversibly to the substrate, making it necessary to minimise the contact surface area (as was necessary for the miniaturised motor) [3].

Currently, microfluidic researchers are undertaking the task of creating in vivo or-

[1] Professor Greg Nordin (Brigham Young University) from his TEDx talk in 2018. *https://www.ted.com/tedx/events/24444*

gans on a microchip to mitigate the soaring costs of R&D. The objective is to produce a set of sophisticated in vitro assays with which drugs could be tested, with the aim of increasing predictability (hit rate) of a new drug before animal testing and human clinical trials. Such devices have been used to diagnose sickle cell disease utilising blood vessel-on-a-chip devices [4]. Due to the absence of moving parts and the relative ease and accessibility of many of these technologies, it has become possible to integrate several elements on the same chip and create lab-on-chip devices. Even though the difficulties involved in the fabrication of these devices have been managed, control of the fluid flow within them is still a problem that needs to be tackled.

This project intends to explore flow instabilities in different micro-geometries in order to enhance mixing and heat transfer. Inertial (or purely-inertial) instabilities are related to Newtonian fluids in laminar regime presenting a complex behaviour. Where steady symmetry-breaking bifurcation occurs and convective mixing regime arises. By adding a small amount of flexible high-molecular-weight polymers to a Newtonian solvent, the inertial hydrodynamic flow behaviour can be considerably modified. A new instability, so-called elastic (or purely-elastic) instabilities, can arise even at very small Reynolds number as a consequence of nonlinearities associated with the elasticity of fluid containing flexible polymers (viscoelastic fluid) within different simple geometries, for instance, a T-shaped mixer, a cross-slot or mixing-separating cells. To narrow the scope to some extent, the focus of this project is on the fundamentals of particular flow instabilities in the micro-scale: principally, those that present stagnation point flows.

## 1.2 Inertial instabilities in microfluidics

As suggested by the title of this dissertation, we are interested in nonlinear behaviours of flowing fluids in different micro-geometries. Compared to traditional methods, micro-scale devices need a small amount of sample to analyse with faster reactions. Additionally, micro-scale geometries have often been associated with negligible effects of inertia due to their small dimensions. Thus, Newtonian fluids are difficult to be well mixed at short length and reasonable time because the flow in these micro-scale geometries is inherently steady and laminar. Therefore, the use of conventional geometrical shape (e.g., straight microchannel) in these micro-devices requires more than several tens of centimetres to achieve the acceptable performance of mixing, which is unacceptable with these compact microdevices.

The rich physics and complex flow behaviours in microfluidic devices have recently drawn the attention of scientists from various disciplines in order to improve the hydrodynamic and thermal characteristics of these micro-systems using alternative techniques that depend on fluid inertia [5, 6]. Thus, micro-scale geometries have been designed in a particular way to increase the contact area and the contact time between fluids, for example, a serpentine channel, a T-shaped device, a cross-slot geometry, and a

mixing-separating cell.

For Newtonian fluids, nonlinear flow behaviors are driven purely by inertia. In a recent review by Haward et al. [7], the significance of the inertial instability in a cross-slot configuration is pointed out and its applications are discussed. Cross-slots, shown schematically in Figure 1.1, exhibit a simple design and is composed of four intersecting channels with two opposing inlets and two opposing outlets. The flow in the cross-slot is easy to control and is able to generate a stagnation point at its geometrical centre. A major characteristic of stagnation point flows is that either fluid elements are subjected to high-velocity gradients for a limited time as they pass through the surrounding region of the stagnation point, or fluid elements trapped at the stagnation point are subjected to high strain rates for an undefined time. For Newtonian fluid streams imposed at the opposite inlets of a cross-slot micro-geometry, a fluid flow bifurcation appears depending upon the Reynolds number ($Re$) at which the flow becomes asymmetric, and a spiral vortex develops due to an engulfment flow regime. The instability can potentially assist in mixing techniques for flows with small Reynolds numbers [7].

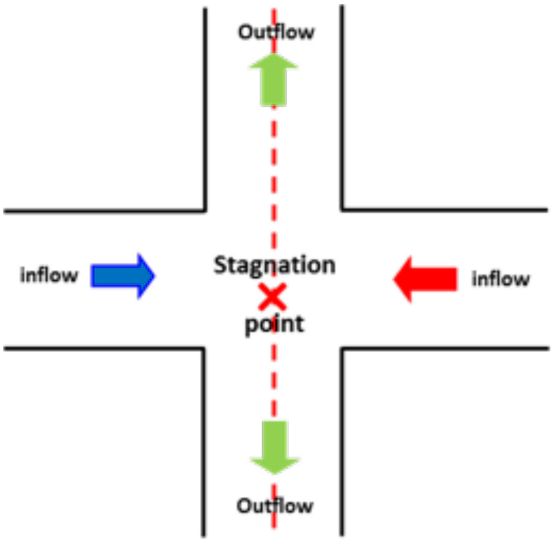


Figure 1.1: Schematic diagram of a cross-slot geometry showing the relevant details: two opposing inlets, two outlets, and the stagnation point.

The Reynolds number ($Re$) is defined mathematically as $Re \equiv \rho U l/\mu$. $Re$ is characterised by one single spatial scale $l$ −characteristic length−, the characteristic velocity of the fluid ($U$), the density ($\rho$), and the dynamic viscosity ($\mu$). For Newtonian fluids, nonlinear flow behaviours are driven purely by inertia. At and above the critical $Re$ value, an instability occurs, and the stable, two-dimensional, and laminar flow within a cross-slot device gives way to a complex three-dimensional flow, which is also steady (Figure 1.2). The characterisation of the flow's stability around a critical Reynolds number ($Re_c$) is therefore essential in understanding device mixing capabilities.

To date, no work has been reported that characterises the effect of the spiral insta-

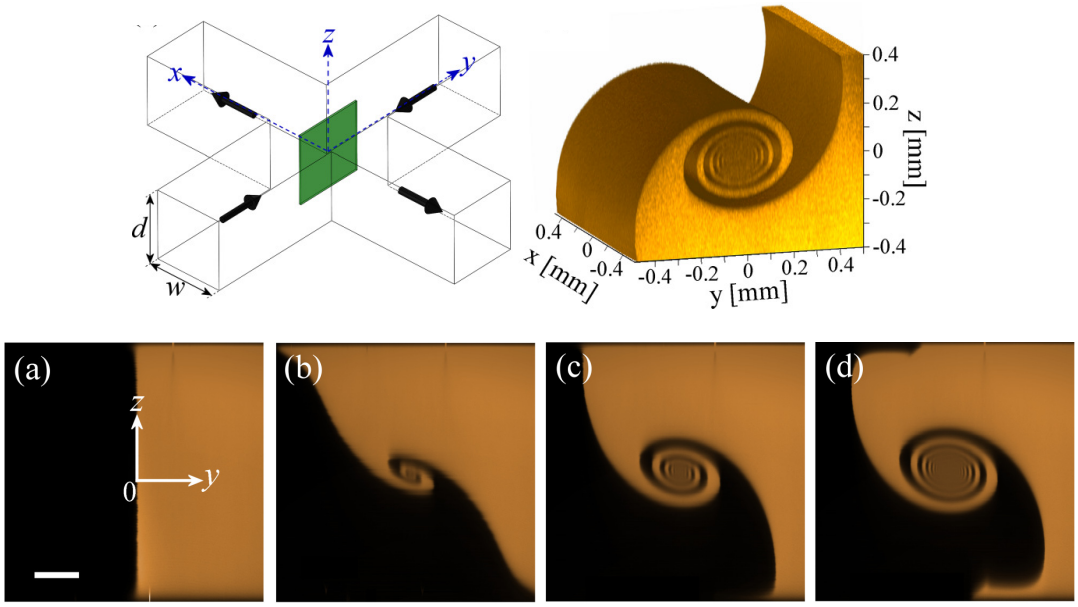


Figure 1.2: Spiral instability in a cross-slot geometry: Confocal experimental imaging ((a)–(d)) showing the steady-symmetric flow and the symmetry-breaking bifurcation - spiral vortex structure (right). Newtonian fluid flow in the cross-slot device with aspect ratio 1 ($\alpha = 1$) under the following conditions: (a) $Re = 15.2$; (b) $Re = 42.8$; (c) $Re = 60.6$; and (d) $Re = 91.0$. [from Haward et al. [7]]

bility observed by Haward et al. [7] on heat transfer. Given the potential applications of improving the heat transfer performance of microfluidic devices (for active cooling, for example), it is pertinent to investigate the influence of this inertial instability on heat transfer. With this idea in mind, and based on the simplicity of cross-slot designs, we investigated the potential of this instability in a cross-slot to promote convective heat transfer at low or moderate values of Reynolds numbers ($Re < 100$). Numerical simulations are exploited to characterise the heat transfer enhancement in greater detail (as the 3D velocity and temperature fields are available) than is possible with the limited experimental data. We also tested other thermal boundary conditions (i.e. uniform wall temperature), which allowed us to quantify the heat transfer enhancement (compared to a channel with no instability) using the Nusselt number.

A T-shaped micro-mixer device, which is a contraction of a cross-slot, has flow entering the channel from two opposite inlets, then reaching a stagnation point before turning 90° and being expelled down the outlet channel. Depending on the Reynolds number, a symmetry-breaking flow bifurcation occurs [8] and the behaviour of the flow after this instability has been shown to increase the mixing performance within microfluidic devices [9]. Three different regimes of laminar flow (symmetric stratified flow, symmetric vortex flow, and, beyond the instability, the so-called *engulfment flow* regime, which is asymmetric) were observed depending on the Reynolds number in the

outflow mixing channel [10, 11, 12, 13]. The instability in a T-shaped geometry is closely related to that reported in the cross-slot device.

The characteristics of fluid flow and mass transfer within square cross-section T-shaped and cross-shaped micromixers have been numerically and experimentally investigated by Ait Mouheb et al. [14, 15] in order to compare the mixing performances of the two geometric configurations. The experimental and numerical results showed that the mixing in the cross-shaped micromixer occurs at lower flow rates than in the T-shaped micromixer. This enhancement in mixing in the cross-shaped micromixer is attributed to the stronger vortex stretching and high shear rate. In addition, the cross-shaped micromixer induces a smaller pressure drop than the T-shaped micromixer due to the existence of two outflow streams. Haward et al. [7] demonstrated (experimentally and numerically) the mechanism of fluid mixing in cross-slot geometries with a range of aspect ratios (depth/width) of 0.4 to 3.87. The results revealed that fluid flow is steady and symmetric (the interface between fluid streams is sharp and vertical) at low Reynolds numbers. However, as the Reynolds number increases above a critical value ($20 < Re < 100$), which is dependent on the cross-slot aspect ratio, the laminar flow experiences a steady symmetry-breaking bifurcation and a spiral vortex structure is created oriented about the central axis of the outflow channels. This spiral instability, the onset of which is described by a Landau model analogous to that used near equilibrium tricritical points, can be harnessed to boost fluid mixing in the cross-slot geometry at these modest Reynolds numbers [7].

Another simple configuration with potential applications in micro-scale flows is the microfluidic mixing-separating cell (also referred to as the *H-geometry*) − two straight square parallel channels with flow from opposite directions interacting through a central gap that allows the streams to mix or remain separate. When compared to a cross-slot, a mixing-separating cell shows many similarities in the fluid motion. The cross-slot device with one pair of aligned arms rotated by 90° towards the other pair would lead to a mixing-separating cell with a $\sqrt{2}H$ gap size at the centre of the device (where $H$ represents the channel height). It is well known that cross-slot devices are sensitive to an inertial instability at modest Reynolds numbers [7]. However, the understanding of these instabilities in different geometries, such as a mixing-separating device and its variations, is very limited. Therefore, in this thesis, a particular aim is to harness a greater understanding of the inertial flow instabilities when varying the gap size in a mixing-separating microfluidic device (hence low $Re$). The characterisation of the flow before and after the bifurcation helps to predict the flow topology and locate the position and orientation of vortex structures within the device, which consequently benefits the design of microfluidic devices to manipulate flow conditions using laminar vortices (e.g. for particle entrapment or mixing).

Moreover, we use experimental results to validate three-dimensional numerical sim-

ulations of the cross-slot geometry. These simulations are exploited to characterise the heat transfer enhancement in greater detail than is possible with the limited experimental data. Furthermore, in the experiments, the surfaces of the cross-slot micro-geometry are considered to be adiabatic due to the material used to manufacture the cross slot. Using the simulations, we can also test other thermal boundary conditions (i.e. uniform wall temperature), which allows us to quantify the heat transfer enhancement (compared to a channel with no instability) using the Nusselt number.

## 1.3 Elastic instabilities in microfluidics

Viscoelastic fluids, materials that exhibit both viscous and elastic characteristics upon deformation, have been an interesting object of study to researchers in various areas. The most common type of fluids with viscoelasticity are polymeric liquids: melts and solutions of polymers. Owing to the elasticity of polymer molecules, as well as the nontrivial polymer-solvent and polymer-polymer interactions, the behaviours of these liquids under certain flow conditions and deformations can be drastically different from those of Newtonian fluids. Classical examples and applications are discussed in Bird et al. [16]. Another example of viscoelastic fluids are surfactant solutions that have formed worm-like micelles [17].

For Newtonian fluids, nonlinear flow behaviours are driven purely by inertia, the impact of which can be measured by the Reynolds number $Re$ (see previous section). For viscoelastic fluids, inertia is no longer the sole source of nonlinearity. Microscopic structures of the fluid, including (e.g. polymeric liquids) individual polymer molecules as well as high-order structures (e.g. clusters and networks) of polymers (in concentrated solutions and melts), interact in a nontrivial way with the macroscopic momentum and mass balances. Therefore, nonlinearity can be significant even at very low $Re$.

The Weissenberg number – $Wi$ – ($Wi \equiv \lambda\dot{\gamma}$) is introduced, and it represents the time scale of the relaxation of polymer $\lambda$ nondimensionalised by the inverse of the characteristic strain rate $\dot{\gamma}$ of the flow. Instabilities can occur even at extremely low $Re$, where inertial effects are negligible; these types of instabilities driven completely by elasticity are very often called as "purely-elastic" or "inertia-less" instabilities [18, 19, 20, 17].

There are numerous problems of interest in the whole range of $Re$ and $Wi$. Different types of elastic instabilities are reported in various experimental conditions, and the best-understood are the so-called "hoop-stress" instabilities, which occur in viscoelastic fluid flows with curved streamlines [18, 21, 19, 20, 22], and instabilities in flow geometries involving stagnation points, such those in rheometric flows [23, 24] and microfluidics [25]. However, in this thesis, we selected one representative example for the case study: experimental investigations of the behaviour of the so-called purely elastic instability in a mixing-separating. For this device, for which a stagnation point is

created at the centre of the symmetry, experimental investigation of these instabilities is very limited. Our goal is to understand these instabilities via experimental analysis when varying the Weissenberg number ($Wi$), in the hope that the resulting mechanism can be applicable to a wider range of problems. According to the literature review, no work has been reported addressing the effect of purely-elastic flow instabilities of a viscoelastic fluid in the mixing-separating micro-geometry.

## 1.4 Project aims and objectives

The objective of the present work is to get a deeper insight into the flow instabilities in different micro-geometries. The technical difficulties because of the small length-scales of these geometries are considered the main challenge that has held the progress towards enhancing mixing and heat transfer. Therefore, we investigate the behaviour of micro-scale flow instabilities numerically and experimentally, which offers an efficient alternative to geometry modification or external forcing. Additionally, the characterisation of the flow before and after the bifurcation helps to predict the formation and confidently locate the core position of vortex structures within the channels, which consequently benefits the designing of microfluidic devices to manipulate flow conditions using laminar vortices, i.e. particle entrapment, mixing, and other applications. More specifically, the present research targets the following objectives:

1. The first objective is to explore the inertial instabilities and changes in flow topology in a mixing-separating microfluidic device. We perform both experiments (using flow visualisation) and numerical simulations in a specific geometry with a gap size of five times the channel height ($g = 5H$). Finding good agreement between the experiments and simulations, we further utilise the simulation technique to explore the effect of varying the gap size ($g$). We demonstrate that both the nature of the instability and the $Re$ at which it occurs varies as the gap size is changed.

2. The results for the mixing-separating device are useful for reference cases as we can vary the gap size without changing the angle ($\alpha$) between the pair or inlet and outlets (which is a particular quirk of the $H$-geometry). Although there is some previous work on the effect of the angle $\alpha$ (albeit for circular cross-section channels)[26], a full study of devices with a variety of angles and gap sizes is required to answer this question with certainty and to firmly establish how the instability relates to both gap size and angle. As the $\alpha$ angle and gap size are geometrically dependent upon each other (i.e. if $\alpha$ is changed, the gap size is changed as a result of the new angle [26]), the second objective is to utilise the simulation technique to investigate the effect of varying the $\alpha$ angle, consequently aggregated to changes in the gap size, which is non-trivial.

3. Previous numerical work [27] has shown that the amount of reverse flow depends on the gap size and Deborah number, and the creeping flow of UCM fluid exhibited an interesting bifurcation pattern, which depends on the gap width. The results have shown a significant asymmetry in the gap region with the fluid tending to flow not reverse around the separating wall. The authors indicate that for intermediate gap widths, a steady bi-stable bifurcation pattern is observed. Two different flow configurations appear at very close Deborah numbers, which made the flow to oscillate periodically. To date, no work has investigated this purely-elastic instability in a mixing-separating micro-geometry experimentally. Therefore, the third objective is to conduct systematic experiments to exploit the purely-elastic shear flow instabilities of a viscoelastic fluid to elucidate the role of elasticity in a mixing-separating cell device using a so-called Boger fluid (a model liquid with near-constant viscosity).

4. To date, no work has been reported that characterises the effect of the spiral instability observed by Haward et al. [7] on heat transfer. Given the potential applications of improving heat transfer performance of microfluidic devices (for active cooling, for example) it is pertinent to investigate the influence of this inertial instability on heat transfer. As such, the fourth objective is to investigate the possibility of utilising this instability in a cross-slot device to promote convective heat transfer at low or moderate values of Reynolds numbers ($Re < 100$). We do this through a combination of three-dimensional numerical simulations and experiments. The numerical simulations are exploited to characterise the heat transfer enhancement in greater detail than is possible with the limited experimental data. Furthermore, in the experiments, the surfaces of the cross-slot micro-geometry are considered to be adiabatic due to the material used to manufacture the cross slot. Using the simulations, we also test other thermal boundary conditions (i.e. uniform wall temperature), which allows us to quantify the heat transfer enhancement (compared to a channel with no instability) using the Nusselt number.

## 1.5 Outline of this document

The contents of this thesis are thus divided into the following parts:

- Chapter 2 presents a review of previous studies.
- In Chapter 3, we present the experimental arrangement and procedure, including a description of the working fluids, calibration procedures, and uncertainties.
- Chapter 4 describes the setup of the numerical simulations, including the boundary conditions, details of a mesh dependence study, validation of the method

against previous work for a straight channel, and bifurcation parameters employed.

- In Chapter 5, we benchmark numerical simulations in a wide gap ($5H$) mixing-separating cell geometry against the experimental results. We also investigate the effect of varying the gap size of the mixing-separating cell through numerical simulations.

- Chapter 6 presents an investigation of the effect of varying the angle between the pair of inlets and outlets on the inertial instability.

- In Chapter 7, we investigate the mechanisms of the flow field becoming time-dependent when using a viscoelastic fluid in the mixing-separating device.

- Chapter 8 explores the enhancement of heat transfer using an inertial instability in cross-slot microfluidic devices.

- In Chapter 9, we present the conclusions and a proposal for future research.

# Chapter 2

# Background

## 2.1 Fluid flow instabilities at micro-scale

The potential to amplify mixing of two confined fluid streams or the capacity to manipulate particles on the micro-scale for different industrial applications has been an upward trend in research papers. This chapter introduces the previous research conducted regarding fluid flow instabilities at the micro-scale. These instabilities can be used to enhance mixing, and particle entrapment or manipulation. In addition, the set of dimensionless numbers used to categorise the flow throughout this thesis are presented, and their meaning is discussed based on the underlying physics.

## 2.2 Mixing in micro-scale flows

In the 1990s, fluid flow operating under unusual or unexplored conditions becomes considerably employed, and the term microfluidics[1] turned very common between scientists, with MEMS (micro electro-mechanical systems)[2] devices being fabricated for chemical, biological, and biomedical application. A simple definition for the term microfluidics is the study of simple or complex, mono- or multiphasic flows which are circulating in artificial microsystems [3].

In the last decade, microfluidic devices have had a significant impact on the biomedical, pharmaceutical, food and chemical industries [2]. With the increasing use of micro-scale devices across the biomedical industry, especially within biomedical diagnostics and chemical fields with emphasis on an improved understanding of chemical reactions [2, 6], the ability to mix two fluid flows or manipulate particles on the micro-scale has become an enticing field of research. Due to the necessarily small scale of these devices ($\leq 1000\mu m$), inertial forces are usually small, and laminar flow is predominant. Consequently, the fluid mixing process in the micro-geometries often relies on molecular

[1] Microfluidics already existed in the 1960s, but its application was limited to developing the analogous systems of microelectronic circuits with the electron flux is the analogue to the fluid flux.

[2] The micro electro-mechanical systems, MEMS, consists of systems whose total size varies between 1 and 300$\mu$m

diffusion, which is notably inefficient when compared to turbulent convective mixing [28, 2].

Micromixers homogenise fluids in small volumes (microliters) without taking much space in satisfactory time-scales [29]. Active mixing schemes implement an external force to the microfluidic mixing system other than the fluid flow, typically by way of a mechanical transducer. Ultrasonic transducers have been shown to improve the mixing performance in mixers by stirring the samples. This method of external excitation generates considerable heat in addition to the system, which alters the reactivity between materials and is difficult to account for in analysis [2]. Passive microfluidic mixers, studied in this thesis, rely on fluid mechanical behaviour induced by geometry and the physical properties of the flow to enhance mixing. As the fluid flow passes through such devices, inertia-driven instabilities induce mixing. Therefore, by studying this complex effect on the flow, stability diagrams can be constructed, and more efficient mixing devices proposed.

## 2.3 Reynolds number influence

The Buckingham's theorem (also known as Π theorem), a key theorem in dimensional analysis, allows the prediction of the consequences of miniaturisation [3]. The usage of the Π theorem, which characterises incompressible Newtonian flows by one single spatial scale $l$ −characteristic length−, demonstrate that such flows are controlled by a single dimensionless number: the Reynolds number ($Re$). The mathematical expression for $Re$ number is:

$$Re = \frac{Ul}{\nu} \tag{2.1}$$

where $U$ is the characteristic velocity of the fluid and $\nu$ is its kinematic viscosity. In microsystems, there are flows associated with moderate Reynolds numbers on the order of hundreds ($Re \approx 100$), and velocities on the order of several meters per second. This Reynolds number is not high enough to produce turbulent flow but is too high to be able to apply the Stokes approximation, which is valid when $Re \approx 1$. The Stokes equation governs flows of incompressible Newtonian fluids as small Reynolds numbers and can be described by:

$$-\frac{1}{\rho}\nabla p + \nu\nabla^2 u + \frac{1}{\rho}F = 0 \tag{2.2}$$

where $\rho$ and $\nu$ are constant fluid physical properties related to density and kinematic viscosity, respectively. $u$ represents the velocity vector and $p$ the pressure. $F$ corresponds to all external forces acting on the microsystem. The flow governed by the

[3] We will not give a demonstration of this theorem; the reader can find this in most books of fluid mechanics [3, 30, 31, 32]

Stokes equation possesses remarkable properties: linearity, reversibility, uniqueness of the solution, reciprocity, and the existence of a minimum of dissipation [3]. Whereas, the domain of moderate Reynolds number ($Re \approx 100$) groups together phenomena often difficult to describe precisely, because they are not asymptotic and are thus difficult to simplify. Therefore, the moderate $Re$ region permit bifurcations of solutions, which can lead to hydrodynamic flow instabilities. In this work, the Stokes flow is not applicable as we are aiming for the flow instabilities when using Newtonian fluids.

## 2.4 Diffusion dominates the mixing process in the microscale

In the context of transport phenomena in a continuum, one extremely important dimensionless number in advection-diffusion problems is the Peclet number ($Pe$). This number measures the relation of advection with respect to diffusion. It can be define as:

$$Pe = \frac{Ul}{D} \tag{2.3}$$

where $U$ is the characteristic flow velocity, $l$ is the size of the system,and $D$ is the diffusion coefficient, or diffusivity. The units of this coefficient are $m^2/s$, and note that it have the same units of the kinematic viscosity $\nu$. Both coefficients are related to a transport of a quantity, which gives an idea of flux. Diffusivity is correlated to the size of molecules and viscous friction forces of the liquid environment, and thus miniaturisation can lead to small diffuse mixing time. The mixing time under the diffusive regime is on the order of $l^2/D$. Table 2.1 below helps to clarify this point as it shows a few values for molecules diffusing in water at 20°C:

Table 2.1: Different values of diffusivity and mixing time for molecules diffusing in water at 20°C

| System | Diffusivity | Mixing |
|---|---|---|
| | $cm^2/s$ | $s$ |
| Dye (fluorescein), in a glass of 10cm | $3 \times 10^{-6}$ | $10^5$ s |
| Dye (fluorescein), in a microsystem of 1 $\mu$m | $3 \times 10^{-6}$ | $10^3$ s |
| Dye (fluorescein), in a microsystem of 100 $\mu$m | $3 \times 10^{-6}$ | 10 s |
| Glycerine, in a glass of 10cm | $4.6 \times 10^{-7}$ | $10^6$ s |
| Enzymes and proteins, in a microreactor of 100 $\mu$m | $1.2 \times 10^{-11}$ | 1000 s |

The higher the Peclet number, the higher the influence of the advective flow dominates over molecular diffusion. Therefore, one can conclude that in the domain of microfluidics the unique way to transfer mass and heat is to let mixing occur naturally by molecular diffusion. The miniaturisation process can thus be expected to lead to

a small $Pe$ number as diffusion is predominant, and the advection terms are negligible. Although, in contrast, the literature shows that there is not a characteristic order of magnitude for the Peclet number, and therefore, some mixers attempt to encourage the appearance of flow instabilities, separation, and recirculation induced by centrifugal forces, all which leads to enhanced mixing [28, 33, 3, 25, 34, 35, 7].

## 2.5 Convective flow associated with inertial instabilities in microfluidics

Different devices (or geometries) have historically been tested to improve mixing performance and characterise flow behaviours providing a greater understanding of governing mechanisms at this scale, as well as the possibilities within this field of research. Microfluidic devices have previously been tested both experimentally and numerically across a variety of geometries such as a T-shaped planar channel with two square opposing inlets and a perpendicular outlet of equal combined area, i.e. maintaining a constant bulk velocity in each channel arm [11]; a serpentine curved channel where the fluid motion is in different direction to the axis of curvature due to the existence of a secondary motion [36]; a cross-slot − planar crossed channel in which two opposed incoming fluid streams impinge on each other, and leave through opposite channel exits [37, 38]; and another simple configuration with potential applications in micro-scale flows is the microfluidic mixing-separating cell (also referred to as the *H-geometry*) − two straight square parallel channels with flow from opposite directions interacting through a central gap that allows the streams to mix or remain separate. When compared to a cross-slot, a mixing-separating cell shows many similarities in the fluid motion. The cross-slot device with one pair of aligned arms rotated by 90° towards the other pair would lead to a mixing-separating cell with $\sqrt{2}H$ gap size at the centre of the device. It is well known that cross-slot devices are sensitive to an inertial instability at modest Reynolds numbers [7]. This instability can often be employed to enhance mixing and heat transfer, offering an efficient alternative to geometry modification or the addition of external forces to the system (e.i. electro-mechanical actuators [39, 40])

Before embarking on a discussion of the flow instabilities in different micro-geometries, it is important to clarify what we mean by the term "flow instability". A mathematical demonstration from Graham and co-workers [41, 42] can help to understand: Consider the flow of a Newtonian liquid (such as water) in the gap between two very long concentric cylinders, driven by the motion of the inner cylinder. At low rotation rates, we would see a flow where the velocities and pressure only varied with radial position and are constant along with the azimuthal and axial directions. We will refer to this flow as the base flow. As the rotation speed is increased, a transition occurs to an axisymmetric (i.e. no variation in the azimuthal direction), axially periodic vortex flow. This flow is qualitatively different from the base flow: in particular, unlike in

the base flow, the velocities and stresses vary in the axial direction. What is interesting is that the base flow is an appropriate solution to the governing equations at all values of the rotation rate. Beyond a critical value of the rotation rate; however, perturbations (even infinitesimal ones) applied to the base flow grow in magnitude until a qualitatively different steady state is reached. We say that the base flow is unstable beyond the critical rotation speed, hence the phrase "flow instability." The qualitative change caused by the variation of a parameter (in this case, the rotation rate of the inner cylinder) is called a bifurcation [41, 42]. As a simple one-dimensional example, consider the differential equation:

$$\dot{y} = \mu y - y^3 \tag{2.4}$$

The equation 2.4 is invariant with respect to the transformation $y \rightarrow -y$, i.e., replacing $y$ by $-y$ results in the same equation. Steady state solutions are obtained by setting $\dot{y}$ to zero (as in equation 2.5).

$$f(y) = \mu y_s - y_s^3 = 0 \tag{2.5}$$

The solutions for equation 2.5 are $y_s = 0$ and $y_s = \pm\sqrt{\mu}$, where the subscript $s$ denotes a steady state. While $y_s = 0$ is a solution for all values of $\mu$, the solutions $y_s = \pm\sqrt{\mu}$ are valid only for $\mu > 0$. In this problem, $y_s = \mu$ and $y_s = -\mu$ bifurcate from the solution $y_s = 0$ at $\mu = 0$. In a small neighborhood of the bifurcation point, the branches $y_s = \sqrt{\mu}$ and $y_s = -\sqrt{\mu}$ are one sided, i.e., they only exist for $\mu > 0$. This type of bifurcation is called a pitchfork. Note that the bifurcating branches $y_s = \sqrt{\mu}$ and $y_s = -\sqrt{\mu}$ are related by symmetry [41, 42].

The equation 2.6 represents the linearization of the one-dimensional example presented here. The stability of the bifurcating branches is determined by the sign of the linearisation of the steady-state equations. If the linearization is positive, the solution is unstable, because small disturbances grow. Otherwise, if the linearization is negative, small disturbances decay, and the solution is stable.

$$\frac{\partial f}{\partial y} = f_y = \mu - 3y_s^2 \tag{2.6}$$

Substituting $y_s = 0$ gives $f_y = \mu$. Therefore, the solution $y_s = 0$ is stable for negative values of $\mu$ and unstable for positive $\mu$. Note that the change in stability occurs at the bifurcation point, $\mu = 0$. Substituting $y_s = \pm\sqrt{\mu}$ in equation 2.6 gives $f_y = -2\mu$, which is negative for $\mu > 0$, the only regime where these solutions exist. Therefore, these solutions are stable. When the bifurcating branch is stable, the bifurcation is said to be supercritical.

The opposite case, a subcritical bifurcation, occurs when the bifurcating branches are unstable. Consider the one-dimensional differential equation as an example of this

type of system:

$$\dot{y} = y^3 + \mu y \tag{2.7}$$

The solutions for equation 2.7 are $y_s = 0$ and $y_s = \pm\sqrt{-\mu}$, where the subscript $s$ denotes a steady state. A similar analysis to the one presented above shows that the steady states $y_s = \pm\sqrt{-\mu}$ only exist for negative values of $\mu$ and are unstable, and the solution bifurcates from $y_s = 0$ at $\mu = 0$.

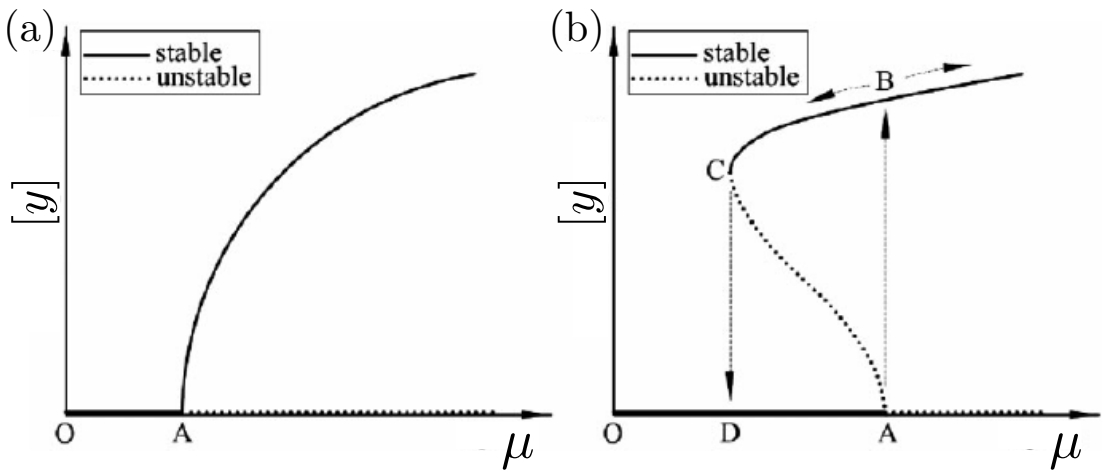


Figure 2.1: Pictorial representation of the two types of bifurcations: (a) supercritical and (b) subcritical. $[y]$ represents a bifurcation parameter, which is some measure of $y$ that captures the features of the transition. The solid line indicates a stable branch while a dotted line indicates an unstable branch [41, 42].

Figure 2.1 shows a pictorial representation of both supercritical and subcritical bifurcations. The stable solutions are denoted by solid lines and the unstable solutions are indicated by dotted lines. $[y]$ represents a bifurcation parameter, which is some measure of $y$ that captures the features of the transition. In figure 2.1(a), the diagram shows a supercritical bifurcation where point A is the bifurcation point. When $\mu$ is larger than a critical point ($\mu_{crit} = A$), the stationary solution loses stability and bifurcates. In figure 2.1(b), the stationary solution loses stability at point A and an unstable solution appears. The unstable periodic solution turns to the left of point A and its amplitude increases with decreasing $\mu$ until the so-called 'saddle-node' bifurcation point C is reached. After that, the unstable solution becomes stable and its amplitude increases with increasing $\mu$. The evaluation of $\mu$ at point C represents the critical value of this type of bifurcation ($\mu_{crit} = C$).

### 2.5.1 Serpentine channel

In a serpentine design (see figure 2.2), the generation of secondary flow due to unbalanced centrifugal forces can promote mixing in Newtonian fluid flows. Essentially,

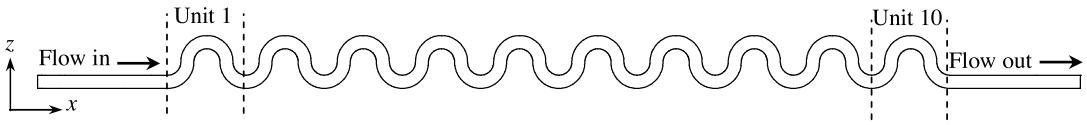


Figure 2.2: Schematic of a serpentine channel.

the fluid flowing in the central parts of channel is forced outwards from the centre of curvature by a centrifugal effect. Conversely, the slower parts along the wall are forced inwards where the pressure is lower, and a so-called *secondary flow* occurs in a plane perpendicular to the main flow direction. Such secondary flows are called *Dean's vortices* after Dean [43], in the late 1920s. Later, in 1983, Berger et al. [44] proposed a mathematical description of the Dean vortices, which originated a dimensionless number, the Dean number. The parameter takes into account the ratio of the channel dimension to the radius of curvature, and it can be expressed as:

$$D_e = Re \left( \frac{H}{2R} \right)^{1/2} \tag{2.8}$$

where $Re$ represents the Reynolds number, $H$ is the channel width, and $R$ is the radius of the curved channel. The curvature ratio parameter ($H/2R$) affects the intensity of the secondary flows (a pair of counter-rotating vortices as in figure 2.3) [36]. Fellouah et al. [45] performed experimental and numerical investigations for Dean instability (centrifugal instability) of laminar flow in 180° curved channels. They adopted a radial gradient of the axial velocity as the precise criterion for detection of Dean instability. The results revealed that the onset of Dean instability for Newtonian fluids (critical Dean number) decreases with increasing the duct curvature ratio. In another hand, the variation of the critical Dean number with duct aspect ratio is less significant.

Sugiyama et al. [47] visualised the patterns of secondary flow in a fully-developed laminar flow region within curved rectangular channels with curvature ratio ranging from 5 to 8 and aspect ratio ranging from 0.5 to 2.5. From flow visualisation, They observed that the secondary flow vortices change with increasing Dean number ($D_e$) as shown in Figure 2.4. For the flow patterns in the case of aspect ratio 1 and curvature ratio 8, only one pair of secondary flow vortices appear in the laminar stable region at low Dean number (figure 2.4a). As the Dean number increases, a retarded layer occurs near the outer wall (figure 2.4b − c) and with further increasing $D_e$, two additional pairs of secondary flow vortices appers at the corners (figure 2.4d − e).

As microfluidics operates at low $Re$, usually viscous forces dominate inertial forces. Although, in the serpentine channel, under specific conditions (i.e., geometry and flow rate), inertial forces cannot be neglected as inertial effects such as the Dean vortices come into play [6]. Dean vortices resulting from inertial effects have been used in microfluidic devices for enhancing mixing [29] and heat transfer [48, 49]. It has been shown

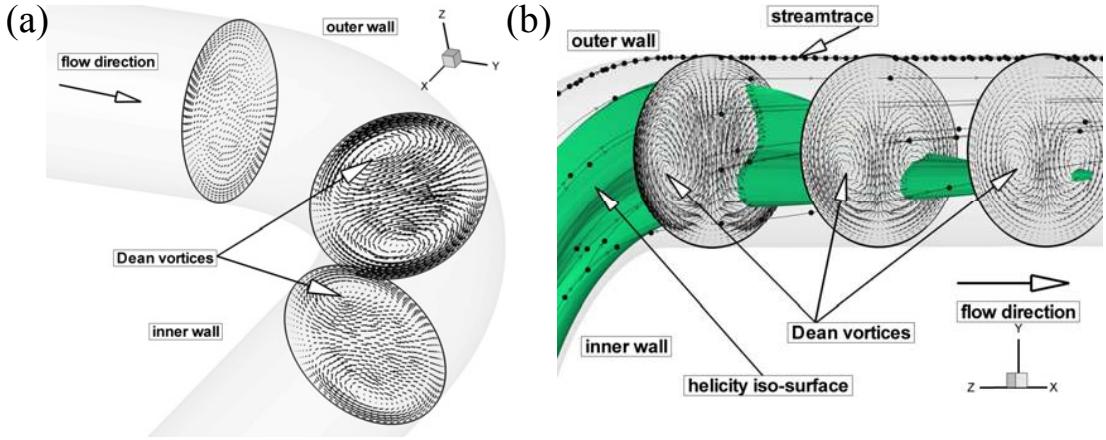


Figure 2.3: Development and evolution of the flow structure of Newtonian fluid in curved tube shown by numerical simulation. a) Velocity vector in different sections in the elbow showing the Dean type vortices ($L = 20R$ entrance length). b) Three-dimensional flow patterns (helicity iso-surface value) and velocity vectors in different sections after the elbow ($L = 20R$ entrance length). [from Bernad et al. [46]]

that the serpentine design in microfluidic devices shows promising mixing behaviour. Zaidon et al. [50] showed that adjusting the length of the serpentine channel and the outlet geometry, the serpentine channels (Design 2 and 3 in the paper) generated high mixing in the micro-scale. At a tolerable velocity magnitude at the outlet, the obtained mass fraction of the mixing ranged from 0.5 to 0.7.

### 2.5.2 T-shaped micro-geometry

Many investigations [10, 51, 11, 12, 13, 52, 53, 54, 55][4] on a micro T-shaped mixer were performed to improve fluid mixing between two streams flowing at a low Reynolds number. This design has flow entering the channel from two opposite inlets and then reaching a stagnation point (SP) before turning 90° and being expelled down the outlet channel (see figure 2.5). The SP is located on a free streamline, which induces a symmetry breaking bifurcation line. The behaviour of the flow after this instability has been shown to increase the mixing performance within microfluidic devices [8].

Three different regimes of laminar flow (symmetric stratified flow, symmetric vortex flow, and, beyond the instability, the so-called *engulfment flow* regime, which is asymmetric) were observed depending on the Reynolds number in the outflow mixing channel [10, 11, 12, 13]. The experimental measurements using microparticle image velocimetry ($\mu$PIV) and laser-induced fluorescence ($\mu$LIF) techniques illustrate that in the engulfment flow the improvement of mixing performance can be achieved because the two inlet streams are forced together into a spiral structure with increasing $Re$.

Fani et al. [56, 57] performed direct numerical simulations and corresponding linear

[4]Papers discussed in this section.

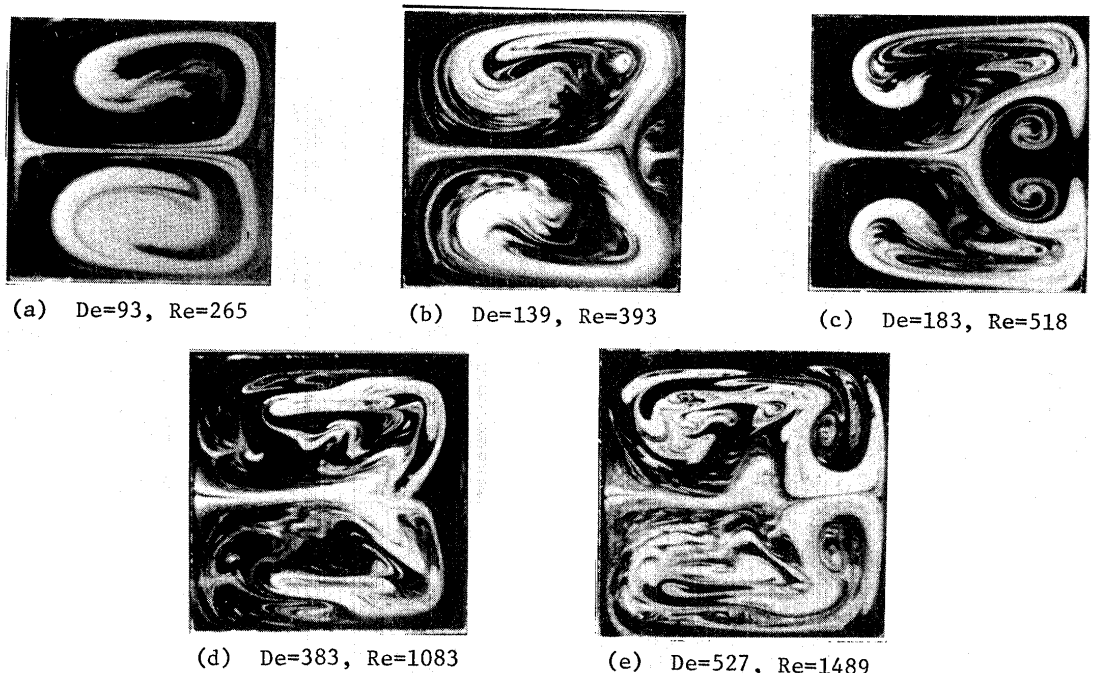


Figure 2.4: Secondary flow patterns (Dean vortices) in a rectangular channel. The flow patterns in the channel of aspect ratio 1 (same size for channel width($a$) and height($b$); $a = b$) and curvature ratio 8. With increasing Dean number ($D_e$) two pairs of additional vortices appear at the corners. [from Sugiyama et al. [47]]

stability analysis for a micro T-mixer (figure 2.6). A sensitivity analysis was utilised to explore the possibility of controlling the instability (using micro wall jets for example). Recent experimental and numerical work by Ault et al. [58] demonstrated the capture of particles in the recirculation regions created by vortex breakdown in a branched junction. It was also found that the junction angle could be varied to either enhance or eliminate the vortex breakdown induced particle capture.

A numerical investigation by Poole et al. [55] explored the critical conditions required for the onset of symmetry-breaking phenomenon in T-channel junctions in terms of aspect ratios, for both inlet and outlet channels. Also, the influence of shear-thinning on the critical Reynolds number was examined through the application of an inelastic Generalised Newtonian Fluid (GNF) model. The numerical results show that the change in flow conditions from symmetric to asymmetric flow is, in most cases, a steady supercritical pitchfork bifurcation. Shear-thinning either promotes or inhibits the bifurcation to asymmetric flow depending on the exact choice of Reynolds number, and this is one of the many examples of the variation of viscosity can affect the stability of the flow [59].

Sarkar et al. [60] conducted numerical simulations to evaluate mixing performance when varying the angle of the opposing inlet channels in a T-junction microfluidic device (see figure 2.7. The computational approach has been validated using experimental and


Figure 2.5: Schematic of a T-shaped mixer.

theoretical data. The results suggest that mixing performance is found to be dependent on the angle between the two inlet arms.

It is noted that a T-shaped geometry is closely related to the cross-slot device which is discussed in more detail in the next section. The characteristics of fluid flow and mass transfer within 400$\mu$m square cross-section T-shaped and cross shaped micromixers have been numerically and experimentally investigated by Mouheb and co-workers [14, 15] to compare the impact of geometric configuration and the degree of freedom for the fluid flow in these micro-systems on mixing performance. In the experiments, Particle Image Velocimetry (PIV) combined with electrochemical methods [14] and micro-Laser Induced Fluorescence ($\mu$LIF) [15] were utilised in order to compare the effectiveness of both micromixers (T-shaped and cross-shaped) for the range of Reynolds numbers from 25 and 50 to 100 and 200 for T-shaped and cross-shaped, respectively. The experimental and numerical results revealed, in terms of the concentration profiles, the mixing enhancement in the cross-shaped micromixer can occur at low flow rates compared to the T-shape. This enhancement in mixing in the cross-shaped micromixer is attributed to the stronger vortex stretching and high shear rate. Also, the cross-shaped micromixer induces a greater degree of freedom for the flowing fluid and a smaller pressure drop than the T-shaped micromixer due to the existence of two outflow streams.

### 2.5.3 Cross-slot device

The cross-slot geometry consists of perpendicular, bisecting channels with opposing inlets and outlets. This arrangement creates a flow field with a stagnation point located at its centre [61] (see figure 2.8). This design is simple, allows ease of control, and has motivated an extensive range of applications in several scientific fields for the mixing of fluids [5, 40, 37, 62]. For Newtonian fluid streams imposed at the opposite inlets of a cross-slot micro-geometry, a fluid flow bifurcation appears depending upon the Reynolds number at which the flow becomes asymmetric, and a spiral vortex develops [40] due to an engulfment flow regime. In this geometry, the maximum trans-

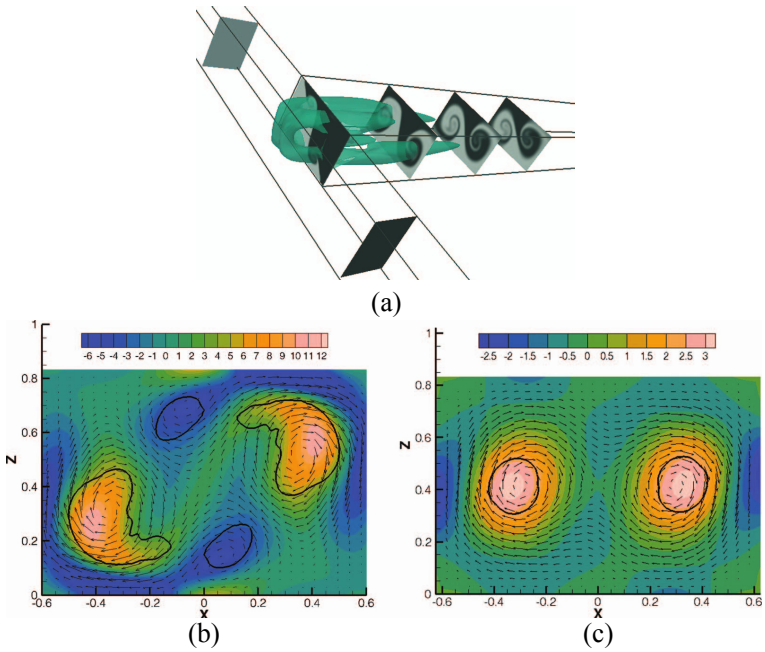


Figure 2.6: Steady engulfment regime in a three-dimensional T-mixer. (a) Vortical behaviour identified according to the $\lambda_2$-criterion at $Re = 160$ and iso-contours of tracers at different $y$-sections along the outlet channel. Vorticity component in the $y$-direction and in-plane velocity vectors at different sections (b) $y = 1$ and (c) $y = 3$; The thick lines locate the boundary of the vortices. [from Fani et al. [56]]

verse velocity component on the horizontal centreline at the central plane is commonly used to determine the critical Reynolds number ($Re_c$) numerically [7, 40, 63]. At and above the critical $Re$ value, an instability occurs, and the stable, 2D and laminar flow within a cross-slot device give place to a complex three-dimensional flow, which is also steady. The characterisation of the flow's stability around $Re_c$ is therefore essential in understanding device mixing capabilities.

The region of the stagnation point, which is formed when two opposed streams collides within the cross-slot device, is characterized by an appreciable curvature of the streamlines. Essentially, the streamlines are convex toward the direction of the singular point in the direction of which the modulus of the velocity vector decreases, which is characteristic of a so-called Taylor-Gortler instability [64]. Figure 2.9 the example of stagnation point formation in two different types of opposed flow interaction (colliding and anti-parallel streams).

Aryshev et al. [64] performed a hydrodynamic stability analysis in the neighborhood of the stagnation point of colliding streams of Newtonian fluid, and the results has proved the absolute instability with respect to standing-wave perturbations situated in the plane dividing the streams. Essentially, the colliding form of interaction of streams promote the formation of a secondary vortex motion with axis coinciding with the line dividing the streams (see figure 2.10). Their experimental results confirmed the arise of

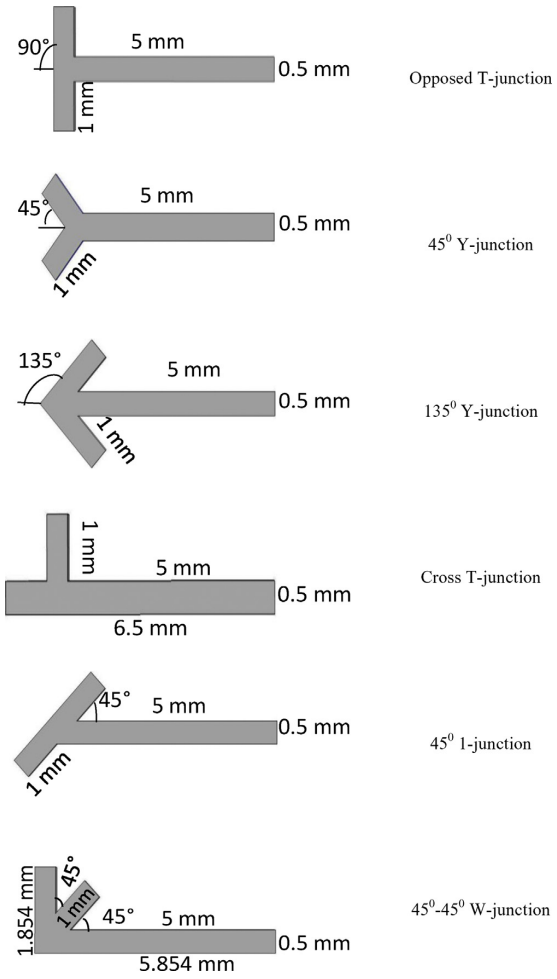


Figure 2.7: Top views of different T-shaped microfluidic junctions to evaluate mixing performance when varying the angle of the opposing inlet channels. [from Sarkar et al. [60]]

vortex structures in the interaction region, which are situated in the plane separating the interacting streams.

In the early 1990s, Kalashnikov and Tsiklauri investigated the stability of laminar flow in rectangular crossed channels experimentally using both Newtonian (water) [37] and non-Newtonian (polyethylene-oxide in water) [38] fluids (see figure 2.11). For the Newtonian fluid and channel aspect ratio of 32 ($d = 0.8$ mm, $h = 26$ mm, $h/d = 32$), they observed that the flow at small Reynolds number ($Re < 55$ when increasing $Re$ and $Re < 43$ when decreasing) is stable, laminar and two-dimensional (coincident with the vertical symmetry plane of the exit channels). However, the flow beyond a certain critical value of Reynolds number in the cross-slot cell becomes unstable and three-dimensional: $Re_{crit} = 55$ and $Re_{crit} = 43$ for increasing and decreasing $Re$, respectively. This kind of instability occurs in the cross-slot flow because a vertical series of fan-shaped vortices arise in the central transverse plane of the outflow channels.

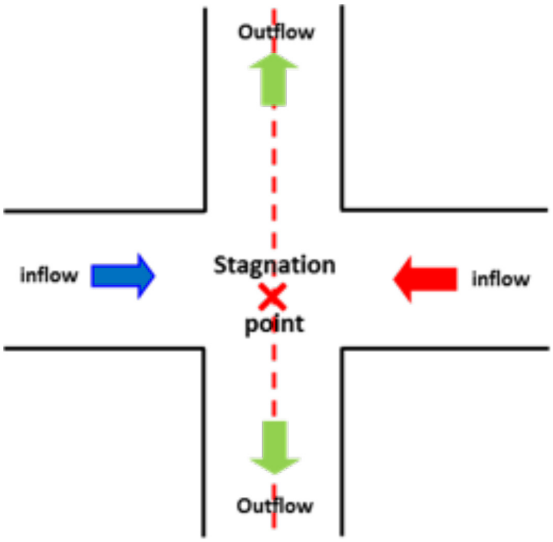


Figure 2.8: Schematic of a cross-slot device.

Wong et al. [65] simulated three-dimensional liquid flow in a cross-shaped micromixer incorporated with static mixing elements for characterising the impact of static mixing elements on the mixing performance (figure 2.12 depicts the static mixing elements). The numerical results showed that the incorporation of static mixing elements in the outflow channel of the cross-shaped micromixer can significantly improve the mixing performance due to the generation of eddies behind these mixing elements. Consequently, the swirling effect of these eddies boosts the contact area between the two incoming fluid streams.

Shih and Chung [66] explored a micromixer with different mixing units to investigate the effect of four geometrical factors on the sensitivity of mixing over a wide Reynolds number range ($0.1 \leq Re \leq 40$). The geometrical factors are gap ratio, number of mixing units, baffle width and chamber ratio. The degree of sensitivity can be ranked as: Gap ratio > Number of mixing units > Baffle width > Chamber ratio. The authors analysed the mixing behavior using numerical simulations and experiments. They also used a statistical method (Taguchi method) for local optimization of the mixer. The results demonstrated that the performance of the micromixer is significantly affected by the gap ratio (width/height) and Reynolds number. Poor mixing is achieved at lower $Re$ flow ($Re \leq 0.5$) by a diffusion-enhanced mechanism (molecular diffusion) while mixing enhancement occurs at higher $Re$ flow ($Re \geq 20$) by a convection-enhanced mechanism (vortex agitation).

An interesting numerical study from Srisamran and Devahastin [67] found that the recirculation and preferential zones appear at a cell with two crossed microchannels, and the diameter of these vortices enlarges with an increase in $Re$. The governing equations were solved using a finite element-based commercial software (FEMLAB 3.0) with the range of Reynolds numbers from 10 to 200 based on the inlet slot width. Oliveira et al.

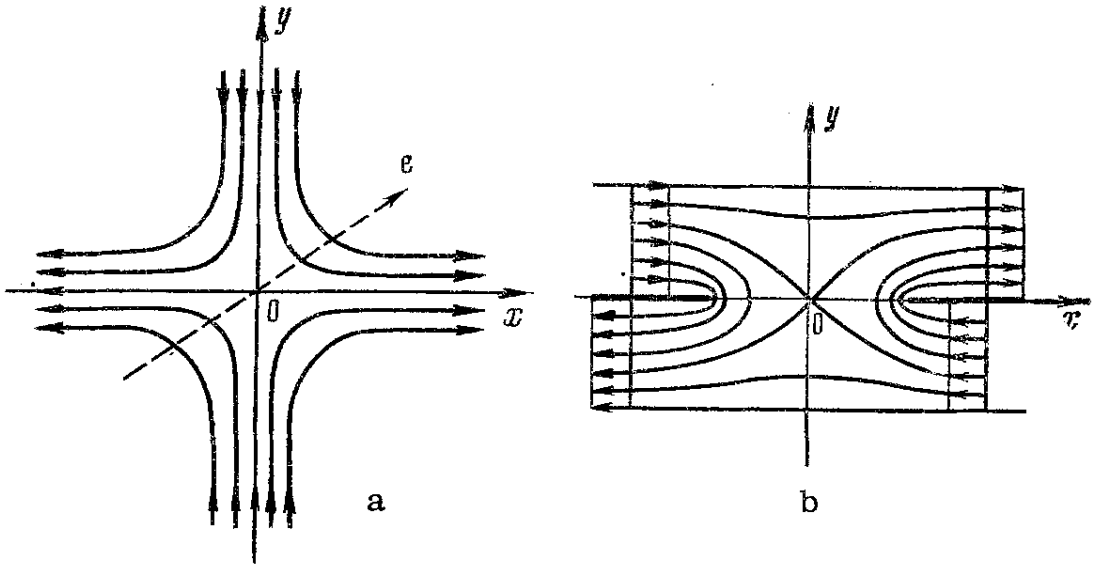


Figure 2.9: Two examples of stagnation point flows: (a) colliding streams and (b) anti-parallel streams. The dashed line shows the initial orientation of a vortex. [from Aryshev et al. [64]]

[68] carried out a systematic numerical and experimental investigation on Newtonian fluid flow through a ($100\mu$m) square cross-section cross-slot geometry comprising three entrances and one exit in order to study the occurrence of divergent streamlines and the onset and enhancement of symmetrical wall-detached recirculations at low Reynolds numbers. From the good agreement between the experimental observations and the numerical simulations, they confirmed the influence of the geometric parameters and of inertia on the fluid flow patterns. The appearance of the central recirculations relies non-monotonically on the relative width of the entrance channels and inertia promotes the appearance of the free vortices. Also, the results showed that the Newtonian fluid flow remains symmetric relative to the horizontal centreline for a wide range of flow conditions ($Re \leq 113$).

Poole et al. [9] concentrated their numerical investigations on a new bifurcation phenomenon through a two-dimensional cross-slot channel. The results showed that the flow remains steady and symmetric at low Reynolds numbers and identical regions of standing recirculation attached to the four corners increase linearly in size with $Re$. Although, beyond a critical Reynolds number ($Re \approx 1490$), the unstable symmetrical solution was evolved to a pair of steady asymmetric solutions as shown in figure 2.15.

Recently Haward et al. [7] exploited experimentally and numerically this flow bifurcation mechanism for fluid mixing in cross-slot geometries with a range of aspect ratios (depth/width), $0.4 - 3.87$. The findings show that fluid flow is steady and symmetric (the interface between fluid streams is sharp and vertical) at low Reynolds numbers

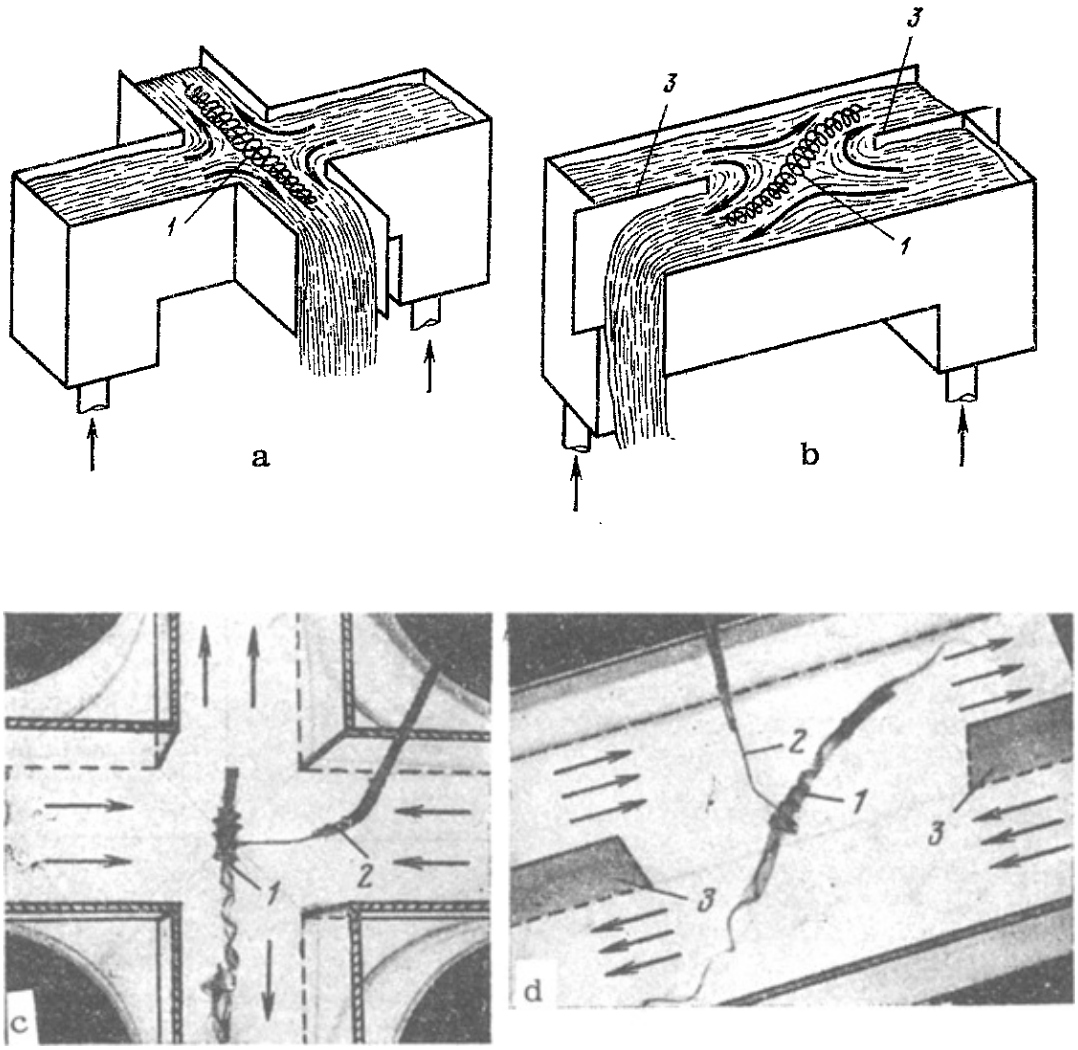


Figure 2.10: (top) Pictorial representation of the vortex formation in two different colliding flow structures. (bottom) Experimental flow visualisations depicting the vortex formation.[from Aryshev et al. [64]]

(see figure 2.16). However, as $Re$ increases above a critical value, which is dependent on the cross-slot aspect ratio ($20 < Re_{crit} < 100$), the laminar flow experiences a steady symmetry-breaking bifurcation and a spiral vortex structure appears at the central axis of the outflow channels as shown in figure 2.16. The instability is described by a Landau model analogous to that used near equilibrium tricritical points, and it was found to be dependent on the cross-slot aspect ratio (see figure 2.17. The authors suggest that the instability can be exploited to increase fluid mixing in this type of geometry at moderate Reynolds numbers ($20 < Re < 100$).

In spite of the great progress in the understanding of the hydrodynamic behaviour (symmetry-breaking bifurcation) of Newtonian fluids occurring in the micro-scale cross-slot device as mentioned in the literature above, the characteristics of convective heat

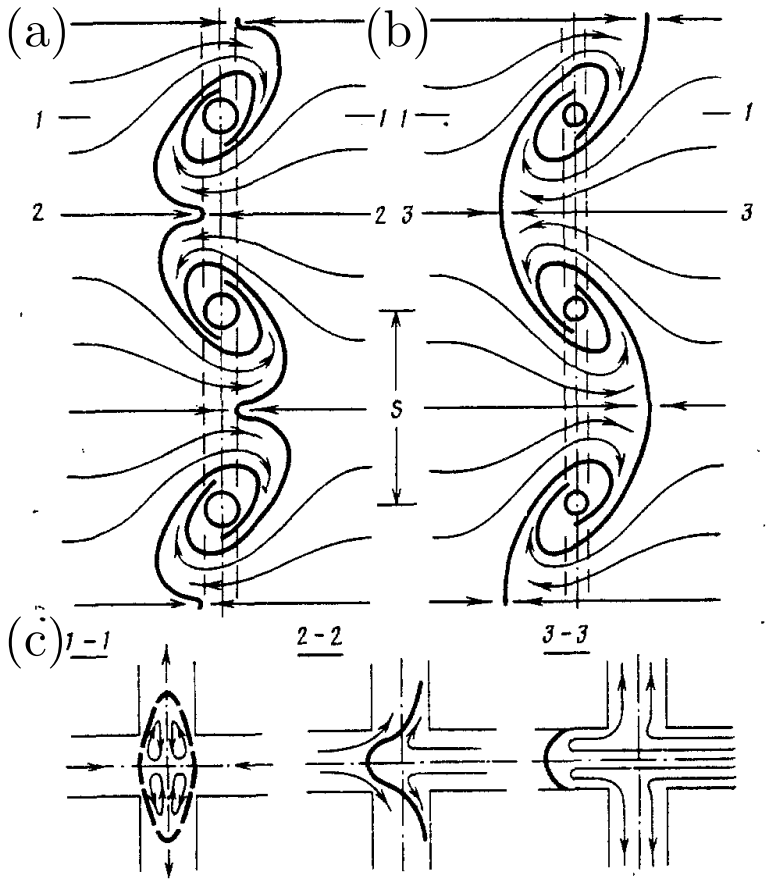


Figure 2.11: Vortical patterns in a cross-slot device for a Newtonian fluid when $Re > Re_{crit}$. In (a) and (b), the streamlines at the vertical streamwise plane. (Note: the dotted lines indicate to the location of the transverse section of the outflow channels). (c) Top view showing the flow features when unbalancing the inlet flow rates. [from Kalashnikov and Tsiklauri [37]]

transfer in the cross-slot geometry still need to be explored. In this thesis, Chapter 8 is dedicated to study numerically the symmetry-breaking bifurcation of Newtonian fluids in the cross-slot micro-geometries in order to promote convective heat transfer at low and moderate values of Reynolds numbers ($20 < Re < 100$). Additionally, the results are benchmarked by experiments performed in a cross-slot device.

### 2.5.4 Mixing-separating cell

There are, of course, numerous problems of interest in the instabilities related to the geometries mentioned in the sections previously discussed. Although, in this thesis, we choose a mixing-separating geometry and study the instability mechanism involving inertial effects. The mixing-separating also referred to as the *H-geometry*, is a simple configuration with potential applications in micro-scale flows. It consists of two straight square parallel channels with flow from opposite directions interacting through a central

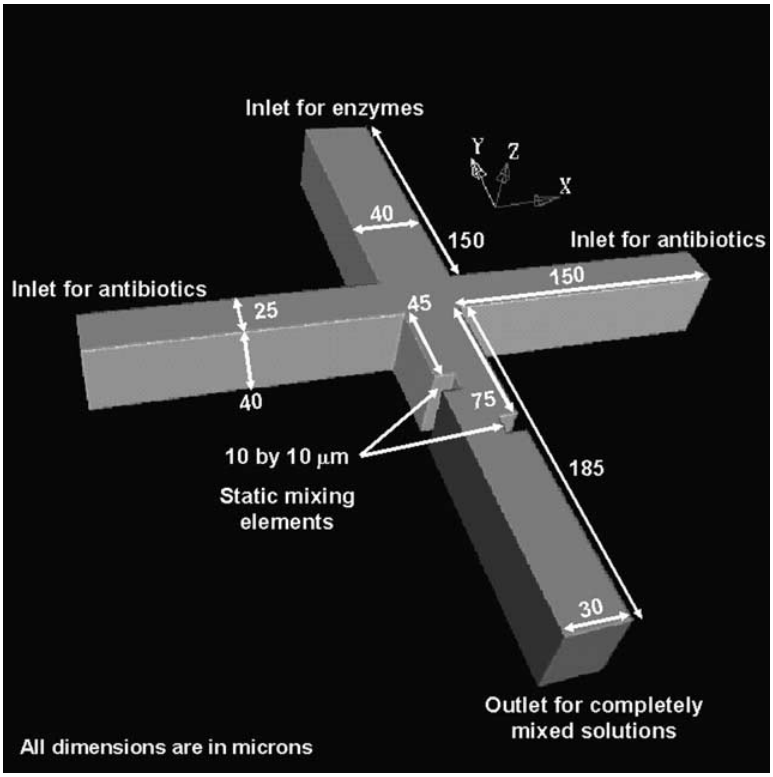


Figure 2.12: The cross-shaped micromixer used in the investigation of mixing by Wong et al. [65]. At the outlet channel, the static mixing elements. [from Wong et al. [65]]

gap that allows the streams ($Q_1$ and $Q_2$) to mix or remain separate (see figure 2.18). The mixing-separating device shows many similarities in the fluid motion when compared to a cross-slot geometry. The cross-slot device with one pair of aligned arms rotated by 90° towards the other pair would lead to a mixing-separating cell with a $\sqrt{2}H$ gap size at the centre of the device (where $H$ is height=width of the channel). The previous section has shown that cross-slot devices are sensitive to an inertial instability at modest Reynolds numbers [7]. To date, no work has been reported that characterises the effect of the inertial instabilities on the mixing-separating cells. Given the potential applications of improving mass and heat transfer performance of microfluidic devices (for active cooling, for example), it is to explore the inertial instability in the mixing-separating device, providing new insight into its physical mechanism. Moreover, we have also investigated the mechanism of the laminar vortices to confidently locate the core position of an individual vortex that could be employed in particle entrapment.

Previous work on mixing-separating cells, shows that a vortical behaviour occurs and becomes more complicated with increasing Reynolds number. Originally proposed by Cochrane, Walters, and Webster [69] and Walters and Webster [70], numerical simulations ($1 < Re < 50$) showed that the size and strength of a central vortex increased as $Re$ is increased, eventually splitting into two vortices at a relatively high $Re$. They employed a finite-difference method to describe numerically the flow of a Newtonian

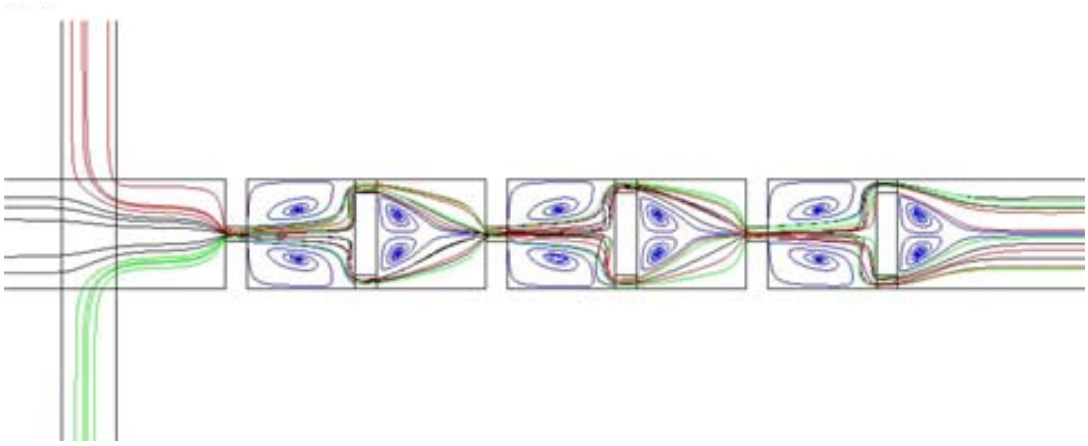

Figure 2.13: Particle trajectory distribution of the adaptive-design micromixer at $Re = 20$ from Shih and Chung [66]. In detail the three different mixing units preseting a convection-enhanced mechanism (vortex agitation). [from Shih and Chung [66]]

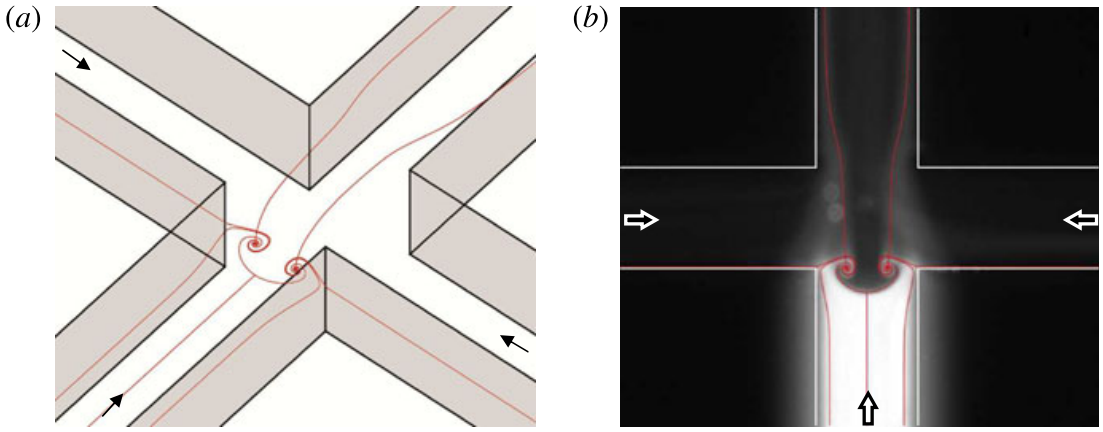


Figure 2.14: Three dimensional nature of the flow at $Re = 113$. (a) 3D streamlines obtained numerically (in red) showing that the flow is highly three-dimensional. (b) Comparison between the experiments (grey-scale image obtained when Rhodamine is injected) and the numerical streamlines (in red). [from Oliveira et al. [68]]

fluid within the device. The simulations were validated by experimental results. These investigators analysed the effects of gap width ($g$) using two different flow configurations: (i) matching flow rates in the two inlet channel arms and (ii) unbalanced inlet flow rates. In the follow-up work [70], thin insert plates with rounded edges were used.

It was found that a wider central gap ($g$) encourages flow to reverse its direction and exit from a different outlet [69] (see figure 2.19). This means the fluid tends to cross from one channel to the other. Experimentally, laser flow-visualisation results were limited to a small range of Reynolds numbers ($Re < 8$) for a wide-gap (five times the height of the channel, $g = 5H = 25$mm) and for a medium-gap ($g = 3H = 15$mm), $Re$ was limited to 25 (see figure 2.20). The experimental apparatus consisted of peristaltic pumps to drive the flow and a catch-and-weigh apparatus to determine the flow rate.

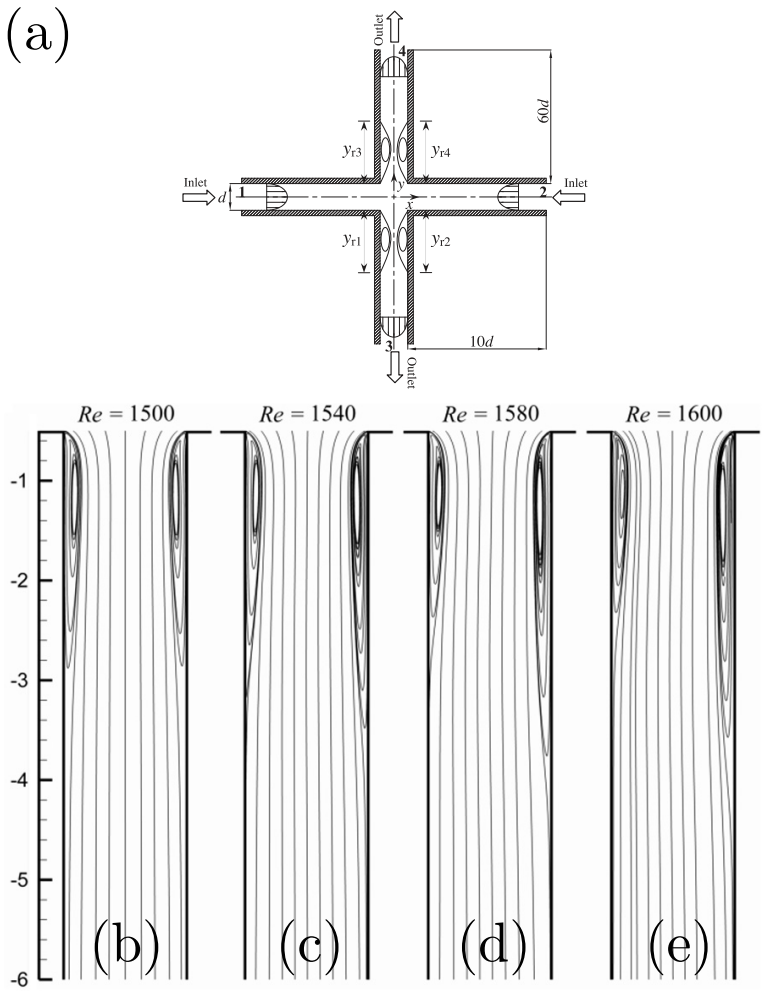


Figure 2.15: Two-dimensional symmetry breaking in steady flows. (a) The numerical 2D schematic of the cross-slot device from Poole et al. [9]. On the bottom, the break of symmetry on the recirculation zones when $Re > Re_{crit}$: (a) Re = 1500; asymmetric growth of recirculation regions beyond bifurcation: (b) Re = 1540, (c) Re = 1580, and (d) Re = 1600. [from Poole et al. [9]]

The channels were made of aluminium with height of 5mm and depth of 20mm. The unavailability of a very refined mechanism for controlling the flow rates with sufficient accuracy was reflected in unbalanced flow streams within the inlets which resulted in differences between numerical and experimental data Walters and Webster [70]. Matching the flow rates accurately was also a challenge in the present project[5].

Clearly, the Numerical simulations from Walters and Webster [70]] showed that the size and strength of a central vortex increases when increasing $Re$, which finally splits into two vortices at a relatively high value of $Re$ ($Re = 50$). The numerical study confirmed that a wider central gap encourages flow to reverse its direction and exit from a different outlet (see figures 2.19 and 2.21).

[5]Chapter 3 discuss the experimental apparatus and the uncertainty of experimental measurements.

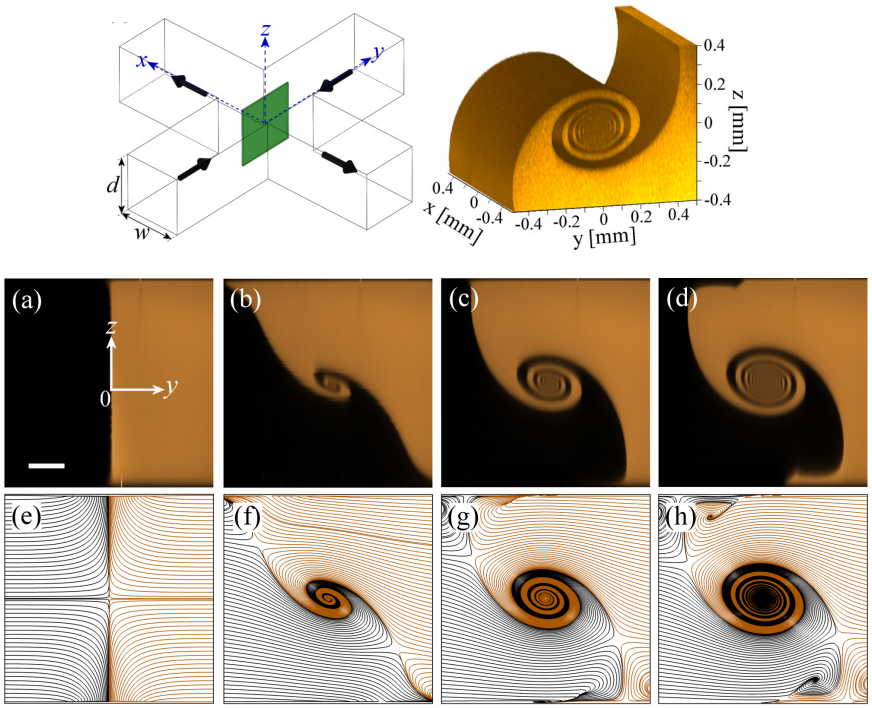


Figure 2.16: Symmetry breaking in three-dimensional steady flows. On top, a 3D schematic diagram of the cross-slot device along with 3D rendering of a vortex structure observed for the flow of water at $Re = 75.8$ in a cross slot with aspect ratio 1 ($\alpha = 1$). On the bottom, confocal experimental imaging (($a$)-($d$)) and numerically generated streamlines (($e$)-($h$)) depicting the evolution of flow structures in the $y$-$z$ plane and $x = 0$ for Newtonian fluid flow in the cross-slot device with aspect ratio 1 ($\alpha = 1$) under the following conditions: (a), (e) $Re = 15.2$; (b), (f) $Re = 42.8$; (c), (g) $Re = 60.6$; and (d), (h) $Re = 91.0$. The numerical result shown in (f) is one of two possible solutions at this $Re$ as a symmetric solution can also be obtained [7]. [from Haward et al. [7]]

The differences between the results for the cross-slot and the mixing-separating geometries can be explained from the different angles of the approaching flows in the vicinity of the stagnation points. In the mixing-and-separating geometry these approach flows are not aligned with the channels and are not orthogonal as occurs in the cross-slot flow (see figure 2.19). Consequently, in the mixing-separating geometry the shear flow is important in the stagnation point region, being absent in the cross-slot flow geometry which is purely extensional in character, except in the vicinity of the channel walls [27].

Humphrey and Li presented an unusual characteristic of the flow inside the mixing-separating cell while increasing $Re$ ($300 < Re < 1000$) experimentally from a stationary state (from rest) [71]. By using water and methylene blue as a dye, a tilted interface delineated the stream interface a few seconds after the flow starting motion from rest. The 2D interface soon transforms into a 3D unsteady flow for $Re = 500$ (see figure 2.22). The authors suggest that transverse pressure gradients imposed by the main motion

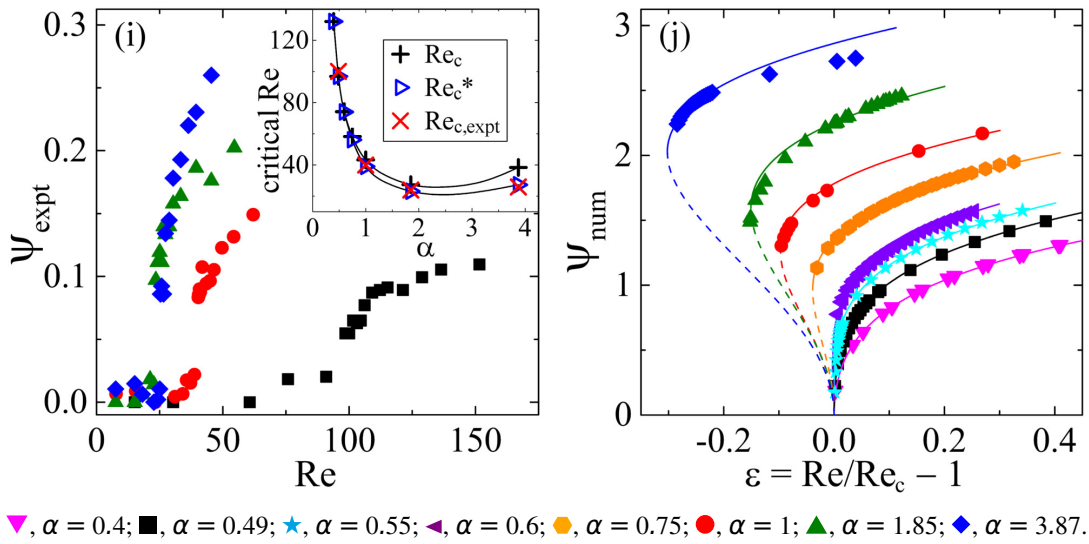


Figure 2.17: (i) The bifurcation parameter ($\psi_{expt}$) applied to different aspect ratio ($\alpha$) when varying Reynolds number ($Re$) at the experimental cross-slot device. The inset shows experimental and numerical critical Reynolds numbers for the instability transition in different aspect ratio geometries ($\alpha$). (j) The numerical bifurcation parameter ($\psi_{num}$) as a function of the control parameter, $\epsilon$, fitted with a Landau sixth-order polynomial. [from Haward et al. [7]]

are responsible for the inclined (tilted) flow interface at a low Reynolds number, and the three-dimensional phenomenon appears as a consequence of span-wise vorticity. Motivated by this experimental outcome, Humphrey et al. used a numerical technique to investigate the vortical behaviour previously noticed in their work. The study was limited to relatively high values of $Re$ ($100 < Re < 300$) where the flow is unstable and time-dependent[72]. The results at low $Re$ show a pair of steady (or quasi-steady) vortices formed in the shared space region (central gap), which become unstable and dynamically complex at high Reynolds numbers.

A variation of the cross-slot geometry is a device with an X-shaped junction where the angle between inlet and outlet channels is less than the 90° of the cross-slot. Correa et al. has been studied X-shaped junction for several angles between 15° and 90° using three-dimensional (3D) simulations [26]. Although, the channel cross-section was circular unlike the square (or rectangular) cross-section studied in our (and much of the previously discussed) work. A variety of vortical structures were observed depending on the angle of the junction and the Reynolds number. Just like the cross-slot is the extreme case of an X-junction where the angle between the channels is 90°, it is notable that the mixing-separating geometry we study here is an extreme case of the X-geometry where the angle is 0° (or 180° depending on your point of view). However, the mixing-separating geometry was not considered by Correa et al. [26]. Despite the work consider the effect of impingement angle (albeit for circular cross-section channels)[26], a full study of devices with a variety of angles and gap sizes is required to firmly

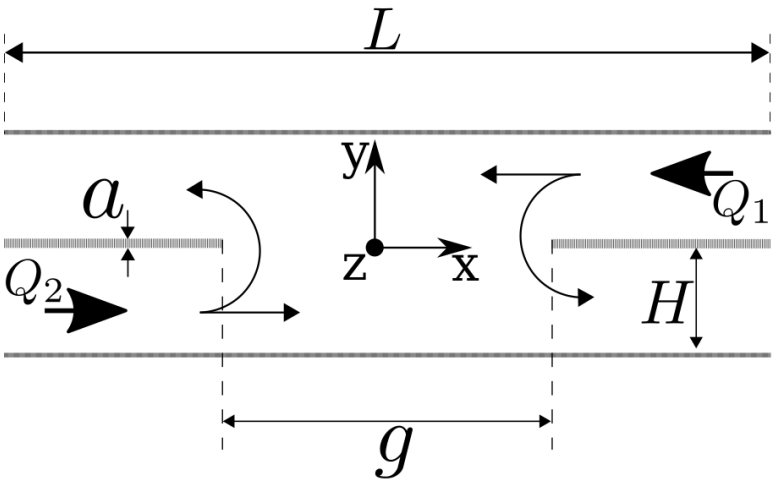


Figure 2.18: Schematic of a mixing-separating cell.

establish how the instability relates to both gap size and impingement angle.

## 2.6 Particle separation in microfluidics

Biological and chemical analysis is typically concerned with molecules and bio-particles with small dimensions. The ability to synthesise monodisperse spherical polymer particles aids in the development of theoretical models for the mechanisms controlling the chemical and physical properties of particulate materials [73]. Subsequently, positioning and separating particles on microfluidic devices creates many challenges [6, 74]. In a different application, studies suggest the use of laminar vortices for particle entrapment, and it has appeared as an attractive biomedical tool. Investigations on a vortical flow cell separation platform show that finite size cancer cells could be captured in a confined cavity microfluidic device as an effect of hydrodynamic forces on vortical laminar flow. As the red blood cells are almost unaffected by these forces due to their small size, the device represents a biomedical application for the inertial instability as it can isolate the cancer cells from blood for liquid biopsy [74, 75]. Besides, studies of the rheology of concentrated dispersions of polymer particles create an exhaustive list of application of polymer colloid particles, such as chromatography, drug delivery, medical diagnostics, encapsulation of species (e.g., proteins or cells), etc. [76].

In a serpentine channel, the mismatch of the flow velocity at the centre and near the walls of the curved channel leads to a pressure gradient in the radial direction that pushes the fluid particles with higher velocity at the centre outward and the fluid near the walls inward to the centre. This effect, a combination of lift and drag forces to centrifugal forces, can be applied to particle/cell separation or focusing. The parameters such as particle size, channel dimensions, and flow rate, play a significant role in the mentioned effect on particles [6, 77] .

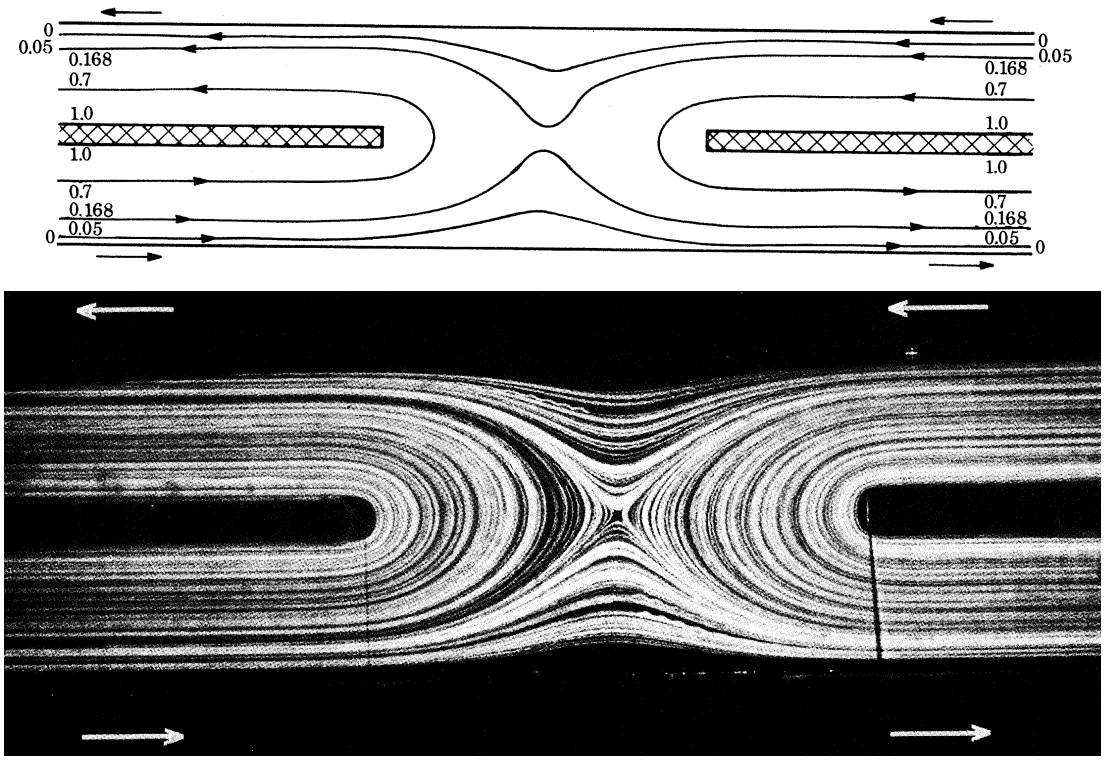


Figure 2.19: Numerical and experimental studies of flow field within a mixing-separating cell from early 1980s [69]. At $Re = 5$, both cases show a stagnation point at the centre of symmetry for a wide gap size – ($5H = 25$mm) five times the height of the channel. [from Cochrane et al. [69]]

## 2.7 Heat transfer in micro-flows

As the use of micro-scale devices increases across many scientific fields such as microtechnology, microelectronics and biotechnology, it has become necessary to improve heat transfer performance of these devices [5]. However, as has been discussed, micro-geometries have usually been associated with negligible inertia and predominantly laminar flow due to the necessarily small scale ($\leq 1000\mu$m) [6]. Consequently, the process of mixing fluid in the micro-geometries often relies on molecular diffusion, which is extremely slow compared with convective mixing. As previously discussed, the cross-slot devices are sensitive to an inertial instability at moderate Reynolds numbers [7], and it has been noticed that the instability can be usefully employed to enhance mixing, offering an efficient alternative to geometry modification, or the addition of external forces to the system (e.i. electro-mechanical actuators [39]). Given that one example of the primary potential applications of microfluidic devices is the active cooling of microprocessors, it is essential to investigate the enhancement this instability provides in the thermal performance. Therefore, we selected the cross-slot device to explore the instability phenomenon in the context of heat transfer.

Srisamran and Devahastin conducted two-dimensional numerical simulations to in-

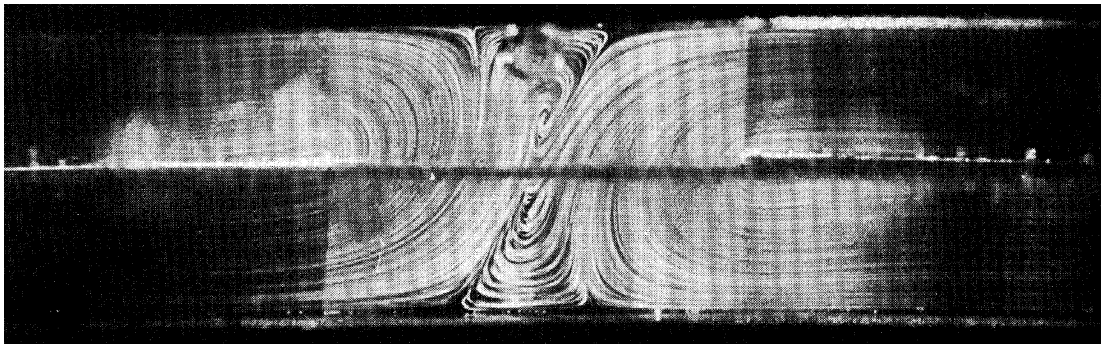

Figure 2.20: Vortical behaviour in the experimental studies within a mixing-separating cell at $Re = 25$. The unavailability of a very refined mechanism for controlling the flow rates limited the experimental conditions. [from Walters and Webster [70]]

vestigate the mixing behaviour of Newtonian and shear-thinning fluids (water and CMC solutions) using a cell with two crossed microchannels [67]. Symmetry was imposed on the problem by modelling only half of the geometry and the governing equations were solved using finite element software with the range of Reynolds numbers from 10 to 200 based on the inlet slot width, and the mixing index (the ratio between the standard deviation of the cross-section fluid temperature and the temperature difference of the inlet streams) of the fluid streams in the range of $0.62 - 1$. The findings showed that recirculation zones appear and the diameter of these vortices grow with increasing Reynolds number. Linear stability analysis and direct numerical simulations were used to investigate a planar cross-junction by Lashgari et al. [78]. It is demonstrated how the instability mechanism can be stabilised or destabilised using boundary modification. A control strategy (wall blowing) is employed to stabilise the flow, significantly increasing the Reynolds number at which the instability occurs.

Similarly, it is found that wall-suction could be used to destabilise the flow. Huchet et al. [79] studied experimentally the flow behaviour and mass transfer using an electrochemical method in a micro-device composed of crossing microchannels. Two hydraulic diameters (833 $\mu$m and 500 $\mu$m) and two flow patterns (crossing-flow and impinging-flow) were used to compare their influence on the mixing performance and mass transfer. The experimental results obtained in the laminar regime are consistent with CFD simulations for Reynolds numbers ranged between 100 and 400. The experimental and numerical results confirmed that the occurrence of hydrodynamic instabilities and three-dimensional flow in the outflow channels can promote mixing processes.

Ait Mouheb and co-workers have numerically and experimentally investigated the characteristics of fluid flow and mass transfer within square cross-section T-shaped and cross-shaped micromixers in order to compare the mixing performances of the two geometric configurations [15, 14]. The experimental and numerical results showed that the mixing in the cross-shaped micromixer occurs at lower flow rates than the T-shaped

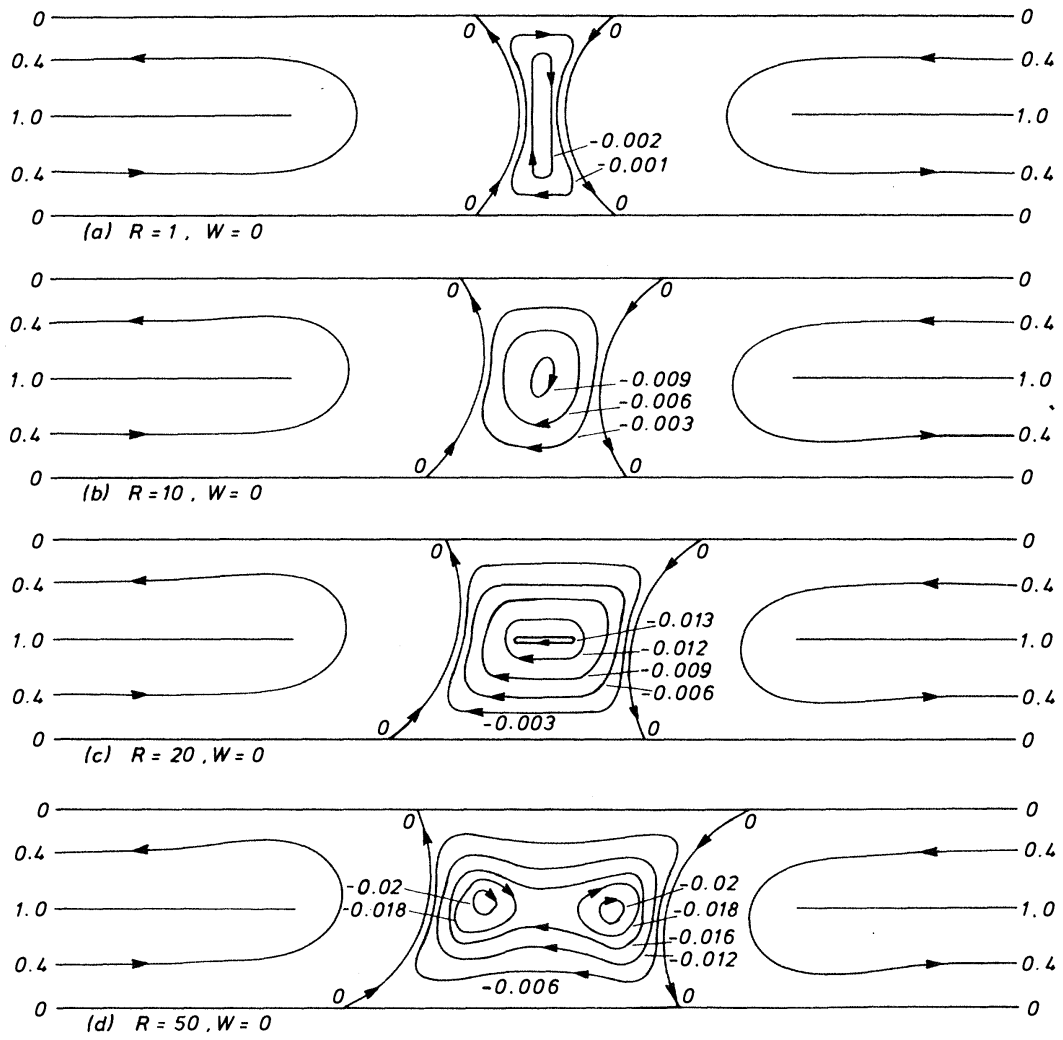


Figure 2.21: Numerical studies showing the vortical flow within a wide gap ($g = 5H =$ 25mm) mixing-separating cell with varying $Re$. [from Walters and Webster [70]]

micromixer. This enhancement in mixing in the cross-shaped micromixer is attributed to the stronger vortex stretching and high shear rate. Also, the cross-shaped micromixer induces a smaller pressure drop than the T-shaped micromixer due to the existence of two outflow streams. Recently Haward et al. [7] demonstrated (experimentally and numerically) the mechanism of fluid mixing in cross-slot geometries with a range of aspect ratios (depth/width) of 0.4 to 3.87. The results revealed that fluid flow is steady and symmetric (the interface between fluid streams is sharp and vertical) at low Reynolds numbers. However, as Reynolds number increases above a critical value ($20 \leq Re \leq 100$), which is dependent on the cross-slot aspect ratio, the laminar flow experiences a steady symmetry-breaking bifurcation and a spiral vortex structure is created oriented about the central axis of the outflow channels as shown in Fig. 1. This spiral instability, the onset of which is described by a Landau model analogous to

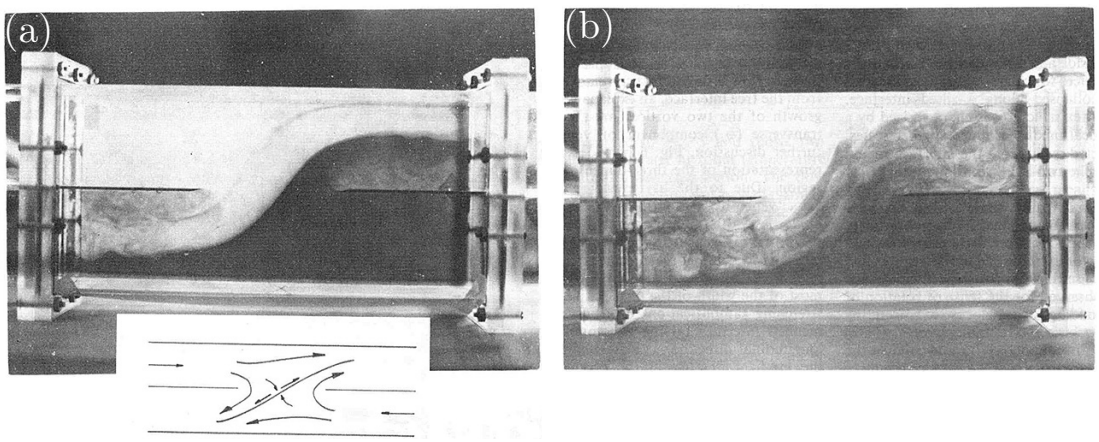


Figure 2.22: (a) Typical two-dimensional flow a few seconds after starting motion from rest showing the stagnation point flow present at low $Re$. (b) Side views of vortex formation process at $Re = 500$. Note: Top flow is from left and bottom flow is from right. [from Humphrey and Li [71]]

that used near equilibrium tricritical points, can be harnessed to boost fluid mixing in the cross-slot geometry at these modest Reynolds numbers.

To date, no work has been reported that characterises the effect of the spiral instability observed by Haward et al. on heat transfer [7]. Given the potential applications of improving heat transfer performance of microfluidic devices (for active cooling for example), it is pertinent to investigate the influence of this inertial instability on heat transfer. As such, the present thesis elucidates the possibility of utilising this instability in a cross-slot to promote convective heat transfer at moderate values of Reynolds numbers ($Re < 100$). We do this through extensively exploring three-dimensional numerical simulations and compare to experimental work. The experiments include measuring specific temperature distributions by monitoring the fluorescence intensity using microscopy techniques with a temperature-sensitive fluorescent dye (Rhodamine-B) [6]. These simulations are exploited to characterise the heat transfer enhancement in greater detail than is possible with the limited experimental data. Furthermore, in the experiments, the surfaces of the cross-slot micro-geometry are considered to be adiabatic due to the material used to manufacture the cross slot. Using the simulations, we can also test other thermal boundary conditions (i.e. uniform wall temperature), which allows us to quantify the heat transfer enhancement (compared to a channel with no instability) using the Nusselt number.

### 2.7.1 Thermal boundary layer and the Nusselt number influence

A thermal boundary layer appears once a fluid flows along a surface maintained at a temperature different from that of the upstream fluid [80]. In the context of thermal

[6]The heat transfer experimental investigation presented in this thesis was performed by Dr Waleed Abed during his PhD in Liverpool, and the details are discussed in chapter 8

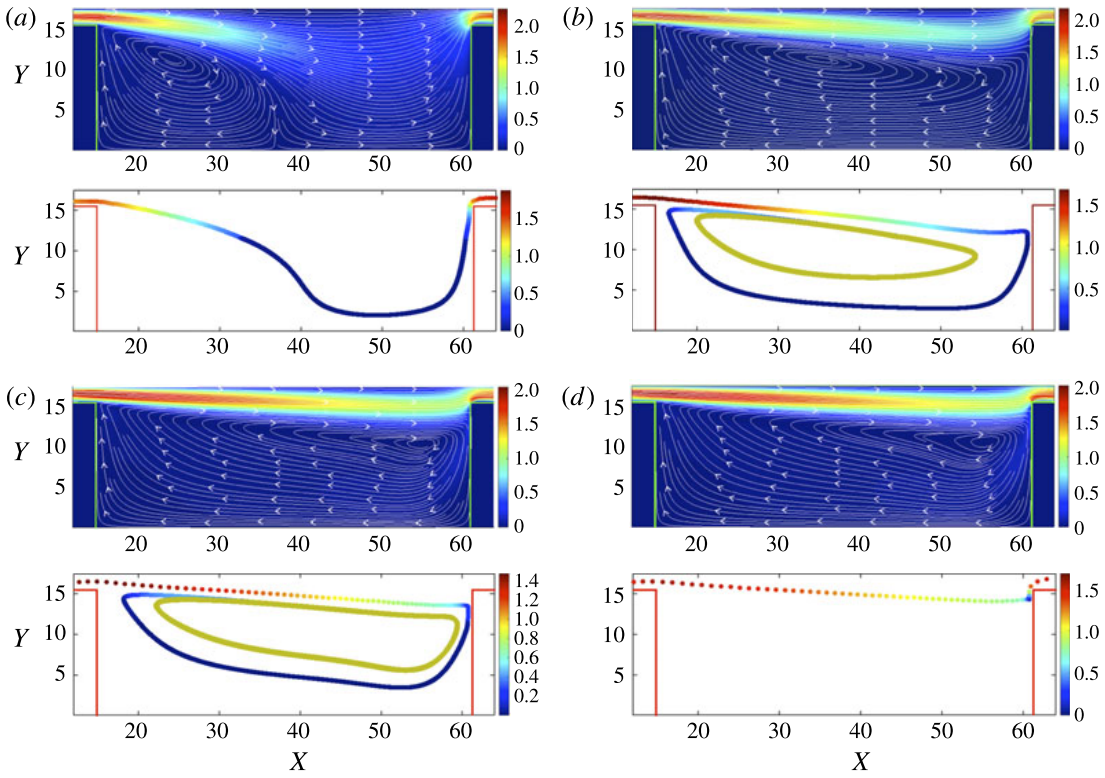


Figure 2.23: On top, fluid velocity magnitude contour inside a cavity with aspect ratio ($\lambda = 3$) at different Reynolds number. At the bottom, colour online representing the LBM simulations of particle trajectory. (a) $Re = 74$, (b) $Re = 123$, (c) $Re = 230$ and (d) $Re = 243$. The velocity magnitudes are computed on a symmetry plane ($z = 1.73$). The limit cycle orbit at $Re = 123$ and $Re = 230$ is illustrated in the figures. [from Haddadi and Di Carlo [74]]

fluids, we can introduce the Prandtl number ($Pr$), which relates a different form of the Peclet number, the thermal Peclet number ($Pe_{th}$), and the Reynolds number [80, 3]. Therefore, the Prandtl number, a ratio of the momentum and thermal diffusivities, can be defined as:

$$Pr = \frac{Pe_{th}}{Re} = \frac{C\mu}{k} \tag{2.9}$$

where $C$ and $\mu$ represents respectively the specific heat capacity and the dynamic viscosity of the fluid. The thermal Peclet number ($Pe_{th}$), defined in equation 2.10, takes into account the thermal diffusivity ($k$). $k$ is define in equation 2.11 below:

$$Pe_{th} = \frac{Ul}{k} \tag{2.10}$$

$$k = \frac{K}{\rho c_p} \tag{2.11}$$

where $\rho$ is the density of the fluid and $c_p$ is its specific heat. $K$ it the fluid thermal

conductivity originally from the Fourier's Law ($q = -K\nabla T$), which relates the local heat fluxes ($q$) and the temperature gradients ($\nabla T$).

In the context of the thermal boundary layer, the Nusselt number −a dimensionless parameter− is the thermal boundary layer what the friction coefficient is to the velocity boundary layer. The Nusselt number, defined in equation 2.12 is a function of the spatial variable $x$, the Reynolds number, and the Prandtl number. It represents the ratio of convection to pure conduction heat transfer [80]

$$Nu = \frac{hl}{k} \tag{2.12}$$

where $h$ refers to the convection coefficient (or exchange coefficient). The exchange coefficient is inversely proportional to the size of the system, and therefore miniaturisation offers an enormous advantage [3].

## 2.8 Elastic instabilities

While Newtonian flows at micro-scale become unstable only at relatively low-to-moderate Reynolds number ($20 < Re < 100$), when the inertial terms in momentum balance dominate, flows of viscoelastic fluids such as polymer solutions and melts are known to have interesting instabilities and nonlinear dynamical behaviors even at extremely low $Re$. These *purely-elastic* instabilities arise in rheometry of complex fluids as well as in many other applications [18, 19]

Viscoelastic fluids often have long polymer molecules dissolved in a fluid, which gives rise to the elastic component. Therefore, the elastic component turns responsible to store the stresses in the fluid and gives rise to fluid memory. Most of the properties of such flows can be easily interpreted by basis of single polymer dynamics where the polymer experiences combined action of stretching by the flow and elastic relaxation. Since the polymer solutions have fluid memory, the stresses in the fluid do not immediately become zero when the fluid motion is ceased, instead, the stresses decay with some characteristic relaxation time, $\lambda$ [81].

In a simple steady shear flow, where the flow is generated by sliding one plate atop another as seen in figure 2.24, with fluid in between, if we assume a lack of slipperiness then the shear stress ($\tau$) is a function of the shear rate ($\dot{\gamma}$) [32].

$$\tau = \mu\dot{\gamma} \tag{2.13}$$

The so-called lack of slipperiness is what we can call *viscosity* (represented by $\mu$), and it is due to the friction between the fluid and surface of the plates. The shear stress $\dot{\gamma}$ is proportional to the velocity gradient (equation 2.14, and the flow persists as long

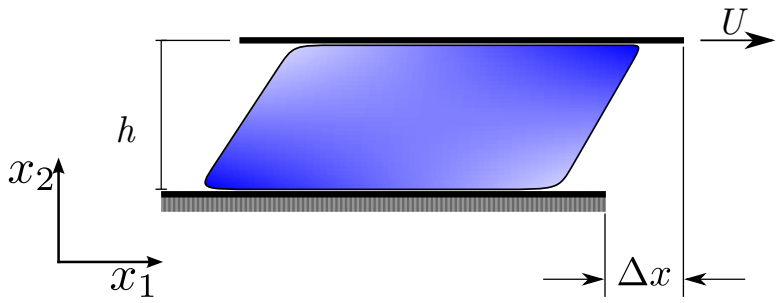


Figure 2.24: Shear flow generated by sliding one plate on top of another. Shear and normal forces may be supplied to keep the plates at a fixed distance.

as the stress is applied [32].

$$\dot{\gamma} = \frac{1}{h}\frac{\mathrm{d}X}{\mathrm{d}t} = \frac{U}{h} \tag{2.14}$$

where $U$ represents the velocity of the upper plate. Many Non-Newtonian fluids show a variable viscosity at different shear rates. The elastic stresses created become the main source of non-linearity in polymeric solution flows at low Reynolds numbers ($Re$), and as a result, elastic instability shows up when the elastic energy overcomes the dissipation due to polymer relaxation. In a simple shear flow of a polymer solution, the elastic stress is anisotropic and characterised by the difference in the normal stresses along the flow velocity direction and the velocity gradient direction.

Instabilities have been investigated and flow-controlling devices have been designed in a series of microfluidic geometries. For instance the flow rectifier with anisotropic resistance from Groisman and Quake [82], the flip-flop memory from Groisman et al. [83], and nonlinear flow resistance from Groisman et al. [83]. Another prospective application of these instabilities is to enhance mixing at lab-on-a-chip length scales [84], where turbulent mixing is absent due to small length scales and an alternative is needed.

The present section is a brief overview of the so-called purely-elastic instabilities. Moreover, the set of dimensionless numbers used to categorise the flow of viscoelastic fluids are presented, and their meaning is discussed based on the underlying physics.

### 2.8.1 Weissenberg number and Deborah number

The Weissenberg number ($Wi$) compares the elastic forces to the viscous forces. The degree of non-linearity in the mechanical properties is expressed by:

$$Wi = \frac{\text{elastic forces}}{\text{inertial forces}} = \frac{\tau_{xx} - \tau_{yy}}{\tau_{xy}} = \lambda\dot{\gamma} = \frac{U\lambda}{L} \tag{2.15}$$

where $L$ and $U$ are the characteristic length scale and bulk flow velocity, respectively. $\lambda$ represents the relaxation time, which is a fluid property. In a viscoelastic fluid, when

fluid motion ceases the stress does not immediately becomes zero. Instead, the stress decays with the relaxation time ($\lambda$), and $\dot{\gamma}$ is the characteristic deformation rate [85].

The Deborah number ($De$) is the ratio between the fluid relaxation time and the flow characteristic time. It represents the transient nature of the flow relative to the fluid time scale, and its mathematical representation is shown in equation 2.16. If the observation time scale is large (small Deborah number), the material responds like a fluid, and if it is small (large Deborah number) the material produces a solid-like response. Under the viewpoint, there is no fundamental difference between solids and liquids; it is only a matter of time scale. In the limit, when $De = 0$ one has a Newtonian liquid, and when $De = \infty$, an elastic solid [85].

$$De = \frac{\lambda}{T} \tag{2.16}$$

### 2.8.2 Purely elastic flow instabilities and Boger fluids

Differently to the Newtonian microfluidic characteristics, the viscoelastic flow in microchannels presents a nonlinear dependence of the flow rate on the driving force. They exceptionally remain steady as long as the driving force does not change, and all of that has to do with the addition of flexible high molecular weight polymers to the working liquid. The mechanical stress on solution of those polymer, the so-called non-Newtonian viscoelastic fluids, depends on the flow history with some characteristic relaxation time ($\lambda$) [16]. Viscoelastic fluids provide a structure in which consequence of non-linear advective and rheological effects produces considerable normal stress resulting in a complex flow behaviour [86]. Therefore, a purely-elastic instability can be observed in microfluidics due to the lack of inertial effects in viscoelastic creeping flows (or Stokes Flow, $Re \approx 1$).

For a broad class of viscoelastic fluid flows inertia effects are usually small, either by nature (e.g. the viscous flow of melts) or by design. An ideal fluid from the viewpoint of the experimentalist is a constant-viscosity fluid which is highly viscous and highly elastic at room temperature. Additionally, at the same time is optically clear. Therefore, the experimentalist could record the kinematics of important flows in the absence of inertia and shear thinning effects, and distinctly distinguish the influence of elasticity. Viscous Boger fluids, a constant-viscosity elastic solutions, named after the Boger's investigations in the 1970s using a maltose syrup-Separan solution. Boger fluids can be used to investigate purely-elastic flow instabilities when the effect of $Re$ is negligible [87].

Supporting numerical simulations for this phenomenon were presented by Poole et al. [88], where it was shown that once the purely-elastic instability appears, the shape of the velocity profile along a line between the corner of the channel and the free stagnation point changes from convex into concave. These types of instability

are generally triggered when a combination of the normal stress in the streamwise direction is coupled with streamline curvature. A well-known dimensionless parameter which rationalizes these curved streamlines instabilities is the $M$ parameter introduced by McKinley et al. [89] (often referred to as the Pakdel-McKinley criteria). This parameter can be considered as the viscoelastic complement of the Görtler number [90] and is defined as:

$$M = \sqrt{\frac{\lambda U}{R}\frac{\tau_{ss}}{\eta_0 \dot{\gamma}}} \tag{2.17}$$

where $U$ is the magnitude of the local velocity, $R$ is the local radius of curvature of a streamline, $\tau_{ss}$ is the normal stress in the streamwise direction, $\eta_0$ is the zero shear rate viscosity of the fluid and $\dot{\gamma}$ is the magnitude of the shear rate. Throughout this paper we will indicate dimensional variables using a tilde. In equation 2.17, the first term on the right hand side can be referred to as a local Deborah number, showing the ratio of the relaxation time of the fluid to the time a disturbance takes to travel along a streamline. As this ratio increases, the chance that a disturbance may grow and lead to instability increases. The second term on the right hand side of equation 2.17 is added to scale properly the effect of the normal stress in the streamwise direction with a reference stress scale. This term is generally in the same order of magnitude as a local Weissenberg number.

### 2.8.3 Instabilities in viscometric flows with curved streamlines

It is reasonable to say that at sufficiently large $Wi$ numbers −and low $Re$ numbers−, the polymer solution has considerable non-linearity in the flow state. For instance, in a curvilinear flow (e.g. Taylor-Couette flow) the normal stress difference gives rise to a volume force acting on the fluid in the direction of the curvature, the elastic hoop stress. The latter also becomes the driving force for a rod climbing effect, as well as an elastic instability [91].

Elastic instabilities at $Wi > Wi_{crit}$ are a path to a chaotic flow in a form of irregular flow patterns. Insignificant inertial effects associated to the highly elastic fluid behaviour generates random chaotic flow. The flow patterns exhibit continuous velocity spectra in a wide range of temporal and spatial scales similar to a inertial turbulent flow. The phenomena was firstly identified in Taylor-Couette [24] and Taylor-Dean [92] flows, and also in cone-and-plate [93] and parallel plates [93, 20] flow geometries. In a swirling flow between two disks, Groisman and Steinberg [20, 84] noted two main flow features: a sharp growth in the flow resistance, and an algebraic decay of velocity power spectra over a wide range of scales. The results show orders of magnitude more effective way of mixing than in an ordered flow. Moreover, the flow shows remarkable properties analogous to inertial hydrodynamic turbulence, hence the term elastic turbulence was

coined by the authors and have been researched further on as the elastic instabilities to promote mixing in polymeric solution flows. Their findings have a tremendous impact in microfluidics applications where mixing rates are often constrained by molecular diffusion [3]. Similar mechanisms drive instabilities in viscoelastic free-surface flows [21, 22] and in the flow within a serpentine curved channel [94, 49].

### 2.8.4 Elastic instabilities in stagnation point flows

In close relation to the viscometric flows with curved streamlines, the instability generated in polymeric stagnant point flows also has potential application in microfluidics. These class of flows are characterised by the formation of a narrow region of fluid with high polymer stress extending downstream from the stagnation point. For instance, stagnation point flow are generated in opposed jets [23, 95], cross-slot [25], two-roll mill [96], and four-roll mill [97, 96] devices.

Different devices (or geometries) have historically been tested to characterise flow behaviours providing a greater understanding of governing mechanisms of the nonlinear growth of the elastic polymer stresses in stagnation point flows. The geometries are basically the same studied in the Newtonian section above, such the T-shaped planar channel [8, 55], the cross-slot crossed channel [37, 25, 98, 61, 99, 35, 100, 63, 86], and the microfluidic mixing-separating cell [69, 70, 27, 101, 102] which motivates the investigations in this work.

### 2.8.5 T-shaped planar channel

Matos et al. and Miranda et al. [103, 104] investigated the flow of a GNF fluid with variable viscosity based on a Carreau-Yasuda model suitable for blood. The authors [105] also investigate the stability of steady planar stagnation flows of a dilute polyethylene oxide (PEO) solution using T-shaped microchannels. A general conclusion is that an increase in elasticity, either by increasing the Deborah number, by decreasing the viscosity ratio, or increasing the extensibility, results in a decrease of the size and intensity of the recirculation eddies formed at the junction. The only exception to this behaviour occurs for the vortex intensity of the horizontal recirculation, which shows a non-monotonic variation due to the additional degree of freedom introduced by the displacement of the separation point [106].

### 2.8.6 Cross-Slot device

It is known that Newtonian fluid in the cross-slot device remains symmetric and stable up to moderate values of Reynolds number. Likewise, the flow field of viscoelastic fluids in the cross-slot is stable and symmetric at low strain rate values, and the polymeric solutions extends along the outflow streamline from the stagnation point. With increasing flow rate (moderate deformation rates), the flow becomes asymmetric, but

remains steady. As the nominal deformation rate is increased further, the asymmetric flow evolves eventually to a time-dependent flow. Kalashnikov and Tsiklauri used a non-Newtonian (polyethylene-oxide in water) [38] fluid to investigate the stability of laminar flow in crossed channels experimentally. The results indicated that the elastic properties of the fluid quantitatively affect the three-dimensional flow in the crossed channels. Initially, the steady symmetry-breaking instability in the experiments was reported by Arratia et al. [25], and confirmed numerically by Poole et al. [88], where the stationary symmetry-breaking instability in the cross-slot geometry has been predicted by conducting simulations using the upper-convected Maxwell model.

Experimentally, numerous experimental investigations were conducted by Haward and co-workers on the cross-slot flow behaviour using various types of solutions such as, atactic Polystyrene (aPS), Cetylpyridinium Chloride (CPyCl) and Sodium Salicylate (NaSal), Poly(ethylene oxide) (PEO), and Hyaluronic Acid (HA). In these studies, two different aspect ratios (depth/width) were used, 5 and 10.5 [107, 108, 109, 110, 111, 61]. Haward and co-workers reported that the effects of shear localisation, which can occur with micellar solutions, may cause these purely-elastic instabilities in cross-slot flows. Sousa et al. observed a series of purely-elastic flow transitions in the viscoelastic fluid flow within a cross-slot device. The flow field evolves from symmetric to steady asymmetric, and eventually to time-dependent depending on the Weissenberg number ($Wi$). Using different aspect ratio of the crossed channels and rheological properties of viscoelastic fluids, the experimental results indicated that a direct transition from a steady symmetric flow condition to an unsteady (time-dependent flow instability) can occurs for lower channel aspect ratio (depth/width $< 0.5$) [35, 86].

### 2.8.7 Mixing-separating cell

Cochrane et al. [69] employed a finite-difference method and selected the UCM model to describe the rheological behaviour of a highly elastic constant-viscosity *Boger* (a discussion about Boger fluids can be found further in this chapter). These investigators analysed the effects of gap width ($g$) using two different flow configurations: (i) matching flow rates in the two inlet channel arms and (ii) unbalanced inlet flow rates. In a follow-up work [70], thin insert plates with rounded edges were used. For both experimental studies it was found that the flow displayed distinctive Newtonian and viscoelastic behaviours, with the occurrence of unidirectional and reversed flows in varying extents.

Only a few investigations were performed to analyse the complex dynamics of viscoelastic fluids in a mixing-separating cell. Afonso et al. [27] has shown that the amount of reverse flow depends on the gap size and Deborah number. Further, no vortex formation was observed. The creeping flow of UCM fluids exhibited an interesting bifurcation pattern, which depends on the gap width. The results have shown a signifi-

cant asymmetry in the gap region with the fluid tending to flow not reverse around the separating wall. The authors indicate that for intermediate gap widths, a steady bi-stable bifurcation pattern is observed. Two different flow configurations appear at very close Deborah numbers, which made the flow to oscillate periodically. This numerical finding motived us to visualise this periodic behaviour in our experimental setup.

Baloch et al. [101] and Echendu et al. [102] have also numerically investigate the mixing-separating device. Using Phan-Thien-Tanner (PTT) and Taylor-Galerkin 2D models respectively, they reported the formation of two central stagnant regions for $1 \leq Re \leq 50$ symmetrically placed about the central horizontal and vertical lines of symmetry through the geometry. Furthermore, when increasing $Re$ ($Re > 50$), these stagnant regions begin to recirculate and grow in size, forming a central vortex in the geometric gap of the domain.

Despite the developments presented by the works of Baloch, Townsend, and Webster [101]; Afonso et al. [27]; and Echendu et al. [102] − using different numerical constitutive models for viscoelastic fluid flows under Stokes flow conditions ($Re \approx 1$) − there is no evidence of any experimental work which deal with the effects of non-Newtonian fluid characteristics on the critical Weissenberg number. Moreover, investigation around the mechanisms of the flow field becoming time-dependent in this geometry is required to explain the mechanisms of the purely elastic instability.

## 2.9 Summary and guidance

The literature discussed in this chapter certainly indicates the applicability of the flow instabilities in microfluidics. Many experiments have revealed a consistent presence of convective mixing and heat transfer enhancement in channel flows under moderate Reynolds ($20 < Re < 100$) number when a instability is triggered. Furthermore, numerical simulations have shown the ability to extrapolate the experimental results and reveal flow features which often are difficult to firmly obtain only through experiments.

Flow visualisation has proved to be useful to capture flow features and topology. Moreover, numerical simulation combined with experimental data is ideally suited to understand the changes in the flow field due to the instabilities. Questions remain over the capacity to trigger, control, and delay these instabilities. Whilst a number of works related to the inertial and elastic instabilities application within T-shaped and cross-slot geometries have been reported, there is only a few investigations available of the flow within a mixing-separating cell. It has been difficult to confirm that the changes in flow topology are related to flow instabilities. Besides, it has been difficult to confirm whether the vortical behaviour in the different geometries are linked to changes in the flow topology, and whether they are in fact flow instabilities.

A 3D numerical investigation combined with experimental flow visualisation is required to clarify these remaining questions. In this work we present an experimental

study using epifluorescence flow microscopy, and the results obtained from it, provides the three-dimensionality of the fluid path in a mixing-separating cells. Numerical simulations complement the studies allowing us to visualise the 3D shape of the flow before and after the instability is triggered, as well as determine if the changes in the flow field show any clear relationship with a flow instability. With particular reference to the application of the flow instability, bifurcation parameters are used to define when the instability occurs and develops, and therefore, we also explore the behaviour of such phenomena on the enhancement of heat transfer in a cross-slot device.

Using the same experimental approach and a model liquid (Boger fluid) with nearly constant viscosity to elucidate the role of elasticity, we explore experimental investigations on the behaviour of the so-called purely elastic instability in a mixing separating to obtain a better understanding the nature of this instability.

# Chapter 3

# Experimental methodology and materials

This chapter discusses the experimental method used for carrying the analysis presented in this thesis. It is divided into four parts. Section 3.1 presents an introduction. In section 3.2, key information about the facility and experimental hardware used for performing experimental flow visualisation and data acquisition. All data discussed herein were taken at the Fluids Laboratory, located at the School of Engineering, at the University of Liverpool. Section 3.3 presents and compares the different working fluids used during the experimental campaign. The fluid characterisation techniques used and the dimensionless parameters are also introduced. Finally, in section 3.4, uncertainties on the experimental measurements are examined in detail.

## 3.1 Introduction

### 3.1.1 Flow visualisation

The experimental flow visualisation technique employed during this project is the epi-fluorescence microscopy (EM). The EM technique emphasises the three-dimensionality of the fluid path based on the fluorescent intensity of the image dye stream [68]. Additionally, pressure drop measurements were also performed across the individual pairs of inlet and outlet using a pressure transducer. Before beginning to discuss the technical details of the experimental set-up, it is important to say a few words about the epifluorescence microscopy technique (EM), why using it, and its advantages over other systems.

The term epifluorescence refers to the fluorescence of an object in an optical microscope when irradiated from the viewing side. Fluorescence is the process by which molecules excited by electromagnetic radiation almost immediately emit a photon [112]. The basis of fluorescence microscopy is the fact that it permits the filtering out of all emission light ($< 500$ nm) from the received signal [113]. Essentially, the EM technique is a non-intrusive flow visualisation method. Therefore, one can obtain fluid

flow patterns without flow disturbances. Moreover, for microfluidic applications, the EM technique can also capture relatively large areas of the flow field. The use of this technique is very commom in direct visualisation process where multiple streams are involved such as in mixing and dispensing [114]. In addition, some fluorescent dyes exhibit a highly temperature-dependant quantum yield that has facilitated a fluorescent-dye based microfluidic thermometry technique, also known as laser-induced fluorescence (LIF) [115, 116].

Till date, the bulk of the microscale flow visualizations have been particle based of which microscale particle image velocimetry ($\mu$PIV) has been the most dominant type. In this system, the velocity vectors are computed by determining the displacement of dispersed particles between two successive time frame images [77]. Despite the advantages of the $\mu$PIV technique, we opted for the EM method. One of the major challenges in particle-based microflow visualization remains to eliminate the noise due to the enhanced relative contribution of using micrometre sized tracer particle compatible with causing least flow disturbance. Moreover, the EM method of microflow visualization, which are primarily designed towards deciphering the flow patterns occurring during micromixing, flow instability and flow transformation, has been progressively developed.

Essentially, the technique for the use of fluorescent dye is achieved by acquiring the luminescent signal of fluorescent dye through an optical arrangement (e.g. a microscope). The objective lenses are most important components of an optical microscopy system and are essentially cylinders containing embedded glass lenses to collect light from the sample. A long-pass optical filter is used to selectively allow the emitted wavelengths from the fluorescent dye. The excitation and the luminous intensity is then captured using by the sensitive CCD camera, and the images can be analysed in a computer using image processing by an in-house Matlab programme which we developed (see figure 3.1).

### 3.1.2 Pressure drop measurements

In pressure-driven flows, the accuracy of pressure measurements depends critically on the sensitivity of the transducer employed. Different pressure sensors covering various differential pressure ranges can be employed according to the pressure drop to measure, which depends on the channel characteristics and the flow rates under study [117].

The differential pressure sensors, typically used in microfluidics, should be calibrated utilizing two different methods: a static column of water for sensors covering small pressure differences and a compressed air line with a manometer for sensors covering higher differential pressures [118]. A power supply powers the pressure sensors and connected to a computer using a data acquisition system to register the data (voltage). Figure 3.4, in section 3.2, shows the calibration curve for the differential pressure sensor,

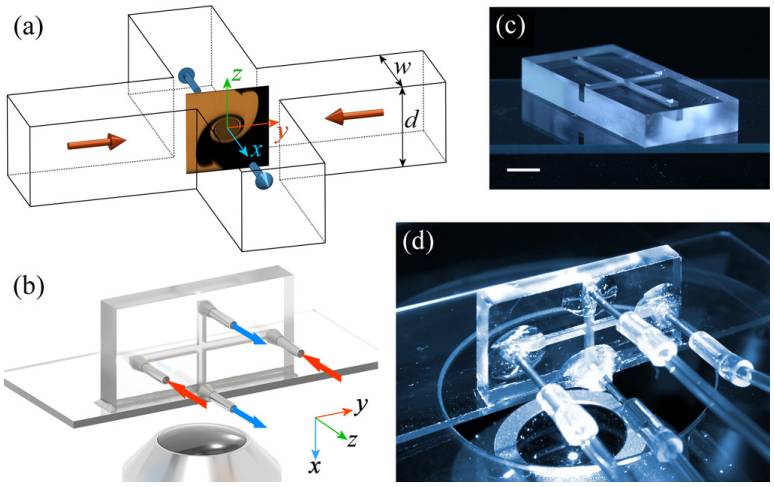


Figure 3.1: A schematic of an apparatus for flow visualisation of the cross-slot geometry. (a) Schematic diagram of a cross-slot device. (b) Design of a microfluidic cross-slot device allowing direct observation of the $y-z$ plane at $x=0$. The device is vertically mounted on an inverted microscope with a long working distance lens, enabling a direct view of the centre of the geometry where the spiral vortex instability forms. (c) A prototype microfluidic cross-slot device fabricated in fused silica. (d) Photograph illustrating the experimental setup with the cross slot mounted on an inverted microscope [from Haward et al. [7]].

which presents a linear dependence of the voltage with the imposed pressure difference (without hysteresis).

Diaphragm-type transducers are the preferred choice for high precision, fast response times and digital output. One must consider the proportionality of sensitivity to the full-scale reading, which means that high-range transducers can give a reduced accuracy in flows with low velocities. Moreover, this type of transducer requires in-situ calibration using reference pressure [119]. Essentially, the voltage output of the diaphragms is calibrated for the differential pressure range using a high-accuracy differential pressure transducer. An analogue-to-digital converter can sample the signal, and the relation between applied pressure drop and the DC voltage output, which is known to be linear (calibration curve, figure 3.4), gives the measured pressure drop values.

### 3.1.3 Microfluidic device fabrication

PDMS (Polydimethylsiloxane) is perhaps the most widely used silicon-based organic polymer in scientific research. It is optically clear and elastic. Its Youngs modulus is determined by the mixing ratio of the 'base' and 'curing agent' (sometimes also referred to as 'crosslinker'). For these reasons, it is often adopted to manufacture microfluidic devices in various types of experiments (e.g., flow visualisation and $\mu$PIV). Typically, a precursor solution of PDMS is poured onto a pre-patterned mould, and subsequent curing completes the formation of PDMS-based channels for microfluidic devices [117].

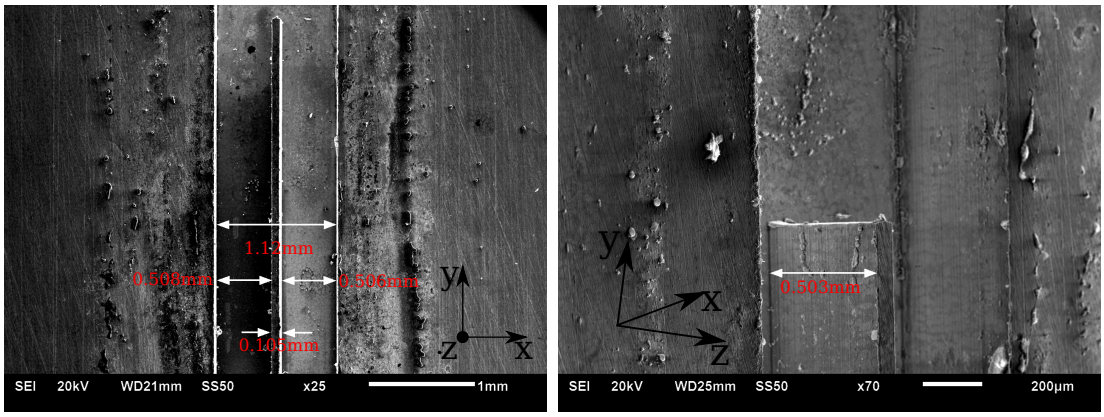


Figure 3.2: SEM (Scanning Electron Microscopy) images of the mixing-separating microchannel resulting from the micromachining process. (left) Top view showing measured channel width and wall thickness. (right) Inclined view to show the wall and channel height.

PDMS is very sensitive to minute changes in applied pressures.The flexibility of a PDMS microfluidic channel can cause elastic deformation under fluid stress and applied pressure. Additionally, conventional PDMS-based micro-fluidic devices only operate at low flow rates (MAX($Re$) $\propto$ Youngs modulus), which limits the throughputs of the devices [118]. While most of the existing literature has a focus on PDMS, We have opted to use Computer Numeric Control (CNC) micro-machining. Using CNC machining, which enables accurate three-dimensional shapes to be obtained, we could adopt a wide range of materials to fabricate our micro-channels (e.g. metal, plastic, and others) to support high pressure and avoid deformation or collapse.

While most of the microfabrication process relies on adding material, micromachining is a subtractive fabrication process. It relies on the use of rotating cutting tools to remove bulk material from the workpiece. The system consists of a worktable for $x-y$ positioning of the workpiece, a cutting tool and a spindle. For micron-sized dimensions, the milling control is usually CNC for automation, repeatability and precision (see figure 3.2) [118]. As per figure 3.2, the measurement accuracy of CNC micromachining procedure was found to be $\pm 5\mu$m.

## 3.2 Experimental setup - Mixing-separating cell

A schematic diagram of the experimental rig is shown in figure 3.3. Flow through the microfluidic system was driven using two identical pressure vessels, which are connected to a compressed air supply. Both pressure vessels were maintained at room temperature. The flow rate was measured for each inflow using a metal tube flowmeter (3750A Ar-Mite Low Flow Armored Flowmeter, BROOKS). According to the manufacturer, the flowmeter measurement accuracy is 5% of the full scale. The metal tube flowmeter

was experimentally calibrated by comparison to a syringe pump (PHD Ultra Harvard Apparatus), which has a certified accuracy of 0.35%, in the range $3 - 80$ml/min. This comparison indicated that the flow rate obtained using the metal tube flowmeter shows good agreement with that obtained using the syringe pump, with an average deviation of approximately 3.5%. The liquid flows through the device and is ultimately ejected into the collecting container. The collected liquid is then weighed instantaneously as a function of time $W(t)$ by a Mettler Toledo (Delta Range, TOLEDO) SB16001 balance (sampling rate of 5Hz and uncertainty $\pm 0.1$g at range of 3200g or below) connected to the computer via a serial port (RS-232C), allowing for a precise measurement of the amount of working fluid collected for a known time. The time-averaged fluid discharge rate ($\dot{m}$) is estimated as $\Delta W/\Delta t$.

The mixing-separating cell device was micro-machined into a piece of brass using CNC machining with a square cross-section channel height of $H = 500 \pm 1\mu$m. The device was encased in polyoxymethylene, an insulating material also known as ACETAL [1]. The cross-section dimensions of the mixing-separating cell flow device were quantified using a Nikon EPIPHOT TME inverted microscope with 100 times magnification, 235 pixels = 500$\mu$m. The combined length of the channel inlet and outlet is $80H$ ($L = 40 \pm 0.1$mm) to ensure fully-developed flow at the central region of the geometry for all Reynolds numbers studied [120]. Four cylindrical holes (with a diameter and depth of 10mm) at the end of each arm of the mixing-separating cell were drilled and tapped so that pressure tappings could be incorporated. The mixing-separating geometry was enclosed by a 6.5mm thick upper wall fabricated from borosilicate glass to maintain a sealed condition while still allowing the flow structure to be visualised (see figure 3.3).

A diaphragm-type differential pressure transducer (DP15-26, Validyne Engineering) with a quoted full-scale accuracy of $\pm 0.25\%$ was employed for measuring the pressure differential between the inlet and outlet of the channel cells combined with a flexible Tygon tube (internal diameter 1 mm). A diaphragm-sensing element model $3 - 42$ with pressure range $0 - 140$kPa was utilised for the pressure-drop measurements. The voltage output for the pressure transducer, which was digitised using a Validyne CD223 digital transducer indicator, was sampled by an analogue-to-digital converter (ADC) at 100 Hz for 60 seconds. The pressure transducer was calibrated at periodic intervals using air against an MKS Baratron differential pressure transducer (MKS Instruments Inc. USA). The relation between the applied pressure drop and the voltage output of the transducer for the diaphragm is linear as shown in figure 3.4.

Minor pressure losses (the inlet and outlet manifolds and corresponding sudden contraction and expansion) associated with the measured pressure drop are estimated using the traditional relationships used in micro-scale [121, 122] where the percentage

[1] The special features of ACETAL are high stiffness, high thermal resistance, low friction and excellent dimensional stability.

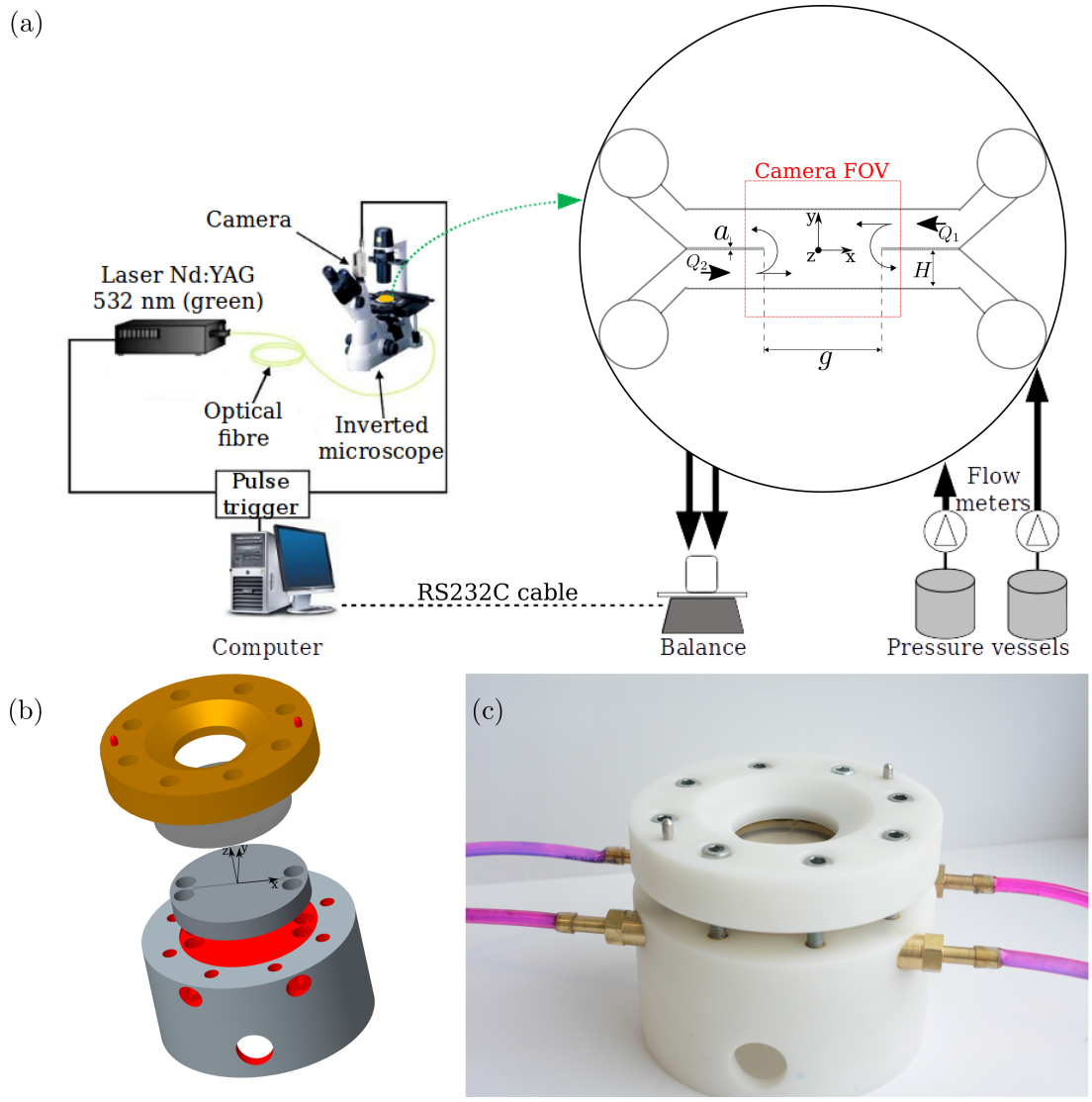


Figure 3.3: (a) A scheme illustrating the experimental apparatus of a microfluidic mixing-separating cell device allowed for direct observation of the $x-y$ plane at $z=0$ and the characteristic channel dimensions ($H = W = 500\mu$m; $g = 5H = 2.5$mm; $a = H/5 = 100\mu$m). The origin is placed at the geometric centre of the device gap ($g$). The rig is mounted on an inverted microscope fitted with a filter cube. A pulsed Nd:YAG laser is used to excite the dyed fluid, and a CCD camera enables to capture the instability formation [notes: 1-not to scale; 2-camera FOV (field of view): 3.2mm x 2.4mm]. (b) The exploded view of the prototype microfluidic device rig. The channels were micro-machined in brass and encased in polyoxymethylene. A 6.5mm thick upper wall fabricated from borosilicate glass to obtain a sealed condition while allowing the flow structure to be visualised. (c) Photograph illustrating the experimental rig set-up assembled.

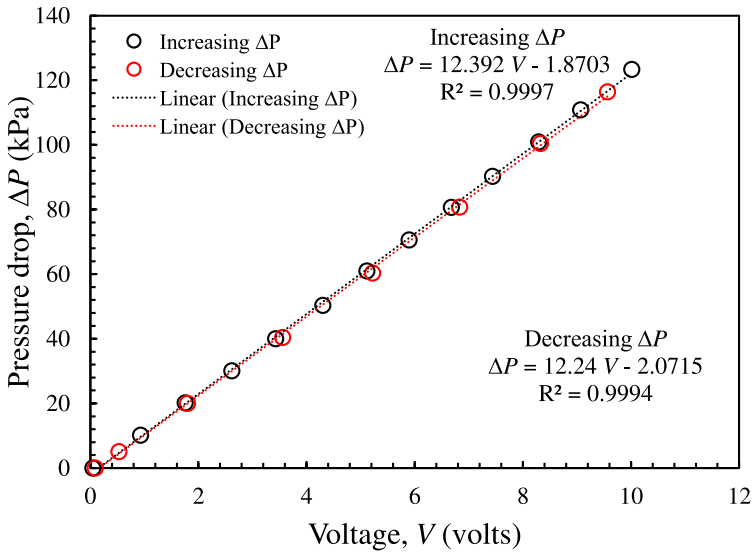


Figure 3.4: Pressure transducer calibration curves.

of these losses to the major pressure drops ranges from just 0.11% at a low flow rate to 2.3% at a high flow rate. Thus, the pressure drop across an individual inlet/outlet pair was approximately equal to that in a straight channel.

Rhodamine-B (ACROS Organics) was chosen as a fluorescent dye to capture the flow patterns in the mixing-separating cell micro-geometry. The Rhodamine-B fluorescent derivative exhibits an excitation maximum at a wavelength of 556 nm and a maximal emission wavelength of 580 nm [115, 123, 124]. The fluid was prepared by dissolving 0.05g (500 ppm) of Rhodamine-B in one litre of working fluid. The optical set-up is composed of an inverted microscope (DMI, Leica Microsystems GmbH) fitted with an appropriate filter cube (excitation BP $530 - 545$nm, dichroic mirror 565nm, barrier filter $610 - 675$nm, Leica Microsystems GmbH), and a pulsed Nd:YAG laser (Solo-PIV III laser, wavelength 532nm, New Wave Research) that is used to excite this fluorescent Rhodamine-B dye with illumination and a charge couple device (CCD) camera. The camera is synchronised with the laser at a repetition rate of 8Hz. All images shown in this work were captured at the centre plane using an 8x microscope objective (Leica Microsystems GmbH), and the camera field of view (FOV), 3.2mm x 2.4mm, thoroughly covers the central region of the device containing the gap. The flow visualisation technique applied here consists of pumping dyed fluid (Rhodamine-B) from one of the inlets while undyed fluid is pumped in the other inlet; both inlets are kept at the same flow rate. Fluid motion starts from rest and, after reaching steady-state conditions in approximately ten (10) seconds, at least fifty images were captured through the upper glass cover of the mixing-separating cell. Pressure readings were

also simultaneously recorded via the data acquisition system.

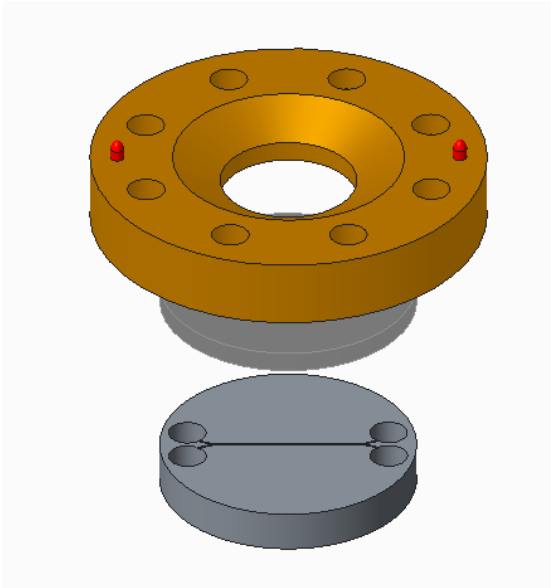

Figure 3.5: Design of the channels micro-machined in brass and encased in polyoxymethylene. A 6.5mm thick upper wall fabricated from borosilicate glass to obtain a sealed condition while allowing the flow structure to be visualised. Note: The immediate availability of the images provides an instantaneous feedback during the experimental setup.

## 3.3 Working fluids

As previously mentioned in chapter 2, fluids are divided into two major categories based on their behaviour, Newtonian and non-Newtonian. Newtonian fluids obey Newton's law of viscous resistance as [30]:

$$\tau = \mu\dot{\gamma} \tag{3.1}$$

where $\tau$ is the shear stress, and $\dot{\gamma}$ is the shear rate. The coefficient $\mu$ represents the fluid dynamic viscosity, which in a Newtonian fluid consists of a constant value at all shear rates. Moreover, the shear stress presents a linear behaviour when varying the shear rate. Conversely, non-Newtonian fluids interestingly show a variable viscosity at different shear rates (apart from Boger fluids which will be discussed later). There are many categories of these non-Newtonian fluids, which can be classified depending on the relationships between shear rate and shear stress [30] [2].

In order to obtain Newtonian fluids with a relatively high viscosity, solutions of glycerine in water were used. The non-Newtonian fluid used in the present research is

[2]The different non-Newtonian fluids classification can be easily found in the literature, and therefore is out of the scope of the present research.

Table 3.1: The measured values of density and viscosity for the Newtonian working fluid

| Temperature | Density ($\rho$) | Viscosity ($\mu$) |
|---|---|---|
| °C | $kg/m^3$ | $Pa.s$ |
| 20 | 1183.6 | 0.0215 |
| 22 | 1183.1 | 0.0201 |
| 24 | 1182.5 | 0.0186 |
| 26 | 1178.4 | 0.0178 |

a water-based polymer solution. The solvent water was distilled using a boiling water distiller to remove nearly all minerals, many chemicals, and most bacteria. All rheological properties were normally measured with and without addition the fluorescent dye to ensure that the rheological properties of viscoelastic solution are constant with adding the dye (Rhodamine-B).

### 3.3.1 Newtonian solution

The working fluid used for the Newtonian experimental measurements was a mixture of glycerine (relative density 1.26, ReAgent Chemical Services) and distilled water with a nominal concentration of 70 per cent glycerine (by weight). The density ($\rho$) and viscosity ($\mu$) of the mixed solution were measured at room temperature (varying from 20°C to 26°C). A density meter (Anton Paar DMA 35N) with a quoted precision of 0.001g/cm$^3$ was used for quantifying the fluid density. A controlled-stress torsional rheometer (Anton Paar MCR302) was utilised to measure the fluid viscosity using a 60mm and 1° cone with a shear rate range from 1s$^{-1}$ to 100s$^{-1}$. The measured values of the density ($\rho$) and viscosity ($\mu$) are given in table 3.1 [3]. It is also convenient to define the dimensionless Reynolds number as in equation (3.2), based on the mean velocity ($U_b = \dot{m}/\rho H^2$) and the channel height ($H$).

$$Re = \frac{\rho H U_b}{\mu} \tag{3.2}$$

The pressure drop ($\Delta p$) between inflow and outflow arms (after subtracting the minor pressure losses as already discussed in section 3.2) and mean fluid flow velocity ($U_b$) were experimentally measured to determine the Darcy friction factor-Reynolds number product, $fRe$:

$$fRe = \frac{2\Delta p H^2}{L U_b \mu} \tag{3.3}$$

where $H$ and $L$ are the square channel depth and the combined length of the inflow and outflow channels, respectively, and $\mu$ is the fluid dynamic viscosity. The uncertainty of

[3] As glycerine absorbs moisture from the ambient, the prepared solutions were stored in sealed plastic bottles

$fRe$, which is associated with the estimated error of each term in Eq. 5.1, is carefully estimated by following the same methodology adopted in [40]. The minimum and maximum uncertainty values of $fRe$ are 1.7% and 11.6%, respectively. The large relative uncertainties refer to the low flow rate region where the small pressure drops generate a significant degree of error (approximately 90% of the total error of the $fRe$ when $Re < 5$). Dimensional inaccuracies (particularly in measuring $H$) also play a significant role in the determination of $fRe$ [121, 48]. The experimental results of $fRe$ were also compared to the conventional theory for a fully-developed flow in a straight channel of a square cross-section ($fRe = 57$ in laminar flow, [125]).

### 3.3.2 Polymeric solution

A model liquid with nearly constant viscosity was employed to investigate the role of elasticity. A so-called Boger fluid that consists of a mixture of Polyethylene glycol (PEG, $M_w = 8x10^3$[g.mol$^{-1}$] [4], Sigma-Aldrich), Polyethylene oxide (PEO, $M_w = 4x10^6$[g.mol$^{-1}$], Sigma-Aldrich), and distilled water. Initially, the required amount of PEO is added to distilled water, and the resultant liquid is slowly mixed using a magnetic stirrer. In another container, the necessary amount of PEG is also added to distilled water and mixed in a magnetic stirrer. After 12 hours, the result is two clear, transparent, and colourless solutions. The PEO and PEG solutions are then combined in another container, and the resultant polymer solution is left to mix gently in a magnetic stirrer for 12 hours. The solution used is characterised before and after the experiments to check for the effect of ageing over time. The fluid properties do not change during the time scale of the experiments, which lasted approximately 1-3 hours. In any case, all prepared polymer solutions were maintained in the refrigerator at 4°C to prevent any potential thermal or bacteriological degradation and used within three days of preparation.

All rheology measurements were conducted at room temperature ($23 \pm 2$°C). A density meter (Anton Paar DMA 35N) with a quoted precision of 0.001g/cm$^3$ was used for quantifying the fluid density. A controlled-stress torsional rheometer (Anton Paar MCR302) was utilised to measure the fluid shear viscosity using a 60mm and 1° cone with a shear rate range from 1s$^{-1}$ to 100s$^{-1}$. The relaxation time of the fluid were measured using a Capillary Breakup Extensional Rheometer (CaBER) [126]. In the configuration used, a small column of fluid (less than 0.2ml) is placed between two cylindrical platens with diameters ($D_p$) of 4mm, the upper platen is moved away from the lower platen almost instantaneously (approximately 50-100ms) (see figure 3.6 for schematic).

The working fluid characterisation includes measuring viscosity, density, and relaxation time. The effect of ageing of the polymer solution was studied by observing the

[4] $M_w$ represents the molecular weight.

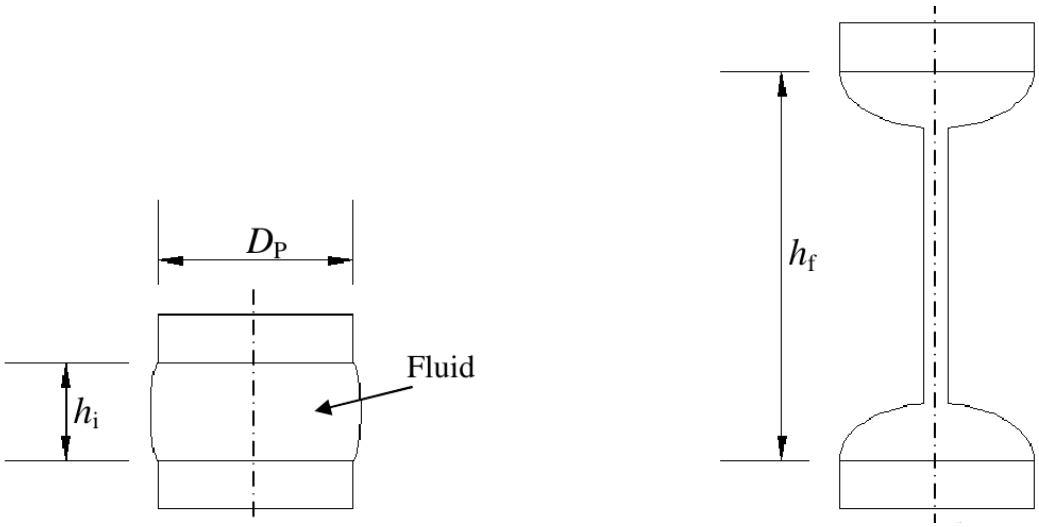


Figure 3.6: Schematic showing the different heights for initial and final CaBER plate positions.

changes in these properties with time for different samples of a single fluid batch on different days. Table 3.2 shows a summary of the measured values. Negligible variations in density were noticed. Figure 3.7 displays that the viscosity is approximately constant for the shear rate range tested. Viscosity does not vary over time for the measurements performed on three different days.

For a Newtonian fluid the uniaxial extensional viscosity is always three times that of the shear viscosity [127]. However, for non-Newtonian fluids, this is not true. Moreover, it is not possible to estimate the extensional viscosity from the shear viscosity or vice versa for non-Newtonian fluids due to the variable properties in these solutions. Therefore, we used extensional rheology to determine the relaxation time ($\lambda$), from which both Deborah and Weissenberg numbers can be determined. The Thermo Haake Capillary Break-up Extensional Rheometer (CaBER) exerts a uniaxial step strain, e.g. by creating a fluid filament, on a sample of the working fluid, and thus measures the reduction in filament diameter due to surface tension over time [126]. In the equipment, a small sample of fluid (around 0.1ml) is placed between two cylindrical platens with diameters of 4mm, then an extensional strain is exerted on the fluid sample when the upper platen is rapidly moved away from the lower platen (approximately 50-100ms). Consequently, the fluid is subject to an extensional strain rate, and a cylindrical fluid filament is formed. The midpoint of the filament diameter decreases over time due to surface tension and the extensional stresses within the fluid element resist this thinning. A laser micrometer (resolution 10$\mu$m) measures the reduction in the midpoint diameter in order to provide information on the extensional properties.

Figure 3.8 presents the measurements of the time decay of the normalised mid-point diameter from the polymer solution filament. The relaxation time can be estimated by

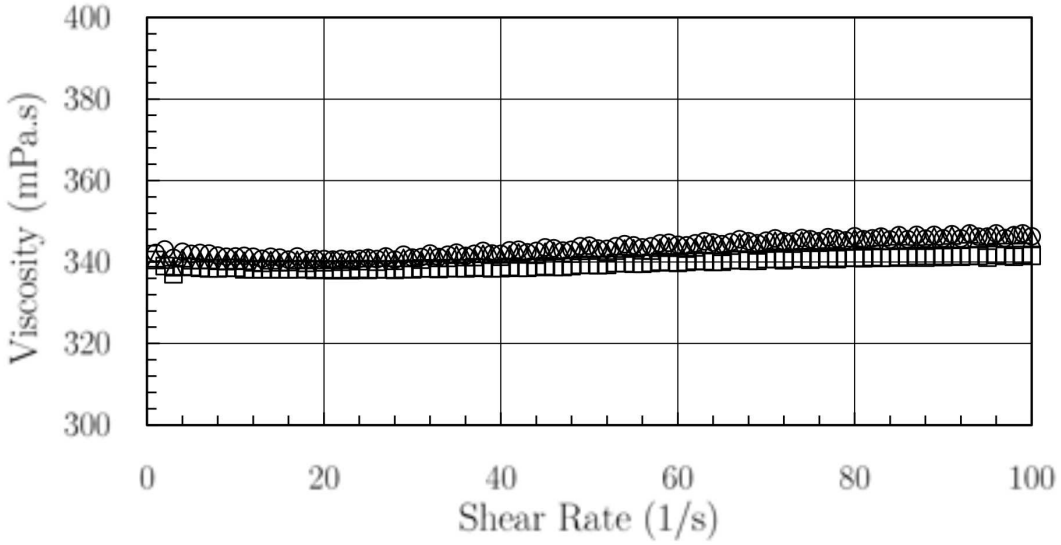


Figure 3.7: Plot of viscosity as a function of shear rate for the polymer solution. Figure shows three different samples of a single fluid batch in three different days. △ Sample 1: 17/08/17, ◯ Sample 2: 24/08/17, □ Sample 3: 31/08/17

Table 3.2: The measured values of density, viscosity and relaxation time for characterisation of working fluid. The effect of ageing of the polymer solution was studied by observing the change in viscosity with time for samples of a single fluid batch in three different days

| Sample | Temperature °C | Density ($\rho$) $kg/m^3$ | Avg. Viscosity ($\mu$) $mPa.s$ | R. time ($\lambda$) $s^{-1}$ |
|---|---|---|---|---|
| 1 | 23 | 1087.9 | 342.1 | 0.09 |
| 2 | 23 | 1088.1 | 342.5 | 0.11 |
| 3 | 23 | 1088.5 | 342.9 | 0.12 |

using the equation:

$$\frac{D_{mid}(t)}{D_0} = \frac{GD_0}{4\sigma}^{\frac{1}{3}} \exp\frac{-t}{3\lambda} \tag{3.4}$$

where $D_{mid}$ is the diameter of mid-point fluid filament at time $t$, $D_0$ is the initial diameter, and $\lambda$ is the relaxation time for the fluid. More precisely, since the stress does not relax as such as the filament diameter decays, $\lambda$ represents the characteristic timescale for viscoelastic stress growth in a uniaxial elongational flow [126, 128]. $G$ is the elastic modulus, and $\sigma$ is the surface tension. By fitting an exponential curve within the elasto-capillary range, $\lambda$ can be obtained (see the red line in 3.8).

The CaBER measurements reveal the relaxation time ($\lambda$) of this Boger fluid, and to check the repeatability of the results, the relaxation time was measured in three different days (see table 3.2).

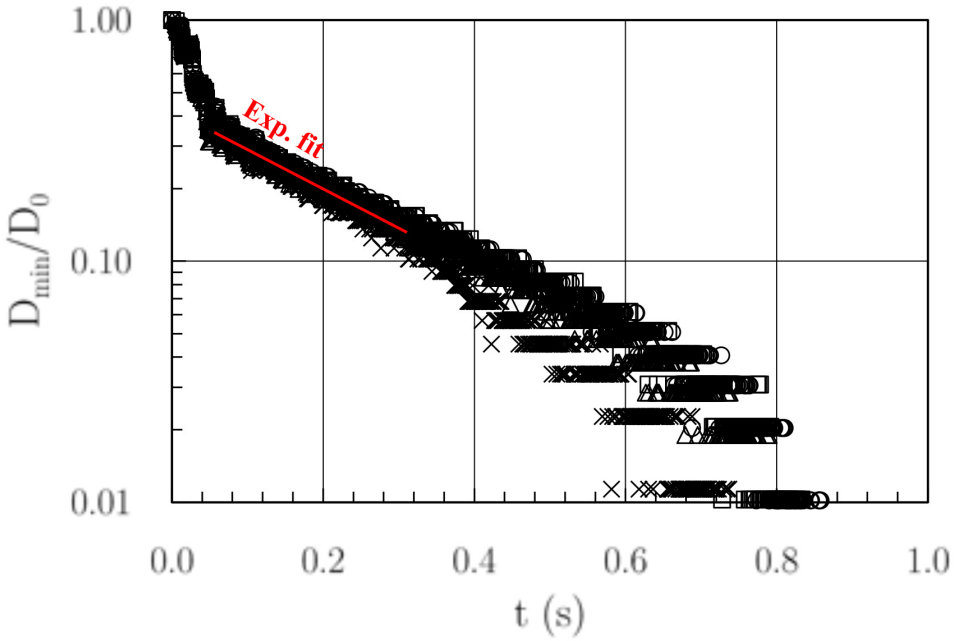


Figure 3.8: Extensional rheology data (CaBER) showing the time dependence of the normalised diameter of the polymer solution filament. The full red line is an exponential fit within the elasto-capillary range (refer to equation 3.4). The figure shows measurements of the time decay of minimum diameter of the filament for different samples of a single fluid batch in three different days. △ Sample 1: 17/08/17, ◯ Sample 2: 24/08/17, □ Sample 3: 31/08/17

## 3.4 The uncertainty of experimental parameters

As suggested in the literature [122, 121], the experimental uncertainties in microfluidic devices can become quite large due to the physical size of the system. Therefore, an accurate determination of the errors in the experimentally measured data is strongly necessary. The standards for determining experimental uncertainties, ASME PTC 19.1 [129] and NIST Technical note 1297 [130], in general states that the total error can be expressed in two parts − the bias error and precision error − as follows:

$$\varepsilon = 2\sqrt{\left(\frac{B}{2}\right)^2 + \left(\frac{\sigma}{\sqrt{N}}\right)^2} \tag{3.5}$$

where $\varepsilon$ represents the total uncertainty, $B$ the bias error, the standard deviation is $\sigma$, and $N$ the number of samples. The measure of systematic error represents the bias error in the equation 3.5. The measured random errors express the precision error in the system.

Propagating errors give the uncertainty of a calculated parameter based upon the

measured variables.

$$\varepsilon p = \sqrt{\sum_{i=1}^{n} \left( \frac{\partial p}{\partial a_i} \varepsilon a_i \right)^2} \tag{3.6}$$

where $\varepsilon p$ represents the error calculated for the parameter $p$, $a_i$ the variable used to calculate $p$, and $\varepsilon a_i$ the uncertainty of the variable $a$. The uncertainty in any parameter is the sum of the uncertainties of the variables used to calculate that parameter.

### 3.4.1 Experimental mass flow rate uncertainties

Applying the equation 3.6, the uncertainties in the mass flow rate measurements using a scale connected to a computer via a $RS-232C$ cable can be determined as follows:

$$\dot{m} = \frac{m}{t} \tag{3.7}$$

$$\varepsilon \dot{m} = \left[ \left( \frac{\partial \dot{m}}{\partial m} \varepsilon m \right)^2 + \left( \frac{\partial \dot{m}}{\partial t} \varepsilon t \right)^2 \right]^{1/2} \tag{3.8}$$

$$\varepsilon \dot{m} = \left[ \left( \frac{1}{t} \varepsilon m \right)^2 + \left( \frac{-m}{t^2} \varepsilon t \right)^2 \right]^{1/2} \tag{3.9}$$

$$\frac{\varepsilon \dot{m}}{\dot{m}} = \left[ \left( \frac{\varepsilon m}{m} \right)^2 + \left( \frac{\varepsilon t}{t} \right)^2 \right]^{1/2} \tag{3.10}$$

### 3.4.2 Flow bulk velocity uncertainties

The uncertainties in flow bulk velocity measurements can be estimated as follows:

$$U_b = \frac{\dot{m}}{\rho H^2} \tag{3.11}$$

$$\varepsilon U_b = \left[ \left( \frac{\partial U_b}{\partial \dot{m}} \varepsilon \dot{m} \right)^2 + \left( \frac{\partial U_b}{\partial \rho} \varepsilon \rho \right)^2 + \left( \frac{\partial U_b}{\partial H} \varepsilon H \right)^2 \right]^{1/2} \tag{3.12}$$

$$\varepsilon U_b = \left[ \left( \frac{1}{\rho H^2} \varepsilon \dot{m} \right)^2 + \left( \frac{-\dot{m}}{\rho^2 H^2} \varepsilon \rho \right)^2 + \left( \frac{-2\dot{m}}{\rho H^3} \varepsilon H \right)^2 \right]^{1/2} \tag{3.13}$$

$$\frac{\varepsilon U_b}{U_b} = \left[ \left( \frac{\varepsilon \dot{m}}{\dot{m}} \right)^2 + \left( \frac{\varepsilon \rho}{\rho} \right)^2 + \left( 2 \frac{\varepsilon H}{H} \right)^2 \right]^{1/2} \tag{3.14}$$

$$\frac{\varepsilon U_b}{U_b} = \left[ \left( \frac{\varepsilon m}{m} \right)^2 + \left( \frac{\varepsilon t}{t} \right)^2 + \left( \frac{\varepsilon \rho}{\rho} \right)^2 + \left( 2 \frac{\varepsilon H}{H} \right)^2 \right]^{1/2} \tag{3.15}$$

### 3.4.3 Reynolds number uncertainties

The uncertainties in the Reynolds number ($Re$) measurements can be estimated as follows:

$$Re = \frac{\rho H U_b}{\mu} \tag{3.16}$$

$$\varepsilon Re = \left[ \left( \frac{\partial Re}{\partial \rho} \varepsilon \rho \right)^2 + \left( \frac{\partial Re}{\partial H} \varepsilon H \right)^2 + \left( \frac{\partial Re}{\partial U_b} \varepsilon U_b \right)^2 + \left( \frac{\partial Re}{\partial \mu} \varepsilon \mu \right)^2 \right]^{1/2} \tag{3.17}$$

$$\varepsilon Re = \left[ \left( \frac{H U_b}{\mu} \varepsilon \rho \right)^2 + \left( \frac{\rho U_b}{\mu} \varepsilon H \right)^2 + \left( \frac{\rho H}{\mu} \varepsilon U_b \right)^2 + \left( \frac{-\rho H U_b}{\mu^2} \varepsilon \mu \right)^2 \right]^{1/2} \tag{3.18}$$

$$\frac{\varepsilon Re}{Re} = \left[ \left( \frac{\varepsilon \rho}{\rho} \right)^2 + \left( 2 \frac{\varepsilon H}{H} \right)^2 + \left( \frac{\varepsilon U_b}{U_b} \right)^2 + \left( \frac{\varepsilon \mu}{\mu} \right)^2 \right]^{1/2} \tag{3.19}$$

$$\frac{\varepsilon Re}{Re} = \left[ \left( \frac{\varepsilon \rho}{\rho} \right)^2 + \left( 2 \frac{\varepsilon H}{H} \right)^2 + \left( \frac{\varepsilon m}{m} \right)^2 + \left( \frac{\varepsilon t}{t} \right)^2 + \left( \frac{\varepsilon \rho}{\rho} \right)^2 + \left( 2 \frac{\varepsilon H}{H} \right)^2 + \left( \frac{\varepsilon \mu}{\mu} \right)^2 \right]^{1/2} \tag{3.20}$$

$$\frac{\varepsilon Re}{Re} = \left[ \left( 2 \frac{\varepsilon \rho}{\rho} \right)^2 + \left( 4 \frac{\varepsilon H}{H} \right)^2 + \left( \frac{\varepsilon m}{m} \right)^2 + \left( \frac{\varepsilon t}{t} \right)^2 + \left( \frac{\varepsilon \mu}{\mu} \right)^2 \right]^{1/2} \tag{3.21}$$

### 3.4.4 Friction factor uncertainties

The uncertainties in the friction factor ($f$) measurements can be estimated as follows:

$$f = \frac{2 \Delta p H}{L {U_b}^2 \rho} \tag{3.22}$$

$$\varepsilon f = \left[ \left( \frac{\partial f}{\partial \Delta p} \varepsilon \Delta p \right)^2 + \left( \frac{\partial f}{\partial H} \varepsilon H \right)^2 + \left( \frac{\partial f}{\partial L} \varepsilon L \right)^2 + \left( \frac{\partial f}{\partial U_b} \varepsilon U_b \right)^2 + \left( \frac{\partial f}{\partial \rho} \varepsilon \rho \right)^2 \right]^{1/2} \tag{3.23}$$

$$\varepsilon f = \left[ \left( 2 \frac{H}{L U_b^2 \rho} \varepsilon \Delta p \right)^2 + \left( 2 \frac{\Delta p}{L U_b^2 \rho} \varepsilon H \right)^2 + \left( -2 \frac{\Delta p H}{L^2 U_b^2 \rho} \varepsilon L \right)^2 + \left( -4 \frac{\Delta p H}{L U_b^3 \rho} \varepsilon U_b \right)^2 + \left( -2 \frac{\Delta p H}{L U_b^2 \rho^2} \varepsilon \rho \right)^2 \right]^{1/2} \tag{3.24}$$

$$\frac{\varepsilon f}{f} = \left[ \left( \frac{\varepsilon \Delta p}{\Delta p} \right)^2 + \left( \frac{\varepsilon H}{H} \right)^2 + \left( \frac{\varepsilon L}{L} \right)^2 + \left( 2 \frac{\varepsilon U_b}{U_b} \right)^2 + \left( \frac{\varepsilon \rho}{\rho} \right)^2 \right]^{1/2} \tag{3.25}$$

$$\frac{\varepsilon f}{f} = \left[ \left( \frac{\varepsilon \Delta p}{\Delta p} \right)^2 + \left( \frac{\varepsilon H}{H} \right)^2 + \left( \frac{\varepsilon L}{L} \right)^2 + \left( \frac{\varepsilon m}{m} \right)^2 + \left( \frac{\varepsilon t}{t} \right)^2 + \left( \frac{\varepsilon \rho}{\rho} \right)^2 + \left( 2\frac{\varepsilon H}{H} \right)^2 + \left( \frac{\varepsilon \rho}{\rho} \right)^2 \right]^{1/2} \tag{3.26}$$

$$\frac{\varepsilon f}{f} = \left[ \left( \frac{\varepsilon \Delta p}{\Delta p} \right)^2 + \left( 3\frac{\varepsilon H}{H} \right)^2 + \left( \frac{\varepsilon L}{L} \right)^2 + \left( \frac{\varepsilon m}{m} \right)^2 + \left( \frac{\varepsilon t}{t} \right)^2 + \left( 2\frac{\varepsilon \rho}{\rho} \right)^2 \right]^{1/2} \tag{3.27}$$

### 3.4.5 $fRe$ uncertainties

The uncertainties in the $fRe$ measurements can be estimated as follows:

$$fRe = \frac{2\Delta p H^2}{L U_b \mu} \tag{3.28}$$

$$\frac{\partial (fRe)}{\partial f} = Re \tag{3.29}$$

$$\frac{\partial (fRe)}{\partial Re} = f \tag{3.30}$$

$$\varepsilon(fRe) = \left[ \left( \frac{\partial (fRe)}{\partial f} \varepsilon f \right)^2 + \left( \frac{\partial (fRe)}{\partial Re} \varepsilon Re \right)^2 \right]^{1/2} \tag{3.31}$$

$$\varepsilon(fRe) = \left[ (Re \varepsilon f)^2 + (f \varepsilon Re)^2 \right]^{1/2} \tag{3.32}$$

$$\frac{\varepsilon(fRe)}{fRe} = \left[ \left( \frac{\varepsilon f}{f} \right)^2 + \left( \frac{\varepsilon Re}{Re} \right)^2 \right]^{1/2} \tag{3.33}$$

$$\frac{\varepsilon(fRe)}{fRe} = \left[ \left( \frac{\varepsilon \Delta p}{\Delta p} \right)^2 + \left( 3\frac{\varepsilon H}{H} \right)^2 + \left( \frac{\varepsilon L}{L} \right)^2 + \left( \frac{\varepsilon m}{m} \right)^2 + ... + \left( \frac{\varepsilon \mu}{\mu} \right)^2 \right]^{1/2} \tag{3.34}$$

$$\frac{\varepsilon(fRe)}{fRe} = \left[ \left( \frac{\varepsilon \Delta p}{\Delta p} \right)^2 + \left( 7\frac{\varepsilon H}{H} \right)^2 + \left( \frac{\varepsilon L}{L} \right)^2 + \left( 2\frac{\varepsilon m}{m} \right)^2 + \left( 2\frac{\varepsilon t}{t} \right)^2 + \left( 4\frac{\varepsilon \rho}{\rho} \right)^2 + \left( \frac{\varepsilon \mu}{\mu} \right)^2 \right]^{1/2} \tag{3.35}$$

Table 3.3: Uncertainty values for measured parameters

| Parameter | Uncertainty | Measurement range |
|---|---|---|
| Cross-section dimensions $[H]$ $(\mu m)$ | $\pm 1$ | $0 - 1000$ |
| Test-section length $[L]$ $(mm)$ | $\pm 0.1$ | $0 - 50$ |
| Pressure transducer $[\Delta p]$ $(kPa)$ | $\pm 0.25\%$ FS | $0 - 350$ |
| Mass $[m]$ $(g)$ | 0.1 | $0 - 3200$ |
| Time $[t]$ $(s)$ | n/a | n/a |
| Density $[\rho]$ $(kg/m^3)$ | $\pm 1$ | 1178 |
| Dynamic viscosity $[\mu]$ $(Pa.s)$ | $\pm 2\%$ | 0.017 |

The main geometric dimensions of the selected test sections, flowrate, pressure and temperature, which represent the independent parameters, are directly measured using various instruments, probes and sensors. The accuracy of these measurement instruments based on manufacturers supplied information, accompanying documentation, and on instruments label of specification may consist of the known sources of errors for example, the resolution, sensitivity, linearity, repeatability, reproducibility, hysteresis and various drifts. The uncertainty in the measurement of these independent parameters is tabulated in table 3.3

# Chapter 4

# Numerical methods and techniques

In this chapter, a description of the computational fluid dynamics (CFD) simulations conducted is discussed together with the bifurcation parameters adopted to investigate the different fluid flow instabilities. As CFD and experimental methods can complement each other, the purpose of this numerical investigation is to extend the range of the investigations beyond the experimental setup.

The chapter is divided into three sections. Section 4.1 presents a brief introduction to the numerical method used. In section 4.2, the numerical procedure employed for discretising the equations of motion in order to study the flow of isothermal Newtonian fluids within a mixing-separating micro-device numerically is described[1]. The reader is introduced to the computational meshes and the grid dependency study conducted to investigate the dependence of the results to the numerical grid. Additionally, an explanation of the methods used to adequately describe the onset and the evolution of the fluid flow instabilities for constant temperature cases.

Section 4.3 part explores the difference when the energy equation is added to the problem when the temperature of inlet streams are different. The different sets of boundary conditions specified for the isothermal and heat transfer cases, and also an introduction of the critical parameter used to quantify the enhancement of heat transfer in a cross-slot micro-device.

## 4.1 Governing equations and numerical method

Using a commercial software, ANSYS workbench (Fluent) version 14.5.7 [131], the numerical method solves the equations of motion, mass conservation, and energy for the boundary conditions imposed in the finite volume method used to perform three-dimensional (3D) flow simulations. The widely-used discretisation methods for numerical computations include finite difference methods, finite volume methods, and finite

[1] In this thesis numerical simulations were done only for Newtonian fluid flow.

elements methods, all of which have their pros and cons.

The Fluent package uses the finite volume method based upon discretising the computational domain into discrete small volumes by a pre-designed grid system. The fluid mass and momentum conservation equations are integrated within each control volume. The method requires high quality orthogonal computational grids as the controlled volume surface integration involves the product of cell surface vector and surface flux vector, which would lead to more cross-Cartesian direction terms in a poorly designed non-orthogonal grid system. These terms are very difficult to approximate in the final linear equation system, and will eventually affect the accuracy and stability of the numerical computation [132]. The geometries investigate in this thesis leads themselves to simple grids. Therefore, in the numerical studies, high quality orthogonal computational grids were employed.

To numerically resolve the governing equations for continuity (Eq. 4.1), momentum (Eq. 4.2), and energy (Eq. 4.3), the fluid flow was assumed incompressible, laminar, single phase, and steady-state;

$$\nabla \cdot u = 0 \tag{4.1}$$

$$\rho(u \cdot \nabla u) = -\nabla p + \mu \nabla^2 u \tag{4.2}$$

$$\rho C(u \cdot \nabla T) = k(\nabla^2 T) \tag{4.3}$$

where $\rho$, $\mu$, $C$, and $k$, constant physical properties, represent density, dynamic viscosity, specific heat capacity, and thermal conductivity, respectively. $u$ represents the velocity vector, $p$ the pressure, and $T$ temperature [30].

Numerical investigations performed in thesis are three-dimensional, and the following sections will present a comprehensive description of the boundary conditions imposed for each case investigated.

## 4.2 Numerical simulations in a mixing-separating cell

For the simulations in the mixing-separating cell, which the results can be found in chapter 5, the fluid properties are assumed constant and temperature independent. The computational domain consists of two opposed square channels interacting through a gap of non-dimensional width $\theta = g/H$ in the middle of a thin separating wall of non-dimensional thickness $\sigma = a/H$ (refer to figure 4.2). The combined length of the inlet and outlet channels was defined as 80 times its height $H$ ($L = 80H$). This length assures that the fluid velocity no longer depends upon the axial distance and the flow is hydrodynamically fully-developed [120] for all Reynolds numbers studied. Preliminary simulations were conducted with identical conditions to the experiments. The density

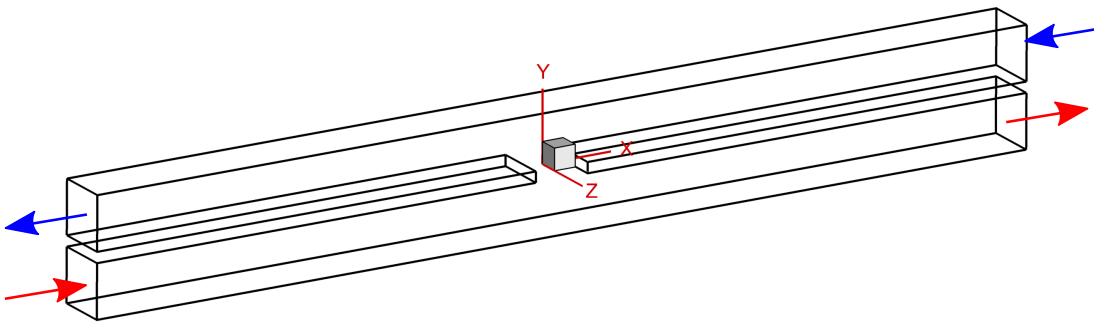


Figure 4.1: Geometry of the mixing-separating cell used to perform the numerical simulations.

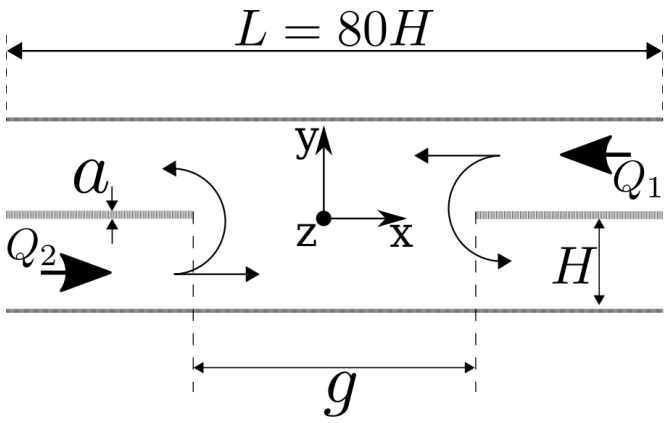


Figure 4.2: Schematic of the imposed inlets and outlets in the numerical method.

and viscosity were constant and equal to the experimentally measured values (table 3.1). The system was non-dimensionalised, such that arbitrary reference values could be used, and it was found (as expected) that the non-dimensional system produced identical results to the simulations that matched the experiments for constant fluid properties. All further simulations were conducted with the arbitrary, non-dimensional system.

The numerical simulations for the mixing-separating cell micro-geometry were carried out using the finite-volume method within ANSYS-Fluent [131]. A modified SIMPLE algorithm developed by Patankar and Spalding [133] was employed for solving the equations in discretised form (pressure-velocity coupling scheme). The equations of momentum are solved with a second-order upwind scheme. All numerical simulations are performed for convergence criteria of all relevant residuals falling to less than $10^{-10}$. A Neumann boundary condition (zero diffusion flux for all flow variables and an overall mass balance correction) was used at the outlets and no-slip conditions at all the walls.

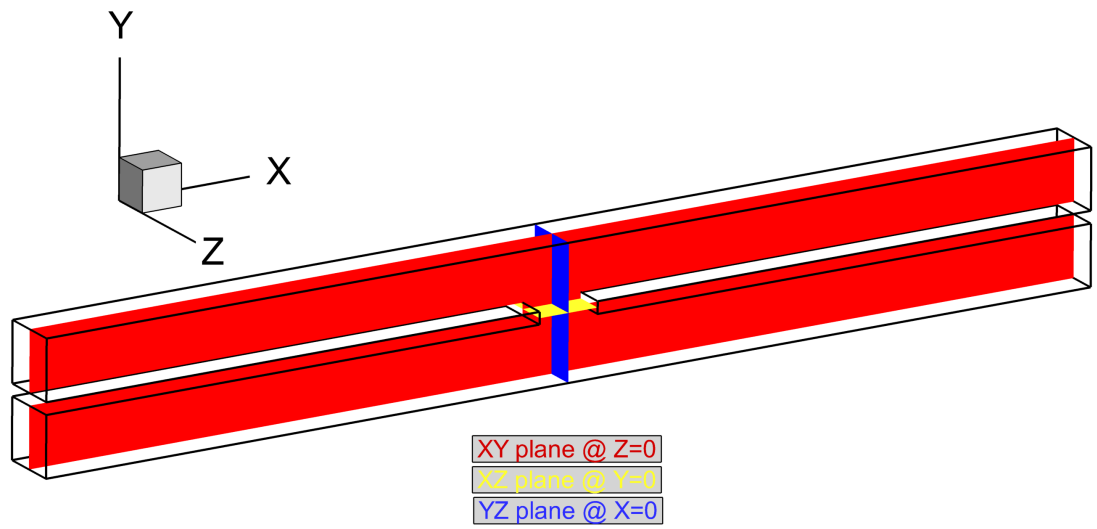


Figure 4.3: Definition of the centre planes $x-y$, $x-z$, and $y-z$.

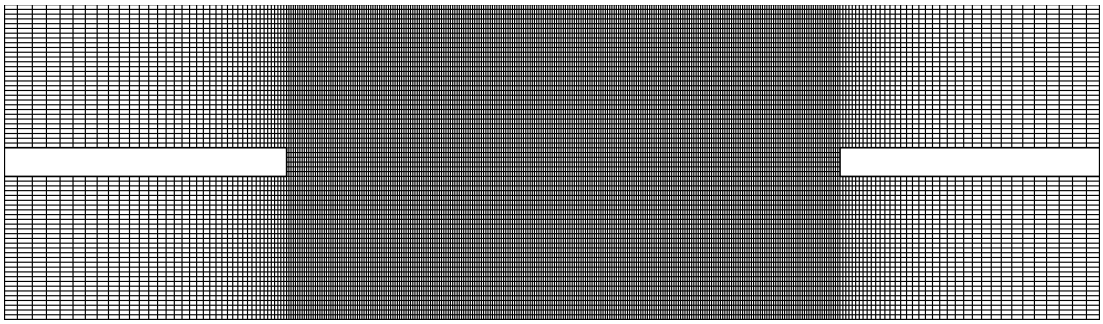

Figure 4.4: Detail of the refinement rate at the central gap of the numerical mesh M4.

### 4.2.1 Computational meshes

The boundary conditions that need to be specified are those for the inlets, outlets, and walls. The centre planes are considered along the $x-y$, $x-z$, and $y-z$, which can be visualised in figure 4.3.

A mesh refinement investigation was conducted to estimate the numerical accuracy of the simulations. A preliminary series of simulations were carried out with five different uniform hexahedral (all quad) computational meshes (shown in table 4.1). The different meshes vary the number of cells across the cross-section with grid resolutions at the $y-z$ plane of 10x10, 20x20, 25x25, 30x30 and 50x50. Along the channel length, at the $x$ direction, a fixed number of cell divisions (100) was applied accompanied by a biased refinement rate towards the geometry centre (bias factor, the ratio of the largest edge to the smallest edge, of 100:1). At the centre of the geometry, where the gap is located, the grid is refined and fully structured (i.e. cubic control volumes, see figure 4.4).

Figure 4.5 shows the variation of the velocity profile associated to the reverse flow

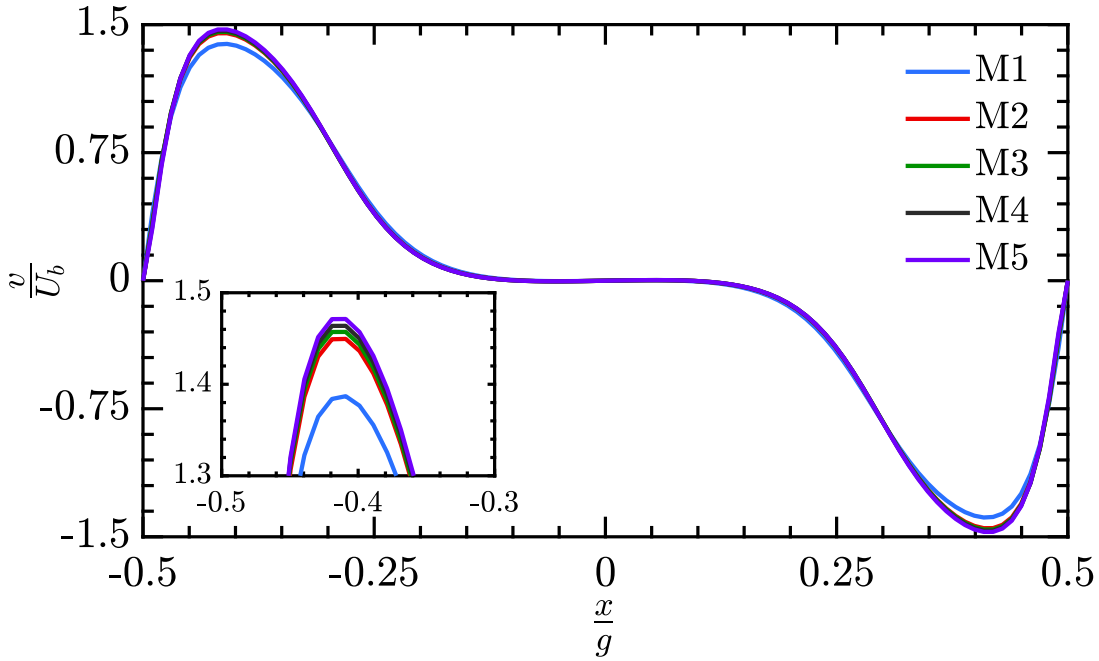


Figure 4.5: Variation of the velocity profile associate to the reverse flow ($v-$velocity component) along the gap size (line along $x$-direction at $y = 0$ and $z = 0$) for the different meshes at a fixed Reynolds number ($Re = 30$). The inset zooms into the region around the maximum value of $v/U_b$.

($v-$velocity component) with increasing mesh refinement for a typical simulation ($Re = 30$). The values were obtained along the gap horizontal centreline on the $x-y$ plane at $z = 0$ and normalised by the bulk velocity ($U_b$). The chosen criterion to determine the accuracy is the maximum value of the $v-$velocity component across the gap between the channels ($v_{max}/U_b$). Firstly, it can be noted that the variation of $v_{max}/U_b$ between the meshes becomes less than 1% when increasing the number of cells above 600,000 in the cross-section. The study revealed that mesh M4 had suitable characteristics for further simulations due to the low percentage error (0.51%) and reasonable number of cells (855,000) for computational time (see figures 4.6 and table 4.1).

Table 4.1: Mesh convergence study. The error represents the percentage error between the value $v_{max}/U_b$ for mesh M5 and the present numerical simulation. M5 was used as reference value due to its very dense mesh.

| Mesh | Cross-section | $v_{max}/U_b$ | Error (%) | Number of cells |
|---|---|---|---|---|
| 1 | 10x10 | 1.387 | 5.73 | 84000 |
| 2 | 20x20 | 1.450 | 1.48 | 380000 |
| 3 | 25x25 | 1.457 | 0.96 | 593750 |
| 4 | 30x30 | 1.464 | 0.51 | 855000 |
| 5 | 50x250 | 1.471 | - | 2375000 |

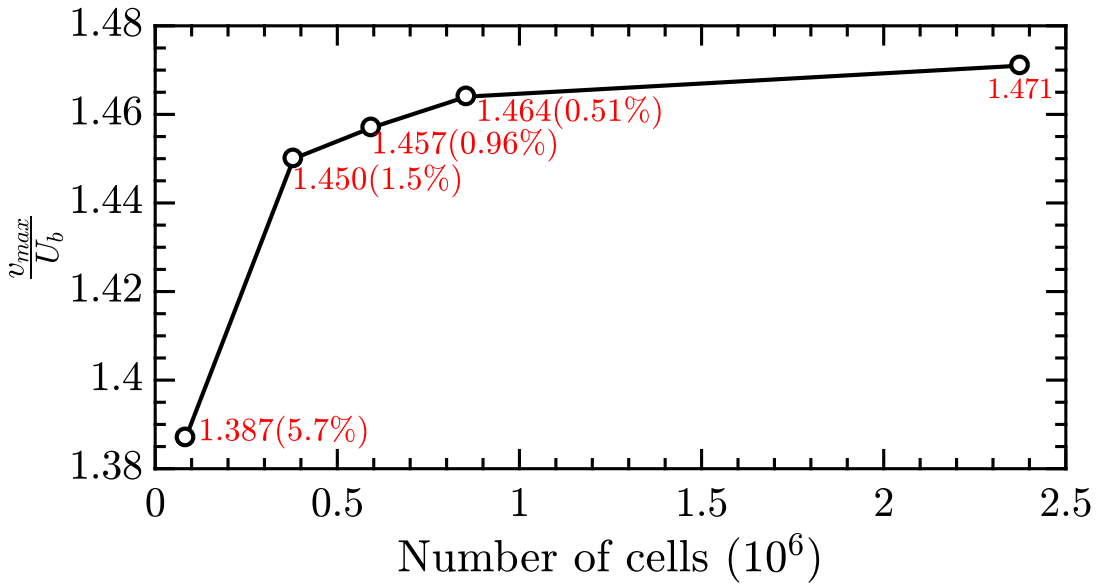


Figure 4.6: Effect of mesh refinement on the maximum value of the $v-$velocity component ($v_{max}/\mathrm{U_b}$) along the gap channel for $Re = 30$. M4 shows a low percentage error (0.51%) for a reasonable number of cells (855000).

### 4.2.2 Gap and angle variation

In chapter 5 we assess the effect of varying the gap size ($g$) of the mixing-separating device by performing numerical studies using geometries with gaps $g = 2H$, $2.61H$, and $3.86H$ in addition to the gap $g = 5H$, the last of which matches the experimental condition. In chapter 6, we investigate the effect of varying the angle ($\alpha$) between the pair of inlets and outlets of the mixing-separating cell device, and effect of that modification on the inertial instability. Figure 4.7 shows an schematic of the different geometries when varying the angle between the pair of inlet and outlet arms from the so-called 'mixing-separating' (0° angle) to a so-called cross-slot (90° angle) where the inlet and outlet channels are orthogonal (including intermediate geometries between these two extremes). In all cases, a stagnation point is generated at the centre of symmetry due to the two opposed inlets and outlets.

When varying the angle between the pair of inlets and outlets of the device, the channels intersect at an acute angle $\alpha$ (see figure 4.8). Consequently, to obtain the stagnation point, the gap $g$ needs to be adjusted. The channel height $H$ is kept constant in all investigation performed in this work. $h$ represents the distance between the outer channel walls (as per figure 4.8), and it varies with $\alpha$. The geometrical correlations between $h$, $g$, and $\alpha$ are as follow:

$$h = 2\sin\left(\frac{\alpha}{2}\right)\left(\frac{H}{\sin\alpha}\right) \tag{4.4}$$

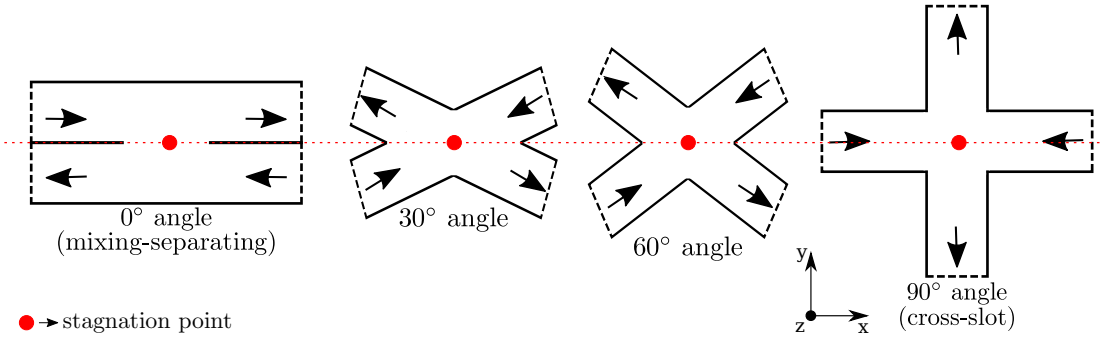


Figure 4.7: Variation of the angle ($\alpha$) between inlets and outlets arms of the a mixing-separating cell. (left to right) From the so-called 'mixing-separating' (0° angle) to a so-called cross-slot (90° angle) where the inlet and outlet channels are orthogonal.

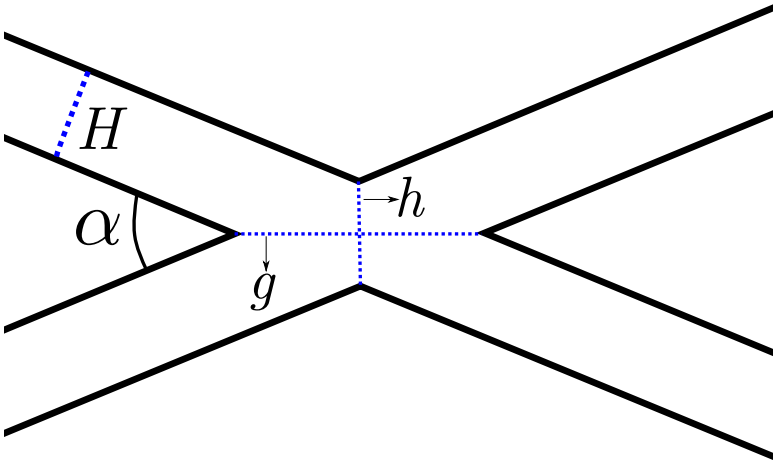


Figure 4.8: Schematic showing the main variables (angle $\alpha$, height of the central gap $h$, and gap size $g$) when varying the angle between the pair of inlets and outlets of the mixing-separating cell device.

$$g = 2\cos\left(\frac{\alpha}{2}\right)\left(\frac{H}{\sin\alpha}\right) \tag{4.5}$$

### 4.2.3 Bifurcation parameters and vortex identification method

It is important to start the numerical analysis by characterizing in detail the flow bifurcation in each device in terms of a flow bifurcation parameter. The parameter is used to define when the instability occurs and develops depending on a critical value of $Re$ ($Re_c$).

**Symmetry analysis: maximum transverse velocity component** – $w_{max}/U_b$

A commonly accepted general definition of symmetry states that an object is symmetrical if one can subject it to a certain operation and it remains invariant after the

operation [134]. The following matrix of equations define transformations in the transverse velocity field, which rotates or reflects the $y$ and $z$ axes through an angle $\theta$ into the $\tilde{y}$ and $\tilde{z}$ axes.

$$\begin{bmatrix} \tilde{y} \\ \tilde{z} \end{bmatrix} = \underbrace{\begin{bmatrix} \cos\theta & -\sin\theta \\ \sin\theta & \cos\theta \end{bmatrix}}_{C^{(i,j)}} \times \begin{bmatrix} y \\ z \end{bmatrix},$$

Instead of the standard interpretation where the coordinate axes rotate themselves, the above representation can be seen as a mapping of points in a given space where the coordinate axes remain fixed.

In this section, we consider only three cases of symmetry: The rotation symmetry (180° rotation), and the reflections through the axis $y$ and $z$. These operations can be expressed by inputting the following values into the matrix $C^{(i,j)}$:

$$C^{(1,3)} = \begin{bmatrix} 1 & 0 \\ 0 & -1 \end{bmatrix}, C^{(2,3)} = \begin{bmatrix} -1 & 0 \\ 0 & 1 \end{bmatrix}, C^{(3,3)} = \begin{bmatrix} -1 & 0 \\ 0 & -1 \end{bmatrix}$$

where the reflectional translation through the $y$-axis is represented by $C^{(1,3)}$ matrix, and $C^{(2,3)}$ corresponds to the reflection through the $z$-axis. The matrix $C^{(3,3)}$ is responsible for rotating the points in a given plane by 180°.

$$C^{(1,3)} = \begin{cases} \tilde{y} = y \\ \tilde{z} = -z \end{cases}$$

$$C^{(2,3)} = \begin{cases} \tilde{y} = -y \\ \tilde{z} = z \end{cases}$$

$$C^{(3,3)} = \begin{cases} \tilde{y} = -y \\ \tilde{z} = -z \end{cases}$$

The analysis of the flow symmetries can be performed mathematically by applying the operations $C^{(1,3)}$, $C^{(2,3)}$, and $C^{(3,3)}$ to the velocity field. At the plane of interest (see figure 4.3 for the symmetry planes studied in this thesis), we evaluated the quantities 4.6 and 4.7 for all grid points in the plane. subsequently, we averaged and subtracted the quantities $V_{mag}$ and $\tilde{V}_{mag}$ at the points $(x, y)$ and $(\tilde{x}, \tilde{y})$ for different Reynolds numbers ($Re$).

$$V_{mag} = \sqrt{u(x,y)^2 + v(x,y)^2 + w(x,y)^2} \tag{4.6}$$

$$\tilde{V}_{mag} = \sqrt{\tilde{u}(\tilde{x},\tilde{y})^2 + \tilde{u}(\tilde{x},\tilde{y})^2 + \tilde{w}(\tilde{x},\tilde{y})^2} \tag{4.7}$$

$$\begin{aligned} m &= \bar{V}_{mag}(Re) - \bar{\tilde{V}}_{mag}(Re) \\ &= \begin{cases} \text{symmetric} & \text{if } m \approx 0 \\ \text{asymmetric} & \text{if } m > 0 \end{cases} \end{aligned}$$

In a cross-slot micro-device, Haward et al. [7] adopted the maximum transverse velocity component recorded along the horizontal centreline on the central plane as an instability growth parameter ($w_{max}/U_b$, see figure C.2), which adequately described the onset and the evolution of the instability when increasing or decreasing $Re$. The flow bifurcation in the cross-slot resulted in a single vortex in the central plane (perpendicular to the streamwise outflow direction) that extended downstream along the outlet channels and remains steady. The transverse velocity field breaks symmetry after the bifurcation and a complex three-dimensional (3D) spiral vortex structure develops. In purely diffusive mixing regimes, Lauga et al. [33] concluded that mixing in planar geometries is dependent on the magnitude of the ratio of the transverse velocity component to the axial component, and the velocity flow field should not present streamwise symmetries. Consequently, the evaluation of symmetries in the transverse velocity field is an attractive option to assess the onset and evolution of an inertial instability.

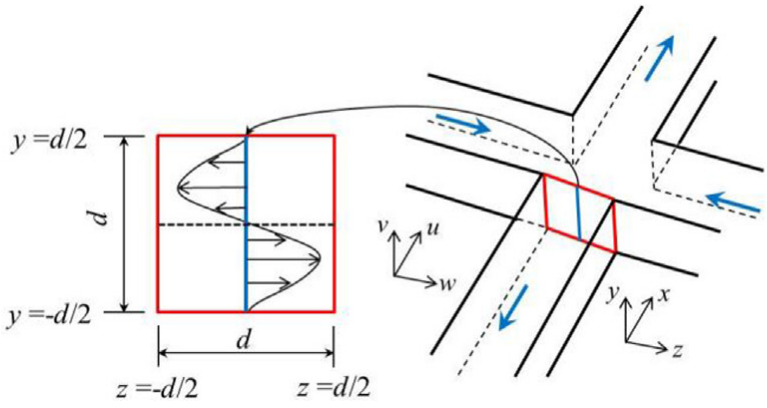


Figure 4.9: Schematic of the cross-slot micro-geometry depicting the entrance plane of the outlet arm, and an example of transverse velocity profile ($w$-component) along the centreline of this plane.

The instability reported in chapter 5 could not be captured by the maximum transverse velocity method. For the majority of the gap sizes investigate in chapter 5, the breaking of flow symmetry does not occur in the $x-y$ plane. Therefore, the $w$ velocity component does not play any role in that instability. Although the method failed to detect the vortices in the $x-y$ plane, it was fundamental in the prediction of the break

of symmetry in the transverse plane which is correlated to an engulfment regime, or a cross-slot like instability.

**Vortex identification** $-\ \lambda_{ci}$

An alternative bifurcation parameter is also proposed in this thesis to complement the investigations. The vortex identification method proposed by Zhou et al. [135], called the swirling strength criterion ($\lambda_{ci}$), has been implemented as it can adequately identify recirculations and vortex structures in the computational data set. In this method, the imaginary portion of the complex conjugate eigenvalue ($\lambda_{cr} \pm \lambda_{ci}$) can be used to capture the swirling motion. The canonical (eigenvalue) matrix for complex eigenvalues is written as $A'$: [135]

$$A' = \begin{bmatrix} \lambda_r & 0 & 0 \\ 0 & \lambda_{cr} & \lambda_{ci} \\ 0 & -\lambda_{ci} & \lambda_{cr} \end{bmatrix} \tag{4.8}$$

and the velocity gradient tensor ($\nabla U$) can be decomposed as:

$$\begin{pmatrix} \bar{\nu}_r & \bar{\nu}_{cr} & \bar{\nu}_{ci} \end{pmatrix} \begin{bmatrix} \lambda_r & 0 & 0 \\ 0 & \lambda_{cr} & \lambda_{ci} \\ 0 & -\lambda_{ci} & \lambda_{cr} \end{bmatrix} \begin{pmatrix} \bar{\nu}_r & \bar{\nu}_{cr} & \bar{\nu}_{ci} \end{pmatrix}' \tag{4.9}$$

where $\lambda_r$ is the real eigenvalue with corresponding eigenvector $\bar{\nu}_r$ and the complex conjugate pair of complex eigenvalues is $\lambda cr \pm \lambda ci$ with corresponding eigenvectors $\bar{\nu}_{cr} \pm \bar{\nu}_{ci}$. The strength of this swirling motion can be quantified by $\lambda_{ci}$ , called the local swirling strength of the vortex. It is important to mention that the local planar (2D) velocity gradient tensor ($\nabla U$) in Cartesian coordinates is defined as:

$$\nabla U = \begin{bmatrix} \frac{\partial u}{\partial x} & \frac{\partial u}{\partial y} \\ \frac{\partial v}{\partial x} & \frac{\partial v}{\partial y} \end{bmatrix} \tag{4.10}$$

The vortex structures produced can be best visualised using colourmaps or isosurfaces. In this work, we combine both visualisation techniques to appraise the vortex generation and amplification (by stretching) with increasing Reynolds number. Additionally, by considering the maximum normalised strength of this swirling motion, quantified by $\lambda_{ci} H^2/\nu$, in a specific plane of interest (i.e. plane $x-y$ and $z = 0$), one can adequately quantify the onset and the evolution of the instability when increasing or decreasing $Re$. $H$ and $\nu$ correspond to the channel height and the kinematic viscosity, respectively. The method has shown an alternative way to describe the growth of the instability when the symmetry breaking (the maximum transverse velocity) method fails.

## 4.3 Numerical simulations in a cross-slot device

Three-dimensional numerical simulations of the cross-slot micro-geometry using the commercial CFD software package Fluent were performed in order to assess the enhancement of heat transfer when a inertial instability is present, and the results are detailed in chapter 8. The CFD simulations performed for the cross-slot geometry consider the fluid flow incompressible, laminar, single phase, and steady-state. The fluid properties were assumed constant and temperature independent, which were a reasonable assumption after conducting several simulations using a Sutherland law model based on the experimentally measured variation of viscosity with temperature. The results shows a small quantitative effect, and qualitatively unchanged (see discussion in section chapter 8, particularly figures 8.2, 8.7, and 8.8). The critical Reynolds number of the bifurcation was completely unaffected by a temperature-dependent viscosity.

The computational domain consists of two bisecting square channels (channel width = channel height = $d = 519$ $\mu$m) with opposing inlets and opposing outlets, resulting in a flow field with a stagnation point at the centre of symmetry [61]. The length of each inlet and outlet channel was defined as 60 times its width $d$ ($L = 60d$). This length assures that the fluid velocity no longer depends upon the axial distance and the flow is hydrodynamically fully-developed [120] for all Reynolds numbers studied.

The numerical simulations of the cross-slot micro-geometry were carried out using the finite-volume method within ANSYS-Fluent [131]. The modified SIMPLE algorithm developed by Patankar and Spalding [136] was employed for solving the equations in discretised form (pressure-velocity coupling scheme). The equations of momentum and energy were solved with a second-order upwind scheme. All numerical simulations were performed for convergence criteria of all relevant residuals falling to less than $10^{-10}$.

### 4.3.1 Computational meshes

A consistent mesh refinement was conducted to estimate the numerical accuracy of the simulations [132]. A preliminary series of simulations was carried out with two groups of three different uniform hexahedral (all quad) computational meshes (as in table 4.2). In the first group the number of cells in the cross-section was varied ($25 \times 25$, $50 \times 50$ and $75 \times 75$) for fixed number of biased cells (growth factor 100:1 towards the centre) along the inlet and outlet channels (see figure 4.10). The second group explores the effect of the variation of the number of cells along the channels (25, 50 and 100) given a fixed number of cells at the cross-section ($50 \times 50$).

The first chosen criterion to determine the accuracy is the maximum streamwise velocity of the fully-developed part of the inlet channel in comparison with the analytical solution for a square duct ($u_{max}/U_b = 2.0979$) [30]. The variation of this quantity with

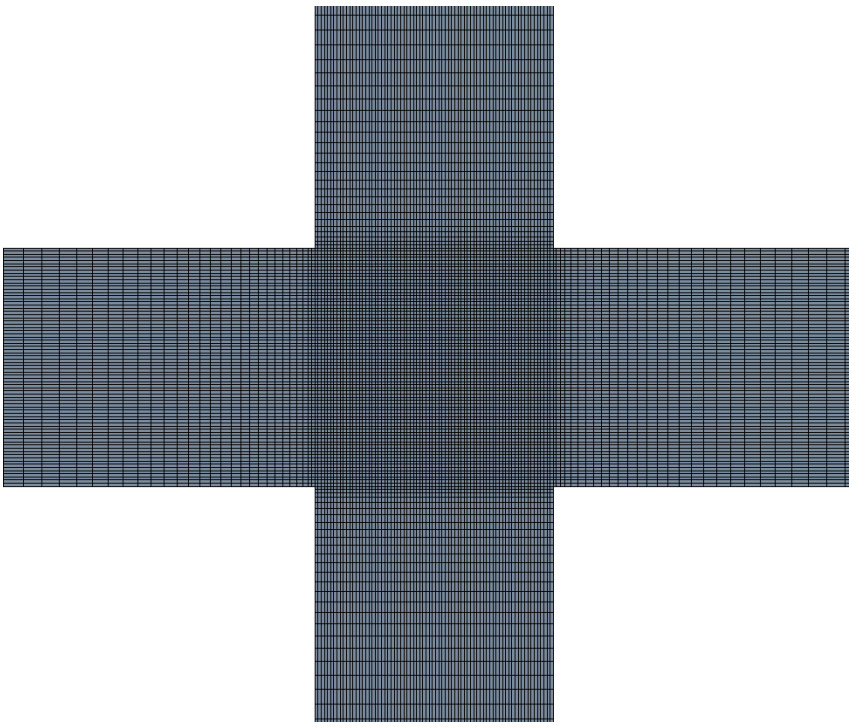

Figure 4.10: Detail of the refinement rate at the centre of the numerical mesh C4.

increasing mesh refinement for a typical simulation ($Re = 100$) is shown in figure 4.11. First, it can be noted that the variation of ($u_{max}/U_b$) between the meshes is less than 1% when varying the number of cells in the cross section. The error found when varying the number of cells along the channel length can be regarded as negligibly small. As stated earlier, previous numerical investigations were carried out by [9] and [7] for Newtonian fluids flowing through cross-slot micro-geometries and a symmetry-breaking phenomenon at the stagnation point was observed beyond a critical $Re$. A steady and symmetric flow for low Reynolds number is replaced by a steady and asymmetric flow beyond a critical value of $Re$.

A steady symmetric flow at the $y - z$ plane at the entrance to the outlet arm, as shown in figure C.2, represents a zero velocity contribution of $w/U_b$ along the central $y - z$ line, consequently the diffusive flow mixing regime is dominant ($w$ represents the spanwise velocity component in $z$ direction). Otherwise, a non-zero contribution of $w/U_b$ indicates flow across the $y - z$ line, i.e. a breaking of symmetry (it should be emphasised that the flow remains steady at all Reynolds numbers studied in this work in accordance with Haward [7]). However, the bifurcation parameter is represented by the maximum transverse velocity ($w_{max}/U_b$) along the $y - z$ line at the outlet channel for different Reynolds numbers [7]. In figure 4.12 the variation of this quantity ($w_{max}/U_b$) with varying cell number can be seen and it was found that the error was less than 1% when increasing the number of cells from 1.2 million to 2.86 million. The mesh

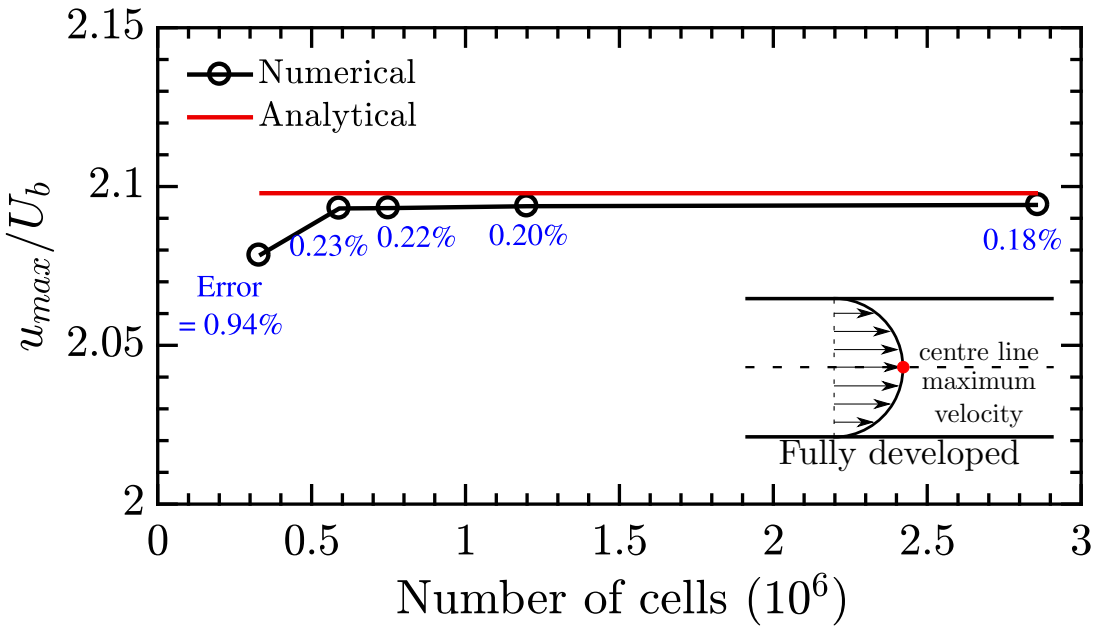


Figure 4.11: Effect of mesh refinement on the maximum normalised velocity ($u_{max}/U_b$) at the inlet channel in fully-developed region.

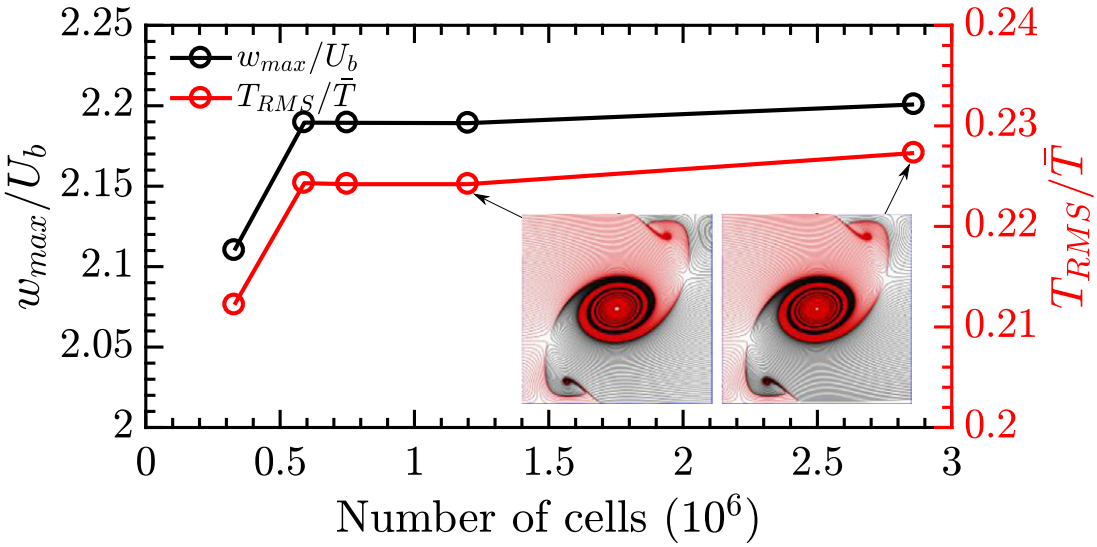


Figure 4.12: Evaluation of the transverse maximum velocity ($w_{max}/U_b$) and the normalized root mean square temperature ($T_{RMS}/\bar{T}$) at the inlet plane to the outlet arm when increasing the number of cells. Insets are streamlines showing spiral vortex structure on the centre plane of the cross for meshes C4 and C5. $Re = 100$ and $Pr = 100$

Table 4.2: Grid independence study for estimating the numerical accuracy using different mesh characteristics for the cross-slot by comparing the analytical solution for the normalised maximum flow velocity ($u_{max}/U_b = 2.0979$) in a square channel in fully-developed flow with the numerical results and also evaluating the maximum value for the transverse velocity at the inlet plane of the outlet arm (depicted in figure C.2). $N_x$ and $N_y$ represents the number of divisions in $x$ and $y$ directions at the cross section. $N_c$ represents the number of division along the inlet and outlet channels and $Gr$ represents the growth rate (bias factor) from the cells along the channels. Note (a): The error in table 4.2 represents the percentage error between the analytical solution of $u_{max}/U_b$ and the present numerical simulation.

| Mesh | $N_x$ | $N_y$ | $N_c$ | $Gr$ | $u_{max}/U_b$ | Error (%)$^{(a)}$ | $w_{max}/U_b$ | $T_{RMS}/\bar{T}$ | Cells $\times(10^6)$ |
|---|---|---|---|---|---|---|---|---|---|
| C1 | 25 | 25 | 100 | 100 | 2.0783 | 0.93 | 2.1101 | 0.2122 | 0.332085 |
| C2 | 50 | 50 | 25 | 100 | 2.0931 | 0.23 | 2.1895 | 0.2243 | 0.590390 |
| C3 | 50 | 50 | 50 | 100 | 2.0932 | 0.23 | 2.1894 | 0.2242 | 0.755390 |
| C4 | 50 | 50 | 100 | 100 | 2.0928 | 0.24 | 2.1892 | 0.2242 | 1.200390 |
| C5 | 75 | 75 | 100 | 100 | 2.0942 | 0.18 | 2.2008 | 0.2273 | 2.863515 |

independence study was conducted after the occurrence of the spiral vortex. This independence can be further demonstrated by the near indistinguishable similarity of flow structures in the centre plane for different meshes as shown in figure 4.13. Figure 4.13 shows streamlines on the centre plane of the cross for meshes C4 and C5 at different $Re$ numbers. The complex spiral vortex flow field is clearly evident and virtually indistinguishable between the two meshes.

As we were primarily interested in heat transfer performance we also examine the root-mean-square of the temperature in this plane to ensure that the mesh is sufficient to resolve the temperature variations. The results are shown in table 4.1 and figure 4.12 and demonstrate that the temperature variation is captured with similar accuracy as the velocity. Therefore, based on this analysis of the grid dependency, all simulations were carried out using mesh C4 (1.2 million cells).

### 4.3.2 Thermal boundary conditions

Two different sets of boundary conditions were specified for the heat transfer problem in this work: adiabatic walls in order to simulate the experimental investigation (hereafter $C1$) and constant wall temperature (hereafter $CWT$). In the former case ($C1$), there is no slip and no heat flux through the walls and theoretical fully-developed laminar velocity profiles [30, 80] were imposed on the inlet streams and the outflow boundary condition (fully developed flow) at the outlets. The mixing and consequently the heat transfer is determined by the interaction between the hot and cold fluid streams flowing from the opposing inlets. The root mean square temperature ($T_{RMS}$) (Eq. 4.11) along the outlet channel was used as a proxy to evaluate the heat transfer between the two

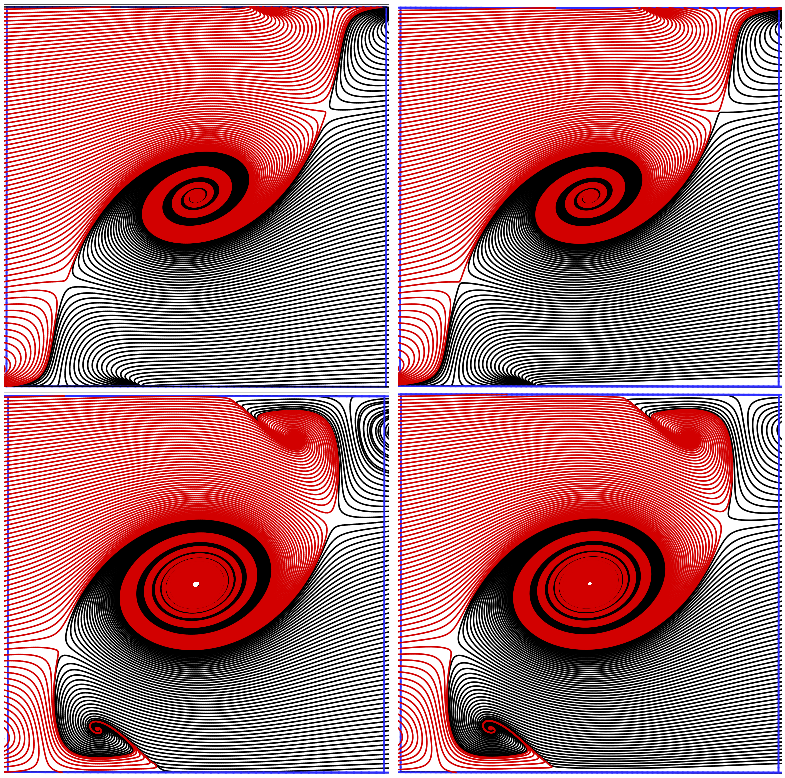

Figure 4.13: Comparison of Mesh C4 (left) and Mesh C5 (right) at $Re = 50$ (top), and $Re = 100$ (bottom).

streams in this case (as a Nusselt number cannot be defined as the mean temperature at every cross-sectional plane is a constant). Non-dimensional $T_{RMS}$ was calculated at each cross-sectional plane in the outlet arms as,

$$\frac{T_{RMS}}{\bar{T}} = \frac{\sqrt{\frac{\sum_{i=1}^{n}(T_i - \bar{T})^2}{n}}}{\bar{T}} \tag{4.11}$$

where $\bar{T} = (T_{in,C} + T_{in,H})/2$ represents the mean temperature.

In the latter case ($CWT$), no slip and uniform temperature was applied on all the walls, theoretical fully-developed laminar velocity profiles [30, 80] were imposed in the cold fluid flow at the inlets while the temperature profile develops and the outflow boundary condition (fully developed flow) was applied at the outlets. As readily expected, a higher temperature gradient exists at the walls, the heat transfer coefficient, $h$, is higher at the thermal entrance region than in the region of fully-developed profiles [125]. The mean Nusselt number ($\bar{Nu}$), under $CWT$ condition, can be defined as [80]:

$$\bar{Nu} = \left(\frac{d}{k}\right) \frac{\dot{m}C(T_{out} - T_{in})}{A_s \Delta T_{lm}} \tag{4.12}$$

where $\dot{m}$ is the mass flow rate and $A_s$ is the surface area available for convection of the cross-slot geometry. $T_{in}$ and $T_{out}$ are the bulk temperatures at the inlet and outlet of the

cross-slot geometry, respectively. $\Delta T_{lm}$ is the logarithm mean temperature difference which is defined as [80]:

$$\Delta T_{lm} = \frac{(T_w - T_{out}) - (T_w - T_{in})}{\ln\left[\frac{T_w - T_{out}}{T_w - T_{in}}\right]} \tag{4.13}$$

where $T_w$ is the constant wall temperature. Numerical calculations for a straight channel with the same dimensions (cross-section and total length) as the cross-slot geometry were conducted to evaluate the thermal efficiency. In order to corroborate the accuracy of the numerical simulations, the mean Nusselt number was compared with the analytical solution from Shah and London [125] and also the numerical simulations performed by Chandrupatla and Sastri [137] and Abed et al. [48]. The numerical simulations were performed imposing both, velocity [30] and temperature [125], theoretical fully-developed profiles at the entrance of the straight channel under a uniform and constant temperature at the walls. Table 4.3 shows an excellent agreement between the results achieved in the current simulations and these benchmark results.

Table 4.3: Mean-Nusselt-number results comparison for the present simulations with other numerical results from Chandrupatla and Sastri [137], Abed et al. [48] and also the analytical solution from Shah and London [125]. Note (a): Deviation from the present numerical simulations using mesh C4.

| | Method | $\bar{Nu}$ | Deviation (%)$^{(a)}$ |
|---|---|---|---|
| Shah and London [35] | Analytical | 2.976 | 0.198 |
| Chandrupatla and Sastri [44] | Numerical | 2.975 | 0.232 |
| Abed et al. [34] | Numerical | 2.9814 | 0.017 |
| Present computational simulation | Numerical | 2.9819 | – |

# Chapter 5

# Inertial instabilities in a mixing-separating device

The overall aim of the present chapter is to harness a greater understanding of the flow instabilities in bisecting channels when varying the gap in a so-called *mixing-separating cell*. The characterisation of the flow before and after the bifurcation helps to predict the formation and confidently locate the core position of vortex structures within the channels, which consequently benefits the designing of micro and nanofluidic devices to manipulate flow conditions using laminar vortices, i.e. particle entrapment, mixing, and other applications. We perform both experiments (using flow visualisation) and numerical simulations in a specific geometry with a gap size of five times the channel height ($g = 5H$). Finding good agreement between experiments and simulations, we further utilise the simulation technique to explore the effect of varying the gap size ($g$).

We demonstrate that both, the nature of the instability and the Reynolds number ($Re$) at which the instability occurs, varies as the gap size is changed. The reader should refer to chapter 3 for the experimental arrangement and protocols description. Chapter 4 describes the setup of the numerical simulations including the boundary conditions, mesh dependence study, and the bifurcation parameters employed.

## 5.1 Experiment and simulations using a wide gap ($g = 5H$)

### 5.1.1 Friction factor

The pressure drop ($\Delta p$) between inflow and outflow arms (after subtracting the minor pressure losses as already discussed in 3) and mean fluid flow velocity ($U_b$) were experimentally measured to determine the Darcy friction factor-Reynolds number product, $fRe$:

$$fRe = \frac{2\Delta p H^2}{L U_b \mu} \tag{5.1}$$

$L$ is the combined length of the inflow and outflow channels. The experimental measurements of friction factor-Reynolds number are shown in figure 5.1. The uncertainty

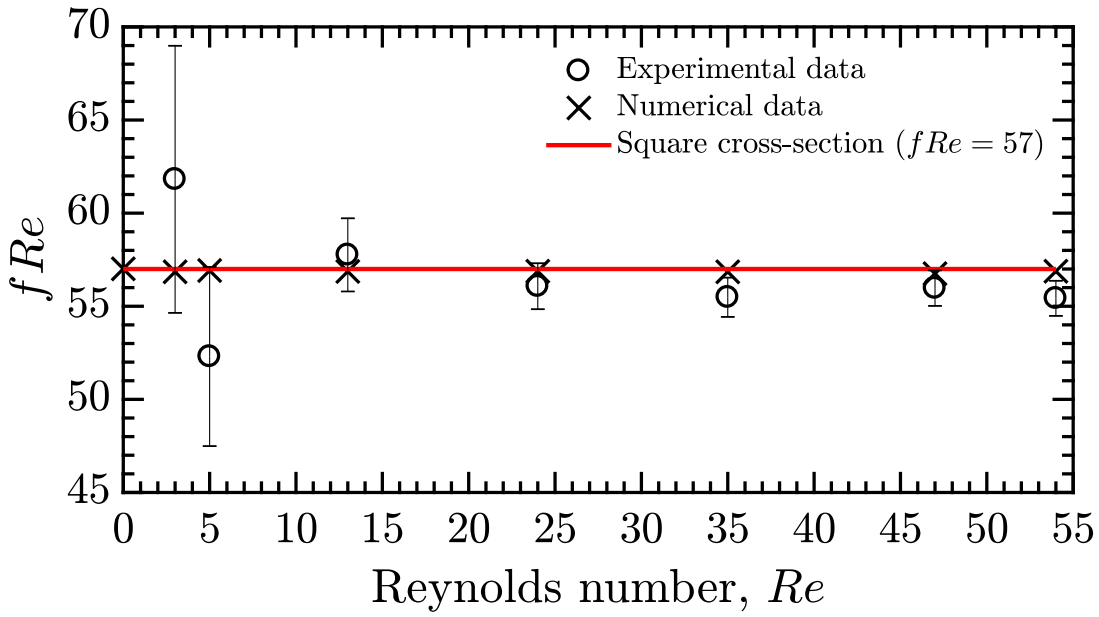


Figure 5.1: Friction factor-Reynolds number product ($fRe$) function of Reynolds number. The error bars indicate that the measured values of $fRe$ and Darcy's equation are within 3% when $Re > 5$. At the lower range of $Re$ ($Re < 5$), there is a significant amount of scattering due to large relative uncertainties (refer to chapter 3).

of $fRe$ (denoted by error bars), which is associated with the measurement of each term in Eq. 5.1, is carefully estimated by following the methodology described in chapter 3. The minimum and maximum uncertainty values of $fRe$ are 1.7% and 11.6%, respectively. The large relative uncertainties occur at low flow rates where the small pressure drops generate a significant degree of error (approximately 90% of the total error of the $fRe$ when $Re < 5$). Dimensional inaccuracies (particularly in measuring $H$) also play a significant role in the determination of $fRe$ [121, 48].

The experimental results of $fRe$ were compared to the conventional theory for a fully-developed flow in a straight channel of a square cross-section ($fRe = 57$ in laminar flow, [125]). When $Re > 5$, the measurements show acceptable agreement with this theoretical value. In this range, the maximum deviation between the measured values of $fRe$ and Darcy's equation is within 3%. The results for $Re > 5$ are also in good agreement with the numerical simulations (which agree with the theory as expected). The pressure drop in the mixing-separating device therefore behaves essentially as flow in a straight channel and any additional pressure loss due to the gap, even after the onset of the instability ($Re > 30$), is small and within our measurement uncertainty (refer to chapter 3). For very low Reynolds numbers ($Re < 5$), there is a significant degree of error in the measured pressure-drop data which can be attributed to the large relative uncertainties at low flow rates and small pressure drops.

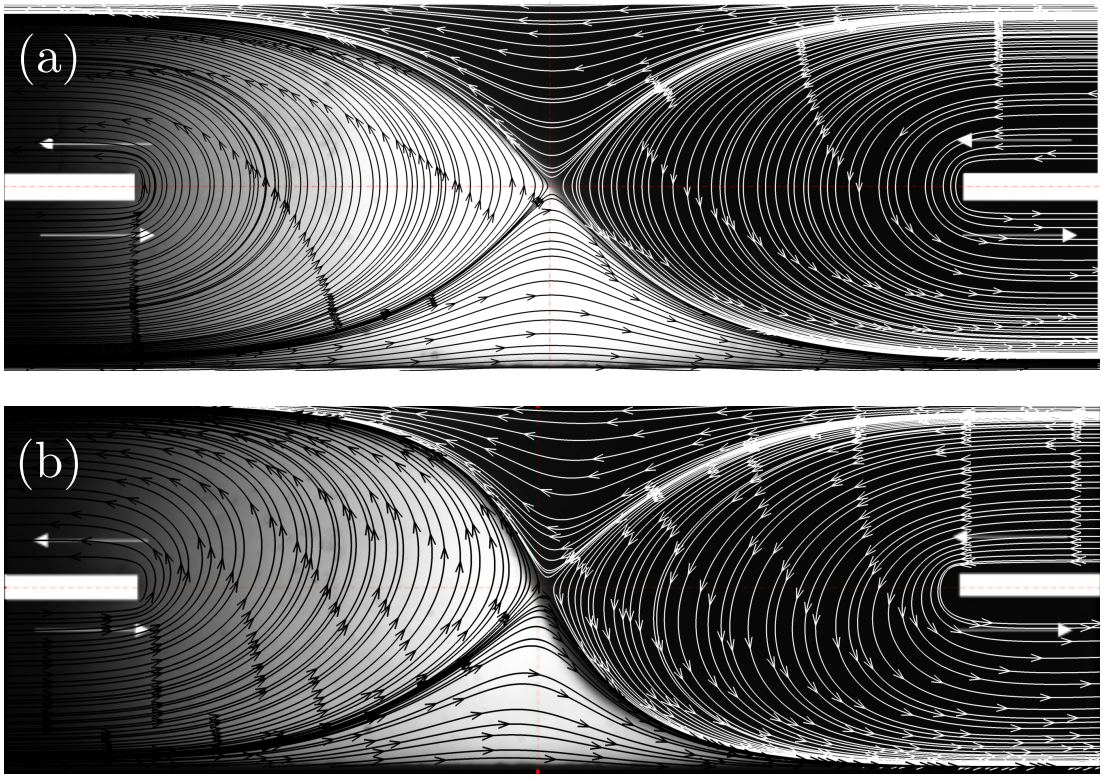


Figure 5.2: Experimental flow visualisation images with rhodamine-tinted stream (white) and on undyed stream (black) prior the onset of any instability. (a) $Re = 2$ and (b) $Re = 29$. The experimental visualisations are superimposed with streamlines at the centre plane of the geometry from the equivalent simulations.

### 5.1.2 Visualisation of the base flow

Figure 5.2 shows flow visualisation using one inlet stream dyed with Rhodamine (white) and one inlet stream undyed (black) with the simulated flow pathlines at $z = 0$ superimposed. The numerical simulations and experimental results show virtually identical flow patterns indicating a very good agreement between the two methods. For the experimental results, it is important to remind that the fluid motion started from rest, and after reaching steady-state conditions (in approximately 10 seconds), at least fifty images were acquired. As the flow field is steady, each image acquired is identical to the set average, and the fluid path is based on the fluorescent intensity of the image dye stream. Therefore, figure 5.2 shows averaged images which represent dye visualisation. For a range of $Re$ from to 2 to 29, experimental and numerical results clearly show the majority of the fluid reverses through 180° in order to exit the device and only a small amount of fluid takes a path straight through the "H".

A distinct tilted interface between the dyed and undyed streams is visible for $Re \leq 29$, resulting from the opposed flows colliding at the stagnation point. The effect of incrementally increasing the Reynolds number from $2 \leq Re \leq 29$ increases the angle of the interface with respect to the $x$-axis, yet the flow remains steady. The

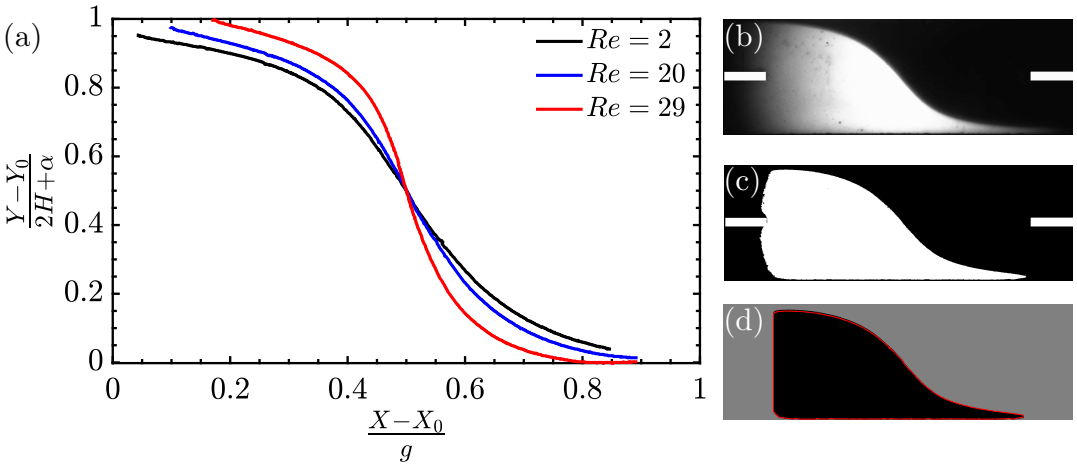


Figure 5.3: (a) The interface between the two fluid streams for different $Re$ obtained using an edge detection, showing an increase in interface angle (with respect to the $x$-axis) with increasing $Re$. Image processing phases identifying edges between the two streams at Re 2: (b) raw figure, (c) binary image, and (d) edge detection.

equivalent numerical simulations reinforce the experimental results. Figure 5.3 shows the evolution of the interface with increasing $Re$. By using the raw grey-scale image, binarising, cropping to the gap width, and applying an edge detection technique, the interface between the two fluid streams can be located (see figure 5.3b-d) [1]. A small deviation in the flow balance between the two streams produced minor variations of the interface position within the "H", hence $X_0$ and $Y_0$ represents small adjustments to relocate the interface to the geometric centre for all $Re$ to enable a proper comparison. Again, $g$, $H$ and $\alpha$ represent the gap size, channel height and wall thickness, respectively (established at chapter 3).

Under creeping flow conditions, the vast majority of the flow turns around the corner of the separating wall, and only a small part of the flow heads straight down to the outlet of the channel. Note that at the stagnation point both inlet flow streams divide in two parts. With increasing $Re$, the interface between flow streams at the gap becomes more inclined and, consequently, more and more fluid reverses its direction. Above $Re = 29$, when the interface is approximately coincident with the $y$-axis (vertical), a vortex appears at the centre of the mixing-separating cell indicating the onset of an instability, although the flow remains steady.

### 5.1.3 Visualisation of the inertial instability

Figure 5.4 shows experimental flow visualisations and simulated streamlines for $Re$ from 29 to 60. At $Re = 30$, just above the onset, a single vortex is present spanning the entire width of the cell. With increasing $Re$, it divides into a pair of co-rotating

[1] Note that for the interface analysis, we trimmed the images within the gap size to remove the dark corners created by the microscope circular FOV.

vortices (as in the example shown at $Re = 40$). Figure 5.4d illustrates the vortices when $Re = 60$. Noticeably, with increasing $Re$, the two vortices separate. It is important to note that the flow remains steady and the vortex structure does not change in time for a fixed value of the Reynolds number. Unlike in the base flow, where a small portion of the flow passed straight through the device, after the onset of the instability. None of the flow takes the path to the opposite exit. In addition, there is a far greater mixing of the two streams due to the central vortex (or vortices at higher $Re$).

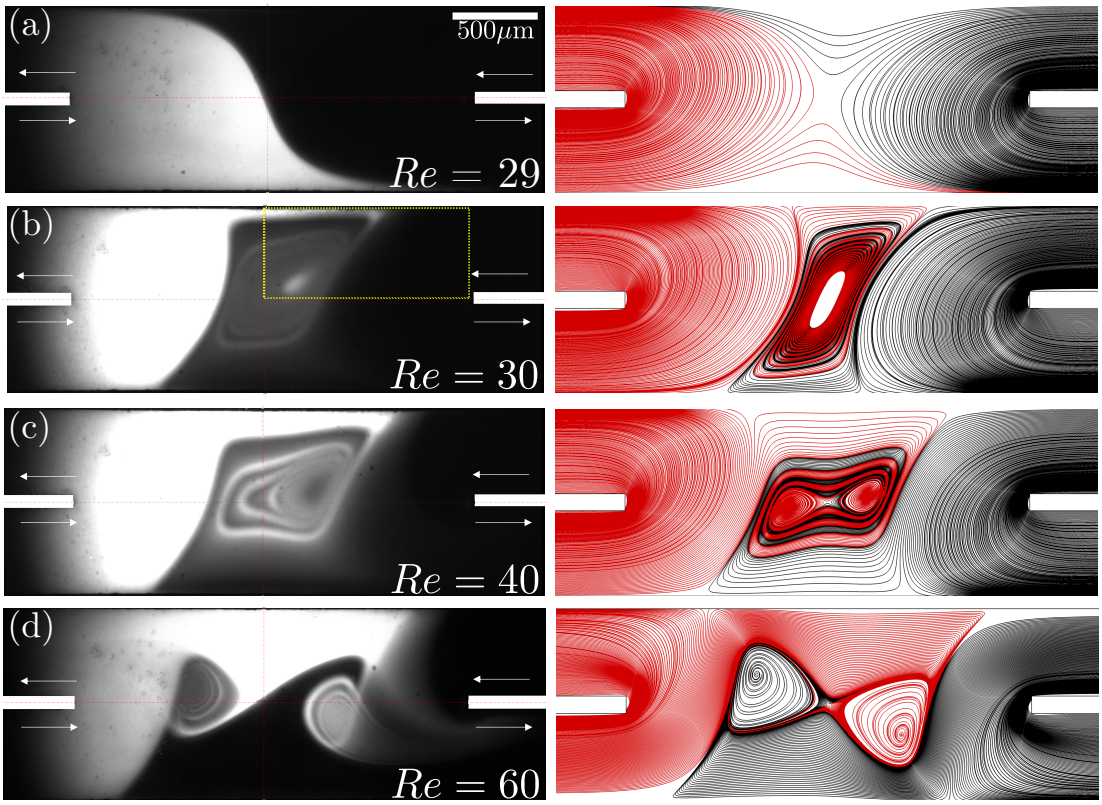


Figure 5.4: Experimental flow visualisation (left-hand side) and numerical streamlines (right-hand side) of the flow in the mixing-separating device at different $Re$. (a) $Re = 29$, before onset of instability; (b) $Re = 30$, single vortex after bifurcation; (c) $Re = 40$, two separate co-rotating vortices; (d) $Re = 60$, the distance between the two vortices has increased.

The results from numerical simulations and experiments agree well regarding the onset ($Re_c$) of the instability. However, one can observe small deviations in the comparative flow visualisations, particularly an absence of perfect rotational symmetry in the experimental results for $Re = 30$ and $Re = 40$ (5.4). A small discrepancy in the flow balance between the two inlets explains this lack of symmetry. Precise matching of the flow rates on the different inlet channels to a high level of accuracy is not straightforward (despite the use of separate flowmeters on both inlets), whereas for the numerical simulations it is trivial to set identical boundary conditions and therefore obtain the perfect rotational symmetry.

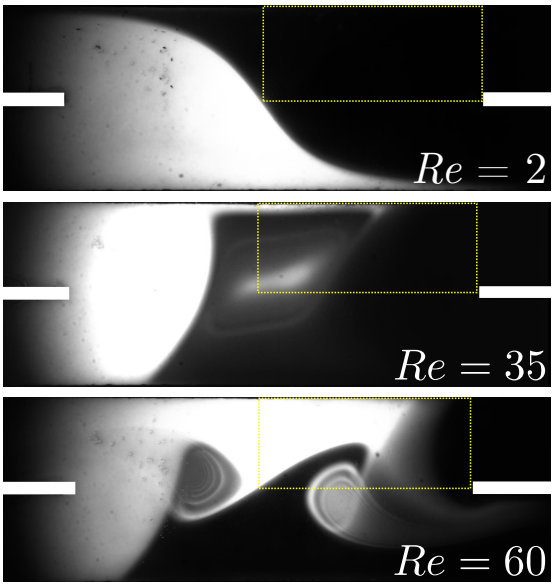


Figure 5.5: Experimental flow visualisation for different $Re$ showing the delimited area of interest (yellow box) for the experimental quantification of stream interaction.

As suggested by Humphrey et al. [72] and verified by our present numerical work, for a large enough Reynolds number ($Re > 185$) the flow becomes time-dependent. However, a detailed study of the time-dependent behaviour of this flow is beyond the scope of the present work, particularly as we are mainly interested in flow at very low $Re$.

### 5.1.4 Characterisation of the instability from experiments

To quantify the onset and growth of the instability in the experimental data, the method suggested by Stroock et al. [28], and also employed by Haward et al. [7], was adopted to evaluate the level of interaction between the incoming fluid streams ($M$) in the central region of the device. By computing the root-mean-square (RMS) of the pixel intensity variation within the vortex region of the experimentally obtained images such as those yellow box in figure 5.5, we quantify the amount of interaction between the two incoming streams within the gap region as,

$$M = \sqrt{\frac{\sum_{i=1}^{n}[(I_i - \langle I \rangle)^2]}{n}} \tag{5.2}$$

where $I_i$ is the grayscale intensity value at pixel $i$, and $\langle\rangle$ indicates an average across all $n$ pixels in the defined area of interest (yellow box in figure 5.4b and 5.5).

Figure 5.6 presents the experimental quantification of the interaction between the two streams (using this $M$ parameter) as a function of the Reynolds number for the mixing-separating cell with $g = 5H$. At $Re$ close to the onset of the instability, the growth of $M$ follows the square root behaviour typical of a supercritical instability.

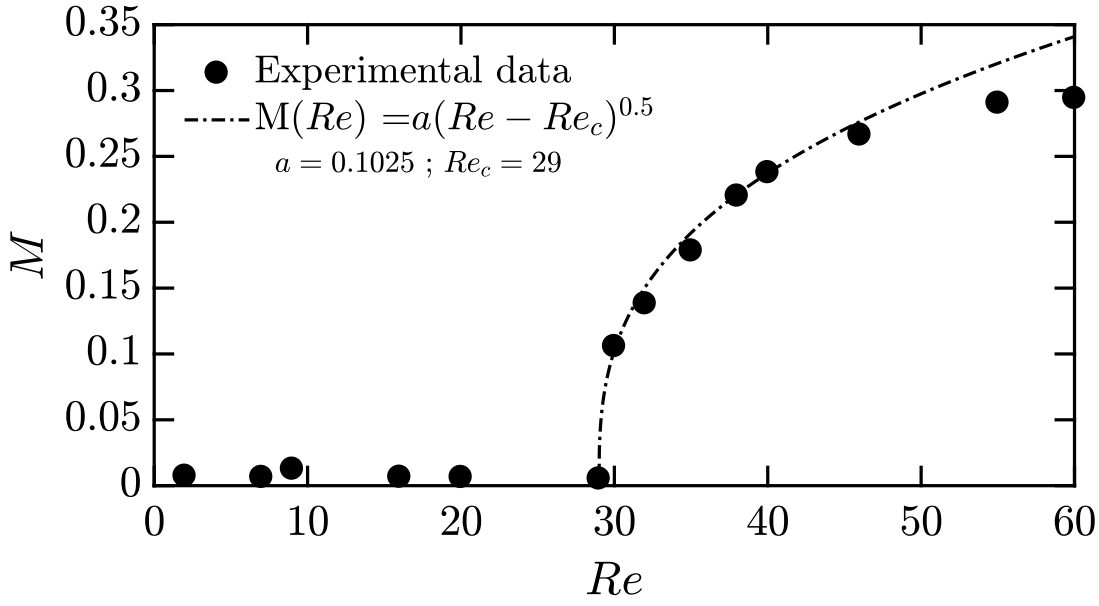


Figure 5.6: characterisation of the instability using the mixing parameter, $M$, from the experiments, exhibiting the square-root growth expected of a supercritical instability close to onset.

The square root fit included in figure 5.6 is very good up to $Re \approx 40$, corresponding to $(Re - Re_c)/Re_c = 1/3$, which is convincing given that we would theoretically expect square-root growth when $(Re - Re_c)/Re_c << 1$. No hysteretic behaviour was observed in either the experimental or numerical results.

### 5.1.5 Characterisation of the instability from simulations

The simulated flow patterns for a wide gap ($5H$) mixing-separating micro-geometry show that a central vortex appears beyond a certain $Re_c$, and by continuously increasing $Re$, the vortex divides into two vortices (as shown in figure 5.4). However, unlike a cross-slot geometry, the transverse velocity component at the central plane of the mixing-separating micro-geometry is zero for the entire range of $Re$ tested in the numerical simulations for $g = 5H$. Therefore, to characterise the instability using the simulated data we employ the swirling strength method explained in section 4.2.3. This enables us to quantify the strength of the swirling motion as well as identify its position.

Figure 5.7 shows the variation of the maximum normalised strength of the swirling motion ($\lambda_{ci}H^2/\nu$), on the centre plane $x$-$y$ ($z = 0$) with Reynolds number. The value of this parameter is zero prior to the formation of the first vortex at $Re = 29$, and displays a square root growth near to the instability onset ($30 < Re < 50$) as expected for a supercritical bifurcation (see inset on figure 5.7).

For Reynolds number far enough away from onset that the square-root character is not expected ($Re > 50$), the instability parameter continues to grow, but linearly (with a gradient of $\approx 4.6$) with $Re$. This demonstrates that the strength of the vortical

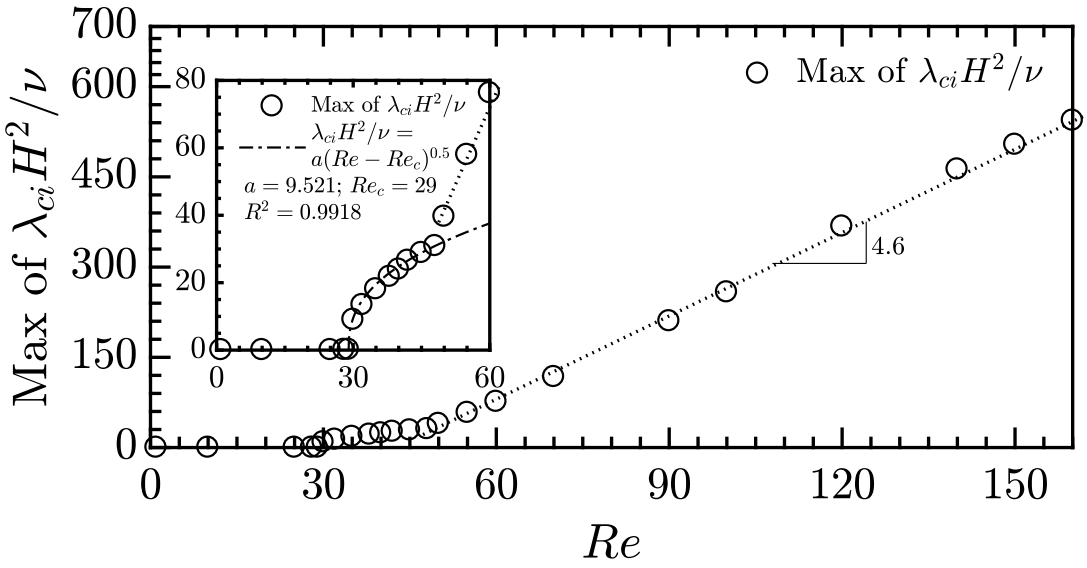


Figure 5.7: The variation of the bifurcation parameter used to analyse the numerical data ($\lambda_{ci,max}H^2/\nu$) with $Re$ for $g = 5H$. The critical Reynolds number is 29 and the inset shows a square-root growth near to the instability onset ($30 < Re < 50$). For $Re$ beyond the region of square-root growth, $50 < Re < 185$, the instability parameter grows linearly (with a gradient $\approx 4.6$).

motion increases in direct proportion to $Re$, which is not unexpected as there are no further major changes in flow topology for the range of $Re$ tested ($50 < Re < 185$) using this gap size ($g = 5H$).

The critical Reynolds number found from experiments ($Re_c = 29$) matches the critical $Re$ found from the simulations. In figure 5.8, the experimental ($M$) and numerical ($\lambda_{ci,max}H^2/\nu$) results are plotted on the same $Re$ axis. Despite minor differences and appreciating the fact that the $y$-axis of the two different bifurcation parameters are necessarily different, the agreement is excellent in terms of the growth of the instability with increasing $Re$ and confirms that the numerical simulations agree with the experimental data. The experimental and numerical data diverges for $Re > 50$ where there is no longer square-root growth of the parameters. This is not surprising as there is no particular reason to expect the strength of the vortex to be intimately linked with the $M$-parameter beyond the initial growth of the instability.

In addition to the streamlines show in figure 5.4 we can also visualise the flow in the mixing-separating device using our swirling strength bifurcation parameter. Figure 5.9 depicts the transition from the base flow to the vortical flow regime as Reynolds number changes from 29 to 30. Velocity direction vectors are included to show the local direction of the flow and highlight the vortical nature. The colormap shows the distribution of swirling strength ($\lambda_{ci}H^2/\nu$), which is entirely zero for $Re = 29$ (before the instability) and is seen to clearly highlight the swirling nature of the flow at $Re = 30$ as there is a sudden and dramatic change to the flow topology caused by the onset of

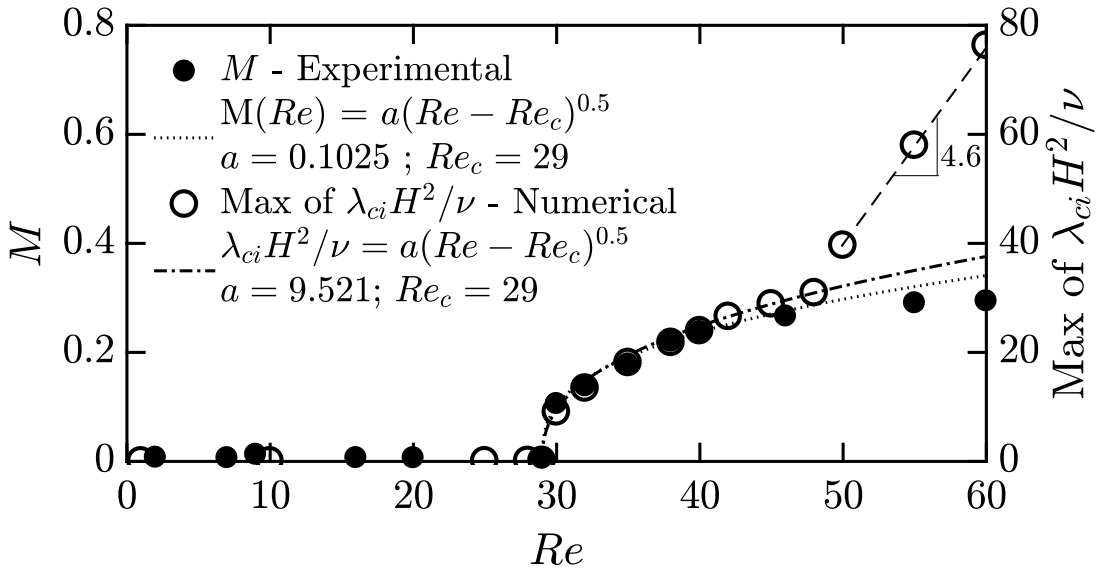


Figure 5.8: The variation of the instability growth parameters $M$ (experimental) and $\lambda_{ci,max}H^2/\nu$ (numerical) with $Re$ for $g = 5H$, showing excellent agreement in the region close to onset ($30 < Re < 45$).

the instability.

Figure 5.10 shows how the flow develops beyond $Re_c$. At $Re = 32$, the single vortex that was present at $Re = 30$ splits into two rotationally-symmetric (through 180°) co-rotating vortices. When near to the onset of the instability, in the region where we still see square-root behaviour ($32 < Re < 50$), these twin vortices change their position as the strength increases with increasing $Re$. However, in the $Re$ range where the bifurcation parameter shows linear growth $Re > 50$, the vortices do not significantly alter their position, although their shape slightly alters as they get stronger. At $Re = 120$, the vortices appear to merge into a single large vortex, although this does not influence the trend of the strength, which continues to grow linearly with $Re$.

## 5.2 Simulations investigating the effect of varying the gap size ($g$)

The previous section has demonstrated that the flow in a mixing-separating with a wide gap ($5H$) is susceptible an inertial instability. The obtained experimental results have served as validation for 3D numerical simulations. In this section we assess the effect of varying the gap size ($g$) of the mixing-separating device by performing numerical studies using geometries with gaps $g = 2H$, $2.61H$, and $3.86H$ in addition to the previously discussed $g = 5H$. We found that not only the critical $Re$ of the instability is affected by the gap size, but also the nature of the instability and the flow symmetries that are broken.

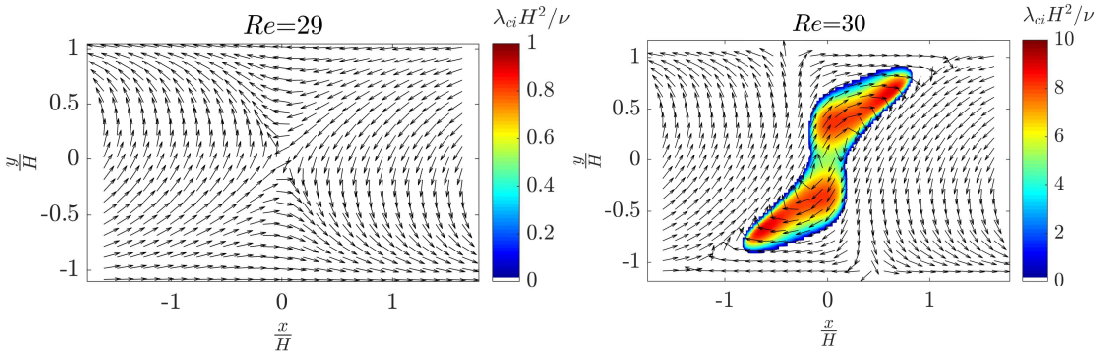


Figure 5.9: The change in flow pattern between the base flow (no vortices, $Re = 29$), and the bifurcated flow just after onset (a single large vortex, $Re = 30$) in a mixing-separating device with $g = 5H$. The colormap shows the swirling strength ($\lambda_{ci}H^2/\nu$) and the vectors show the direction of the velocity field.

Table 5.1: Critical Reynolds number for mixing-separating microfluidic devices with different gap sizes ($g$). Two different instabilities ($\lambda_{ci}$ and $w$) are possible depending on the gap size. Of the gap sizes tested only $g = 2.61H$ exhibited both types of instability.

| $g$ | $2H$ | $2.61H$ | $3.86H$ | $5H$ |
|---|---|---|---|---|
| $Re_c$ ($\lambda_{ci}$) | – | 23 | 26 | 29 |
| $Re_c$ ($w$) | 51 | 84 | – | – |

### 5.2.1 Instability onset for different gap sizes

In the previous section, we showed that the instability in a wide gap ($g = 5H$) mixing-separating microfluidic device is supercritical with $Re_c = 29$. By running identical numerical simulations for different gap sizes we are able to reveal how the $Re_c$ changes as the gap size is decreased. The results, summarised in table 5.1, shows that by reducing the gap size the critical $Re$ of the instability that was found to be present in the $g = 5H$ mixing-separating device decreases from $Re_c = 29$ at $g = 5H$ to $Re_c = 23$ at $g = 2.61H$. At smallest gap tested ($g = 2H$) the instability is not present at all. However, at this gap, we observe a different instability at $Re = 51$. This instability is similar to the engulfment instability seen in the cross-slot device in earlier work [7, 40] and the appropriate bifurcation parameter is the maximum transverse velocity ($w_{max}/U_b$). Of the four gap sizes tested only the $g = 2.61H$ device exhibited both types of instability, with the $\lambda_{ci}$ instability occurring at a much lower Reynolds number ($Re_c = 23$) than the $w$ instability ($Re_c = 84$).

### 5.2.2 Results of simulations with $g = 3.86H$

If the gap size of the mixing-separating device is reduced from $5H$ to $3.86H$, although the critical $Re$ is reduced (from $Re_c = 29$ to $Re_c = 26$), the growth of the instability with $Re$ is very similar as can be seen in figure 5.11 (when compared to 5.7). The

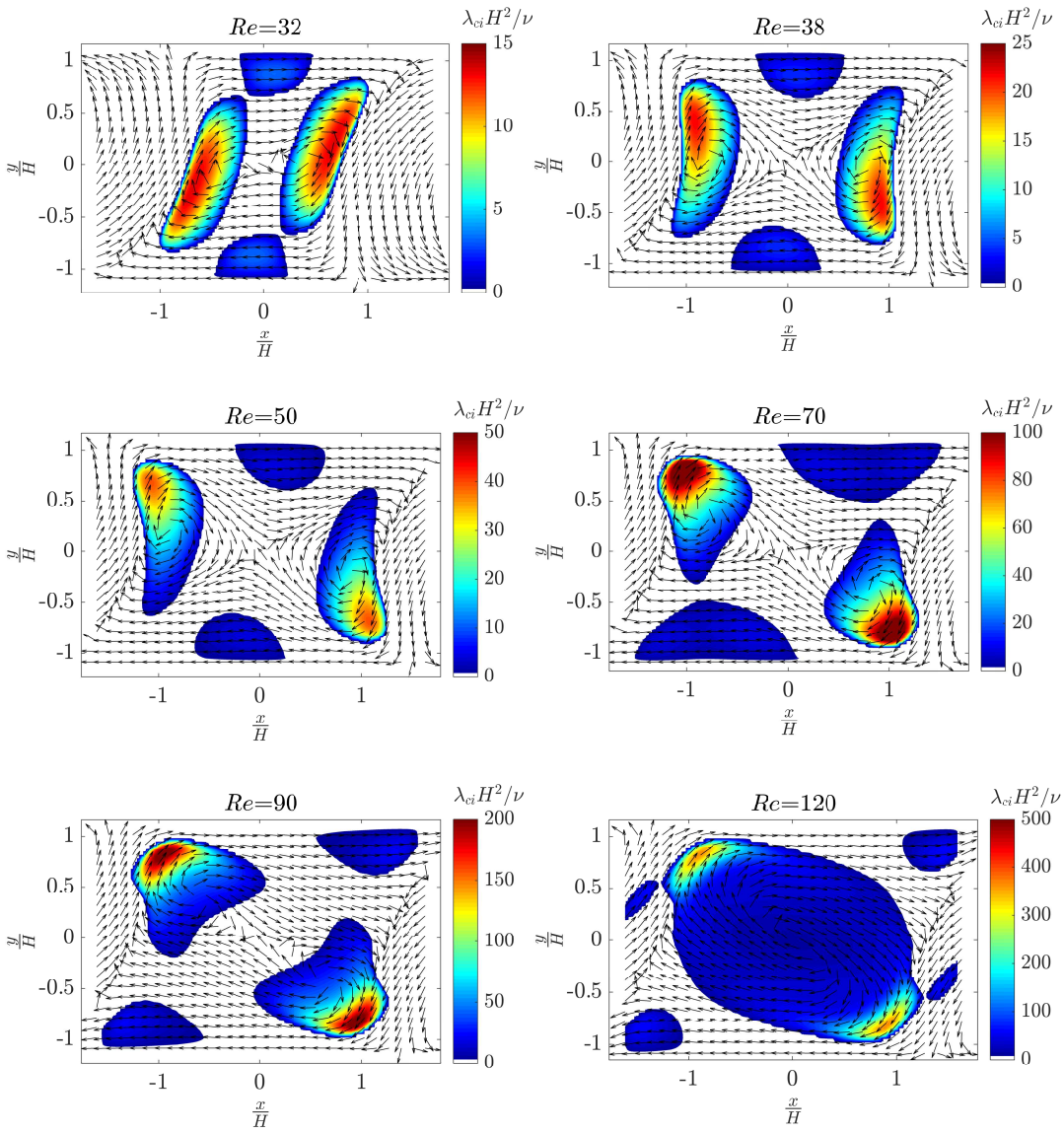


Figure 5.10: The evolution of the vortices with $Re$ in a mixing-separating device ($g = 5H$). From $Re = 32$ to $Re = 50$, the cores of the two vortices gradually alter their positions. In the region $50 < Re < 90$, the vortices do not alter their positions significantly. The vortices merge into a large vortex at $Re = 120$. Rotational symmetry is preserved for all $Re$. Vectors show the direction of the velocity only.

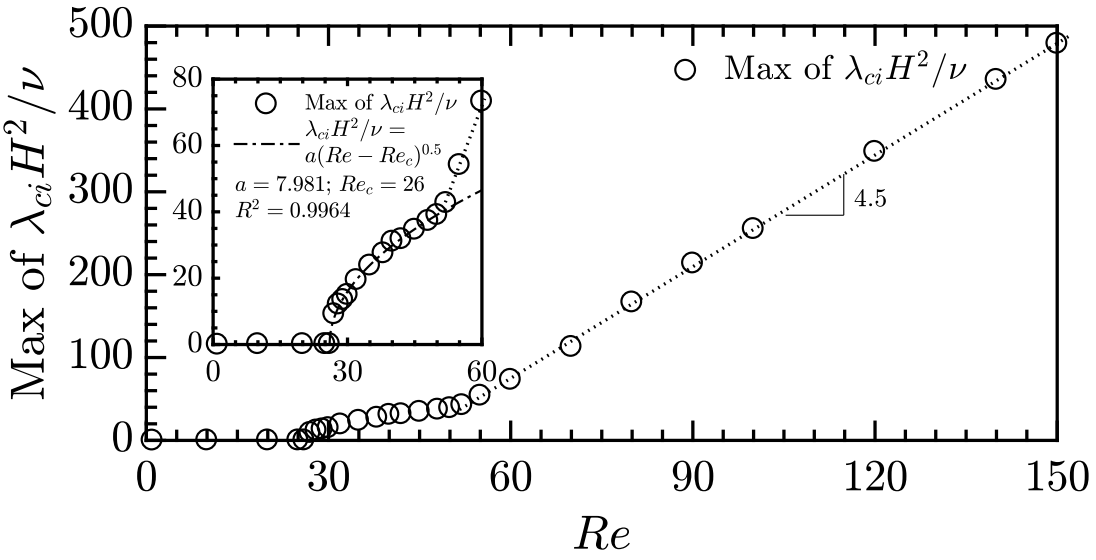


Figure 5.11: Variation of the bifurcation parameter for the device with a gap size of $3.86H$. The instability critical $Re$ number is 26. Close to the onset, the bifurcation parameter $\lambda_{ci}$ fits a square root function. Similar to a $5H$ gap, when $Re > 50$, the growth of the instability is linear with a gradient $\approx 4.5$.

instability is again shown to be supercritical (following a square root function near to onset) and away from onset ($Re > 50$) it is linear with a very similar gradient.

Despite the growth of the bifurcation parameter with $Re$ being very similar for $g = 5H$ and $g = 3.86H$ there are some significant differences in the flow fields (compare figure 5.12 with figures 5.9 and 5.10. Below the onset of the instability there is little difference. At $Re = 27$, two vortices appear close to the walls at the gap of the mixing-separating cell. This is similar to the $g = 5H$ device at onset, but in the $g = 3.86H$ case the vortices are more distinct from each other. Larger changes ensue as $Re$ is increased. In the $g = 5H$ device there is a significant separation of the vortices in the $x$-direction, this is not present in the $g = 3.86H$ device, presumably because of the confinement due to the smaller gap. As such the vortices begin to merge at $Re$ only a little above onset. By $Re = 50$ the vortices have merged into a single large vortex, which then persists largely unchanged at higher $Re$ (a single large vortex did not appear until $Re = 120$ in the $g = 5H$ device). It is up until this merging that the bifurcation parameter follows the square-root growth typical of a supercritical instability. After the single large vortex has formed there is linear growth of the strength of the vortex, but no further significant change in the flow topology.

### 5.2.3 Results of simulations with $g = 2.61H$

The device with a gap of $g = 2.61H$ is the only one (of those tested) that exhibits two types of instability. As shown in figure 5.13, the first instability is the $\lambda_{ci}$ instability, similar to the $g = 3.86H$ and $g = 5H$ devices, but occurring slightly earlier at $Re = 23$,

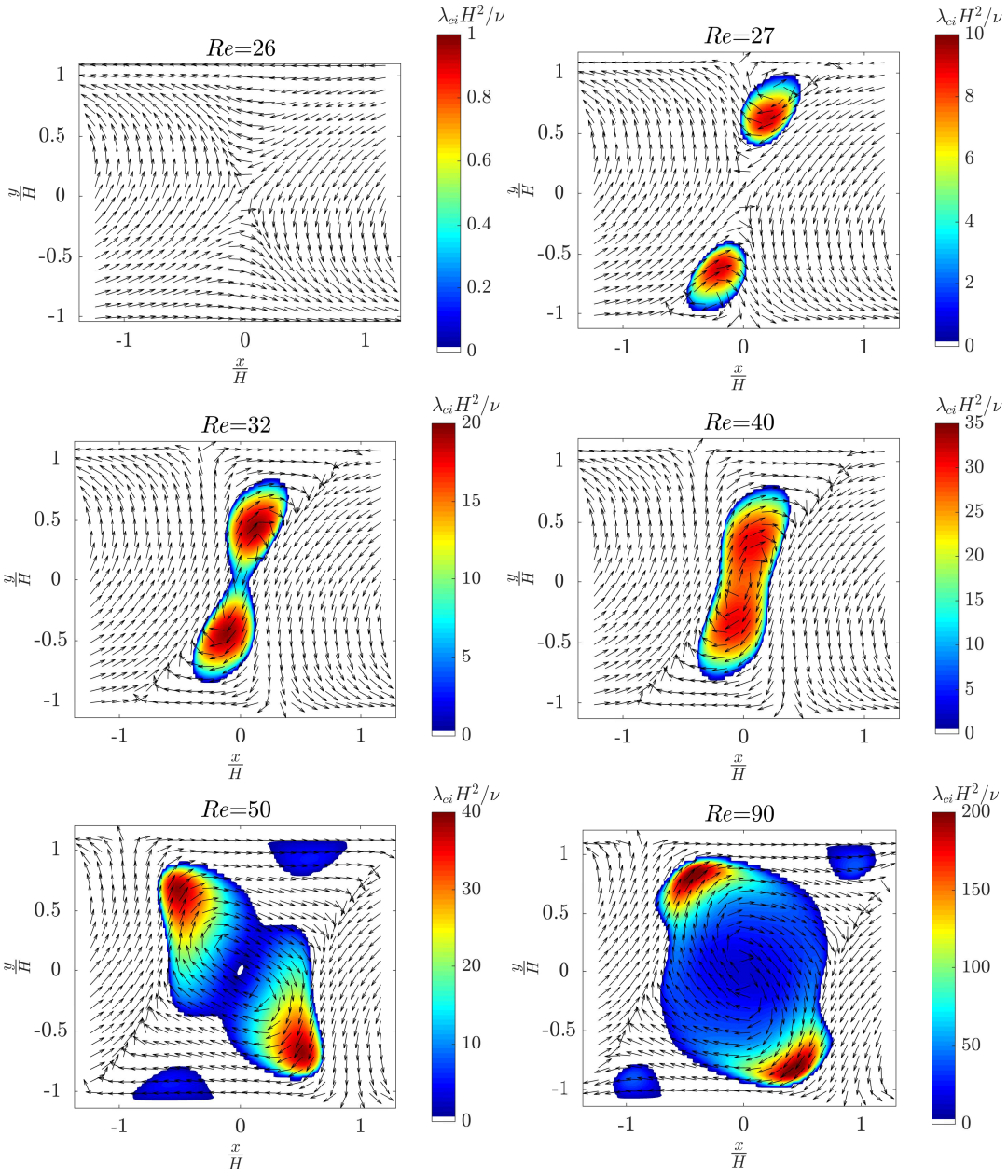


Figure 5.12: The evolution of the vortices with $Re$ in a mixing-separating device ($g = 3.86H$). Before the instability there are no vortices ($Re = 26$), at onset two vortices appear ($Re = 27$) and then merge as $Re$ is increased ($27 < Re < 50$). One large vortex is formed and persists at higher $Re$ (e.g. $Re = 90$). Rotational symmetry is preserved for all $Re$. Vectors show the direction of the velocity only.

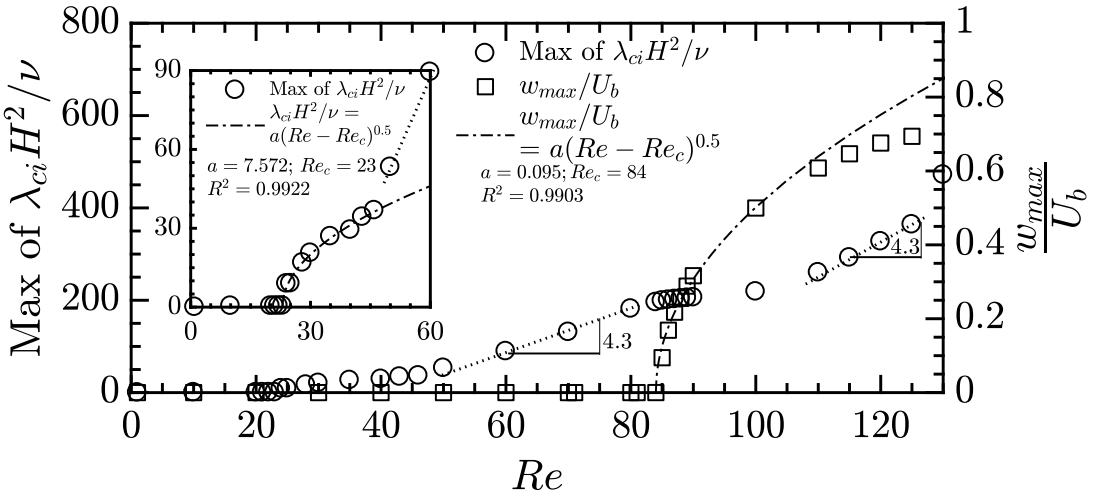


Figure 5.13: Variation of the bifurcation parameter for the device with a gap size of $2.61H$. The critical $Re$ number is 23. Close to the onset, the bifurcation parameter fits a square root function. Similar to the $g = 5H$ and $g = 3.86H$ gaps, when $Re > 50$, the growth of the instability is linear with a gradient $\approx 4.3$. At $Re = 84$ the second supercritical instability occurs (seen in the square-root growth of $w_{max}/U_b$) and interrupts the linear growth of $\lambda_{ci}$ parameter until $Re > 100$.

and developing with a square-root growth. This is followed by a linear increase with $Re$ (with a gradient $\approx 4.3$), again very similar to the devices with wider gaps. However, at $Re = 84$ this growth stalls and the second instability appears, this time manifested in the transverse velocity component ($w_{max}$), indicating a break of symmetry in the $y$-$z$ plane. This instability is also supercritical and follows a square-root growth until $Re \approx 100$. Beyond this $Re$ the original ($\lambda_{ci}$) instability, the strength of which does not grow while the second instability grows, returns to linear growth with the same gradient as it had before the onset of the second instability.

The evolution of the vortices in the $x$-$y$ plane with $Re$ for the $g = 2.61H$ device (figure 5.14) is similar to the $g = 3.86H$ device (figure 5.12). A pair of co-rotating vortices emerges across the gap at onset. These occupy a very similar $x$-location and are separated in the $y$-direction, following the trend previously observed as the gap size is reduced. As $Re$ is further increased the vortices coalesce, after which they broadly remain on a fixed position, their strength increasing. The onset of the second instability (in $w_{max}$) does not affect the arrangement of the vortices in this plane, although the rate at which their strength increases is slowed whilst the second instability grows.

At $Re > 84$, the bifurcation parameter $w_{max}/U_b$ measured on the $z = 0$ plane being non-zero indicates a breaking of symmetry. This is shown by the streamlines in the $y$-$z$ plane in figure 5.15. Prior to this instability the flow (as viewed in this plane) is split into four reflectionally and rotationally symmetric quadrants with no interation between the streams. At the onset of the instability the $w-$component of

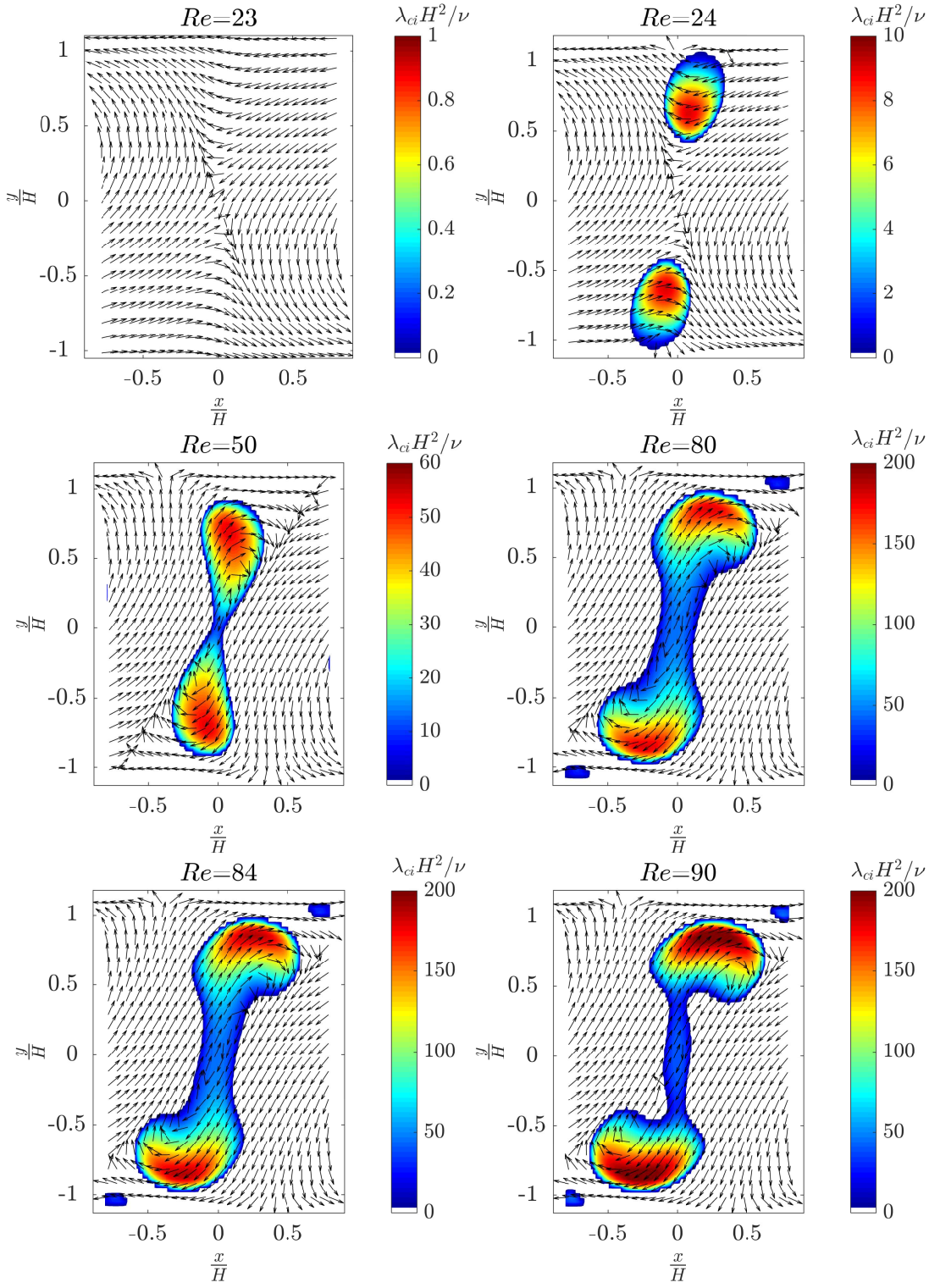


Figure 5.14: The evolution of the vortices with $Re$ in a mixing-separating device ($g = 2.61H$). Before the instability there are no vortices ($Re = 23$), at onset two vortices appear ($Re = 24$) and then merge as $Re$ is increased ($Re \approx 50$). One long, slender vortex spanning the channel is formed and persists at higher $Re$ (e.g. $Re > 70$). The onset of the second instability at $Re = 84$ has no significant effect on the vortex in this plane. Rotational symmetry is preserved for all $Re$. Vectors show the direction of the velocity only.

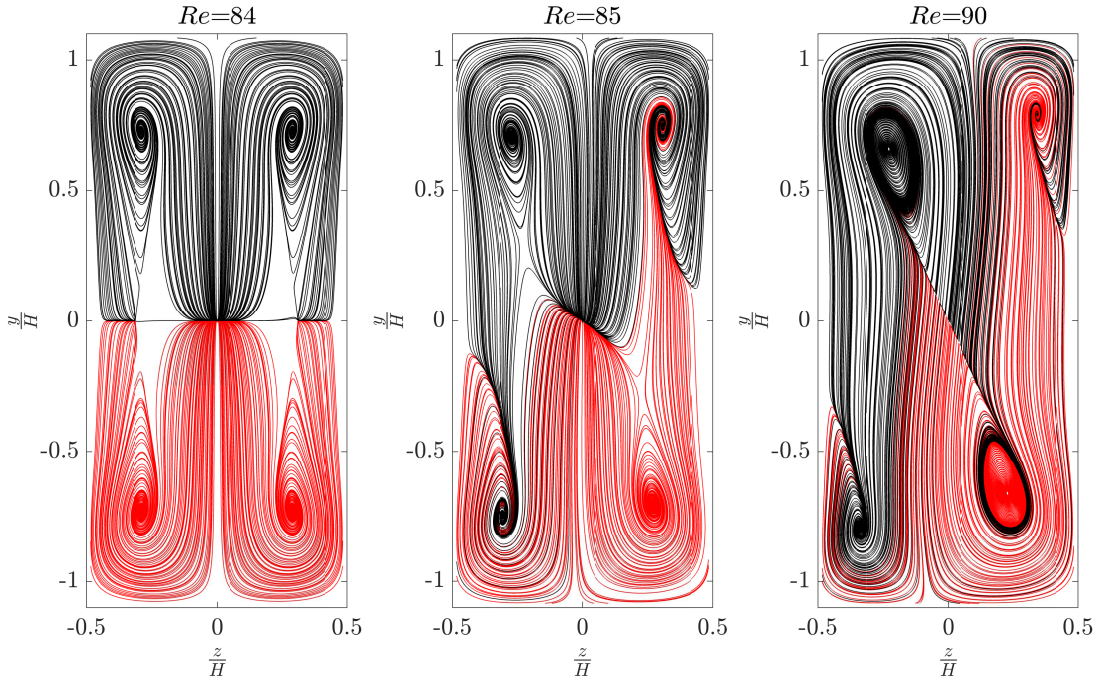


Figure 5.15: Streamlines on the $y$-$z$ plane of the $g = 2.61H$ device before and after onset of the $w_{max}/U_b$ instability. At $Re = 84$ the flow is reflectionally symmetric about $z = 0$ and $y = 0$, at $Re = 85$ the symmetry in both these planes is broken and the $w$-component of velocity on the $z = 0$ plane is non-zero. The extent of the asymmetry grows as $Re$ is further increased (e.g. see $Re = 90$) although rotational symmetry is preserved throughout. The streamlines are 3D and coloured by the inlet from which they originate, they therefore leave the plane in this 2D plot.

velocity on the $z = 0$ plane becomes non-zero and all the reflectional symmetries are broken, although the rotational symmetry (180° about $y = 0$, $z = 0$) is preserved. The instability causes the streams from the two different inlets to interact and by $Re = 90$ fluid from each inlet has entered all four quadrants when it reaches this central plane. Although this instability has been identified using the same bifurcation parameter as is used in the cross-slot device, it is distincly different from that engulfment instability as it does not result in a single large vortex in the $y$-$z$ plane.

### 5.2.4 Results of simulations with $g = 2H$

At the narrowest gap tested ($2H$), the swirling motion at the $x$-$y$ plane (quantified using $\lambda_{ci}H^2/\nu$), which was observed for all other gap sizes, is completely absent for the entire range of $Re$ tested ($1 < Re < 120$). However, the maximum transverse velocity ($w_{max}/U_b$) parameter becomes non-zero and fits a square root function near to the critical Reynolds number ($Re_c = 51$). Figure 5.16 displays both bifurcation parameters, demonstrating that $\lambda_{ci}H^2/\nu$ is always zero and $w_{max}/U_b$ shows supercritical behaviour.

It is worth noting that if two of the arms of a cross-slot device were rotated 90° then

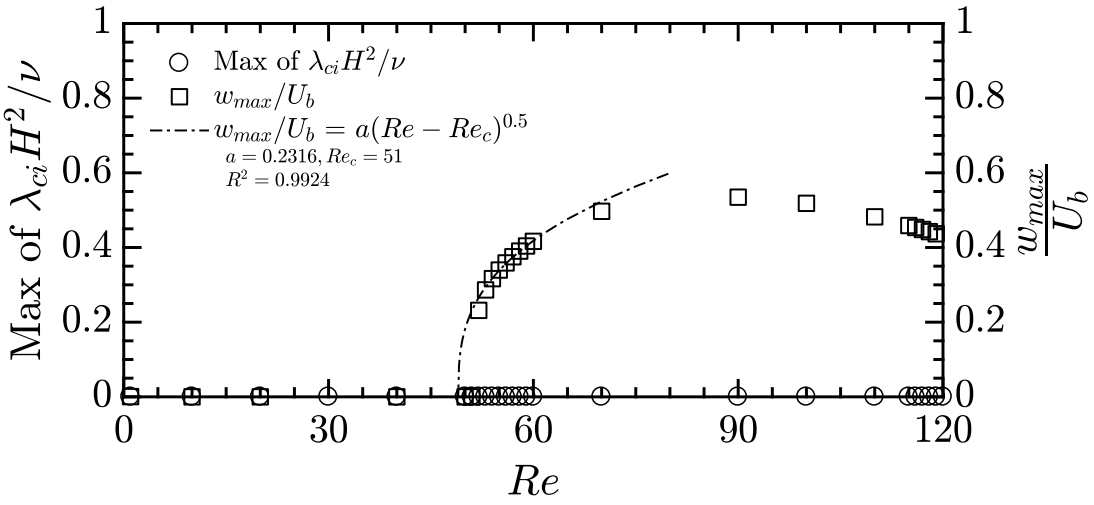


Figure 5.16: Variation of the bifurcation parameter for the $g = 2H$ geometry. There is no instability in $\lambda_{ci}$, which is zero for all $Re$. Instead, the first and only instability is similar to the second instability in the $g = 2.61H$ device, where the $w_{max}/U_b$ parameter highlights a supercritical bifurcation, i.e. it fits a square root function near to onset ($Re_c = 51$) and no hysteresis.

it would be a mixing-separating device with $g = \sqrt{2}H$. It is therefore apparent that our mixing-separating device with $g = 2H$ is geometrically closest to the cross-slot device. The only instability that occurs in the mixing-separating device with $g = 2H$ is highly reminiscent of the instability seen in a cross-slot device with aspect ratio of unity. As seen in figure 5.17, above the onset of the instability a large spiral vortex forms in the $y$-$z$ plane providing significant mixing of the two fluid streams. This is very similar to the engulfment instability seen in the cross-slot and demonstrates that this instability is not wholly dependent on the specific angle at which the two streams collide as both 90° (cross-slot) and 180° (mixing-separating) result in a very similar flow (although the instability in the cross-slot is sub-critical for square cross-section channels). In fact, it appears that the size of the gap is a more important parameter (as this instability does not appear at large gap sizes). This presents the question of whether this instability would occur if the flows collide at other angles between 90° and 180°. It seems logical that it would indeed occur if the gap was small.

Although there is some previous work on the effect of the $\alpha$ angle (albeit for circular cross-section channels)[26], a full study of devices with a variety of angles and gap sizes is required to answer this question with certainty and to firmly establish how the instability relates to both gap size and $\alpha$ angle. However, the current chapter indicates that the gap size is of primary importance in determining which instability occurs. As $\alpha$ and gap size are geometrically dependent upon each other (i.e. if $\alpha$ is changed, the gap size is changed as a result of the new angle [26]). Therefore our results for the mixing-separating device are useful for reference cases as we can vary the gap size

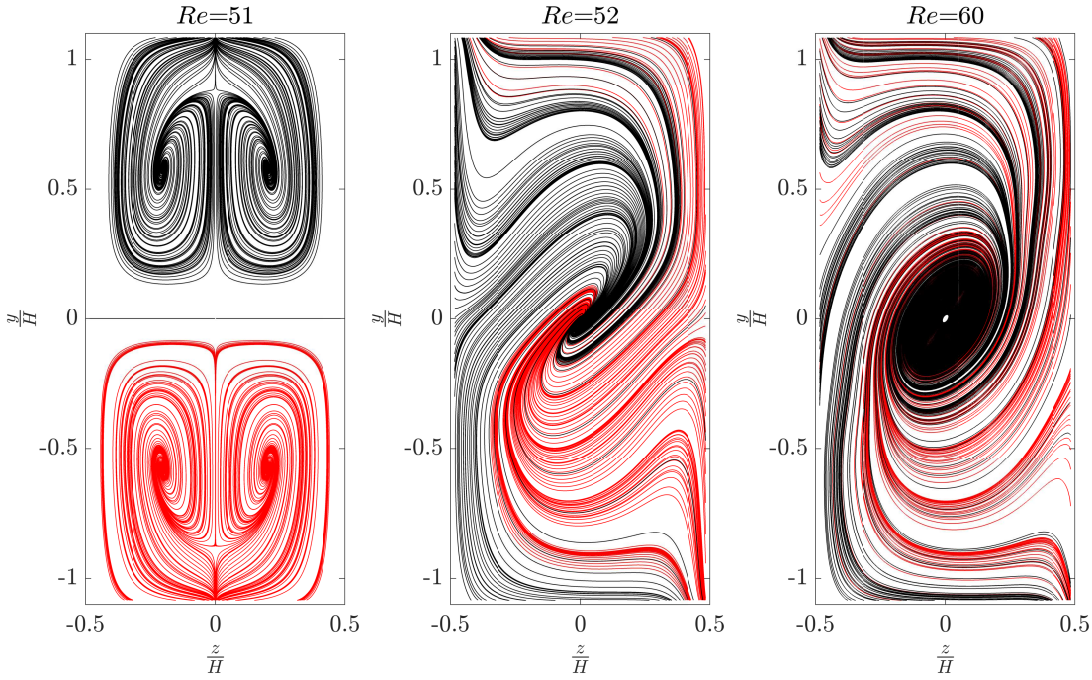


Figure 5.17: Streamlines on the $y$-$z$ plane of the $g = 2H$ device before and after onset of the $w_{max}/U_b$ instability. At $Re = 52$ the reflectional symmetry is broken and the $w$-component of velocity on the $z = 0$ plane is non-zero. This is an engulfment instability, and as $Re$ is further increased (e.g. see $Re = 60$) a large spiral vortex is formed providing significant mixing of the two fluid streams. Rotational symmetry is preserved throughout. The streamlines are 3D and coloured by the inlet from which they originate, they therefore leave the plane in this 2D plot.

without changing $\alpha$ (which is a particular quirk of the $H$-geometry).

## 5.3 Summary

In summary, this numerical investigation of the flow in mixing-separating ($H$-geometry) microfluidic devices with gap sizes, $g = 2H$, $2.61H$, $3.86H$, and $5H$ has demonstrated that two different inertial instabilities are possible at low Reynolds numbers in the steady flow regime. Which of the two instabilities occurs is primarily dependent of the size of the gap, as well as the Reynolds number ($Re$). Complementary experiments providing flow visualisations in a a mixing-separating device with $g = 5H$ match the results of the numerical simulations very well, providing a validation of the numerical technique, which is applied to additional gap sizes. Moreover, the devices with large gaps ($g = 3.86H$ and $g = 5H$) favour the onset of a vortical flow instability in the $y$-$z$ plane, which we have detected and quantified using swirling strength ($\lambda_{ci}H^2/\nu$). In particular, the strong dependence of the instability on the gap size is revealed.

In this chapter, we provided a database that highlights the importance of the gap size in the design of the mixing-separating microfluidic device ($H$-geometry). Ad-

ditionally, we present information regarding the onset ($Re_c$) of two types of inertial instabilities over a range of gap sizes which are viable choices for microfluidic applications.

# Chapter 6

# Effects of angle variation on the inertial instability

The previous chapter explored flow instabilities in a microfluidic mixing-separating when varying the gap ($g$). Sarkar et al. [60] conducted numerical simulations to evaluate mixing performance when varying the angle of the opposing inlet and outlet arms channels in a T-junction microfluidic device. Correa et al. [26] explored the changes in flow topology in a $X$-shaped junction when varying the angle ($\alpha$) between crossed circular cross-section channels and the Reynolds number. Motivated by these two works, we investigate the flow instabilities in bisecting channels when varying the angle between the pair of inlet and outlet arms from a so-called 'mixing-separating' (0° angle) to a so-called cross-slot (90° angle) where the inlet and outlet channels are orthogonal. The study will include intermediate geometries between these two extremes.

The $\alpha$ angle and gap size are geometrically dependent upon each other. As per figure 4.8 and equations 4.4 and 4.5, if $\alpha$ is changed, the gap size is changed as a result of the new angle. Therefore, the gap size is very important, and any change in other aspects of the geometry (e.i.: $\alpha$ angle) affects the gap size. For instance, when $\alpha$ is 30°, the gap size should be $g = 3.86H$. In the literature, Correa et al. [26] neglected the importance of the gap size in their work. Therefore, by taking into account the constraints in the gap size when varying $\alpha$, we investigate the effects of these changes on the inertial instabilities. Moreover, we compare the $X$-shaped geometries with the particular gap size mixing-separating devices.

Until now, the literature does not present any work related to flow instabilities when varying the geometries from a so-called 'mixing-separating' cell which consists of two straight square parallel channels with flow from opposite directions and a central gap that allows the streams to interact, mix or remain separate (often referred to as the 'H' geometry) to a so-called cross-slot where the inlet and outlet channels are orthogonal including intermediate geometries between these two extremes. In all cases, a stagnation point is generated at the centre of symmetry due to the two opposed inlets

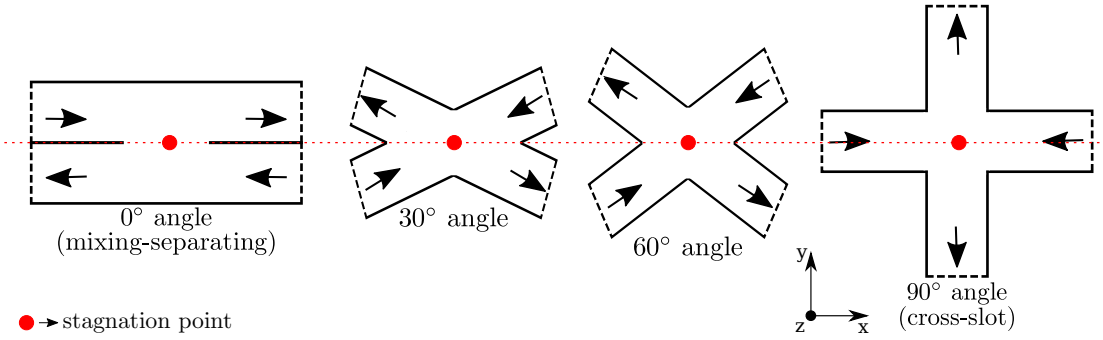


Figure 6.1: Stagnation point generated when varying the angle between the pair of opposing inlet and outlet channels. From a mixing-separating cell device to a cross-slot device.

and outlets (see figure 6.1). The overall aim of this chapter is to numerically investigate the inertial flow instabilities when varying the angle between the inlet and outlet arms considering our validated numerical method.

## 6.1 Geometry selection

In order to enhance the understanding of the mechanisms underlying the bifurcation flow within devices with fluid streams imposed from opposed inlets, the current section evaluates new designs of micro-geometries by performing numerical studies on the effect of varying the angle between the pair of inlets and outlets of the mixing-separating cell device. When changing $\alpha$, the gap size also changes. A 30° degree geometry have a gap $g = 3.86H$. In a 45° geometry, gap size is $g = 2.61H$, and $g = 2H$ in a 60° geometry. Therefore, the $g = 3.86H$, $g = 2.61H$, and $g = 2H$ mixing-separating devices ($H$-shaped) match the $X$-shaped devices 30°, 45°, and 60° angle.

## 6.2 Instability variation: from subcritical pitchfork to supercritical

In a cross-slot geometry, which has orthogonal inlets and outlets (90° angle between the inlet and outlet arms, results from previous work show that the common instability parameter ($w_{max}/U_b$) shows a hysteretic behaviour, and the symmetry-breaking bifurcation is a subcritical pitchfork [40]. The critical Reynolds number encountered when increasing $Re$ is 53 and, when decreasing $Re$, the critical value is 39. Different works [7], [138], and [63] reported the same critical Reynolds number ($Re_c \approx 40$) with decreasing $Re$ when using a cross-slot geometry with a similar aspect ratio, $AR = 1$ (squared ducts). While for the increasing $Re$ ramps, the onset of the instability published by [7] and [63] is at $Re_c \approx 46$. Noticeably, the hysteresis observed in our numerical simulations for Newtonian fluids depends on the level of noise and therefore on many factors

(for instance, the numerical solver, numerical method, and mesh size applied). Thus, in this thesis, for the cross-slot geometry (90° angle) considered in this study, we report our values previously published [40].

Figure 6.2 illustrates that when a 60° angle geometry is used, $w_{max}/U_b$ shows no hysteresis. Close to critical Reynolds number, the instability parameter varies like a square root function $a(Re - Re_c)^{0.5}$, typical of supercritical bifurcations. It is apparent when the Reynolds number is smaller than 57 ($Re < Re_c$), the instability parameter is negligible. When $Re$ is over 57, the instability parameter becomes non-zero due to the appearance of a vortical flow. Similarly to the cross-slot geometry (90° angle), the reflectional flow symmetry of the transverse velocity field breaks after this critical state.

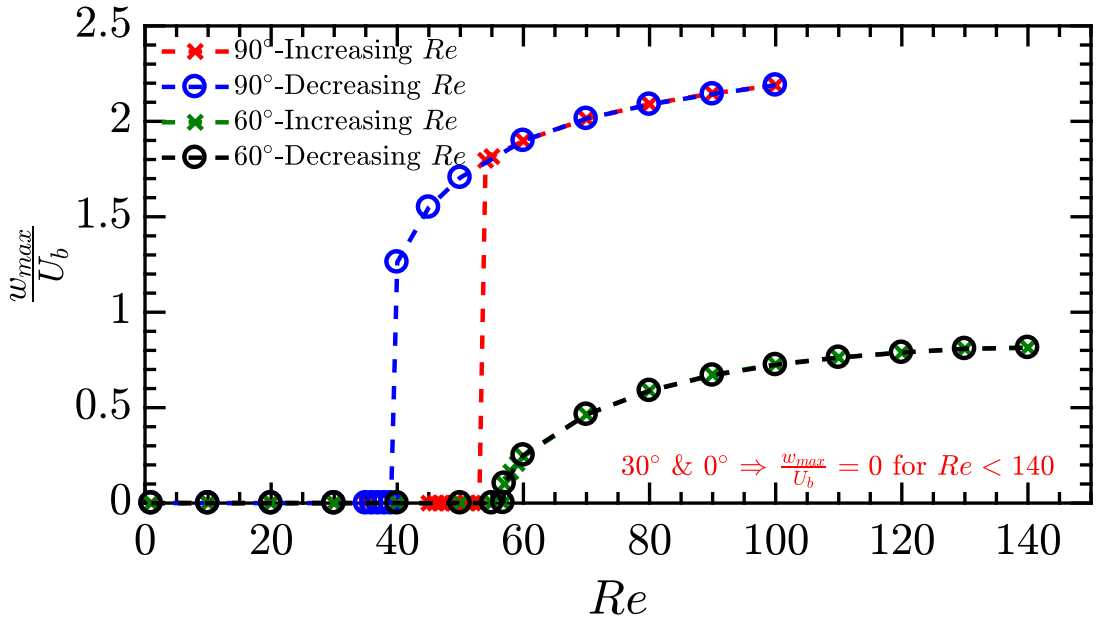


Figure 6.2: The maximum transverse velocity ($w_{max}/U_b$) along the centreline $y = 0$ on the plane $y$-$z$ (refer to figure 6.3 top right-hand side) with increasing and decreasing Reynolds number on different angle geometries. From 90° angle to 60°, the instability changes from a subcritical pitchfork with hysteresis to a non-hysteretic supercritical. Moreover, the instability growth parameter ($w_{max}/U_b$) is zero for the $Re$ numbers tested ($Re < 140$) on geometries 30° and 0°. (Note that the data presented here for a 90° angle geometry was extracted from our previous study [40].)

## 6.3 60° X-shaped geometry compared to a $g = 2H$ mixing-separating

Figure 6.3 demonstrates how the streamlines on $x$-$y$ plane evolves when increasing $Re$ in a 60° angle geometry. A pair of vortices appears at $Re > 40$, although the transverse flow field at the centre plane ($y$-$z$ plane and $x = 0$) keeps streamwise symmetry. Figure 6.3b demonstrates the break of symmetry at the transverse velocity field at $Re = 57$

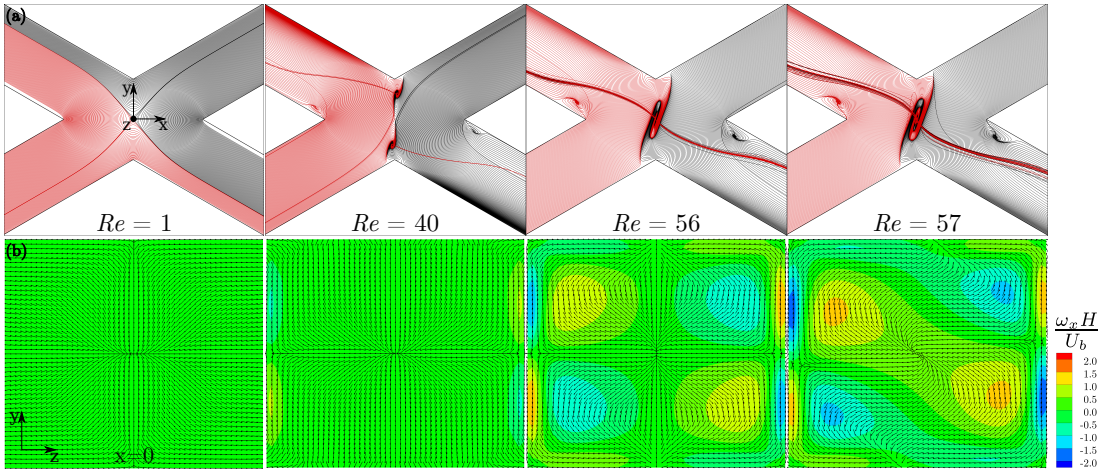


Figure 6.3: (a) Numerically-determined streamlines depicting the evolution of the flow structure in the plane $x$-$y$ and $z = 0$ for fluid flow in a 60° angle geometry. Panels (a) show the results for progressively increasing $Re$. (b) The colour scale indicates the dimensionless vorticity ($\omega_x H/U_b$) over the plane $x = 0$, and superimposed velocity vectors exhibit the directionality of the flow in the cross-section. The flow breaks its reflectional symmetry when a nonzero transverse velocity component appears for $Re > Re_c$, although (a) shows a vortical behaviour for $Re < Re_c$.

by showing the dimensionless vorticity ($\omega_x H/U_b$) over the plane, and also by exhibiting the superimposed velocity vectors that display the directionality of the flow in the cross-section.

In a mixing-separating device ($H$-shaped) with the narrowest gap tested ($g = 2H$), the swirling motion at the $x$-$y$ plane (quantified using $\lambda_{ci}H^2/\nu$), which was observed for all other gap sizes, is completely absent for the entire range of $Re$ tested ($1 < Re < 120$). In the other hand, when changing $\alpha$ (60° angle geometry) and keeping the gap size constant ($g = 2H$), two vortices appear close to the walls at the gap of the 60° $X$-shaped geometry. This is similar to the mixing-separating devices with wide gaps (such as $g > 2H$) at the onset, but in the $g = 3.86H$ case the vortices are more distinct from each other. Larger changes ensue as $Re$ is increased. As reported in chapter 5, in the $g = 5H$ device there is a significant separation of the vortices in the $x$-direction. Noticeably, this is not present in the 60° $X$-shaped device.

Certainly, by combining the change in the angle $\alpha(60°)$ with the confinement due to the smaller gap, significant differences appear in the flow fields of the $X$-shaped and $H$shaped geometries with the same gap size at the $x$-$y$ plane. The vortices, which are not present in the $H$-geometry, begin to merge at $Re$ only a little above onset ($Re = 40$). By $Re = 56$ the vortices have merged into a single large vortex, which then persists largely unchanged at higher $Re$ (a single large vortex did not appear until $Re = 120$ in the mixing-separating $g = 5H$ device).

There are similarities between the $X$- and $H$-shaped devices. For instance, at

the $y$-$z$ plane, there is also a break of symmetry in the 60° geometry at the critical Reynolds number ($Re_c = 57$, see figure 6.3) which is characteristic of the instability in a cross-slot geometry. Again, it is worth noting that if two of the arms of a cross-slot device were rotated 90°, then it would be a mixing-separating device with $g = \sqrt{2H}$. It is, therefore, apparent that $X$-shaped 60° geometry is even closer than our mixing-separating device with $g = 2H$ to the cross-slot device. The only instability that occurs in the mixing-separating device with $g = 2H$ is highly reminiscent of the instability seen in a cross-slot device with an aspect ratio of unity (engulfment instability, as seen in figure 5.17). Although, the change in the angle creates a swirling motion at the $x$-$y$ plane, which is not present in mixing-separating device with the same gap size.

The results demonstrate that the engulfment instability seen in the cross-slot is not wholly dependent on the specific angle at which the two streams collide. It only confirms that the size of the gap is a more critical parameter (as this instability does not appear at large gap sizes) as the engulfment instability indeed occur if the gap is small.

## 6.4 30° X-shaped geometry compared to a $g = 3.86H$ mixing-separating

Further, the numerical investigations show when the geometry angle is 30° and 0°, the instability parameter ($w_{max}/U_b$) gives a zero value for the whole range of the $Re$ tested ($Re < 140$). Nevertheless, streamwise vortices involved in the destabilisation flow process can be seen. Figure 6.4 shows a central vortex formation on the plane $x$-$y$ at $Re = 20$, and also secondary motions appear at the edge of the corners near to the beginning of the outlet channels for a 30° geometry. By increasing $Re$, the central vortex splits into a pair of co-rotating vortices. On the $x$-$y$ plane, the flow keeps its rotational symmetry all through the range of $Re$ assessed. Conversely, there is no reflectional flow symmetry when increasing Reynolds for the 30° angle geometry.

By changing the angle between the pairs of inlet and outlet arms, the flow structure distinctly changes for a small angle and wide gap (30° and $g = 3.86H$). The evolution of the vortices in the $x$-$y$ plane with $Re$ for the device with 30° and $g = 3.86H$ (figure 6.4) is similar to the $g = 3.86H$ mixing-separating device (figure 5.12). A pair of co-rotating vortices emerges across the gap at the onset. These occupy a very similar $x$-location and are separated in the $y$-direction, following the trend previously observed in chapter 5. As $Re$ is further increased the vortices coalesce, after which they broadly remain on a fixed position, their strength increasing.

Similar to a $H$-shaped with $g = 3.86H$ device, the second instability (in $w_{max}$) does not appear in this $X$-shaped geometry. The maximum transverse velocity instability parameter ($w_{max}/U_b$) is always zero regardless of Reynolds number. The transverse flow field at the centre plane does not show a substantial contribution of vorticity. On

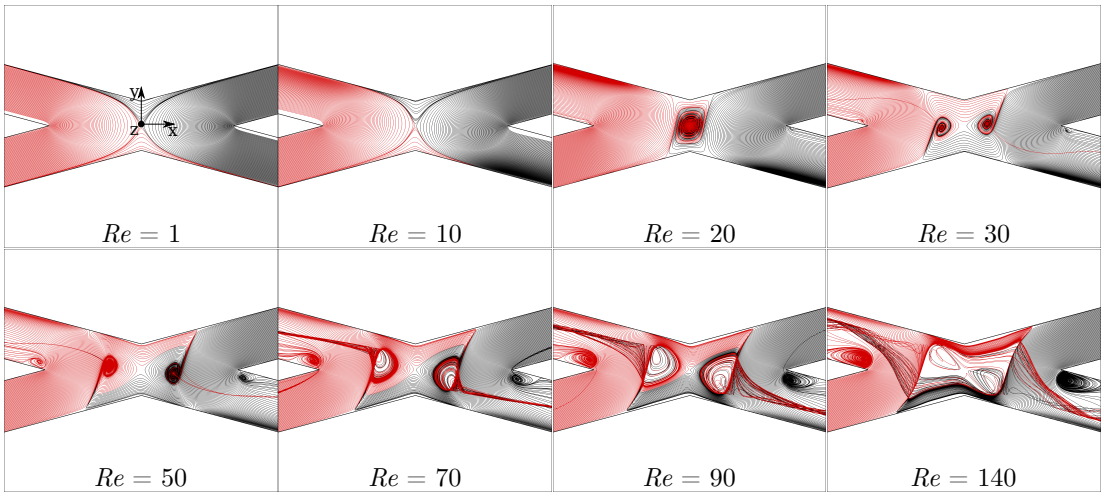


Figure 6.4: Flow development with increasing $Re$ illustrated by numerical streamlines in the plane $x$-$y$ and $z = 0$ for a 30° angle geometry. Panels show with progressively increasing $Re$ a central vortex appears for $Re = 20$. By increasing $Re$, the central vortex splits into a pair of co-rotating vortices, and secondary motions rise at the edge of the corners near to the beginning of the outlet channels.

Figure 6.5, the top panels represents the numerical streamlines in the plane $x$-$y$ and $z = 0$ superposed by the isosurfaces of vortex core regions at $Re = 90$ for a 60°,$g = 2H$ and a 30°,$g = 3.86H$ geometry. The bottom panels are displaying the dimensionless vorticity ($\omega_x H/U_b$) over the central cross-section plane of the channel (plane $y$-$z$ plane and $x = 0$) superposed by the velocity vectors showing the directionality of the flow.

Figure 6.5 clearly shows that the engulfment instability (cross-slot like) depends on the size of the gap. The small gaps change the interaction between the two streams, which is more favourable for the engulfment regime, which is predominant in the $y$-$z$ plane. Although, in the wide gaps, the interaction is predominant in the $x$-$y$ plane in the form of swirling motion (co-rotating vortices).

### 6.4.1 Flow development along the outlet channels

Along the outlet channels of the studied geometries, when the rate of change of momentum is negligible, the flow field restores the developed state showing a parabolic velocity distribution (the Hagen-Poiseuille flow) as it approaches the exit. Figure 6.6 illustrates cross-sectional velocity magnitude (normalised by the bulk flow velocity) on four different $y$-$z$ plane sections along the outlet arms of a 60° and 30° angle geometries with distances of $0H$ (outlet starting plane), $2H$, $4H$, and $8H$, where $H$ is channel height (or hydraulic diameters in this case). Comprehensible, the flow is less susceptible to recover its parabolic velocity profile under high Reynolds number. In fact, at $8H$ distance from the entrance of the outlet arm, the flow does not restore the parabolic profile for $Re = 140$ in both geometries as illustrated in the figure.

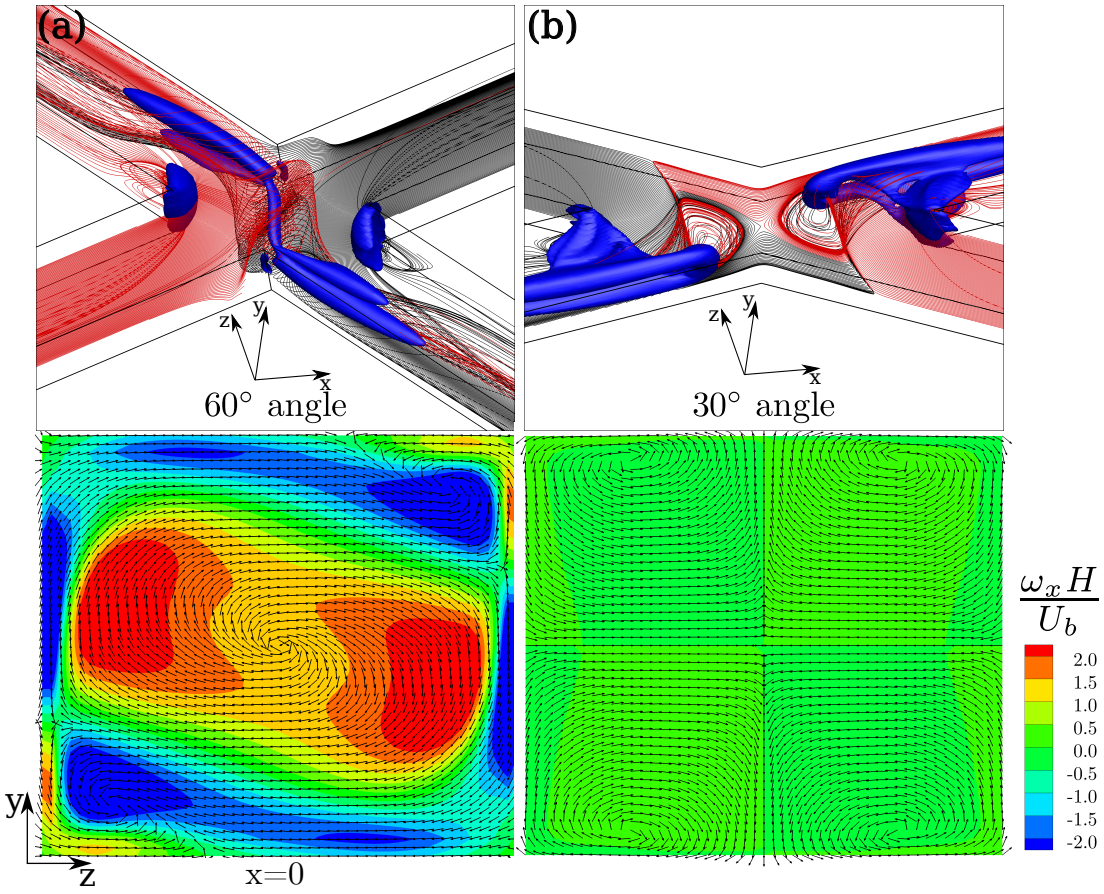


Figure 6.5: Top panels: Numerical streamlines in the plane $x$-$y$ and $z = 0$ and the isosurfaces of vortex core regions at $Re = 90$ for (a) 60° and (b) 30° angle geometry. Bottom panels: The colour scale indicates the dimensionless vorticity ($\omega_x H/U_b$) over the plane over the central cross-section plane of the channel (plane $y$-$z$ plane and $x = 0$) superposed by the velocity vectors showing the directionality of the flow.

Compared with 60° of angle geometry, the flow in 30° angle geometry seems more susceptive to recover its ts parabolic velocity profile. Apparent in figure 6.6(b), the flow reaches quicker the fully developed state in a 30° geometry. At $8H$ distance from the entrance of the outlet arm, the flow can reestablish the parabolic profile for $20 < Re < 90$. Moreover, the velocity flow field keeps its reflectional symmetry. In a 60° of angle geometry (6.6(a)), where symmetry breaks, the flow cannot recover its fully developed form when tested at the same $Re$ numbers. The results show that the flow stability changes along the outlet arms depending on the geometry angle, which could be beneficial depending on the desired application. Noticeably, as the engulfment instability appears only in the 60° angle geometry, we can conclude that this type of instability promotes a stronger mixing in a small channel length when comparing to the swirling motion present in the 30° angle geometry at the $x$-$y$ plane.

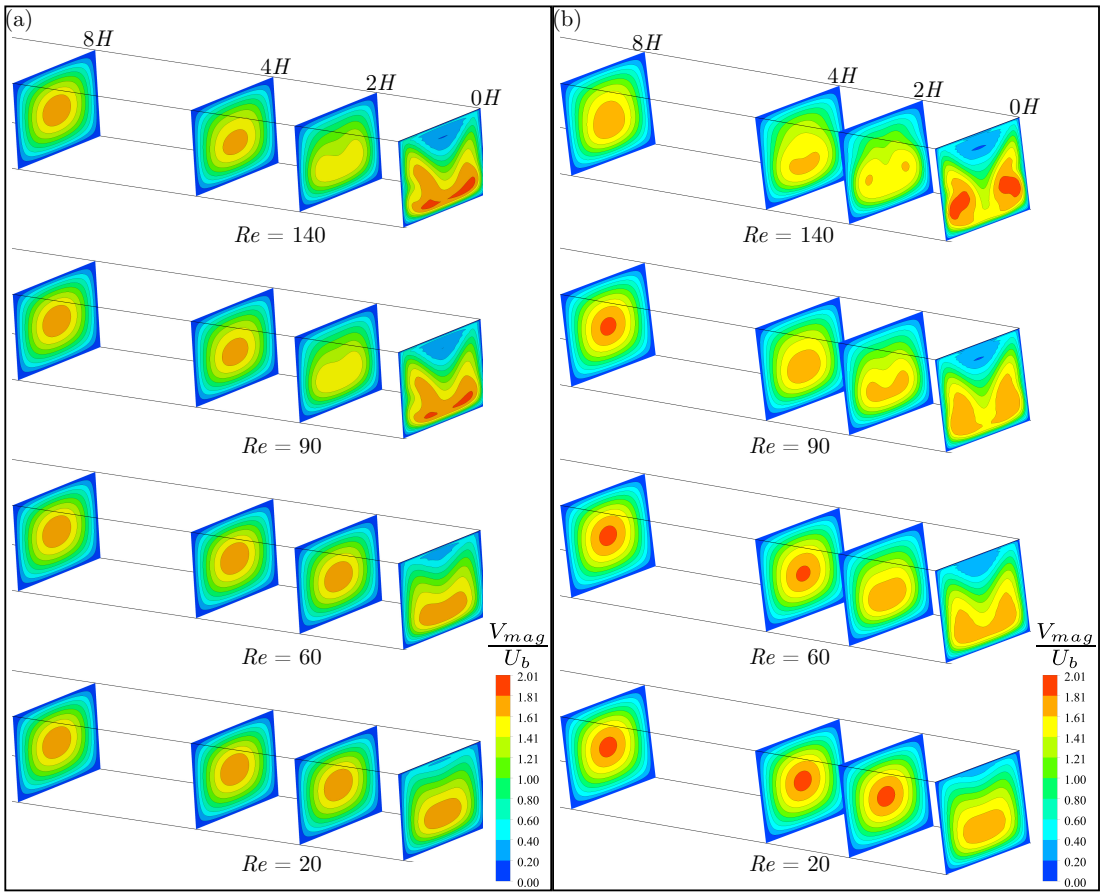


Figure 6.6: Cross-sectional velocity magnitude (normalised by the bulk flow velocity) on four different planes along the outlet arm with distances of $0H$ (outlet starting plane), $2H$, $4H$, and $8H$ channel heights (or hydraulic diameter) from the entrance of (a) a 60° angle geometry, and (b) 30° angle. The flow cannot restore its parabolic flow profile even after $8H$ distance from the entrance for all $Re$ numbers tested when the angle is 60°. Conversely, for a 30° the flow field is symmetric and can reach the fully developed form for $20 < Re < 90$.

## 6.5 Summary

The numerical investigation has improved our understanding of the mechanisms underlying in this flow instability variation. By varying the angle $\alpha$ between the inlet and outlet arms, the instability parameter ($w_{max}/U_b$) have confirmed the instability change from subcritical pitchfork in a 90° angle geometry (cross-slot) to supercritical in a 60° angle without hysteresis. After the instability onset, the transverse flow field at the central plane breaks its symmetry, and $w_{max}/U_b$ increases following a square root function when $Re - Re_c)/Re_c << 1$.

Comparing the $X$-shaped geometries to the similar gap size mixing-separating devices, we confirmed that the engulfment instability seen in the cross-slot is not wholly dependent on the specific angle at which the two streams collide. The results have confirmed that the size of the gap is a more important parameter (as this instability does not appear at large gap sizes) as the engulfment instability indeed occur if the gap was small. The symmetric transverse velocity flow field at the central plane restricted the use of the instability parameter $w_{max}/U_b$ for wide gap size geometries (30°,$g = 3.86$). Moreover, along the outlet channels, the flow field demonstrates that can it restore the developed state showing a parabolic velocity distribution in a small channel length when changing the angle $\alpha$ (i.e. from 60° to 30°) due to the different instability present (engulfment instability or swirling flow). These findings could be beneficial depending upon the desired application.

# Chapter 7

# Elastic instabilities in a mixing-separating cell micro-device

Compared to traditional macro-scale mixing methods, microfluidic devices provide an excellent alternative with lower cost, improved portability and shorter operational time. For example, a potential to reduce blood processing time from an hour to a few minutes [2]. Currently, microfluidic researchers are undertaking the task of creating in vivo organs on a microchip to mitigate the soaring costs of R&D. The aim is to produce a set of sophisticated in vitro assays with which drugs could be tested, with the hope to increase predictability (hit rate) of a new drug before animal testing and human clinical trials. Such devices have been used to diagnose sickle cell disease utilising blood vessel-on-a-chip devices [4]. Viscoelastic fluids (materials that exhibit both viscous and elastic characteristics upon deformation) have been a fascinating object of study to researchers in various areas. The non-Newtonian fluids (e.g., polymeric solutions, colloidal suspensions, blood, chocolate, paint and cosmetics) are fluids which the value of viscosity is not constant. Therefore, inertia is no longer the sole source of nonlinearity.

The works of Baloch, Townsend, and Webster [101]; Afonso et al. [27]; and Echendu et al. [102], where the investigations were carried out using different numerical constitutive models, we decided to conduct experimental investigations on the mixing-separating cells for viscoelastic fluid flows under creeping (or Stokes flow) conditions ($Re << 1$). Therefore, in this chapter, using the same experimental approached previously utilised, a model liquid with nearly constant viscosity was employed to investigate the role of elasticity. A so-called Boger fluid that consists of a mixture of Polyethylene glycol (PEG, $M_w = 8x10^3[g.mol^{-1}]$ [1], Sigma-Aldrich), Polyethylene oxide (PEO, $M_w = 4x10^6[g.mol^{-1}]$, Sigma-Aldrich), and distilled water (fluid preparation follows the protocol described in the chapter 3). The main aim of this investigation explores the onset and nature of a purely elastic instability in the mixing-separating device with

[1] $M_w$ represents the molecular weight.

$g = 5H$.

## 7.1 Flow visualisation on the elastic instability

To avoid the effect of inertia, small Reynolds numbers ($Re = \rho H U_b/\eta_t << 1$) are required. The total viscosity ($\eta_t$) contains two contributions: the solvent dynamic viscosity $\eta_s = 274$ mPa.s (PEG+Water) and the polymeric viscosity $\eta_p = 68$ mPa.s (PEO+Water). This gives a factor $\beta = 0.8$ which is commonly chosen for benchmarks of Oldroyd-B model fluids [139] [2], [3].

$$\beta = \frac{\eta_s}{\eta_t} = 0.8 \tag{7.1}$$

The Weissenberg number ($Wi$),defined as $Wi = U\lambda/H$, compares the elastic forces to the viscous effects, where $H$ and $U$ are the channel height and bulk flow velocity, respectively, $\lambda$ represents the relaxation time, which is a viscoelastic fluid property (when fluid motion ceases the stress does not immediately become zero) [85].

Experimental flow visualisations provide a qualitative picture of the interaction between the two inlet streams (dyed and undyed), which will closely reflect the fluid mixing. Initially, we acquired 50 individuals images at a rate of 8Hz using the same apparatus described in 3.2.

### 7.1.1 Steady states

At low $Wi$ ($Wi < 1.9$), the velocity field is virtually unaffected by the polymer molecules, and the flow field is similar to the one in Newtonian fluids, which was previously demonstrated in chapter 5. Figure 7.1(a,b) shows averaged images which represent dye visualisation at different $Wi$. A distinct tilted interface between the dyed and undyed streams is observed, resulting from the opposed flows colliding at the stagnation point. There is indeed no significant mixing between streams at this range of Weissenberg numbers.

The effect of incrementally increasing the Weissenberg number from $0 \leq Wi \leq 1.9$ (depicted in figure 7.1) did not change the flow within the channel cross-section. The tilted fluid interface rotates anti-clockwise, making the interface line approach the vertical. As such, regarding the mixing, only purely diffusive mixing occurs at the interface between the two streams. In a cross-slot geometry, the highest streamline curvature occurs near the stagnation point, in which extensional flow dominates. High extension rate is also found near the corners due to the no-slip walls [108, 109]. Similarly, in a

[2] In a linear stability analysis with an Oldroyd-B model, the literature shows that one can qualitatively predict the onset and structure of the transitions observed in experiments performed with Boger fluids. [24, 92, 139]

[3] Discussion about numerical models for viscoelastic fluid flow simulations are beyond the scope of this thesis, although more details can be found in [27, 101, 102].

mixing-separating at low $Wi$ ($Wi < 1.9$), the extent to which polymers are deformed is barely noticeable. Although, at $Wi = 2$ (figure 7.1), the situation is very different. Time fluctuations could be seen in the flow field in mixing-separating device, and it could have been caused primarily by the polymers being stretched in either the extensional flow near the stagnation point and corners, or the shear flows near the walls.

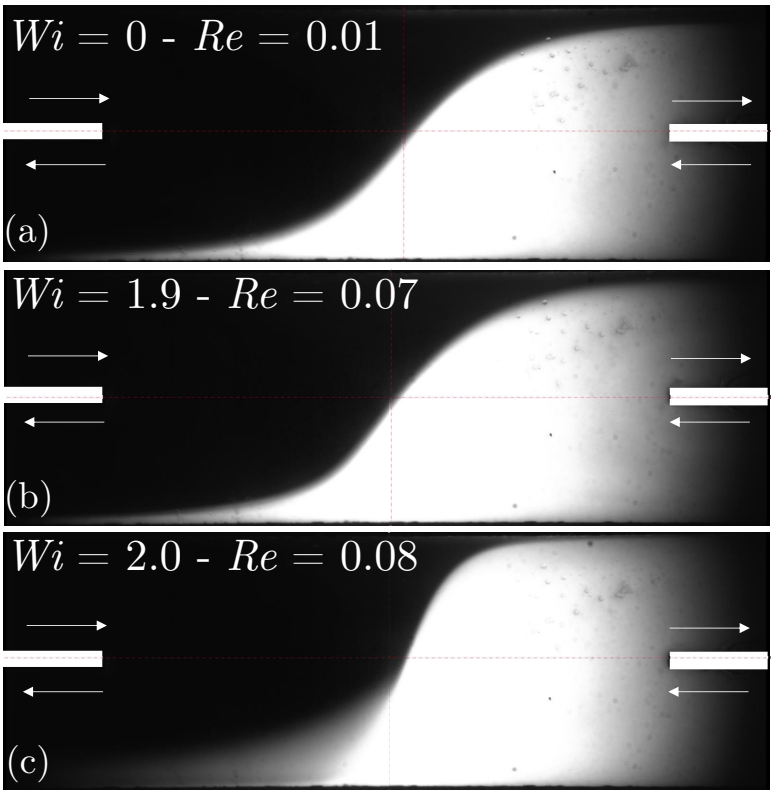


Figure 7.1: (a) Experimental Steady flow pattern for $Wi = 0$ using fluorescent dye (average over 50 images at 8Hz) (b) Steady flow for $Wi = 1.9$ (c) onset of flow fluctuations on time: $Wi = 2.0$

Figure 7.1(c) indicates the start of an instability with the onset at $Wi = 2.0$ (bifurcation point). Therefore, an in-depth investigation is required, and it would help to evidence this assumption.

### 7.1.2 Periodic flow

By using the same image processing technique previously used in section 5.1.2, the interface between the two streams can be located. The elastic instability can be evaluated by calculating the area formed between the two streams at the centre of the device. Therefore, we developed an algorithm to find the curve delineating both streams at the centre of the mixing-separating cell. Figure 7.2(a) shows the area, delineated by the red line, referring to the dyed stream ($\text{area}_{\text{light}}$). It can be noticed that the area is trimmed within the gap size. Moreover, the calculations include both streams, and then the undyed stream generates another area ($\text{area}_{\text{dark}}$).

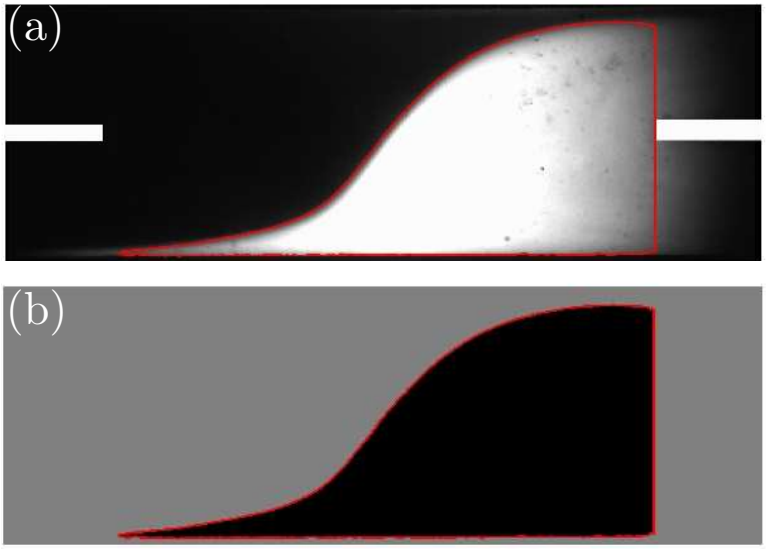


Figure 7.2: (a) Interface between the two fluid streams detected by the edge detection algorithm. (b) The algorithm calculates the area delimited by the red line in detail.

The algorithm returns a defined $N(t)$ parameter described as:

$$N(t) = \frac{\text{area}_{\text{dark}}}{\text{area}_{\text{dark}} + \text{area}_{\text{light}}}$$

$$N(t) \begin{cases} = 0.5 & \text{(symmetry)} \qquad \text{if } \text{area}_{\text{dark}} = \text{area}_{\text{light}} \\ \neq 0.5 & \text{(asymmetry)} \qquad \text{if } \text{area}_{\text{dark}} \neq \text{area}_{\text{light}} \end{cases}$$

which takes into account the ratio between areas filled by each stream, and therefore the symmetry. The temporal variation of $N$ with the Weissenberg number ($Wi$) represents a quantitative analysis of the temporal evolution of the effect of viscoelasticity on the flow near the stagnation point.

The system stays near the steady-state solution for a long time ($t < 15$s), before the small initial perturbation grows to a noticeable extent. Following, the instability parameter $N$ oscillates with increasing amplitude; then it reaches a limit. After that, the system fluctuates around the steady state with a quasi-fixed magnitude and frequency, i.e. it approaches a limiting cycle. Figure 7.3 shows the variation of $N$ with time for a fixed $Wi$ number after the system reached the amplitude limit. This clearly identifies the existence of a periodic flow.

As mentioned earlier, time-dependent instabilities have been observed in viscoelastic stagnation-point flows in both opposed-jet and cross-slot geometries. In particular, the study from Li and Graham [140] is very similar to the one reported in this study. The cases of symmetry break in a cross-slot geometry, experiments from Arratia et al. 2006 and simulations from Poole et al. 2007, there were no restrictions on the pressure at the boundaries, and a constant-flow rate constraint was applied at the flow

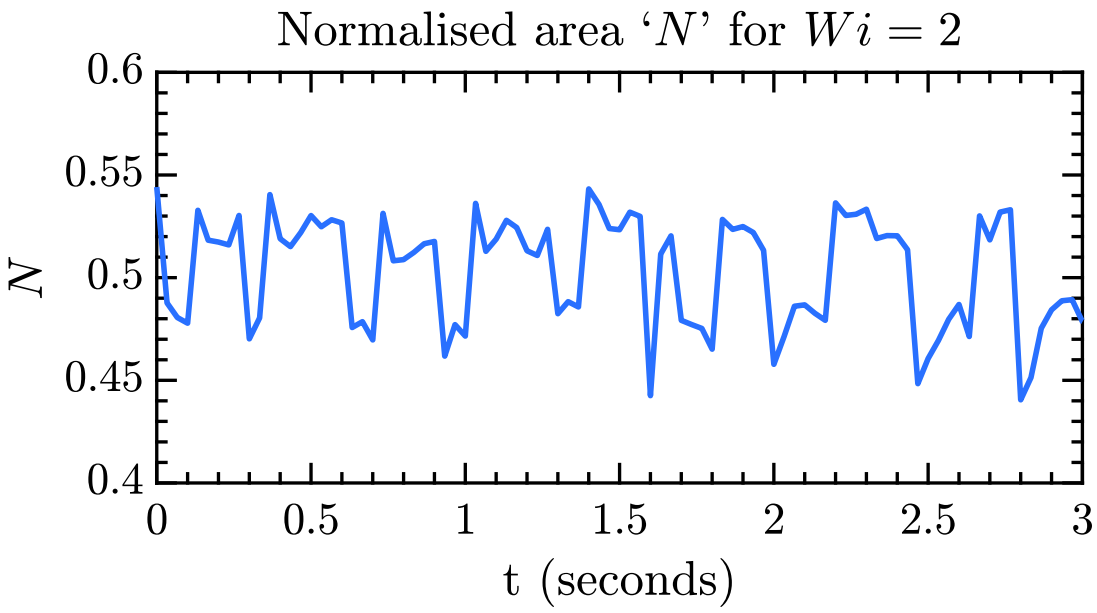


Figure 7.3: Temporal variations of the parameter $N$ for flow at $Wi = 2.0$ in the mixing-separating device.

entrances instead. In this study, we followed the same protocol, and we could observe a symmetry-breaking instability. According to the literature, the instability should occur at low values of $De$, which, in our case, refers to the low values of $Wi$ ($Wi_c = 2.0$).

## 7.2 Single-sided amplitude spectrum

The $N$ criteria chosen to captures the main phenomenological characteristics of the periodic oscillation seems to identify the periods in these investigations fairly. Although the choices of cutoff values are, to some extent arbitrary, we have found that changing these values within a reasonable range does not qualitatively affect the following discussion. Figure 7.4 shows the amplitude of $N$ in the temporal frequency domain $f = 1/T$ ($T$ is the period) for $Wi = 2$. A main peak is produced corresponding to a dominant frequency $f = 2.6$Hz close to the characteristic elastic frequency $f_e = 1/2\lambda = 4.2$. Interestingly, the higher amplitude peak is obtained with $f$ approaching the flow frequency $f_{flow} = U_b/L_c = 1.8$ (method adopted in the calculations from [109]). Such a finding suggests the possible existence of a resonant mechanism in which the main liquid elastic mode interacts with the periodic modulation of the geometry. The flow visualisation corresponding to this mode is smooth in space and weakly oscillating in time in a way that its changes are difficult to visualise on single snapshots and can be better appreciated in the videos provided within the supplemental material (see section A of the appendix).

At high frequencies, amplitudes do not drop suddenly to zero, but they undergo a slightly continuous decay. One could say that the results do not exclude the existence

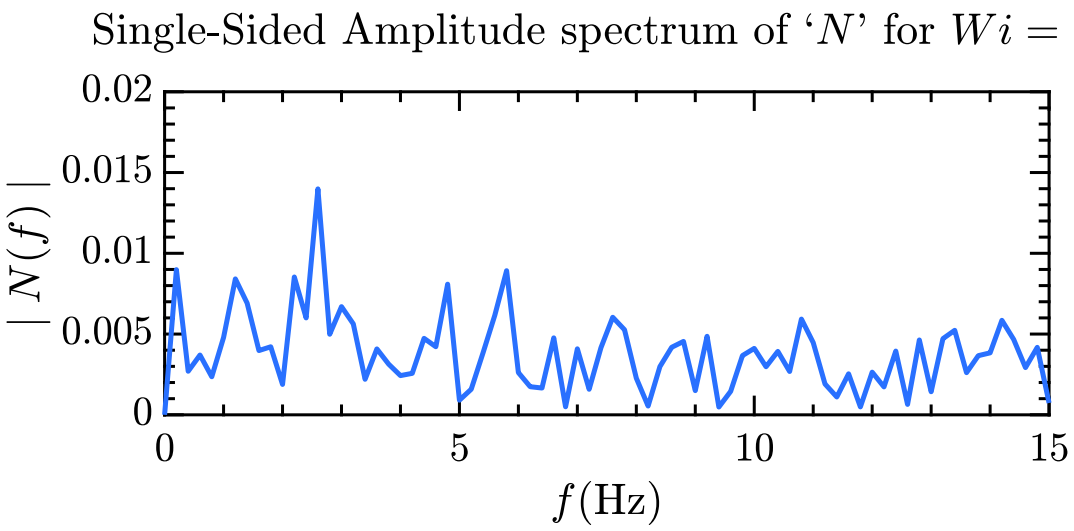


Figure 7.4: Single-sided amplitude spectrum of $N$ for flow at $Wi = 2.0$ in the mixing-separating cell.

of a spurious, resolution-dependent behaviour. Therefore, to reduce the high-frequency noise, it is necessary to exclude those frequencies of which we found to be an excellent compromise to maintain the same signal structure and reduce the high-frequency signal noise. Using a quasi-steady signal as a base, we calculate the high frequencies to be excluded from the periodic states. Figure 7.5 shows the amplitude of $N$ (denoted as the signal) as a function of time and frequency. For the time domain, we subtract the mean from the data. By removing the trend, we focus the analysis on the fluctuations in the data as a linear trend typically indicates a systematic increase or decrease. While trends can be meaningful, for the case of these analyses, removing the trend yields a better insight. In the frequency domain, we normalised the modulus of $N$ by the maximum amplitude of the absolute $N$.

Mathematically, what the FFT (more appropriately the discrete Fourier transform) extracts the components of a signal of finite length. Generally, for signal analysis, the FFT is used on signals of infinite length. Therefore, the detrending and windowing methods are ways to deal with the fact that we are approximating an infinitely-long signal with a finite-length one. Detrending removes the mean or linear trend. Windowing is a typical manoeuvre where the discontinuities at the beginning and end of the segment are gradually attenuated to zero and then lessening their effect on the spectrum. This is achieved by multiplying the spectrum by the chosen window. Figure 7.6(a) shows a Hann window in a rounded waveform, and a proposed mixed window (Hann/Rectangular with $r = 0.15$). The mixed window rapidly attenuates the edges of the signal to zero. If windowing is not applied, an abrupt cutoff at the edges of the signal, such as the impulse at the end of the segment. In summary, windowing the signal makes the approximation of a finite-length to an infinitely-long signal with as

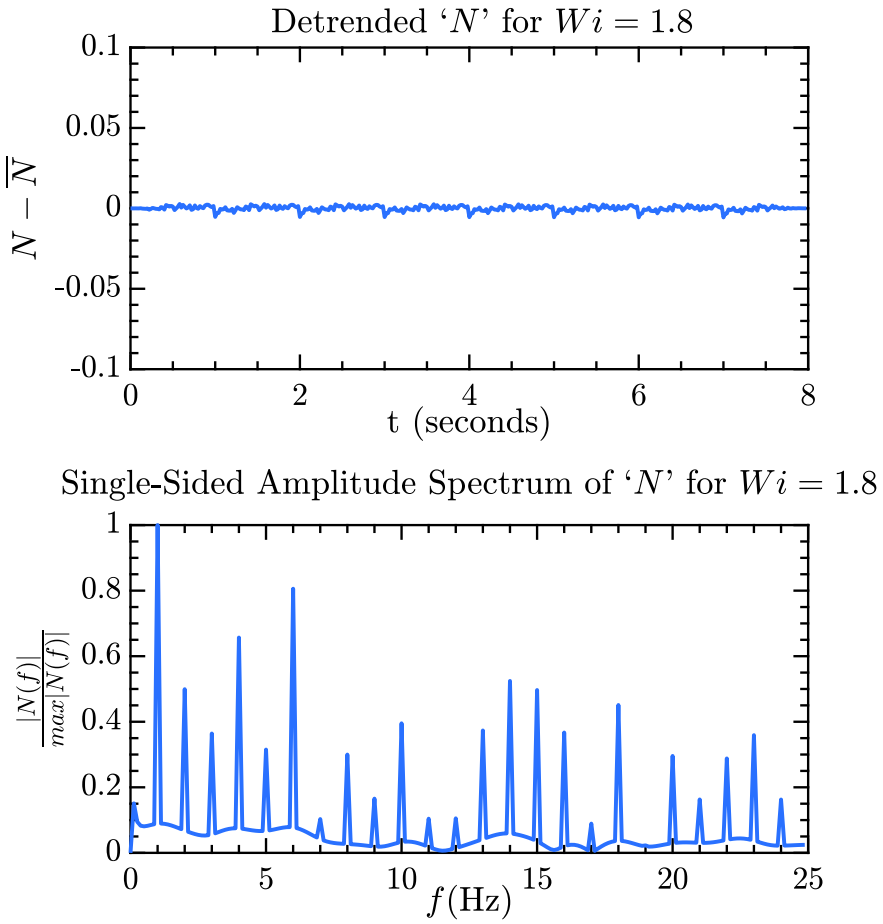


Figure 7.5: (top) Quasi-steady signal of $N(t)$ for $Wi = 1.8$ before the bifurcation ($Wi_c$). (bottom) FFT of the signal showing the high frequencies to be excluded from the periodic states when ($Wi > Wi_c$).

the DFT acts as the signal's N$^{th}$ data point overlaps to the first, making the DFT treat the data as a continuous signal. Figure 7.6(b-c) shows how the impulse at the end of the segment could introduce frequency components that interfere with the detection of the frequencies that represent the periodicity of the signal.

We have used the FFT algorithm on MATLAB$^{TM}$ to compute the fast Fourier transform (FFT) of the signals acquired during the experimental campaign. Essentially, the Fourier analysis converts a signal from its original domain (time, in this case) to a representation in the frequency domain and vice versa. The fluctuations of dye concentration, in our case represented by the $N$ parameter, show a periodic behaviour at low $Wi$, which is no longer observed when $Wi$ increases. Figure 7.7 presents the single-sided amplitude spectrum as a function of frequency computed from $N$ (area dye concentration) of some of the time series, which will be presented hereafter. In figure 7.7, for low $Wi$, the single-sided amplitude spectrum shows the presence of marked peaks, namely a fundamental frequency and some harmonics, as highlighted in the inset on figure 7.7. When $Wi$ increases (e.g. $Wi \leq 6$), the fluctuations of the $N$ progressively

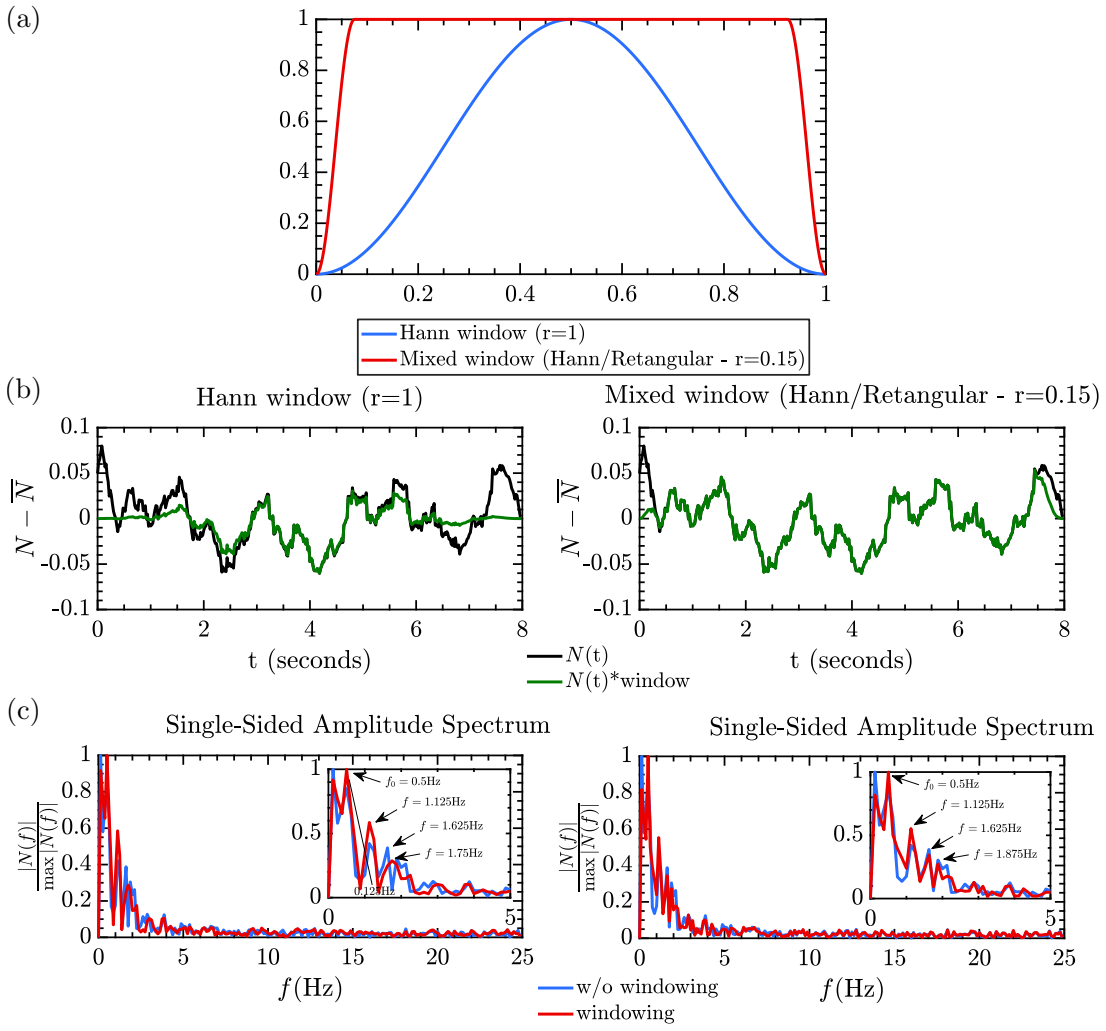


Figure 7.6: (a) An example of a Hann window in a rounded waveform, and a proposed mixed window (Hann/Rectangular with $r = 0.15$). Note that The mixed window rapidly attenuates the edges of the signal to zero. (b) Applying the windowing for the same example signal using two different windows from the figure above. (c) FFTs of the example signal with and without applying the detrending and windowing methods. The left represents the FFT applied with a Hann window method and Right the proposed mixed window (Hann/Rectangular with $r = 0.15$).

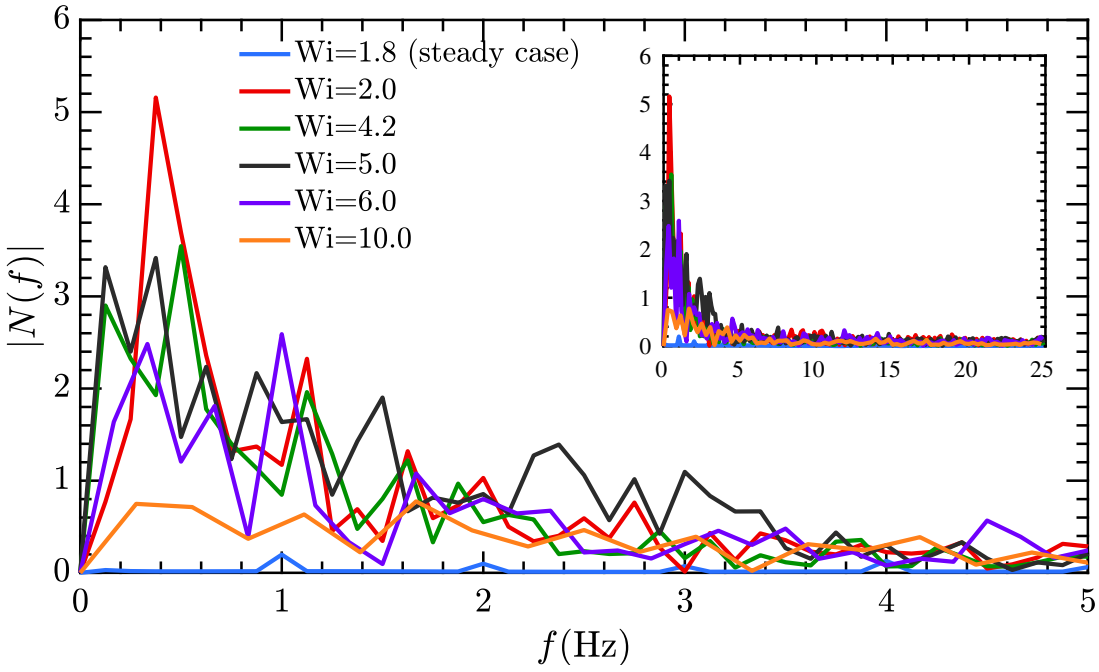


Figure 7.7: Single-sided amplitude spectrum of $N$ for flow at different $Wi$ numbers in the mixing-separating cell. The inset shows the full spectrum ($f < 25$) and the plot shows a zoom at the low frequencies ($f < 5$).

lose their typical sinusoidal behaviour but the amplitude spectrum still show the main frequency ($f_0$) but now with a broader distribution. As $Wi$ continues to increase ($Wi > 6$), the range of frequencies of the amplitude spectrum further broadens, and may even show broad frequency tails, eventually becoming a continuous distribution. It is important to note that when the amplitude spectrum becomes continuous, the decay with frequency is over at least three orders of magnitude for the flow conditions investigated experimentally. Note that in this study, sampling at 50Hz (maximum sampling rate) the highest frequency that can be analysed without introducing errors is 25Hz (Nyquist limit).

For all flow conditions explored with $Wi > 10$, the fluctuations along time of the $N$ parameter are visible, but the corresponding amplitude spectrum shows the absence of distinctive frequency peaks. Therefore, the fluctuations are shown to be aperiodic in time exhibiting a broad region of frequencies. No distinct characteristic frequencies are discernible in the amplitude spectrum for large values of $Wi$, and in this cases, it is possible to infer that the unsteady flow behaviour observed with the Boger solution is complex, although it is not necessarily in the elastic instability regime.

## 7.3 Purely elastic instability: periodic behaviour

The amplitude spectrum of the fluctuations of $N$ shows the presence of marked peaks, namely the fundamental frequency and some of harmonics. The time series of $N$ can

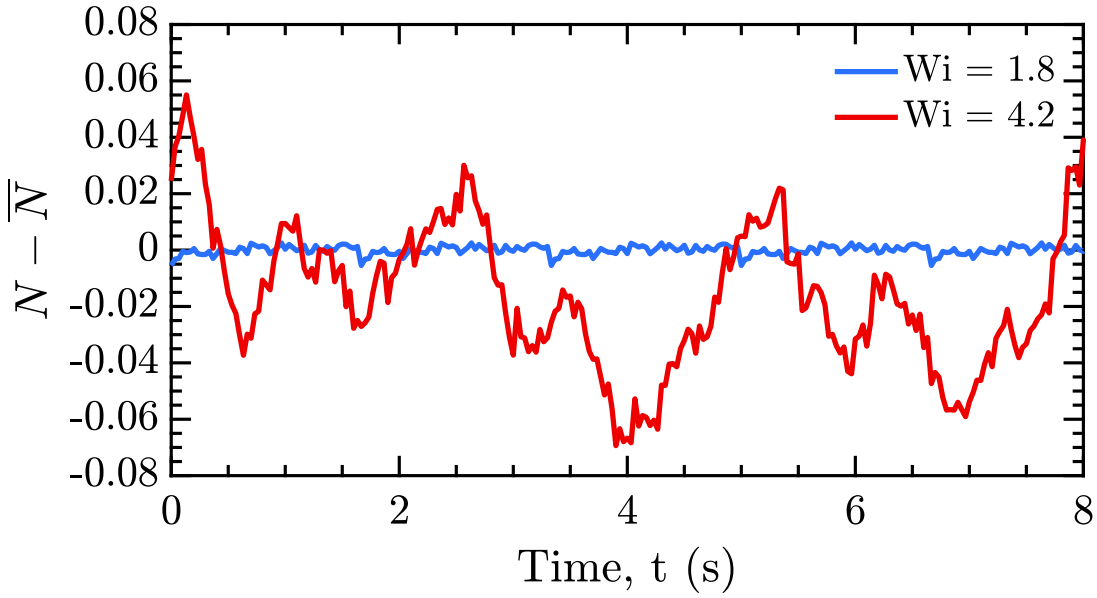


Figure 7.8: fluctuations on time of the quantity $N - \bar{N}$ before and after the onset of the instability at $Wi = 2.0$. Clearly, the amplitude of $N$ is higher when far from the onset (for instance, $Wi = 4.2$).

display this periodic, as illustrated in 7.8. The fluctuations of the dye concentration, represented by the parameter $N$, show a periodic behaviour at $Wi > Wi_c$. In figure 7.8, for $Wi = 1.8$, the viscous effects prevail over the elastic nonlinearities, and consequently, the flow is symmetric, and $N$ does not vary with time. The tiny fluctuations observed are due to noise in the signal measurements and represent less than 1% variation when compared to the maximum fluctuation in the region of $Wi > Wi_c$. After the onset of the first elastic instability ($Wi = 2$), we can observe flow instabilities, in which the flow field becomes asymmetric and periodic. Figure 7.8 shows that the frequency of fluctuation of $N$ is higher when increasing $Wi$ (for instance, the curve $Wi = 4.2$ in the figure).

Figure7.9 illustrates delimited area ($N$) in different time instants for the steady-state at $Wi = 1.8$ (left-hand side), and the periodic flow at a Weissenberg number higher after the onset of the instability, $Wi = 4.2$ (right-hand side). Time starts from an arbitrarily chosen snapshot on the periodic orbit at the central region near the stagnation point is shown. At the beginning of the cycle for $Wi = 4.2$, $N$ is negative as there is flow contraction at the region very close to the stagnation point (dyed stream), while the undyed stream is occupying a larger area in most of the gap region. As time goes on, a region of liquid moving downstream away from the stagnation point changes $N$ at different instants. This "wake" region of fluid at the stagnation point changes the sign of $N$, and a new cycle starts (figure 7.8).

Figure 7.10 shows the time series obtained by continuously temporal calculations of the $N$ parameter along the centre of the mixing-separating cell. At $Wi = 1.8$, the

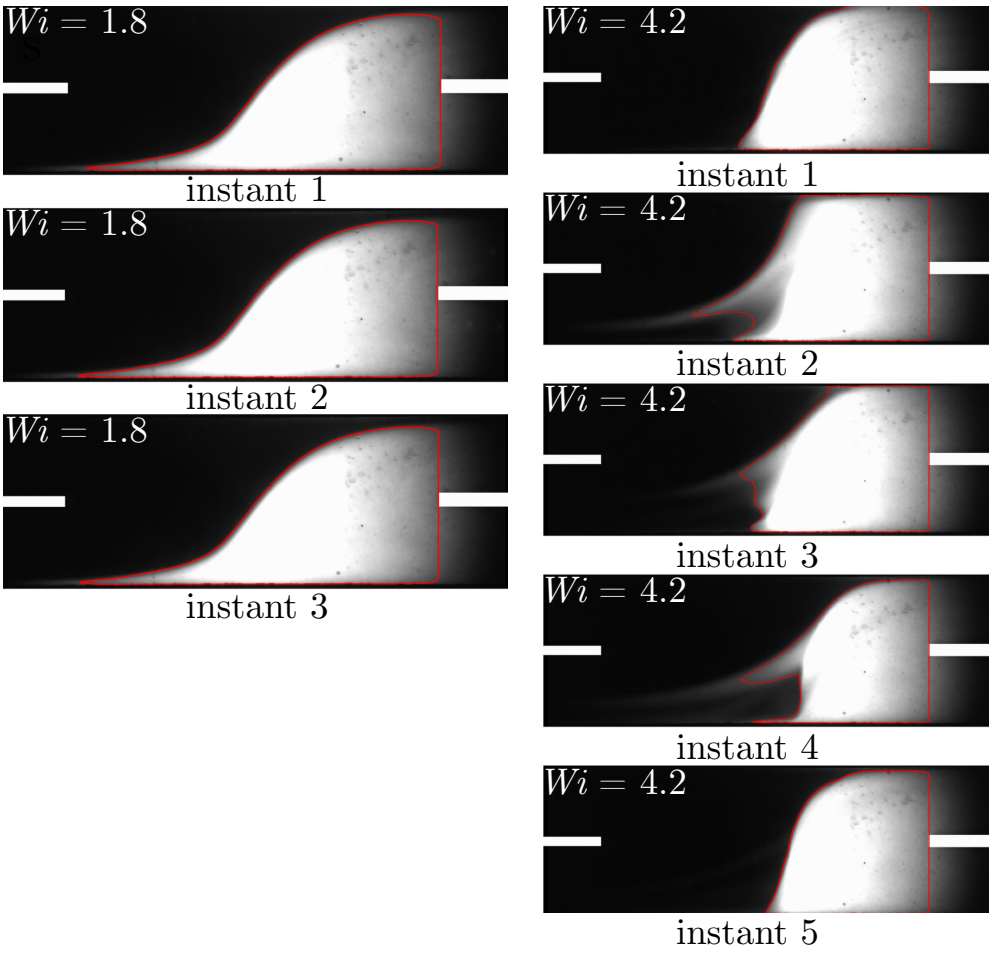


Figure 7.9: Experimental flow visualisation in the mixing-separating cell micro-geometry using fluorescent dye (Rhodamine-B) for different Weissenberg numbers ($Wi$). Red box delineating the interface between the two streams for calculations of the $N$ parameter. Figure shows different instants in time of the fluctuations when $Wi > Wi_c$.

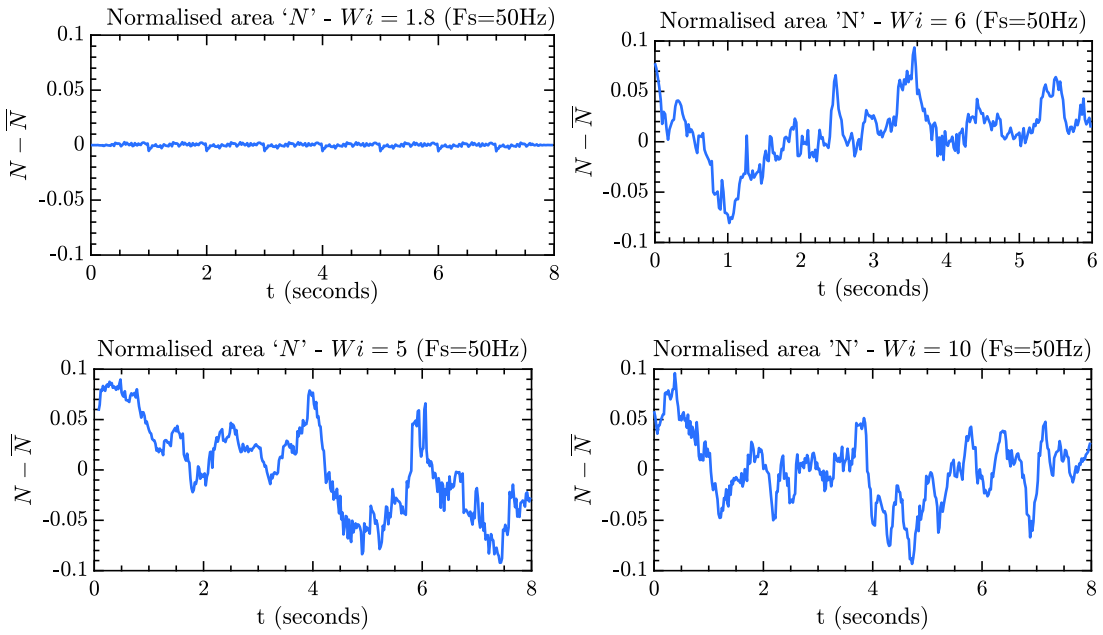


Figure 7.10: Temporal variations of the parameter $N$ for flow in the mixing-separating device at different Weissenberg numbers ($Wi$). Figure shows the variation of $N$ before and after the bifurcation ($Wi > Wi_c$).

steady-state case, the fluctuations are negligible. Although, when increasing $Wi$ above the onset of the elastic instability, elastic nonlinearities prevail over inertial effects and consequently that the observed flow instabilities are purely-elastic. The fluctuations along time of the $N$ parameter are clearly visible, and the corresponding amplitude spectrum (7.7) show distinctive frequency peaks and some harmonics, demonstrating that these fluctuations are periodic in time.

## 7.4 Supercritical instability: Hopf bifurcation

Figure 7.11 shows the root-mean-square deviations over one period of $N$ from its steady-state values, normalized by the corresponding steady-state values $N$, as a function of $Wi$ for all the cases where we found periodic flows. $N_{RMS}$ is define as follows:

$$\frac{N_{RMS}}{\bar{N}} = \frac{\sqrt{\frac{\sum_{i=1}^{n}(N_i - \bar{N})^2}{n}}}{\bar{N}} \tag{7.2}$$

Data points for $N_{RMS}$ obtained from our experimental results are fitted with a function of the form $a(Wi - Wi_c)^b$, with $b$ fixed at 0.5. Good agreement is found for our data with the 1/2 power law, characteristic of a supercritical Hopf bifurcation ([141, 140]). The critical Weissenberg number $Wi_c$ is identified to be 2.0 by this fitting.

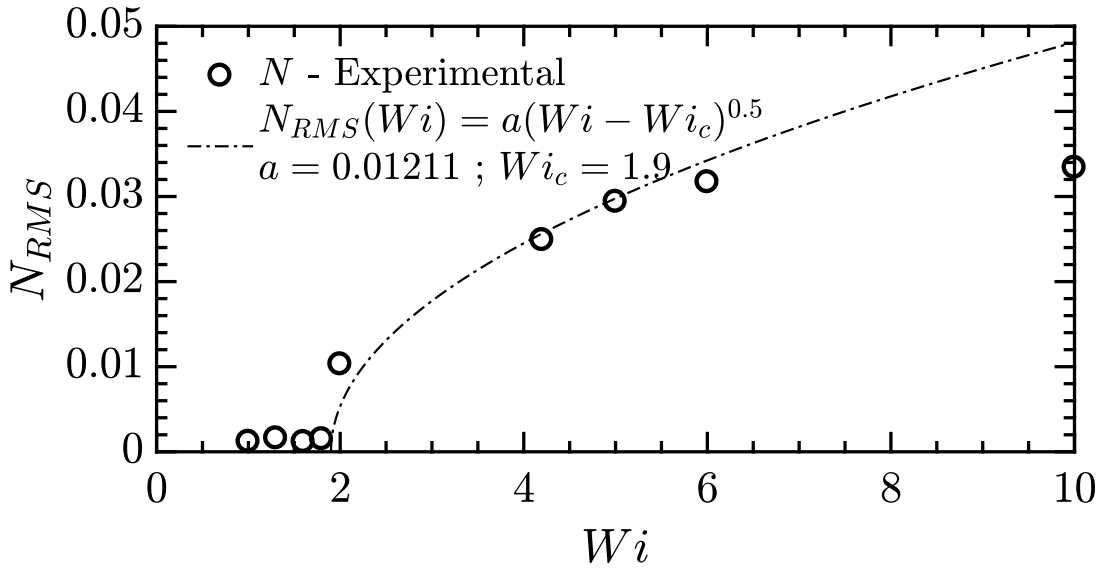


Figure 7.11: The $N_{RMS}$ when varying $Wi$ number for data points obtained from our experimental results. The data are fitted with a function of the form $a(Wi - Wi_c)^b$, with $b$ fixed at 0.5 (characteristic of a supercritical instability).

## 7.5 Summary

In summary, this chapter highlights the appearance of an elastic instability in the mixing-separating microfluidic device ($H$-geometry) when using a polymeric solution. Additionally, we present information regarding the onset ($Wi_c$), and we propose a quantitative analysis which showed the supercritical behaviour of this instability (characteristic of Hopf bifurcations).

Although we present an investigation of the time-dependent behaviour of this instability after bifurcation, the nature of these oscillatory events is yet unclear. How these events are triggered and what roles they play in the elastic instability processes will be necessary for further understanding the applicability in polymeric solutions. Therefore, as we believe that this instability could be helpful for various microfluidic applications, we will propose some further investigation later on chapter 9.

# Chapter 8

# Inertial instabilities in a cross-slot micro-geometry

The present chapter investigates the potential of utilising the inertial instability in the cross-slot micro-geometries to promote convective heat transfer at low Reynolds numbers. This is the first thermal characterisation and performance assessment of a device that has very significant potential thermal applications. Three-dimensional numerical simulations of the cross-slot geometry (see a schematic in figure 8.1) have been performed to clarify the effect of the purely-inertial flow instability on the heat transfer in the cross-slot micro-geometry [1]. The results are compared to the experimental temperature distributions measured by monitoring the fluorescence intensity using microscopy techniques with a temperature-sensitive fluorescent dye (Rhodamine-B) [2].

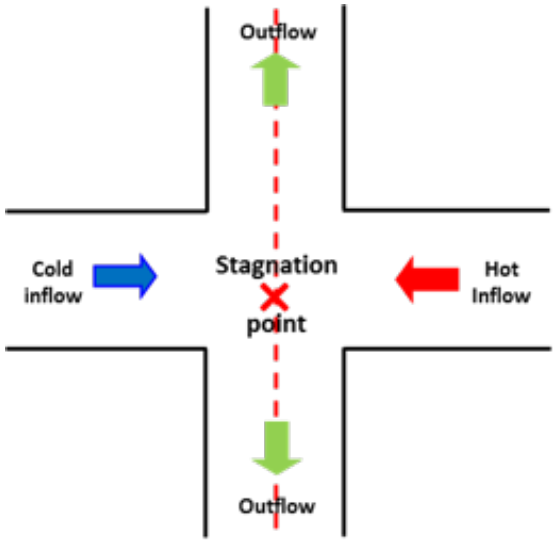


Figure 8.1: Schematic of a cross-slot device.

[1] Part of the results presented in this chapter was published in [40].

[2] The experimental results presented in this chapter were performed by Dr Waleed Abed during his Ph.D. in Liverpool using the same protocol described in chapter 3.

## 8.1 Experimental procedure

In this part, the idea is briefly outline the experimental boundary conditions adopted during Dr Waleed abed experimental campaign, and to give an overall idea about Dr Abed fluorescent-dye based microfluidic thermometry technique, also known as laser-induced fluorescence (LIF) [113, 116]. In the experimental work, the surfaces are considered to be adiabatic due to the material used to manufacture the cross slot rig, polyoxymethylene − an insulating material also known as ACETAL (density: 1.41 g/cm$^3$, melting point: 175 °C). The hot and cold fluid streams are injected into the cross-slot through the opposed inlets. Fundamentally, assuming no heat losses, the heat gained by the cold fluid stream must be equal to the heat rejected by the hot fluid stream. Therefore, the mean temperature at the inlet and exit should, under these ideal conditions, be equal. The average fluid temperatures were measured at the entrances ($T_{in,C}$ and $T_{in,H}$) and exits ($T_{out}$) in order to quantify any potential systematic deviation from the ideal conditions. The result shows that the average deviation of the non-dimensional mean temperature ($\theta$) from the ideal mean value with varying Reynolds number is 6%. Moreover, the parameter $\theta$ is always lower than the mean ($\theta = 0.5$) indicating a small amount of heat is lost by the fluid as it flows from inlet to exit.

Additionally, the experimental investigations in the cross-slot shows that the flow essentially behaves as the flow in a straight channel and any additional pressure loss due to the cross, even after the onset of the instability ($Re > 40$) is small and within the measurement uncertainties [3].

The working fluid used for the experimental measurements was a mixture of glycerine (relative density 1.26, ReAgent Chemical Services) and distilled water with a concentration of 70 per cent glycerine (by weight). The density and viscosity of the mixed solution were measured at the mean fluid temperature (the average fluid temperature between hot and cold inflow streams). A density meter (Anton Paar DMA 35N) with a quoted precision of 0.001 g/cm$^3$ was used for quantifying the fluid density. A rotational controlled-stress rheometer (TA Instruments Rheolyst AR-1000N) was utilised to measure the fluid viscosity using a 6 cm, 2° acrylic cone with a shear stress range from 0.02 Pa to 50 Pa (uncertainty in viscosity ±2% [142]). In addition, the specific heat capacity of the working fluid was estimated from textbook values [143]. The measured values of the density and viscosity are given in table 8.1.

[3] In-depth information about the experimental results obtained by Dr Waleed Abed investigations on the cross-slot can be found in [40] and also in his Ph.D. thesis.

Table 8.1: The measured values of density and viscosity for the working fluid.

| Temperature °C | Density kg/m$^3$ | Viscosity Pa.s |
|---|---|---|
| 20 | 1183.6 | 0.0226 |
| 24 | 1183.2 | 0.0186 |
| 28 | 1182.5 | 0.0154 |
| 32 | 1181.0 | 0.0131 |
| 36 | 1179.4 | 0.0116 |
| 40 | 1176.2 | 0.0097 |
| 44 | 1173.5 | 0.0085 |

## 8.2 Preliminary simulations

Preliminary simulations were conducted with identical conditions to the experiment where the reference values for the hot and cold inlet streams were $T_{in,H} = 48°C$ and $T_{in,C} = 20°C$ respectively. As the viscosity of the fluid varies with temperature, It was investigated the influence this would have on the results by fitting a Sutherland viscosity law of the form, $\mu = C_1 T^{3/2}/T + C_2$, to the experimental measurements of viscosity at various temperatures (measured using a rotational rheometer with temperature control). Figure 8.2 shows the relationship between temperature and viscosity, and the goodness ($R^2$) value of the fit was 0.9899. By running simulations using this relationship between viscosity and temperature and comparing them with the constant viscosity results, It was found to have a small quantitative effect on the results of the simulations, which were qualitatively unchanged. The critical Reynolds number of the bifurcation was completely unaffected by the variable viscosity.

Therefore, density and viscosity were assumed constant and equal to the experimentally measured values at the mean temperature (see table 8.1). The specific heat capacity and thermal conductivity were estimated to be 3098.9 J/kgK and 0.385 W/mK respectively [143]. The system was non-dimensionalised, such that arbitrary references values could be used, and it was found (as expected) that the non-dimensional system produced identical results to the simulations that matched the experiments for constant fluid properties. All further simulations were conducted with the arbitrary, non-dimensional system.

### 8.2.1 Temperature distribution

Both the experimental measurements and the numerical simulations provide a quantification of the temperature distribution and hence an understanding of the convective heat transfer in the cross-slot geometry. The experiments also provide a qualitative picture of the mixing of the two streams (dyed and undyed), which will closely reflect the temperature distribution if it is primarily determined by the fluid mixing. Figure

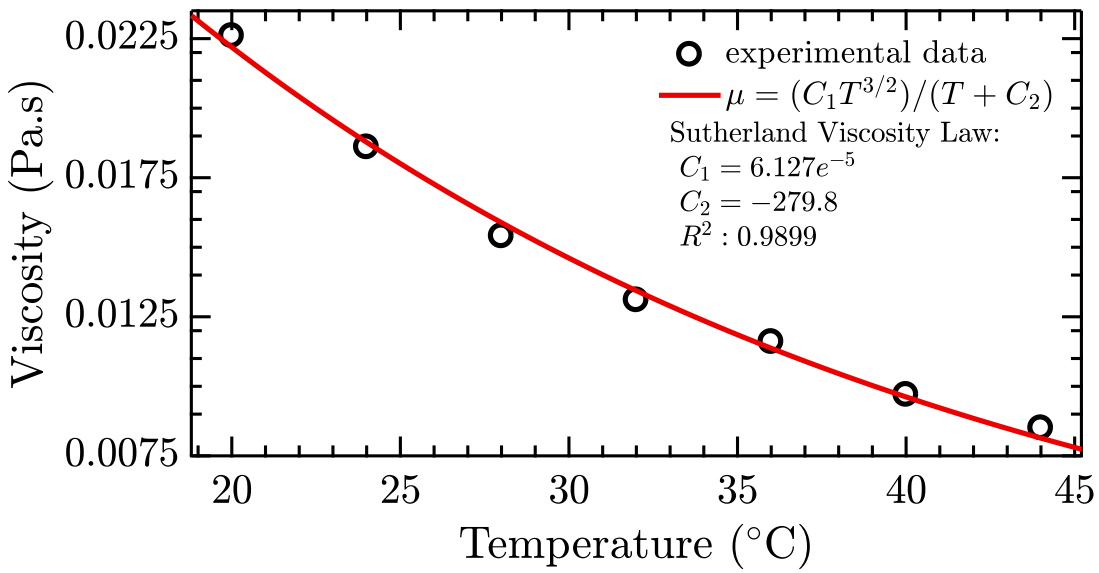


Figure 8.2: The relationship between temperature and viscosity fitting a Sutherland viscosity law.

8.3(a) shows images which represent dye visualisation for isothermal flow (both inlets at room temperature $21 \pm 0.5°C$), whilst the experimental and numerical temperature distribution patterns are shown in figures 8.3(b) and 8.3(c) respectively. These distributions are shown for the region where the two streams meet and also for regions $20d$ downstream of the stagnation point. The numerical temperature distribution in the cross-slot was computed through a half depth ($d/2$), i.e., top-down integral, of the channel and then compared with the experimental visualisation of the temperature-sensitive dye. The isothermal images for $Re = 36.6$ in figure 8.3(a) illustrate a distinct sharp symmetric boundary between the dyed and undyed streams at the stagnation point and this separation is also observable along the outflow channels, although the boundary between the two streams is not as sharp, indicating there is a small amount of diffusive mixing. There is certainly no significant mixing between streams at low Reynolds numbers and the flow appears steady, laminar and symmetric. As such, in terms of the heat transfer, only conduction occurs at the interface between the two streams. This is clearly shown in the experimental temperature patterns in figure 8.3(b), which shows two streams, one hot and the other cold, separated by a very narrow region where conduction occurs. Although some small variations are observed (particularly in the hot stream) they are primarily associated with the inaccuracy of the imaging technique rather than an indication of any significant heat transfer occurring. The experimental picture is reinforced by the equivalent numerical simulation in figure 8.3(c), which shows two sharply separated streams at very different temperatures and an extremely narrow region between the two streams where conduction occurs.

Figures 8.4 and 8.5 show the same as figure 8.3 but for Reynolds numbers equal

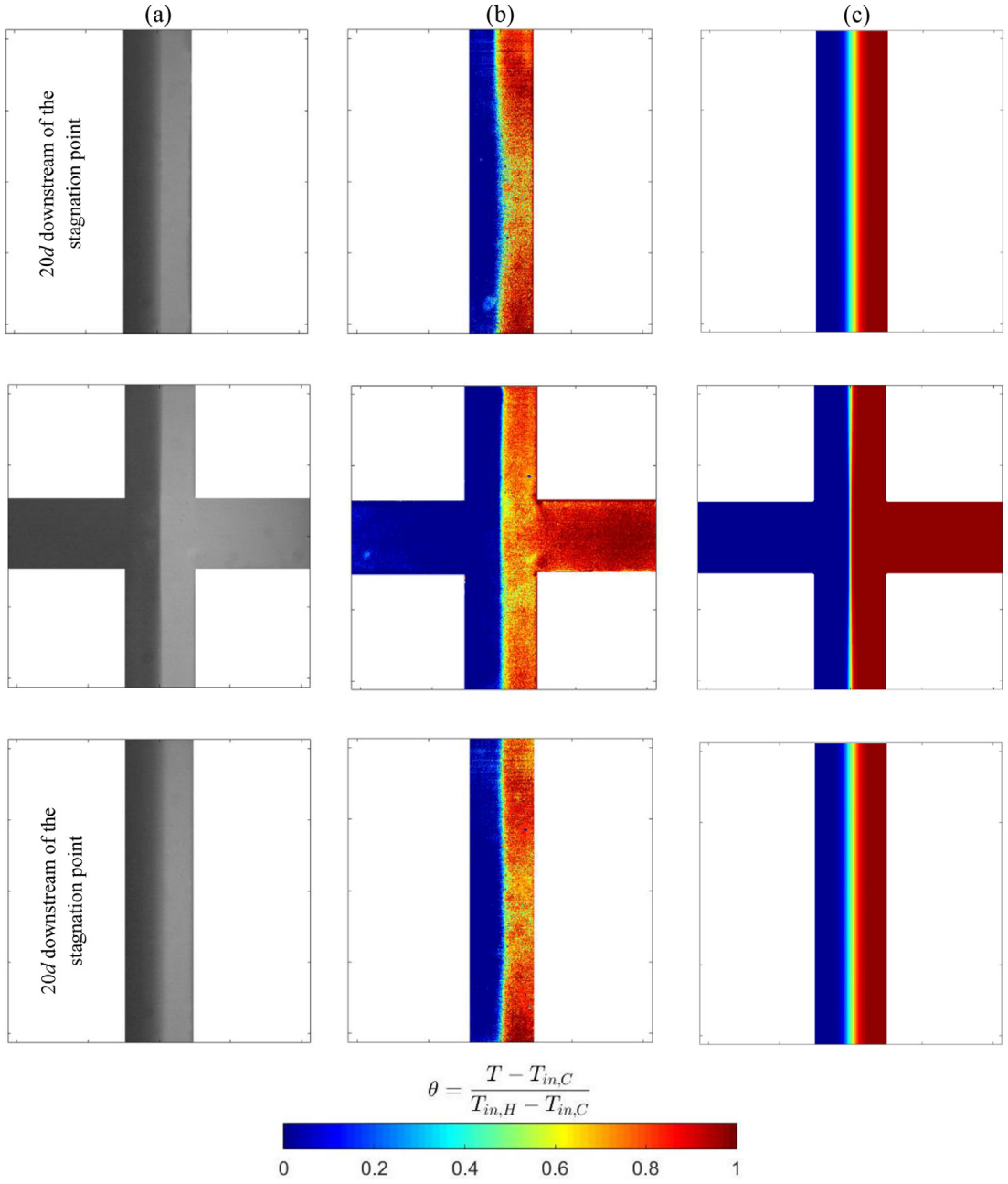


Figure 8.3: Symmetric flow and temperature distribution patterns in the cross-slot micro-geometry, at the centre of the cross-slot and $20d$ downstream of the stagnation point in each outlet arm for $Re = 36.6$. (a) Grayscale images illustrating the development of isothermal flow structure (b) Experimental visualisation of the temperature-sensitive dye and (c) Numerical temperature distribution.

to 46.3 and 80.6, respectively. When the Reynolds number increases beyond a certain critical value ($Re > 40$) [7], it is known that a symmetry-breaking bifurcation occurs and an axially-oriented spiral vortex is created along the outflow channels. This is apparent in the images in figures 8.4(a) and 8.5(a) as this spiral vortex promotes the mixing process in the cross-slot. The two streams are now much less distinct after they have met and the dye through the outlet arms is much more uniform than it was for $Re = 36.6$.

Convective heat transfer also arises between the hot and cold fluids as shown in figures 8.4 and 8.5(b, c). The three-dimensional behaviour of the bifurcated flow enhances the heat transfer between the hot and cold fluids by convection along the outflow channels. For $Re = 46.3$ the experimental temperature distribution still shows some signs of two distinct hot and cold streams, but they are clearly much less distinct than at $Re = 36.64$. The two streams appear more distinctly in the simulations, although it is still observable that some convective heat transfer has occurred. Where the two streams meet it appears that the cold stream is 'dominating' over the hot stream. In reality, in this case, the hot stream has been swept underneath the cold stream and therefore, due to the visualisation technique, it is seen less prominently.

The experiments at $Re = 80.6$ in 8.5(b) show an increasingly even temperature distribution, whereas, although the simulations in figure 8.5(c) still show two streams, greater mixing is noticeable. In particular a similar temperature distribution pattern is observed in the experiments and simulations for $Re = 80.6$ where the two streams meet at the centre of the cross. It is clear that the single central vortex is dominating the flow and entwining the two streams. Overall both the experimental and numerical temperature distributions indicate that the heat transfer is enhanced by the presence of the spiral vortex, but there are clearly some qualitative and quantitative differences.

To quantitatively assess the enhancement of heat transfer in the outflow arms of the cross-slot, histograms of normalised temperature are constructed for the symmetric ($Re = 36.6$) and asymmetric ($Re = 46.3$ and $Re = 80.6$) flow regimes using the experimental images and numerical data corresponding to the FOV $20d$ downstream of the stagnation point. Figure 8.6 shows the probability density functions (PDFs) of this normalised temperature distribution ($\theta$). As illustrated from figure 8.6(a), two peaks are observed in both the experimental and numerical data around $\theta = 0$ (which corresponds to the cold inlet stream temperature) and $\theta = 1$ (which corresponds to the hot inlet stream temperature) for the symmetric flow regime ($Re = 36.6$). This is because there is a clear separation (no mixing) between the hot and cold streams along the outflow channels. There is a quantitative difference between the experiments and simulations in that the peaks in the experimental data are not as distinct. This difference can be attributed to the accuracy of the captured images using the temperature-sensitive fluorescent dye with the digital camera and heat losses. Qualitatively, however, below the

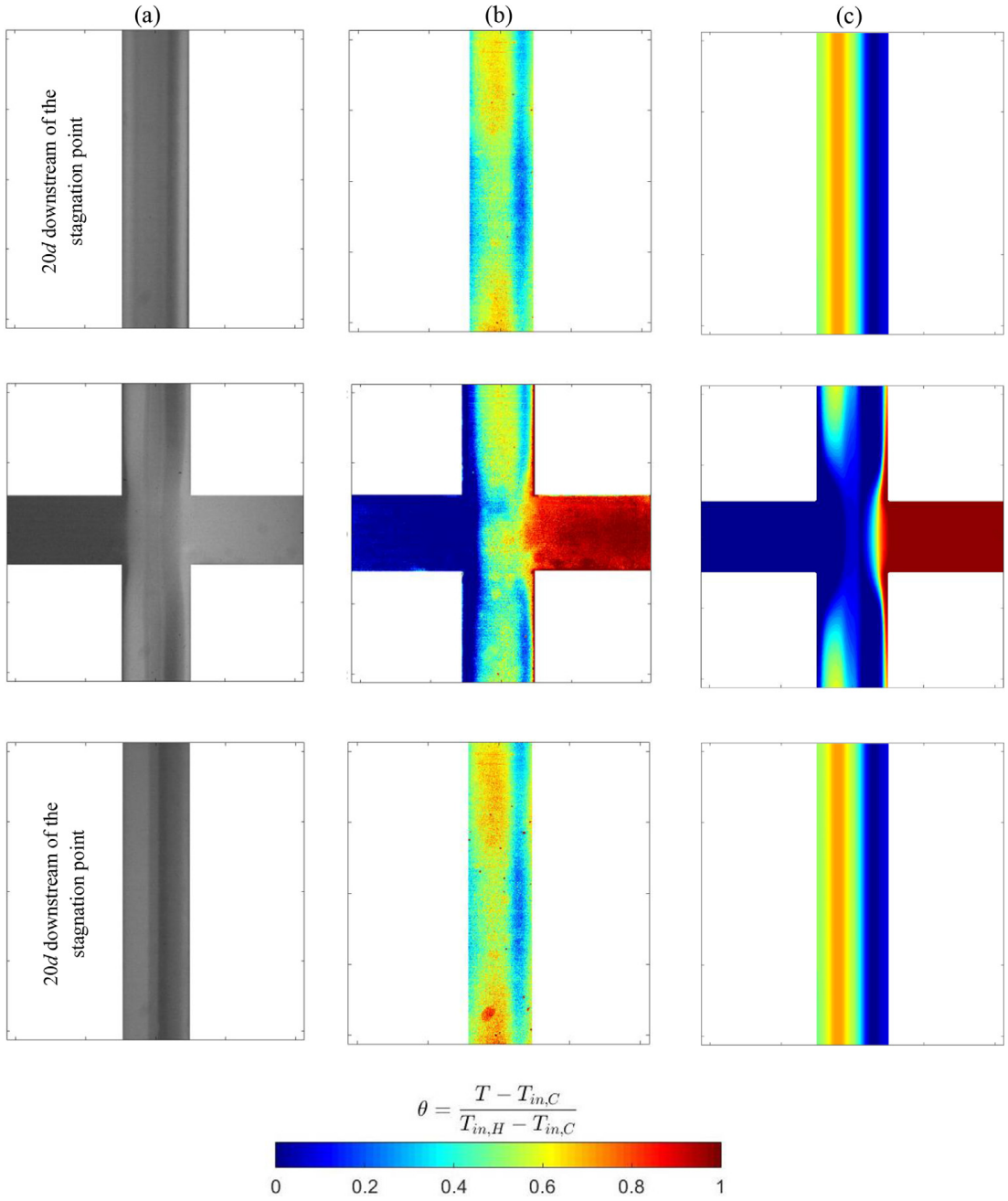


Figure 8.4: Asymmetric flow and temperature distribution patterns in the cross-slot micro-geometry, at the centre of the cross-slot and $20d$ downstream of the stagnation point in each outlet arm for $Re = 46.3$. (a) Grayscale images illustrating the development of isothermal flow structure (b) Experimental visualisation of the temperature-sensitive dye and (c) Numerical temperature distribution.

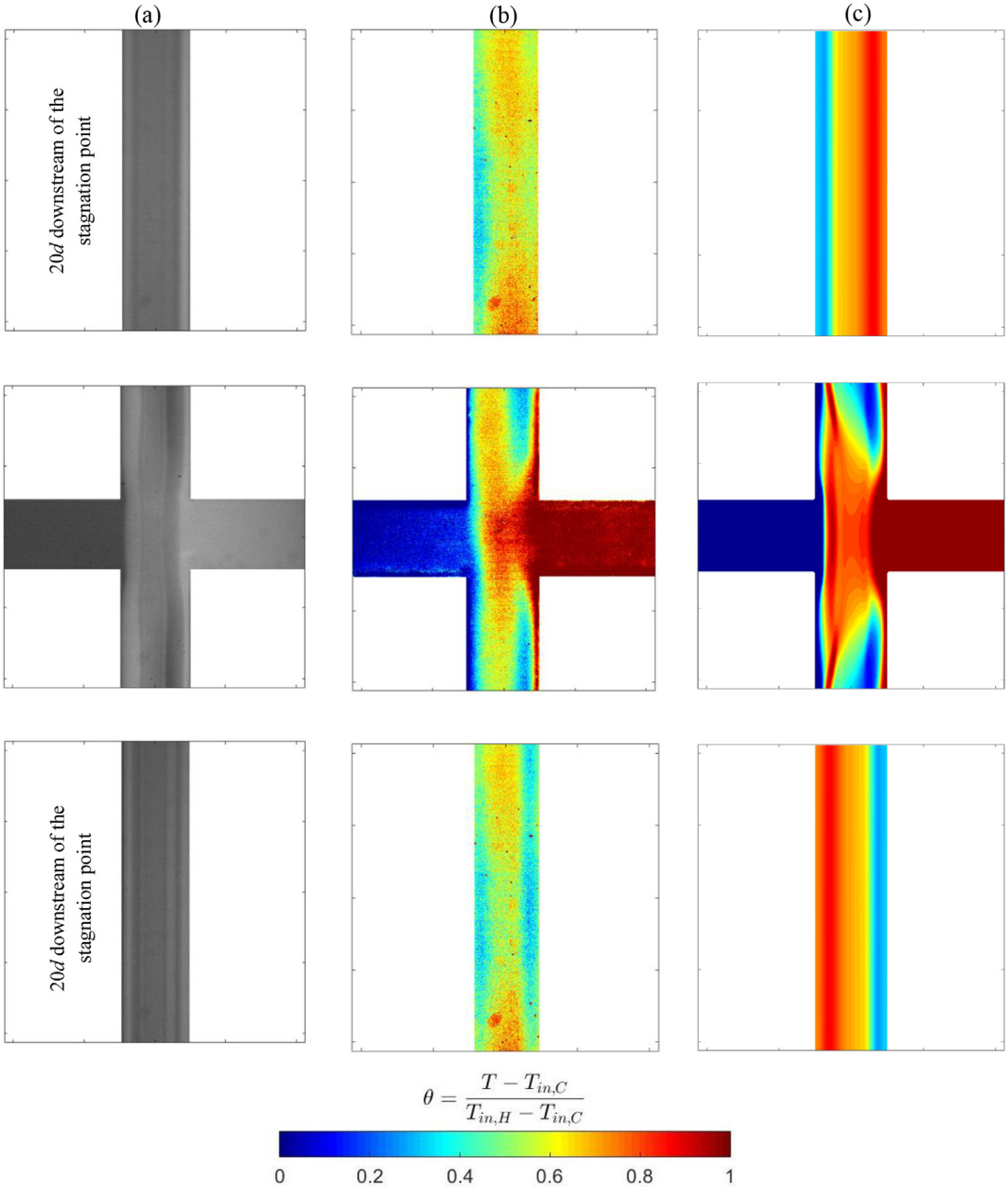


Figure 8.5: Asymmetric flow and temperature distribution patterns in the cross-slot micro-geometry, at the centre of the cross-slot and $20d$ downstream of the stagnation point in each outlet arm for $Re = 80.6$. (a) Grayscale images illustrating the development of isothermal flow structure (b) Experimental visualisation of the temperature-sensitive dye and (c) Numerical temperature distribution.

critical Reynolds number, the temperature distribution from experimental and numerical data shows a reasonable agreement. Also included in figure 8.6 are simulations using a temperature-dependent viscosity, which are found to produce rather similar results to the constant viscosity simulations. Although there are small quantitative differences they are not as significant as the differences between the experimental and numerical results and therefore do not explain this discrepancy (which can be attributed to the experimental technique).

The histogram in figure 8.6(b) for the asymmetric flow is dramatically different to the symmetric flow with far more occurrences of average temperature values and far fewer at the extremes of hot and cold. This demonstrates the improved mixing and heat transfer between the hot and cold streams that the instability provides. This effect is seen even more clearly in the asymmetric flow regime at $Re = 80.6$ where the distribution of the normalised temperature from the experiment resembles a Gaussian distribution with its peak at approximately $\theta = 0.6$ as shown in figure 8.6(c). This indicates that because of the convective mixing between the hot and cold streams the temperature distribution has been significantly altered towards a more uniform distribution (which would be $\theta = 0.5$ throughout the channel by definition). In fact, there are virtually no values corresponding to either $\theta = 0$ or $\theta = 1$, showing that the extremes of temperature have been eliminated, which is in stark contrast to the symmetric flow regime. The normalised temperature from the numerical simulations shows an approximately flat distribution except at the extremes of temperature, which occur much less frequently, as depicted in figure 8.6(c). Although the simulations show that the temperature is not as uniform as seen in the experiments it is still apparent from this flat distribution that the spiral vortex has had a significant influence and the distribution is much more uniform than in the symmetric case.

Examination of the temperature distributions (shown in figure 8.7) also demonstrate that the effect of a viscosity variation with temperature is not large. However, it is possible to discern some differences between the two distributions in figure 8.7. These differences can be highlighted by plotting the variation of temperature along the centre of the cross ($x = 0$), which is shown in figure 8.8. It is clear that when a variable viscosity is used the cold stream penetrates slightly further into the cross and the temperature in the central region of the cross is a little higher. Although there are clear quantitative differences they are relatively small ($< 10\%$) and do not affect the conclusions at all. In particular they do not explain the discrepancies between the experiments and simulations as shown in figure 8.6, where it is compared the histograms of temperature for the simulations (with and without variable viscosity) with the experiments. It is seen that, although there is a small difference between the two sets of simulations, the difference in the experimental results is still much more pronounced, which can be attribute to the experimental technique for capturing the temperature

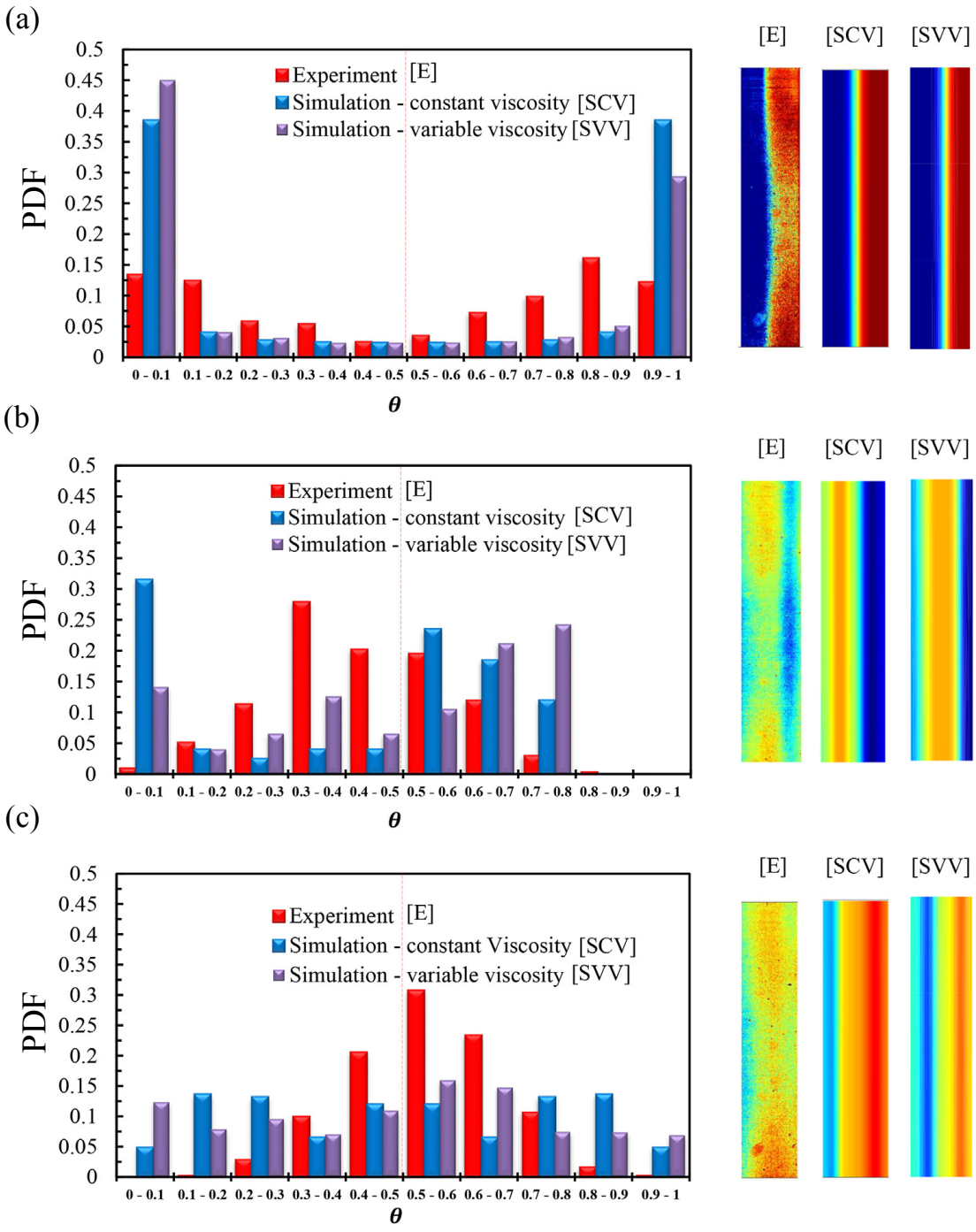


Figure 8.6: Experimental ([E], in red), simulation with constant viscosity ([SCV], in blue), and simulation with temperature dependent viscosity ([SVV], in purple) probability density function (PDF) for the normalised temperature ($\theta$) in the FOV $20d$ downstream of the cross-slot centre: (a) symmetric flow regime ($Re = 36.6$), (b) asymmetric flow regime ($Re = 46.3$), and (c) asymmetric flow regime ($Re = 80.6$). Right hand side shows temperature distribution, $20d$ downstream of the cross, to highlight data on which PDFs are based. See figures 8.3, 8.4, and 8.5 for colour map values.

distribution.

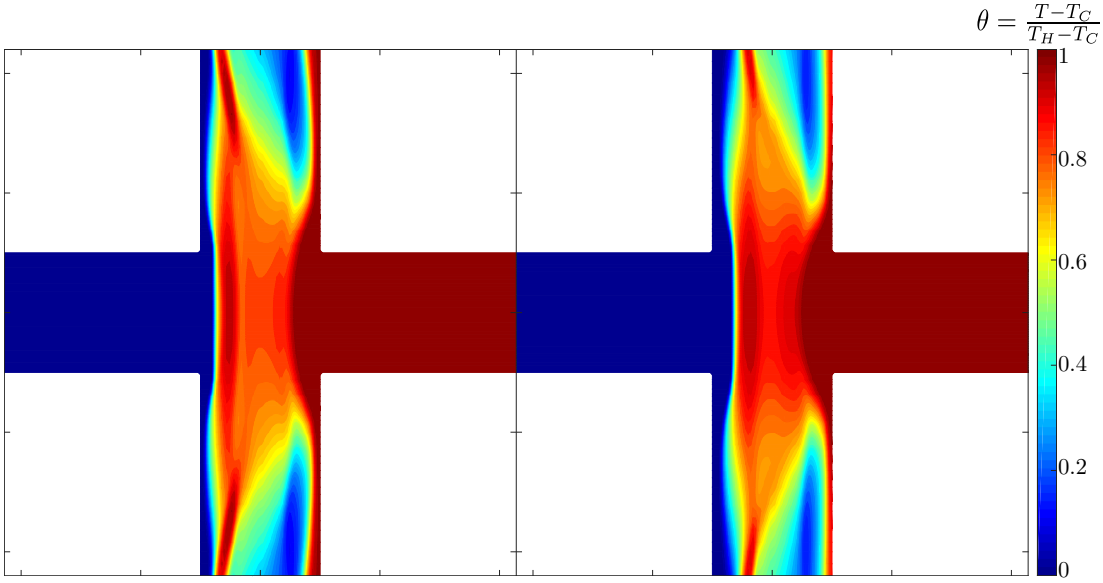


Figure 8.7: Constant viscosity (left) and variable viscosity (right) temperature distributions at $Re = 80.6$

The difference between the experiments and the simulations can be attributed to the imaging method, as stated previously. It is to be expected that a flow visualisation technique gives an indication of the overall flow pattern and temperature distribution, but not necessarily accurate quantitative results, whereas the numerical simulations give quantitative predictions. Indeed comparing figure 8.6(a) with figure 8.6(b) and (c) shows that both the symmetric and asymmetric flows are perceived to be more uniform in the experiments than in the simulations. Given that the effective baseline ($Re = 36.6$) is more uniform in the experiments it can be no surprise that the altered conditions ($Re = 46.3$ and $Re = 80.6$) are also more uniform as it is a result of the technique employed. However, the Reynolds number trend is broadly similar in the experiments and simulations and both demonstrate the positive effect the spiral vortex has on heat transfer.

### 8.2.2 Hysterisis

The results of the numerical simulations at very low Reynolds number show that the flow remains steady and symmetric. However, at Reynolds number of approximately 40, based on average velocity, a steady bifurcation is observed beyond which the symmetrical flow is replaced by an asymmetrical flow. Two sets of numerical simulations were carried out by firstly simulating at very high $Re$, well beyond critical conditions and then by reducing the Reynolds number in small steps near to the critical condition to evaluate the transitional point from asymmetric to symmetric flow and secondly by starting at clearly stable conditions and steadily increasing the Reynolds number to

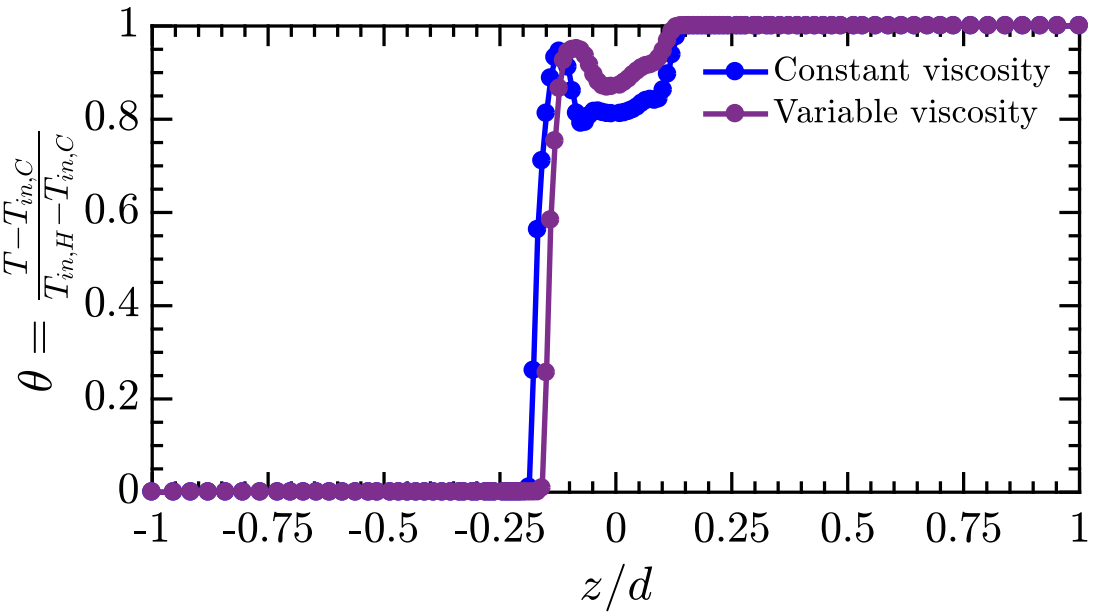


Figure 8.8: Normalized temperature ($\theta$) variation along the line $x = 0$ for constant and temperature-dependent viscosity at $Re = 80.6$

observe the transition from symmetric to asymmetric flow. As shown in figure C.2, a non-zero value for the normalised transverse velocity ($w$) along the centreline $y = 0$ at the $y$-$z$ outlet plane is used to indicate asymmetric flow. The differences between figures C.2(b) and C.2(c) show the effect of initial conditions on the simulations. In particular the flow remains symmetric up to $Re = 53$ when $Re$ is increased, whereas the symmetry does not return until $Re = 39$ when $Re$ is decreased. Thus, the symmetry-breaking bifurcation in this case is a subcritical pitchfork in agreement with Haward et al. [40].

Figure 8.9 presents the maximum values of the normalised transverse velocity ($w_{max}/U_b$) along the centreline $y = 0$ at the $y$-$z$ inlet plane of the outlet arm of the cross-slot for different Reynolds numbers. Two solution branches exist between $Re = 39$ and $Re = 53$ clearly demonstrating that the system is hysteretic.

Also depicted in figure 8.10 is a comparison of the temperature contours (discussed already in detail in section 4.3) which show that an increase of Reynolds number beyond the critical value leads to a more uniform temperature distribution due to convective mixing and heat transfer. The distributions shown for $Re = 46.3$ are for the decreasing $Re$ branch as the instability has clearly occurred. The solution branch that is stable up to $Re = 53$ cannot physically be achieved in the laboratory experiments, presumably because the disturbances inherent in the experiment (e.g. from fluctuations in the inlet velocity or geometric disturbances) are too large for the flow to remain stable/symmetric.

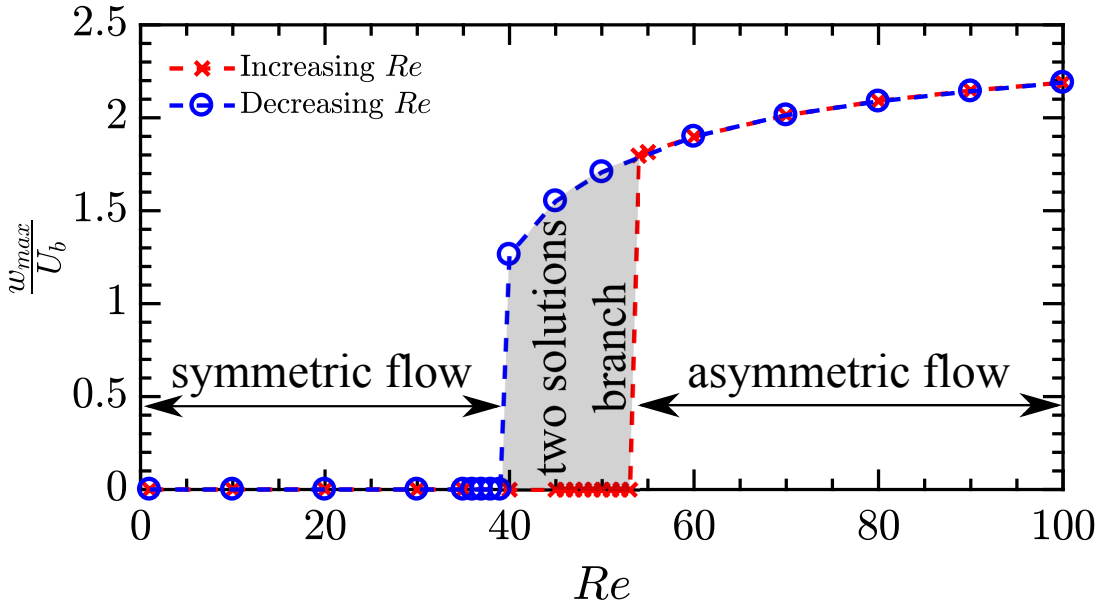


Figure 8.9: The maximum transverse velocity ($w_{max}/U_b$) along the centerline ($z = 0$) of the inlet to the outlet arm with increasing and decreasing Reynolds number. The critical Reynolds numbers ($Re_c$) are 39 when increasing $Re$ and 53 when decreasing $Re$.

## 8.3 Estimation of the heat transfer enhancement

### 8.3.1 Simulations with adiabatic walls

As a Nusselt number cannot be calculated for this set-up (as the mean temperature at any cross-sectional plane downstream of the cross is constant from energy conservation), the root-mean-square of the temperature ($T_{RMS}$) is used to evaluate the heat transfer between the two different streams within the outlet channel of the cross-slot micro-geometry under the adiabatic walls condition ($C1$). This enables us to quantify how effectively the asymmetric, convective flow regime can improve heat transfer when compared with the symmetric flow regime. As previously noted in figure 8.9, the flow becomes asymmetric above a critical Reynolds number ($Re > 40$). In order to obtain symmetric cases beyond the critical $Re$ a quarter cross-slot was simulated and symmetry was imposed as the boundary conditions to avoid the instability, therefore ensuring the flow is always symmetric, even at $Re > 40$. It is important to note that poor heat transfer between the two streams is characterised by high values of $T_{RMS}$ as enhanced heat transfer will work to make the distribution more uniform and therefore reduce the $T_{RMS}$. Figures 8.11, 8.12, and 8.13 shows the results for $T_{RMS}$ for several Reynolds number and three Prandtl numbers ($Pr = C\mu/k$) in the outlet channel of the cross-slot and also in a quarter-geometry (symmetry-imposed). The $T_{RMS}$ versus an inverted non-dimensional Graetz number, $Gz^{-1} = x/(dRePr)$, is used to show the behaviour along the length of the outlet channel in different flow conditions. The enhancement

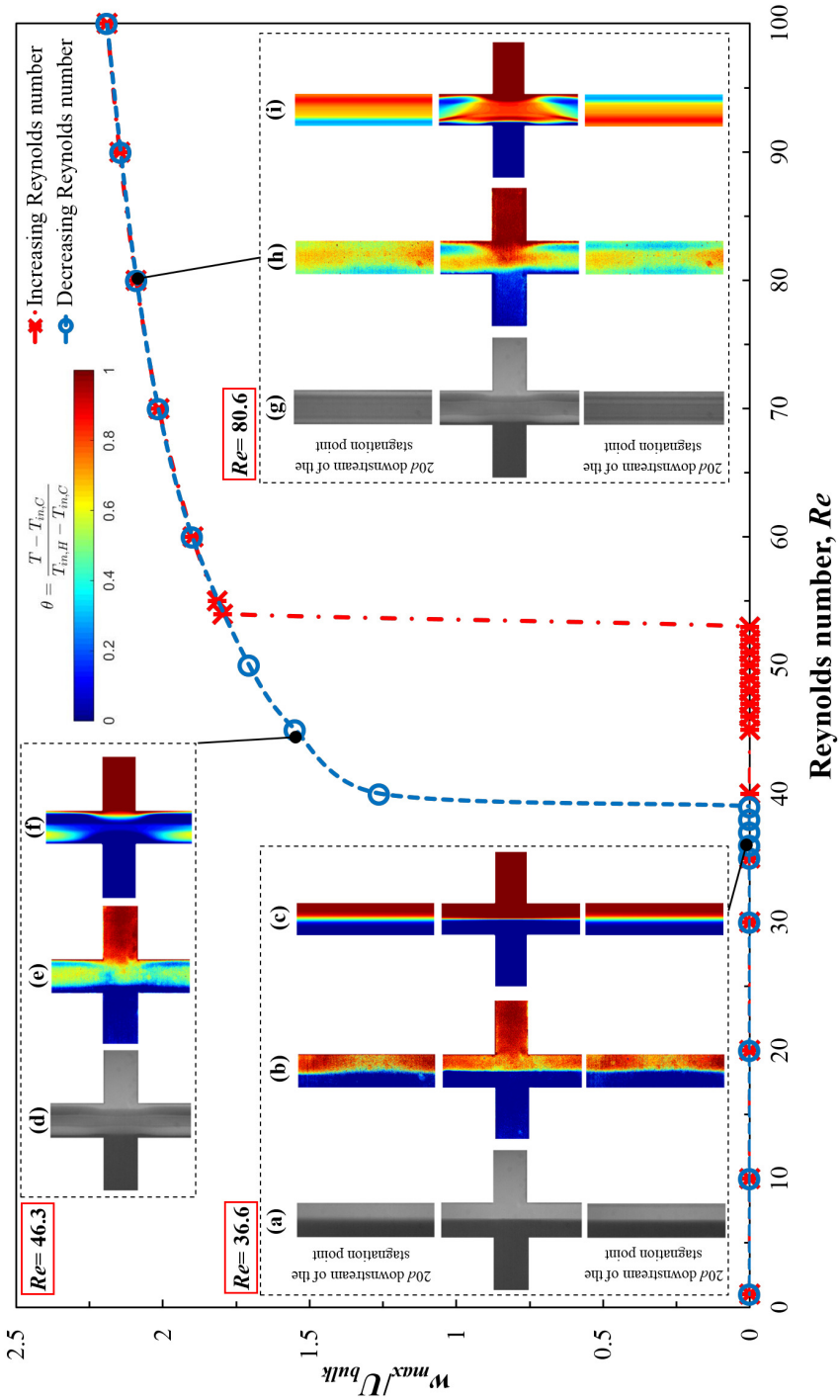


Figure 8.10: Maximum transverse velocity ($w_{max}/U_b$) along the centerline ($z = 0$) with increasing and decreasing Reynolds number. Insets (a, b, c) from figure 8.3 where $Re = 36.6$, (d, e, f) from figure 8.4 where $Re = 46.3$, and (g, h, i) from figure 8.5 where $Re = 80.6$.

of the heat transfer is evaluated by dividing the $T_{RMS}$ values for the asymmetric case by the corresponding $T_{RMS}$ values for the symmetric case at the same $Gz^{-1}$ number. Therefore, figures 8.14, 8.15, and 8.16 present the ratio of $T_{RMS}$ for the asymmetric case to the $T_{RMS}$ for the symmetric (symmetry-imposed) case.

It is readily seen that the $T_{RMS}$ for symmetry-imposed cases collapse for the entire Reynolds number range and there is no effect of Prandtl number. This is due to the dominance of diffusion/conduction in all cases of the symmetric flow situation (the temperature contours at figure 8.3(c) show the high segregation of the flow field). In contrast, the asymmetric cases show significant variations with both $Pr$ and $Re$. For $Re_c < Re < 70$ (see curves: red for $Re = 40$, green for $Re = 45$, and black for $Re = 50$ in figures 8.11, 8.12, and 8.13), heat transfer is enhanced by the instability for all $Pr$ numbers and the trend with $Re$ is monotonic in that increasing $Re$ increases the heat transfer enhancement (see figures 8.14, 8.15, and 8.16).

For $Re > 70$ (see curves: purple for $Re = 70$ and yellow for $Re = 100$ in figures 8.11, 8.12, and 8.13), although heat transfer is enhanced with respect to the symmetric case, it deviates from the monotonic trend with $Re$ at high $Pr$ and $Gz^{-1}$. In fact, for $Pr = 10$ and $Pr = 100$, a $Re$ of 50 gives superior heat transfer performance far downstream of the cross centre than $Re = 70$ and $Re = 100$. Closer to the cross centre this is not the case and the monotonic trend with $Re$ can still be observed. We therefore suppose that the unusual behaviour at $Re = 70$ and $Re = 100$ is due to a hydrodynamic development length effect (from the centre of the cross) related to the decay of the axially-oriented spiral vortex formed by the instability. At low $Re$ the decay of the vortex will be dominated by diffusion and this length will be constant (proportional to $d$ and independent of $Re$), at high $Re$ ($Re > 200$) the decay length will be set by a convective length scale (scaling like $\approx Re = 1$). At intermediate Reynolds number ($10 < Re < 200$) the decay of the vortex, or the development length of the flow back to a fully-developed exhibits a mixed scaling [120].

Moreover, as there is no other mechanism that creates transverse velocity ($w$) except for the vortex, by plotting the bifurcation parameter $w_{max}/U_b$ versus $Gz^{-1}$ (as shown in the figure 8.17 for $Pr = 10$), it is clear that the vortex intensity drops rapidly at a certain $Gz^{-1}$ indicating a transition from a convective to a conduction dominated regime. For the higher Reynolds numbers with the unusual behaviour ($Re = 70$ and $Re = 100$) this occurs at a lower $Gz^{-1}$. This indicates that the point at which the vortex is largely eliminated has a non-trivial relationship to $Re$, which the scaling with $Gz^{-1}$ does not fully resolve. However, this would only be of primary concern for very long outlet arm lengths. After the vortex has been eliminated conduction dominates and it is seen that the $T_{RMS}$ curves start to converge and the heat transfer enhancement plateaus and then starts to drop ($Pr = 100$ has not reached this point, but it would be expected at higher $Gz^{-1}$). In the extreme case where the length of the channel tends

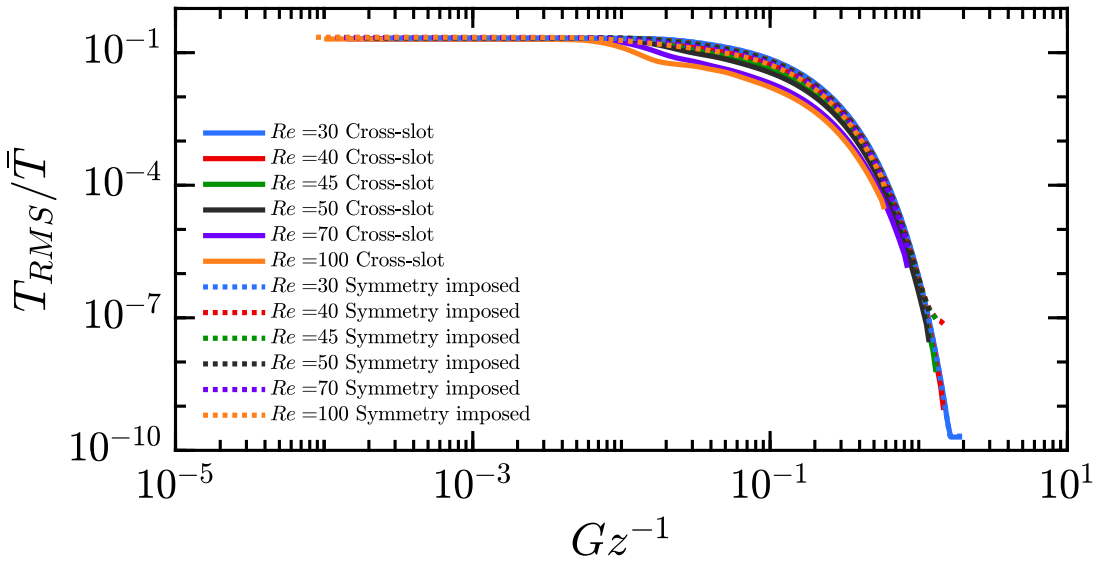


Figure 8.11: Normalised $T_{RMS}$ (Eq. 4.11) as function of inverted Graetz number, $Gz^{-1} = x/(dRePr)$, for various Reynolds number ($Re$) and $Pr = 1$ Prandtl number. Dashed curves represent symmetric cases; solid curves lines represent asymmetric cases.

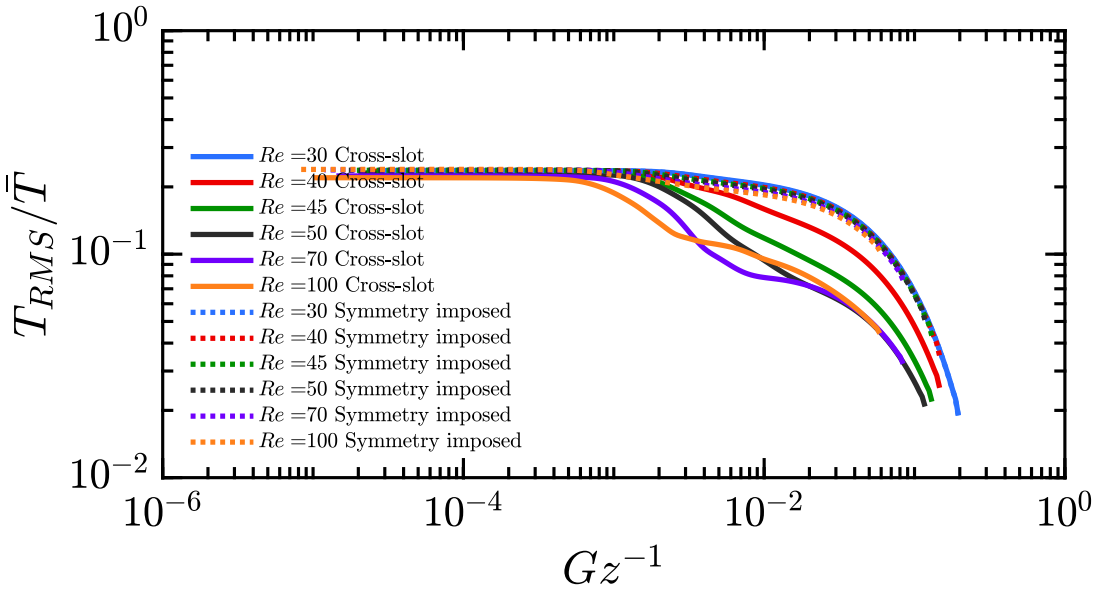


Figure 8.12: Normalised $T_{RMS}$ as function of inverted Graetz number, $Gz^{-1}$, for various $Re$ and $Pr = 10$. Dashed curves represent symmetric cases; solid curves lines represent asymmetric cases.

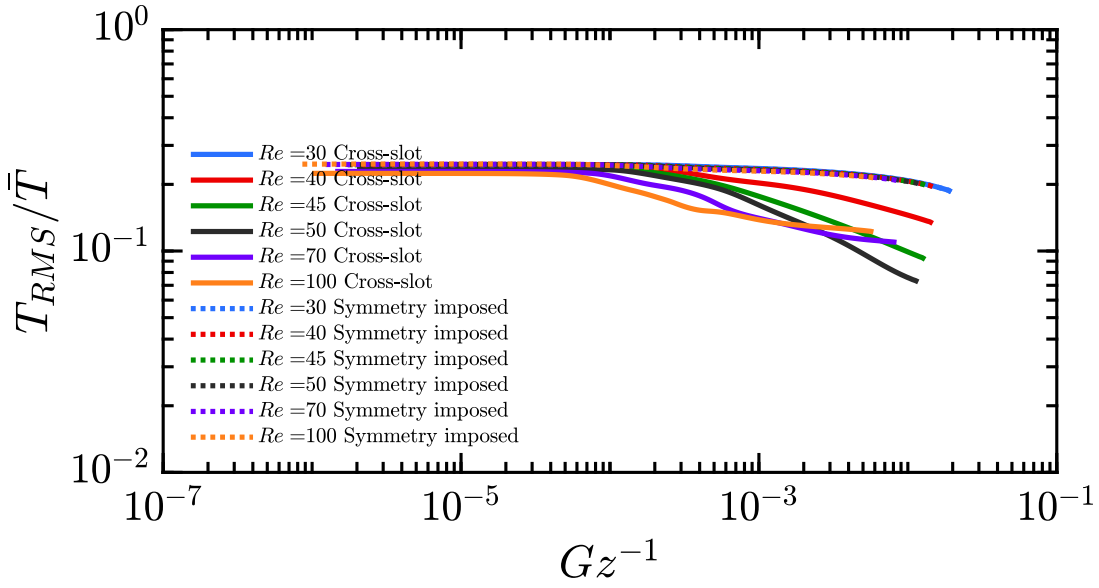


Figure 8.13: Normalised $T_{RMS}$ as function of inverted Graetz number, $Gz^{-1}$, for various $Re$ and $Pr = 100$. Dashed curves represent symmetric cases; solid curves lines represent asymmetric cases.

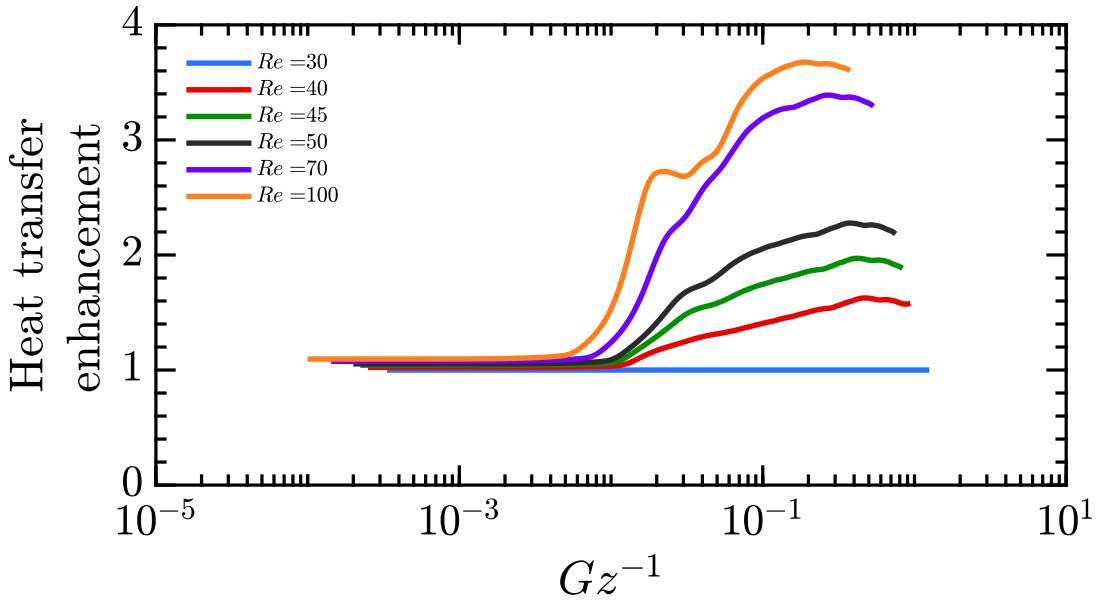


Figure 8.14: Heat transfer enhancement, representing the $T_{RMS}$ ratio calculated between the asymmetric and symmetric cases for $Re$ and $Pr = 1$.

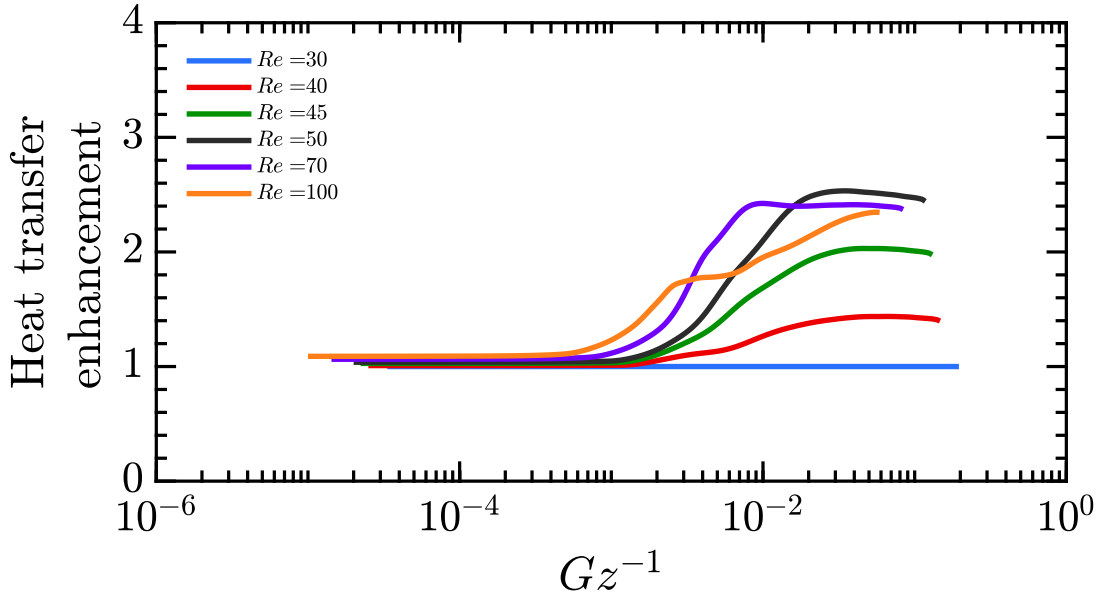


Figure 8.15: Heat transfer enhancement, $T_{RMS}$ ratio between the asymmetric and symmetric cases for $Re$ and $Pr = 10$.

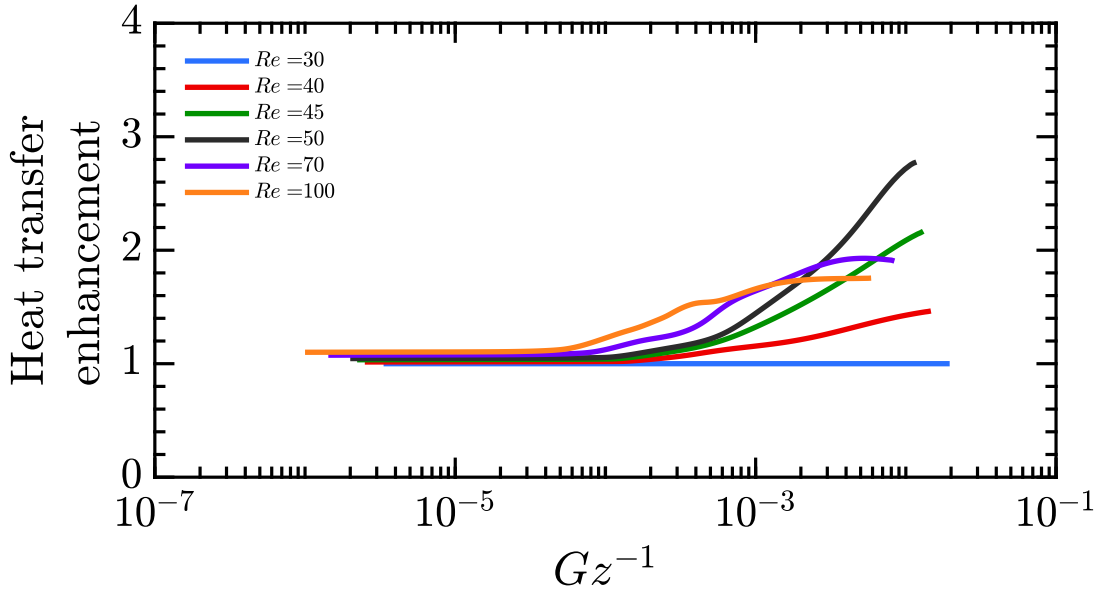


Figure 8.16: Heat transfer enhancement, $T_{RMS}$ ratio between the asymmetric and symmetric cases for $Re$ and $Pr = 100$.

towards infinity the flow would approach uniformity such that $T_{RMS}$ would approach zero and the enhancement measure would be unity (i.e. no enhancement). However, the advantage of the instability is that it can provide a much higher level of heat transfer in a relatively short channel.

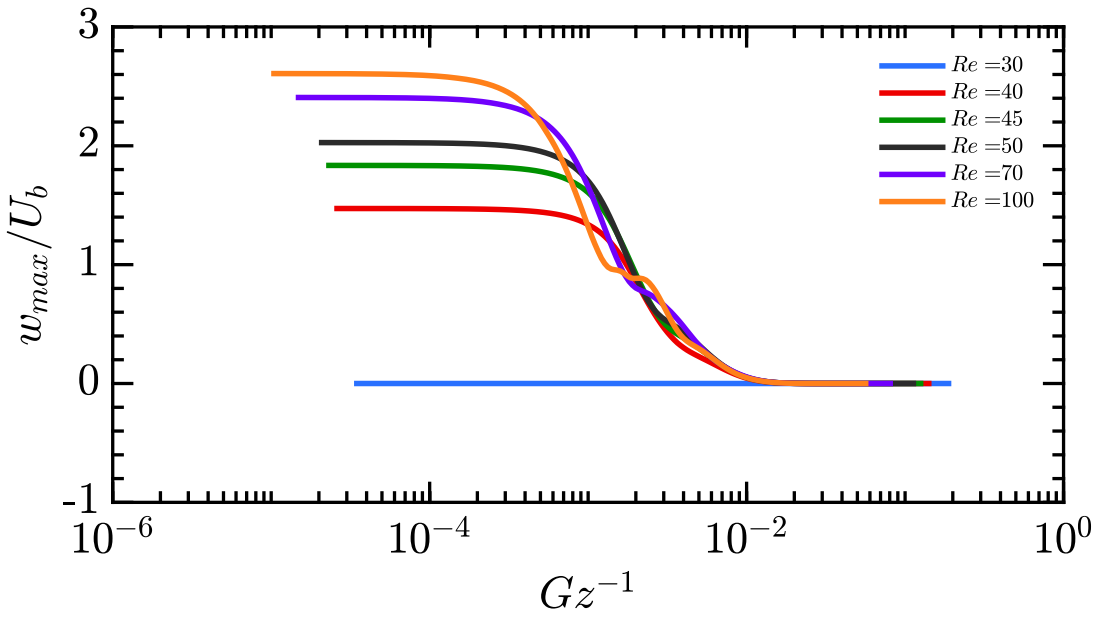


Figure 8.17: The evolution of the bifurcation parameter, maximum transverse velocity ($w_{max}/U_b$), with varying $Gz^{-1}$ along the outlet channel for $Pr = 10$.

For convenience, the inverted non-dimensional Graetz number ($Gz^{-1}$) was used to show the behaviour along the length of the outlet channel in different flow conditions. Clearly, the advantage of the instability is that it can provide a much higher level of heat transfer in a relatively short channel. This instability can be usefully employed to enhance mixing, and figures 8.18, 8.19, and 8.20 show the root-mean-square of the temperature ($T_{RMS}$), used to evaluate the heat transfer between the two different streams within the outlet channel of the cross-slot micro-geometry, as function of the normalised position ($x$) along the outlet channels, $x/d$, for various $Re$. Again, the heat transfer is enhanced by the instability for all $Pr$ numbers with increasing $Re$.

Figures 8.21, 8.22, and 8.23 characterise the enhancement in thermal performance provided by the inertial flow instability along the normalised position ($x$) in the outlet channels, $x/d$, for various $Re$. The results reiterate what it is pointed out in this section, where it is presented a first thermal characterisation and performance assessment of a device that has very significant potential thermal applications.

### 8.3.2 Simulations with constant temperature walls

In the case of constant wall temperature ($CWT$) and fluids of the same temperature flowing into the inlets, the Nusselt number can be employed to quantify the enhance-

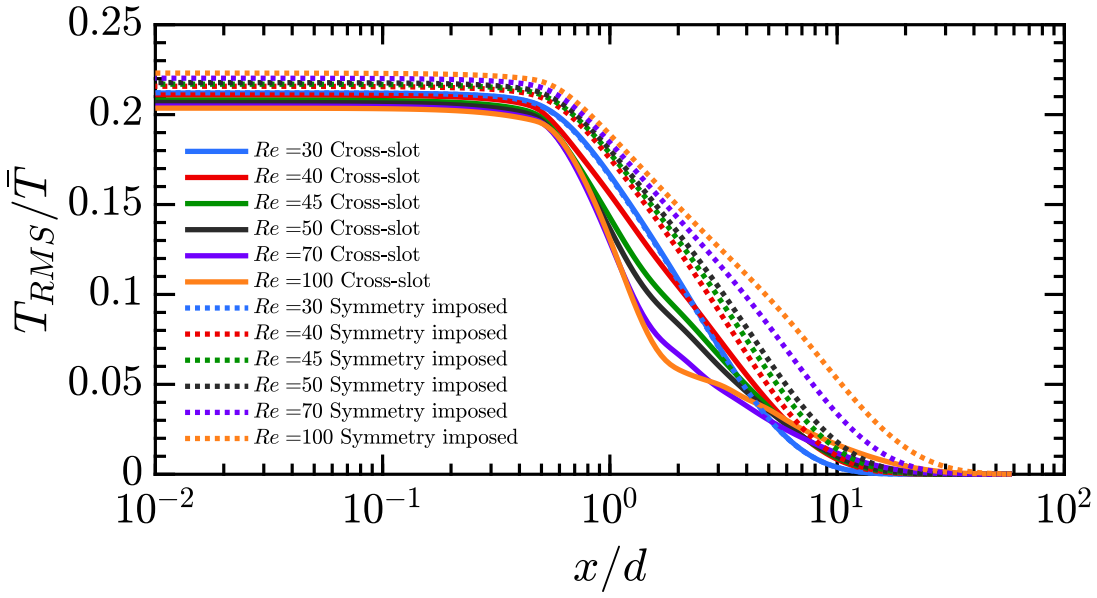


Figure 8.18: Normalised $T_{RMS}$ (Eq. 4.11) as function of the normalised position ($x$) along the outlet channels, $x/d$, for various Reynolds number ($Re$) and $Pr = 1$ Prandtl number. Dashed curves represent symmetric cases; solid curves lines represent asymmetric cases.

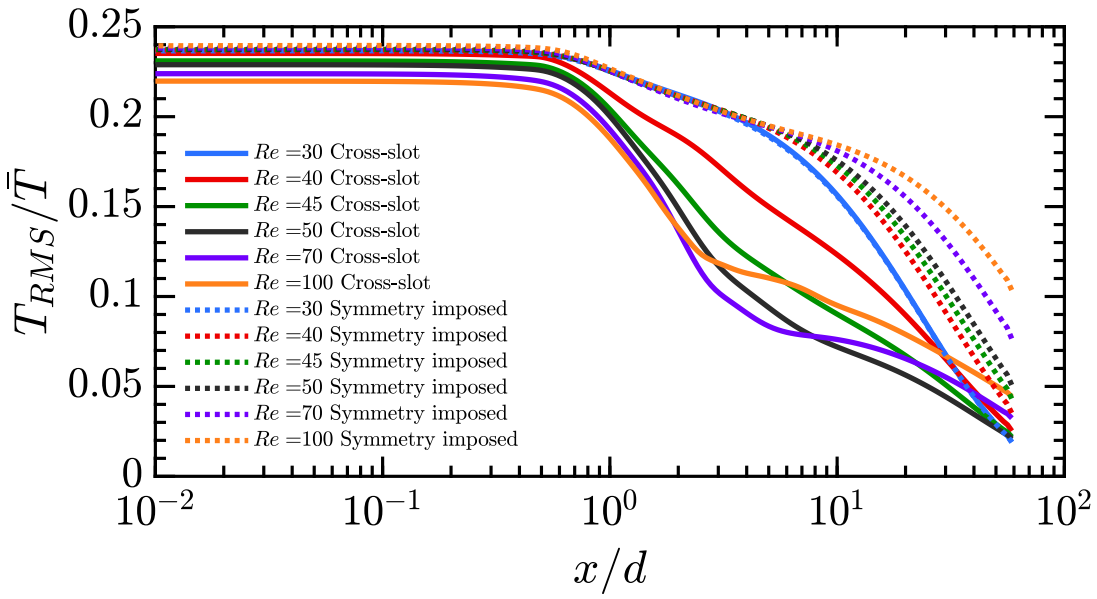


Figure 8.19: Normalised $T_{RMS}$ as function of the normalised position ($x$) along the outlet channels, $x/d$, for various $Re$ and $Pr = 10$. Dashed curves represent symmetric cases; solid curves lines represent asymmetric cases.

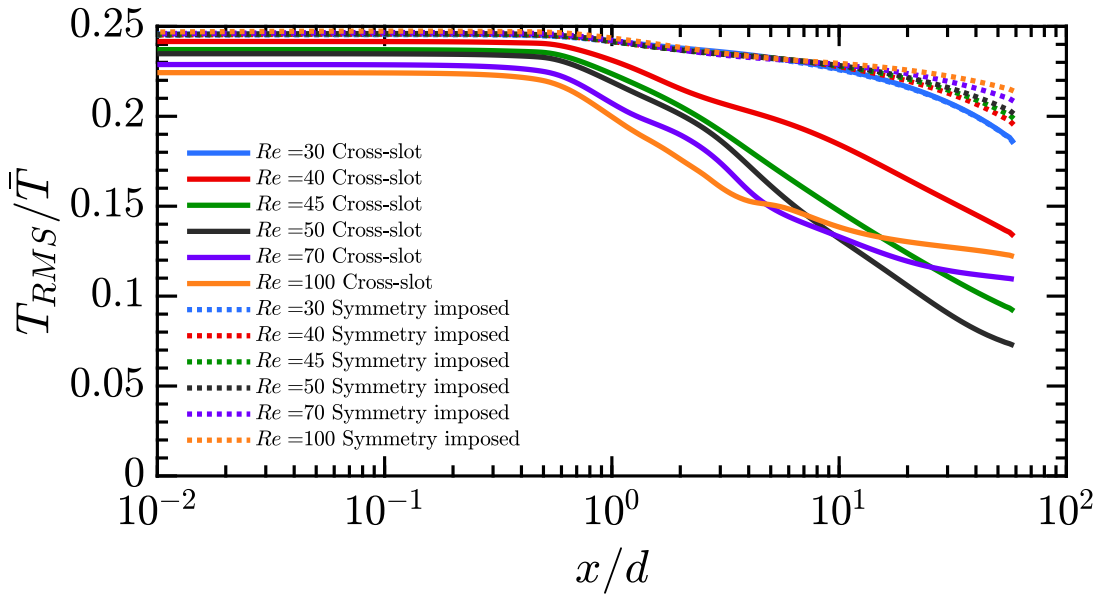


Figure 8.20: Normalised $T_{RMS}$ as function of the normalised position ($x$) along the outlet channels, $x/d$, for various $Re$ and $Pr = 100$. Dashed curves represent symmetric cases; solid curves lines represent asymmetric cases.

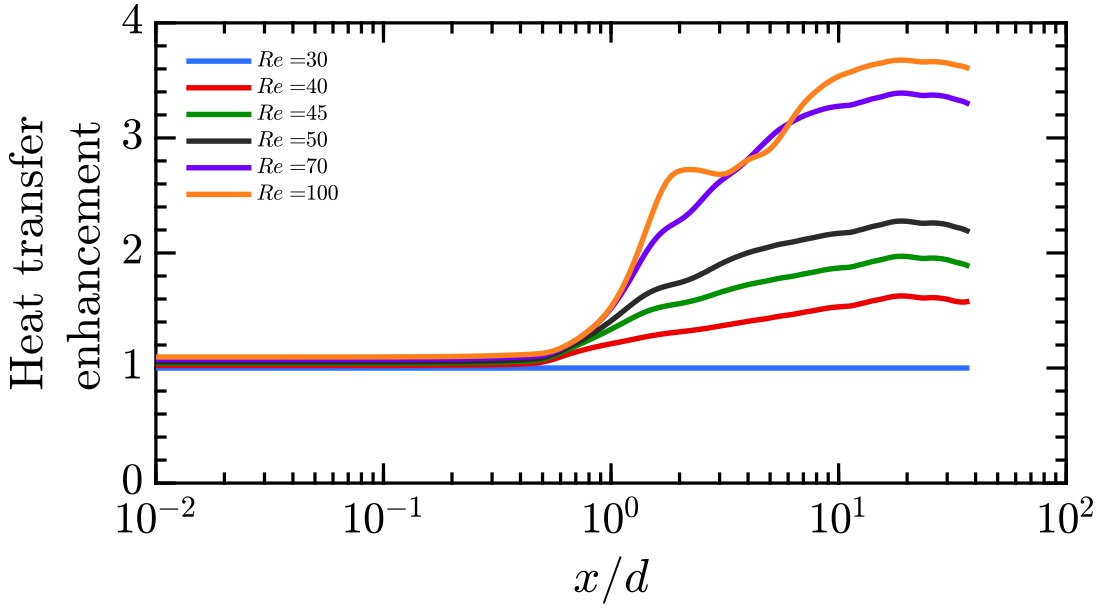


Figure 8.21: Heat transfer enhancement, representing the $T_{RMS}$ ratio calculated between the asymmetric and symmetric cases for $Re$ and $Pr = 1$ as function of the normalised position ($x$) along the outlet channels, $x/d$.

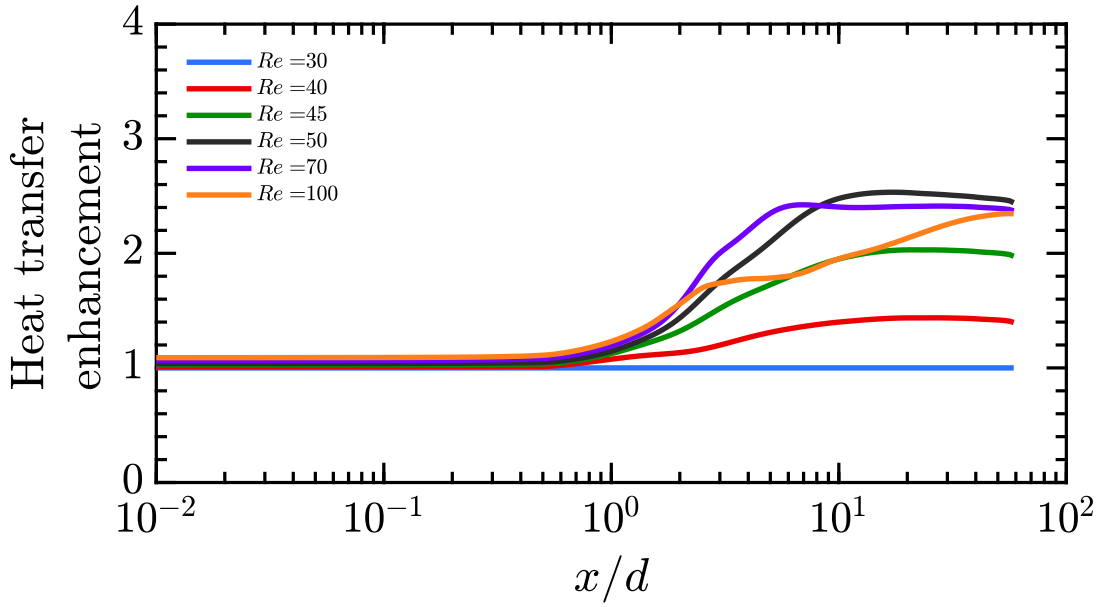


Figure 8.22: Heat transfer enhancement, $T_{RMS}$ ratio between the asymmetric and symmetric cases for $Re$ and $Pr = 10$ as function of the normalised position ($x$) along the outlet channels, $x/d$.

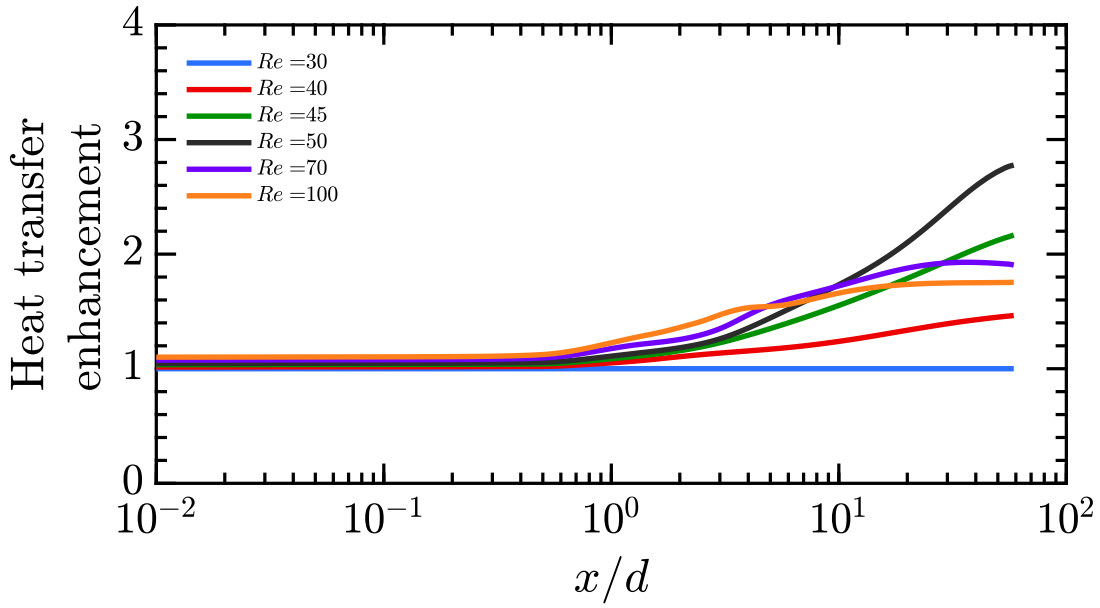


Figure 8.23: Heat transfer enhancement, $T_{RMS}$ ratio between the asymmetric and symmetric cases for $Re$ and $Pr = 100$ as function of the normalised position ($x$) along the outlet channels, $x/d$.

ment of the heat transfer in the cross-slot compared to a straight channel of equivalent length. Steady-state simulations were performed over a range of Reynolds numbers and Prandtl numbers in order to evaluate the effect of the symmetry-breaking instability. The validation presented in table 4.3 provided confidence in the simulations and also enables an insight into the convective heat transfer in the thermal entrance region within the cross-slot microchannel, where the Nusselt numbers ($Nu$) are higher [125]. Therefore, we avoid the developed region where $Nu$ becomes constant in our calculation and focus on a region around the centre of the cross.

In figure 8.24, the instability can be seen to modify the mean Nusselt number and exhibits a hysteretic behaviour. For $Re > Re_c$, the cross-slot was more efficient than a straight channel in terms of heat transfer, presenting significantly higher values of mean Nusselt number (up to 2.4 times higher). The figure presents the ratio between mean $Nu$ for the cross-slot and for a straight channel with equivalent length ($20d$). Under $CWT$ conditions a strong dependency on $Pr$ is apparent. With increasing $Pr$ the mean Nusselt number ratio between the cross-slot and a straight channel also increases, consequently enhancing the heat transfer for all $Re > Re_c$. In figure 8.25, a heat transfer correlation is proposed for the enhancement of the cross-slot over a straight channel as a function of $RePr^n$. For $n = 0.084$, the curves for different $Pr$ broadly collapse such that,

$$\frac{\bar{Nu}_{cross}}{\bar{Nu}_{straight}} = 0.014 RePr^{0.084} + 0.43 \text{ for } Re > 40. \tag{8.1}$$

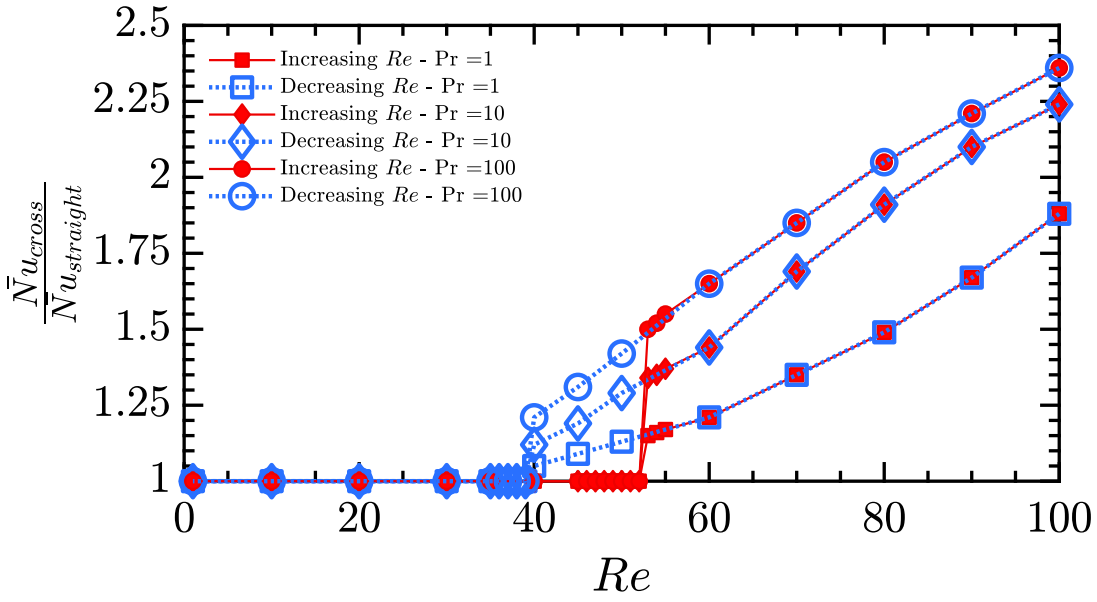


Figure 8.24: Variation of the ratio between mean Nusselt number for the cross-slot and straight channel for increasing and decreasing Reynolds numbers under constant wall temperature ($CWT$) boundary condition.

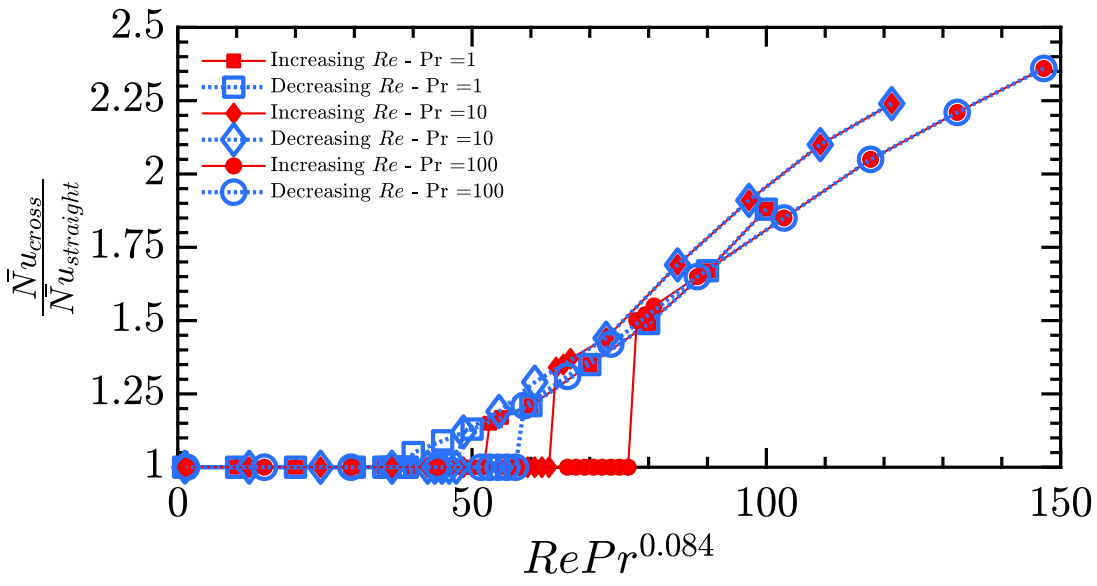


Figure 8.25: Mean Nusselt number ratio as a function of the product of $Re$ and $Pr^n$. In the correlation shown, $n = 0.084$.

## 8.4 Summary

In summary, the heat transfer characteristics of a microfluidic cross-slot device were investigated through experimental measurements and numerical simulations. The particular focus was to assess the potential to enhance the heat transfer performance of such devices using an instability (a subcritical pitchfork bifurcation at this aspect ratio) that creates an axially-oriented spiral vortex down the outlet arms. One of the primary potential applications of such microfluidic devices is active cooling of electronic devices (such as microprocessors). It is therefore of great interest to characterise the enhancement in thermal performance provided by the mentioned flow instability.

Experimentally the walls of the device were approximately adiabatic and hot and cold fluid streams were injected into the cross-slot through opposed inlets over a range of Reynolds number from 3 to 80. Steady temperature distribution patterns were obtained using a temperature-sensitive fluorescent dye. It was seen that when the Reynolds number increases above a certain critical value ($Re > 40$), the temperature distribution in the outlet arms becomes significantly more uniform, indicating an improved heat transfer between the two streams caused by the spiral vortex.

Numerical simulations with boundary conditions matching the experiments agree well with respect to the critical $Re$ of the instability, although there are some differences in the details of the captured temperature distributions, which can be attributed to the limitations of the experimental imaging technique. As expected, a hysteretic behaviour was observed in the simulations, which was absent from the experiments, and showed the existence of a solution branch on which the instability was delayed until $Re = 53$

(similar to the isothermal study of Haward et al. [40]). These simulations suggest that the enhancement of heat transfer increases with increasing Re, although for long outlet channels (in which the vortex has decayed) the picture is less clear and the data for $Re > 70$ exhibits a complex behaviour. However, the asymmetric flow field beyond the instability always exhibits an enhancement of the heat transfer compared to the symmetric flow.

Constant wall temperature ($CWT$) boundary conditions could be applied to the simulations (although not the experiments), which enabled the calculation of a Nusselt number. Under these conditions, the instability provides good enhancement of the heat transfer for all asymmetric cases. The critical $Re$ does not depend on $Pr$, but the magnitude of the heat transfer enhancement is a function of $Pr$, which can be broadly accommodated using a simple correlation of the form $Re.Pr^n$.

# Chapter 9

# Conclusions and future recommendations

## 9.1 Inertial instabilities

- **Inertial flow instabilities in a wide gap ($g = 5H$) mixing-separating microfluidic device**

  The results from numerical simulations and epifluorescence microscopy show that the flow in a wide gap mixing-separating ($5H$) device under Stokes flow ($Re \approx 1$) produces a tilted fluid interface at its central gap when two opposed streams collide at a stagnation point. A significant part of the flow curves around the separating walls and reverses its direction. With increasing Re, the two-dimensional (2D) flow interface inclines and approaches the vertical, increasing the amount of reverse flow. At $Re = 30$, the fluid motion becomes three-dimensional (3D), and a vortex appears at the centre of the mixing-separating cell, although, the flow remains steady.

  By continually increasing $Re$, the vortex divides into a pair of co-rotational symmetric vortices. Consequently, the core of the two vortices separates. Notable, the flow remains steady, the vortex structure does not change in time for a fixed value of a Reynolds number, and no additional pressure loss due to the gap could be noticed; even after the onset of the instability ($Re > 30$), the flow behaved like in straight square cross-section ducts. Most importantly, we show for this complex flow the importance of understanding flow stability conditions. The $\lambda_{ci}$ approach allows us to predict vortex formation and transitions numerically, and the 3D numerical simulations and the experimental flow visualisations show a first qualitative and quantitative agreement. We noticed that this instability preserve the flow symmetry in the flow field.

- **Effects of varying the gap size in mixing-separating device**

  The systematic performed numerical simulations have improved our understand-

ing of the mechanisms underlying in the flow instabilities encountered in this device. A numerical investigation of the flow in mixing-separating ($H$-geometry) microfluidic devices with gap sizes, $g = 2H$, $2.61H$, $3.86H$, and $5H$ has demonstrated that two different inertial instabilities are possible at low Reynolds numbers in the steady flow regime. Which of the two instabilities occurs is primarily dependent on the size of the gap as well as the Reynolds number ($Re$). The two different instability growth parameters, ($\lambda_{ci}$ and $w_{max}/U_b$), have respectively detected the onset and growth of the swirling motion for different gap size and the evolution of a so-called engulfment regime, or cross-slot like instability. The devices with large gaps ($g = 3.86H$ and $g = 5H$) favour the onset of a vortical flow instability in the $y$-$z$ plane, which we have detected and quantified using swirling strength ($\lambda_{ci}H/\mu$). This instability is seen to be supercritical as its growth follows a square-root close to the onset and no hysteresis is apparent. The $Re$ at which the onset first occurs increases as the gap size is increased, but only slightly ($Re_c = 26$, for $g = 3.86H$ and $Re_c = 29$ for $g = 5H$).

This instability also occurs at $g = 2.61H$, but with this gap size a second instability occurs at somewhat higher $Re$ (first instability at $Re = 23$, second at $Re = 84$). The second instability is seen in the transverse velocity component ($w_{max}/U_b$ is used as a bifurcation parameter) and breaks reflectional symmetries similar to a cross-slot device. It too is supercritical as it also follows a square-root close to the onset and is not hysteretic. At the smallest gap size tested ($g = 2H$) only the $w_{max}$ instability occurs (at $Re = 51$) and $\lambda_{ci}$ is zero for all $Re$ tested. This instability is very similar to the cross-slot engulfment instability, and a spiral vortex is formed just like in the cross-slot flow.

- **Angle variation in the mixing-separating cell**

  The numerical investigation has improved our understanding of the mechanisms underlying in this flow instability variation. By varying the angle between the inlet and outlet arms, the instability parameter ($w_{max}/U_b$) have confirmed the instability change from subcritical pitchfork in a 90° angle geometry (cross-slot) to supercritical in a 60° angle without hysteresis. After the instability onset, the transverse flow field at the central plane breaks its symmetry, and $w_{max}/U_b$ increases following a square root function when $Re - Re_c)/Re_c << 1$.

  Although there is some previous work on the effect of the angle $\alpha$ (albeit for circular cross-section channels)[26], the results demonstrate that the engulfment instability seen in the cross-slot is not wholly dependent on the specific angle at which the two streams collide. It only confirms that the size of the gap is a more critical parameter (as this instability does not appear at large gap sizes) as the engulfment instability indeed occur if the gap is small. The current chapter

indicates that the gap size is of primary importance in determining which instability occurs. As $\alpha$ and gap size are geometrically dependent upon each other (i.e. if $\alpha$ is changed, the gap size is changed as a result of the new angle [26]), isolating the effect of $\alpha$ and gap size is non-trivial. Therefore our results for the mixing-separating device are useful for reference cases as we can vary the gap size without changing the angle $\alpha$ (which is a particular quirk of the $H$-geometry).

Comparing the $X$-shaped geometries to the similar gap size mixing-separating devices, we confirmed that the engulfment instability seen in the cross-slot is not wholly dependent on the specific angle at which the two streams collide. The results have confirmed that the size of the gap is a more important parameter (as this instability does not appear at large gap sizes) as the engulfment instability indeed occur if the gap was small. The symmetric transverse velocity flow field at the central plane restricted the use of the instability parameter $w_{max}/U_b$ for wide gap size geometries (30°,$g = 3.86$). Moreover, along the outlet channels, the flow field demonstrates that can it restore the developed state showing a parabolic velocity distribution in a small channel length when changing the angle $\alpha$ (i.e. from 60° to 30°) due to the different instability present (engulfment instability or swirling flow). These findings could be beneficial depending upon the desired application.

- **Heat transfer enhancement in a cross-slot microfluidic device**

  In this study, the heat transfer characteristics of a microfluidic cross-slot device were investigated through numerical simulations and compared to existing experiments. The particular focus was to assess the potential to enhance the heat transfer performance of such devices using an instability (a subcritical pitchfork bifurcation at this aspect ratio) that creates an axially-oriented spiral vortex down the outlet arms. One of the primary potential applications of such microfluidic devices is active cooling of electronic devices (such as microprocessors). It is therefore of great interest to characterise the enhancement in thermal performance provided by the mentioned flow instability.

  Numerical simulations with boundary conditions matching the experiments agree well concerning the critical $Re$ of the instability, although there are some differences in the details of the captured temperature distributions, which can be attributed to the limitations of the experimental imaging technique. As expected, a hysteretic behaviour was observed in the simulations, which was absent from the experiments, and showed the existence of a solution branch on which the instability was delayed until $Re = 53$ (similar to the isothermal study of Haward et al. [40]). These simulations suggest that the enhancement of heat transfer increases with increasing Re, although for long outlet channels (in which the vortex

has decayed) the picture is less clear and the data for $Re > 70$ exhibits a complex behaviour. However, the asymmetric flow field beyond the instability always exhibits enhancement of the heat transfer compared to the symmetric flow.

Constant wall temperature ($CWT$) boundary conditions could be applied to the simulations (although not the experiments), which enabled the calculation of a Nusselt number. Under these conditions, the instability provides good enhancement of the heat transfer for all asymmetric cases. The critical $Re$ does not depend on $Pr$, but the magnitude of the heat transfer enhancement is a function of $Pr$, which can be broadly accommodated using a simple correlation of the form $Re.Pr^n$.

## 9.2 Elastic instabilities

- **Elastic instabilities in a mixing-separating device**

  Complementary experiments providing flow visualisations in a mixing-separating device using a so-called Boger fluid, we were able to show the viscoelastic stagnation point flow in a steady-state condition. Additionally, with increasing $Wi$, the flow becomes time-dependent. At around $Wi = 2$, the steady-state solution loses stability, and a periodic flow takes place in the mixing-separating cell. Flow is characterised by time-dependent fluctuations, specifically, alternating positive and negative deviations of the proposed $N(t)$ parameter from the steady-state in the stagnation point.

  Although we present an investigation of the time-dependent behaviour of this instability after bifurcation, the nature of these oscillatory events is yet unclear. How these events are triggered and what roles they play in the elastic instability processes will be necessary for further understanding the applicability in polymeric solutions. Therefore, as we believe that this instability could be helpful for various microfluidic applications, we will propose some further investigation later in this chapter.

## 9.3 Overall conclusions

- **Inertial instabilities in mixing-separating microfluidic device**

  The work provides a greater understanding of the instabilities in these mixing-separating microfluidic devices through the characterisation of the flow over a range of $Re$ for several gap sizes. In particular, the strong dependence of the instability on gap size is revealed. The similarity of the instability in the small gap size $H$-geometry to the more extensively studied cross-slot brings into question the importance of the geometrical arrangement in these devices as a very similar

flow can be achieved with the inlet arms parallel or perpendicular to the outlet arms. This perhaps indicates a route to designing more compact devices. In any case, we provide a database that highlights the importance of gap size in the design of such devices and provides information regarding the onset $Re$ of two types of inertial instabilities over a range of gap sizes which are viable choices for microfluidic applications. Moreover, the ability to engineer fluid flows by changing the geometry angle introduces a new useful capability that could lead to better decisions when selecting the ideal microfluidic device, and also potentially beneficial in a variety of other applications.

- **Heat transfer enhancement in a cross-slot device**

  The investigation has confirmed the potential of this purely-inertial instability to enhance the heat transfer at the micro-scale, provided a Reynolds number greater than 40 can be reached. The effect is particularly useful for achieving a high level of heat transfer in a short channel length, which has clear benefits in microfluidic devices.

- **Elastic instabilities in a mixing-separating microfluidic device**

  The greater understanding and characterisation of the flow before and after symmetry-breaking, in both Newtonian and viscoelastic fluids, help predict the formation of an instability. Thus, depending on the desired application, the correct choice of the geometry and fluid will lead to a desired and controlled instability mechanism.

## 9.4 Future Work

This thesis has provided a significant contribution to the understanding of inertial and elastic instabilities in the micro-scale geometries. Although there are still some areas that require further investigation.

- **Dynamics of viscoelastic flow in the mixing-separating device**

  Our study on viscoelastic flows within the mixing-separating device raises more questions than it answers. Although it does not provide a complete mechanism for the elastic instabilities in the geometry, nor does it offer a clear explanation of the flow transition, a new direction has been pointed to understand the regime of high $Wi$ viscoelastic instability. In particular, the oscillatory fluctuations provides an important clue that might lead to the eventual revelation of the nature of this instability. Further knowledge is needed about this newly-recognised bifurcation: understanding its nature and its connection with the Hopf bifurcation (supercritical instability) is the most crucial task in the future.

With the current experimental method and data, the short-term plan is to quantify the differences between these data and numerical simulations. Results on oscillatory behaviour of the instability ($Wi > Wi_c$) discussed in Chapter 7 is based on a typical example, although other instances should be examined to ensure that those observations are not specific to the selected set of data, more general analysis on the flow and polymer relaxation time should be performed. As reviewed in chapter 2, the amount of reverse flow depends on the gap size and Deborah number, and the creeping flow of UCM fluids exhibited an interesting bifurcation pattern, which depends on the gap width. Afonso et al. [27] indicate that for intermediate gap widths, a steady bi-stable bifurcation pattern is observed. Two different flow configurations appear at very close Deborah numbers, which made the flow to oscillate periodically. Although qualitative, we have shown a smooth dependence of the instability on $Wi$. To test these dependencies ($Wi$ and gap size), one needs to effectively divide the investigation into the two categories: gap variation and $Wi$ variation.

- **Dynamics of viscoelastic flow in the $X$-shaped device**

  In chapter 6, we demonstrate that the angle $\alpha$ and gap size are geometrically dependent upon each other. If $\alpha$ is changed, the gap size is changed as a result of the new angle. Therefore, the gap size is very important, and any change in other aspects of the geometry (e.i.: the angle $\alpha$) affects the gap size. Therefore, by taking into account the constraints in the gap size when varying $\alpha$, to complement our investigations on the effects of these changes on the inertial instabilities, one needs to compare the $X$-shaped geometries with the particular gap size mixing-separating devices when using viscoelastic fluids.

  From a nonlinear dynamics point of view, the distinct separation of the influence of the gap size and the angle $\alpha$ suggests modification on the elastic instability. In the Newtonian instability, we saw that the gap size changes combined to the angle $\alpha$ changes could modify the instability. Consequently, the different scenarios are shown.

- **Delay of symmetry-breaking instability in cross-slot geometries using a passive flow-control mechanism**

  In viscoelastic fluid flow, the cross-slot stagnation point flow is one of the benchmark problems in fluid mechanics as it allows large strains to develop and can, therefore, be used for extensional rheometry. In such a flow, beyond a critical value in which the ratio of inertia force to viscous force is high enough, inertia can break the symmetry. Another form of symmetry-breaking has also been observed for purely-elastic cases in creeping flow regimes, which is perhaps an unwanted

phenomenon if used as a rheometer. In one very recent work, a passive control mechanism is introduced by adding a cylinder at the geometric centre of the cross-slot geometry to replace the free stagnation point with "pinned" stagnation points at the surface of the cylinder. In the current modified geometry, effects of the blockage ratio (the ratio of diameter of the cylinder to the width of the channel), the Weissenberg number (the ratio of the elastic forces to viscous forces) and extensibility parameter ($e$) are investigated in 2D numerical simulations using a simplified Phan-Thien and Tanner model. It is shown that the blockage ratio for fixed solvent-to-total viscosity ratio has a stabilising effect on the associated symmetry-breaking instability.

Further results show that the Weissenberg number and $e$ parameter have a destabilising and stabilising effect, respectively. Numerical simulations supported by experimental results show that the suggested modifications, replacing the free stagnation point with pinned stagnation points, can change the supercritical nature of the instability in the cross-slot geometry (see figure 9.1 for details of the experimental rig used). The investigation also suggests that the proposed geometry modification can be an effective approach to reach a higher flow rate while retaining steady symmetric flow in a cross-slot.

Although the results have been published, further knowledge is needed about this newly-recognised delay of symmetry-breaking instability in cross-slot geometries when considering the inertial instabilities (Newtonian fluid).

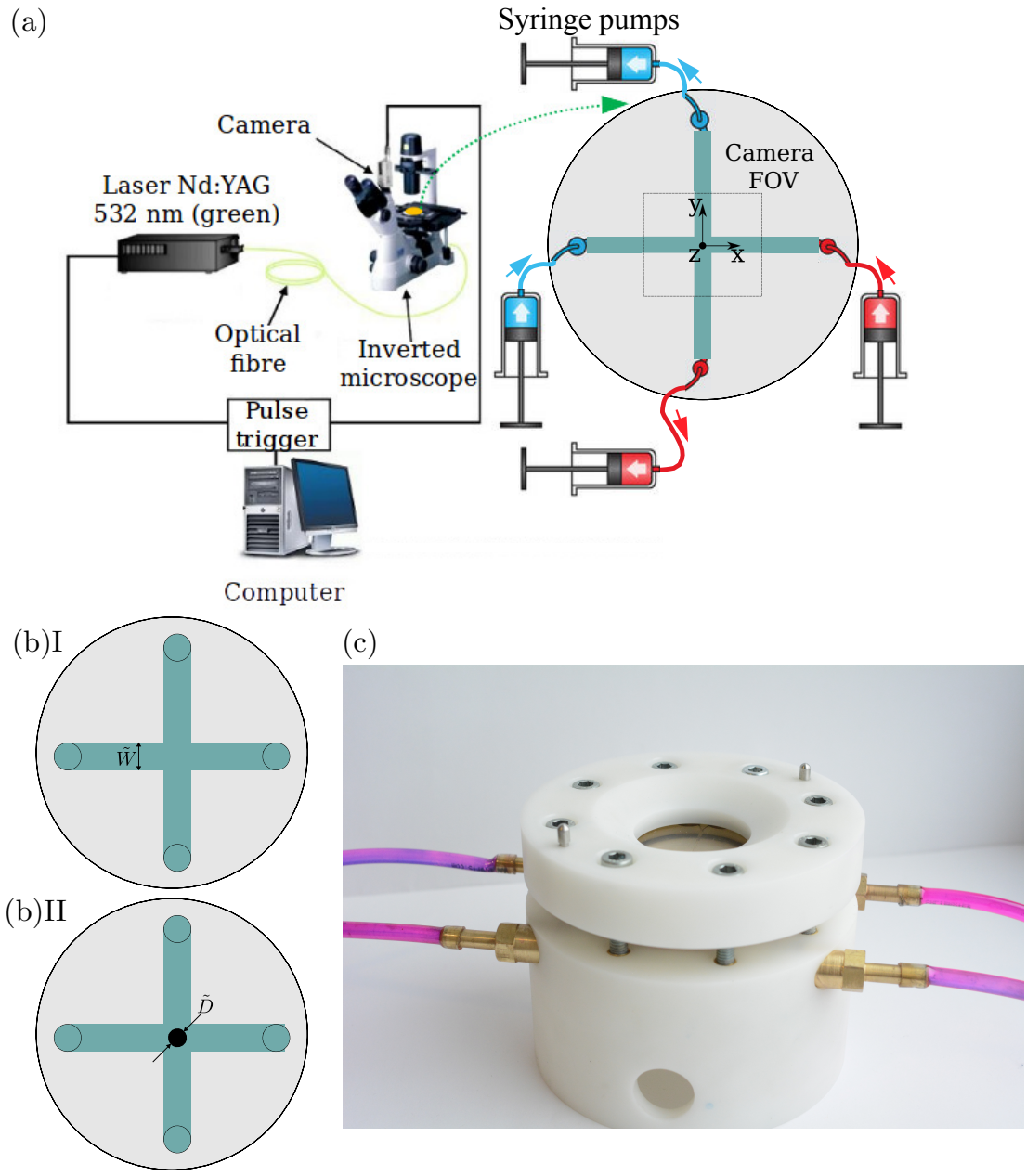


Figure 9.1: (a) A scheme illustrating the experimental apparatus of a microfluidic cross-slot device allowed for direct observation of the $x$-$y$ plane at $z = 0$ and the characteristic channel dimensions ($H = W = 500\mu$m; $g = 5H = 2.5$mm; $a = H/5 = 100\mu$m). The origin is placed at the geometric centre of the device gap ($g$). The rig is mounted on an inverted microscope fitted with a filter cube. A pulsed Nd:YAG laser is used to excite the dyed fluid, and a CCD camera enables to capture the instability formation [notes: 1-not to scale; 2-camera FOV (field of view): 3.2mm x 2.4mm]. (b) The exploded view of the prototype microfluidic device rig. The channels were micro-machined in brass and encased in polyoxymethylene. A 6.5mm thick upper wall fabricated from borosilicate glass to obtain a sealed condition while allowing the flow structure to be visualised. (c) Photograph illustrating the experimental rig set-up assembled.

# Appendix A

# Supplemental material

This appendix provides the internet link for the direct access to the supplemental material (videos) of viscoelastic flows in the mixing-separating geometry, used in chapter 7 of this thesis.

links: `https://www.dropbox.com/sh/bcwul65fz2x37lq/AABdADUyBmPOigmoetl41z5ga?dl=0` or `www.cercatrova-research.com`

# Appendix B

# Symmetries

Figure B.1 shows the analysis of the flow symmetries for the $x$-$y$ plane with increasing $Re$. It clearly depicts that reflection symmetry breaks with inertia.

In a $5H$ gap size under creeping flow ($Re \leq 1$), the velocity field is symmetric, although, it becomes reflectional asymmetric when inertia is triggered with increasing Reynolds number (see figure B.2). Figure B.1 shows that the growth of the asymmetry parameter was practically linear with increasing the $Re$. The results indicate that a different bifurcation parameter should be applied to complement the investigations.

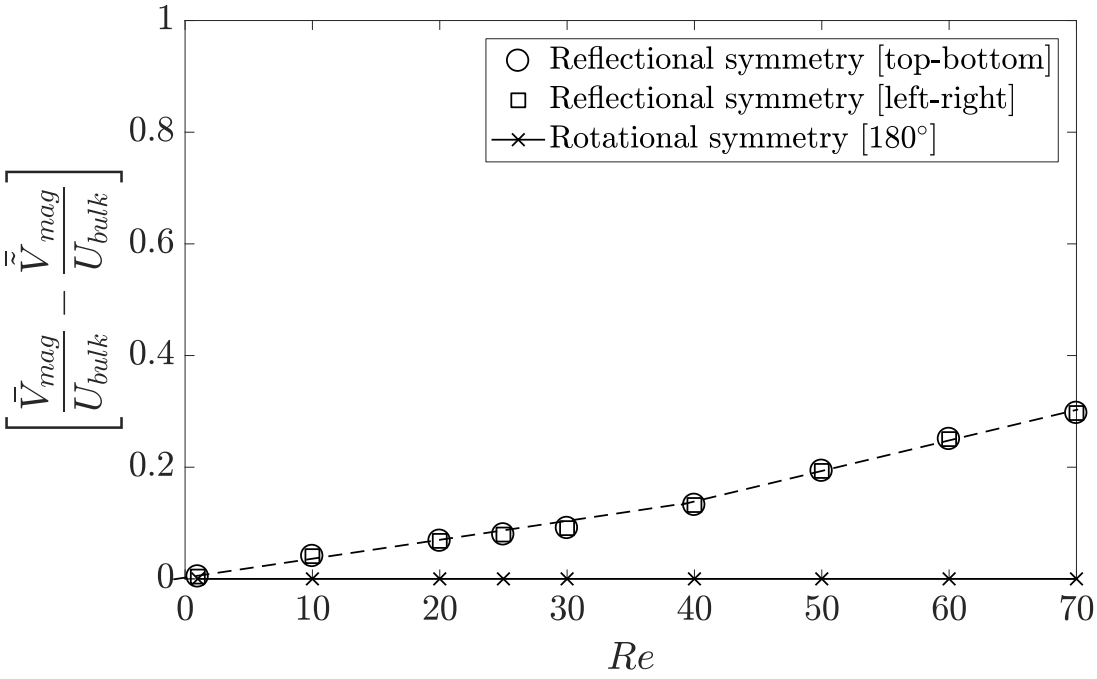


Figure B.1: Symmetry analysis at the $x$-$y$ plane with increasing $Re$. The results show that the inertial effects breaks reflectional symmetry in the flow field.

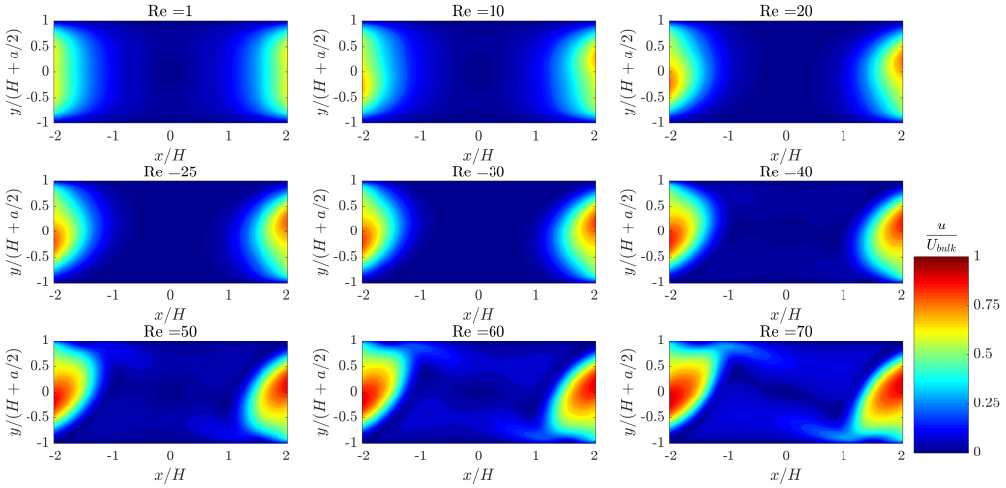


Figure B.2: Normalised velocity magnitude at the $x$-$y$ plane for different Reynolds number.

# Appendix C

# Transverse velocity bifurcation parameter $w_{max}/U_b$

Figure C.1 shows the evolution of the parameter $w_{max}/U_b$ for different gap sizes in mixing-separating cell with increasing Reynolds number.

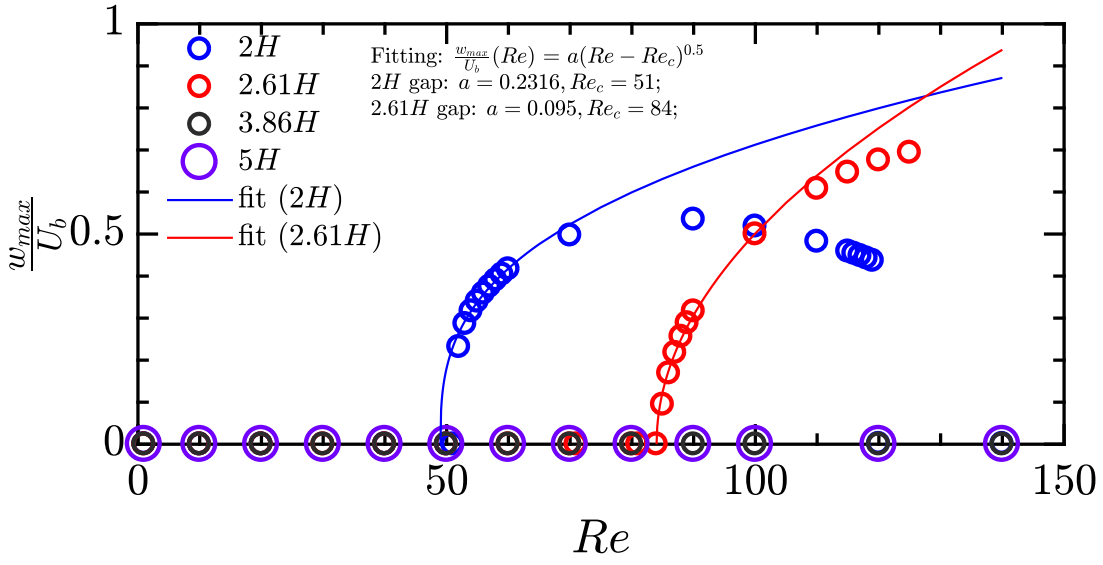


Figure C.1: The $w_{max}/U_b$ parameter applied at the $x$-$y$ plane for different gaps with increasing $Re$.

Figure C.2 shows the evolution of the parameter $w_{max}/U_b$ for in a cross-slot geometry with increasing Reynolds number.

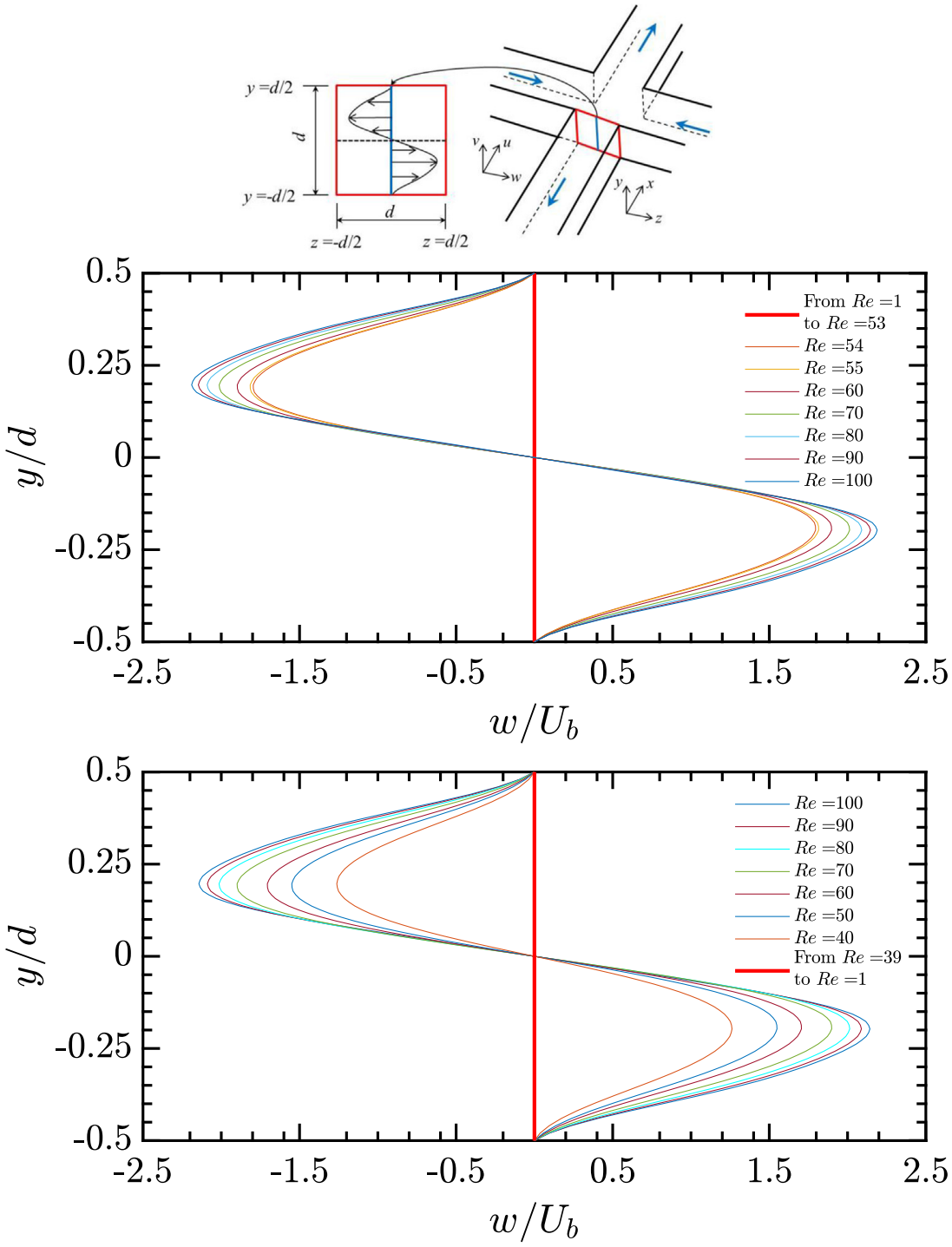


Figure C.2: Enlarged schematic diagram of the cross-slot micro-geometry depicting the inlet plane of the outlet arm and the transverse velocity profiles along the centreline of this plane with increasing and decreasing Reynolds number.

# Bibliography


[1] E. K. Parker, A. V. Nielsen, M. J. Beauchamp, H. M. Almughamsi, J. B. Nielsen, M. Sonker, H. Gong, G. P. Nordin, and A. T. Woolley. 3D printed microfluidic devices with immunoaffinity monoliths for extraction of preterm birth biomarkers. *Anal. Bioanal.Chem.*, pages 1–9, 2018. doi: 10.1007/s00216-018-1440-9.

[2] C. Lee, C. Chang, Y. Wang, and L. Fu. Microfluidic mixing: a review. *Int. J. Mol. Sci.*, 12(5):3263–3287, 2011. doi: 10.3390/ijms12053263.

[3] P. Tabeling. *Introduction to microfluidics*. Oxford University Press on Demand, 2005.

[4] E. K. Sackmann, A. L. Fulton, and D. J. Beebe. The present and future role of microfluidics in biomedical research. *Nature*, 507(7491):181, 2014. doi: 10.1038/nature13118.

[5] T. M. Squires and S. R. Quake. Microfluidics: fluid physics at the nanoliter scale. *Rev. Mod. Phys.*, 77(3):977, 2005. doi: 10.1103/revmodphys.77.977.

[6] D. Di Carlo. Inertial microfluidics. *Lab. Chip*, 9(21):3038–3046, 2009. doi: 10.1039/b912547g.

[7] Simon J. Haward, Robert J. Poole, Manuel A. Alves, Paulo J. Oliveira, Nigel Goldenfeld, and Amy Q. Shen. Tricritical spiral vortex instability in cross-slot flow. *Phys. Rev. E*, 93(3):031101, 2016. doi: 10.1103/physreve.93.031101.

[8] J. Soulages, M. S. N. Oliveira, P. C. Sousa, M. A. Alves, and G. H. McKinley. Investigating the stability of viscoelastic stagnation flows in T-shaped microchannels. *J. Non-Newtonian Fluid Mech.*, 163(1-3):9–24, 2009. doi: 10.1016/j.jnnfm.2009.06.002.

[9] R. J. Poole, G. N. Rocha, and P. J. Oliveira. A symmetry-breaking inertial bifurcation in a cross-slot flow. *Comput. Fluids*, 93:91–99, 2014. doi: 10.1016/j.compfluid.2014.01.008.

[10] M. Engler, N. Kockmann, T. Kiefer, and P. Woias. Numerical and experimental investigations on liquid mixing in static micromixers. *Chem. Eng. J.*, 101(1-3): 315–322, 2004. doi: 10.1016/j.cej.2003.10.017.

[11] D. Bothe, C. Stemich, and H.-J. Warnecke. Fluid mixing in a T-shaped micromixer. *Chem. Eng. Sci.*, 61(9):2950–2958, 2006. doi: 10.1016/j.ces.2005.10.060.

[12] N. Kockmann, T. Kiefer, M. Engler, and P. Woias. Convective mixing and chemical reactions in microchannels with high flow rates. *Sens. Actuators, B*, 117(2): 495–508, 2006. doi: 10.1016/j.snb.2006.01.004.

[13] A. Soleymani, E. Kolehmainen, and I. Turunen. Numerical and experimental investigations of liquid mixing in T-type micromixers. *Chem. Eng. J.*, 135:S219–S228, 2008. doi: 10.1016/j.cej.2007.07.048.

[14] N. A. Mouheb, A. Montillet, C. Solliec, J. Havlica, P. Legentilhomme, J. Comiti, and J. Tihon. Flow characterization in T-shaped and cross-shaped micromixers. *Microfluid. Nanofluid.*, 10(6):1185–1197, 2011.

[15] N. A. Mouheb, D. Malsch, A. Montillet, C. Solliec, and T. Henkel. Numerical and experimental investigations of mixing in T-shaped and cross-shaped micromixers. *Chem. Eng. Sci.*, 68(1):278–289, 2012. doi: 10.1016/j.ces.2011.09.036.

[16] R. B. Bird, R. C. Armstrong, and O. Hassager. *Dynamics of polymeric liquids*. Wiley, New York ; Chichester, 2nd edition, 1987.

[17] R. G. Larson. *The structure and rheology of complex fluids*. Oxford University Press, New York ; Oxford, 1999.

[18] R. G. Larson. Instabilities in viscoelastic flows. *Rheol. Acta*, 31(3):213–263, 1992. doi: 10.1007/bf00366504.

[19] E. S. G. Shaqfeh. Purely elastic instabilities in viscometric flows. *Annu. Rev. Fluid Mech.*, 28(1):129–185, 1996. doi: 10.1146/annurev.fl.28.010196.001021.

[20] A. Groisman and V. Steinberg. Elastic turbulence in a polymer solution flow. *Nature*, 405(6782):53, 2000. doi: 10.1038/35011019.

[21] S. H. Spiegelberg and G. H. McKinley. Stress relaxation and elastic decohesion of viscoelastic polymer solutions in extensional flow. *J. Non-Newtonian Fluid Mech.*, 67:49–76, 1996. doi: 10.1016/s0377-0257(96)01475-9.

[22] M. D. Graham. Interfacial hoop stress and instability of viscoelastic free surface flows. *Phys. Fluids*, 15(6):1702–1710, 2003. doi: 10.1063/1.1568340.

[23] A. Chow, A. Keller, A. J. Muller, and J. A. Odell. Entanglements in polymer solutions under elongational flow: a combined study of chain stretching, flow velocimetry and elongational viscosity. *Macromolecules*, 21(1):250–256, 1988. doi: 10.1021/ma00179a048.

[24] Susan J. Muller, Ronald G. Larson, and Eric S. G. Shaqfeh. A purely elastic transition in Taylor-Couette flow. *Rheol. Acta*, 28(6):499–503, 1989. doi: 10.1007/bf01332920.

[25] P. E. Arratia, C. C. Thomas, J. Diorio, and J. P. Gollub. Elastic instabilities of polymer solutions in cross-channel flow. *Phys. Rev. Lett.*, 96(14):144502, 2006. doi: 10.1103/physrevlett.96.144502.

[26] P. G. Correa, J. R. Mac Intyre, J. M. Gomba, M. A. Cachile, J. P. Hulin, and H. Auradou. Three-dimensional flow structures in X-shaped junctions: effect of the Reynolds number and crossing angle. *Phys. Fluids*, 31(4):043606, 2019. doi: 10.1063/1.5087641.

[27] A. M. Afonso, M. A. Alves, R. J. Poole, P. J. Oliveira, and F. T. Pinho. Viscoelastic flows in mixing-separating cells. *J. Eng. Math.*, 71(1):3–13, 2011. doi: 10.1007/s10665-010-9384-x.

[28] A. D. Stroock, S. K. Dertinger, A. Ajdari, I. Mezic, H. A. Stone, and G. M. Whitesides. Chaotic mixer for microchannels. *Science*, 295(5555):647–651, 2002. doi: 10.1126/science.1066238[doi].

[29] K. Malecha, L. J. Golonka, J. Baldyga, M. Jasinska, and P. Sobieszuk. Serpentine microfluidic mixer made in LTCC. *Sens. Actuators, B*, 143(1):400–413, 2009. doi: 10.1016/j.snb.2009.08.010.

[30] F. M. White. *Viscous fluid flow*. New York ; McGraw-Hill Higher Education, 2006; 3rd ed, 2006.

[31] B. J. Kirby. *Micro-and nanoscale fluid mechanics: transport in microfluidic devices*. Cambridge university press, 2010.

[32] F. A. Morrison. *An introduction to fluid mechanics*. Cambridge University Press, 2013.

[33] E. Lauga, A. D. Stroock, and H. A. Stone. Three-dimensional flows in slowly varying planar geometries. *Phys. Fluids*, 16(8):3051–3062, 2004. doi: 10.1063/1.1760105.

[34] O. S. Pak, L. Zhu, L. Brandt, and E. Lauga. Micropropulsion and microrheology in complex fluids via symmetry breaking. *Phys. Fluids*, 24(10):103102, 2012. doi: 10.1063/1.4758811.

[35] P. C. Sousa, F. T. Pinho, M. S. N. Oliveira, and M. A. Alves. Purely elastic flow instabilities in microscale cross-slot devices. *Soft Matter*, 11(45):8856–8862, 2015. doi: 10.1039/c5sm01298h.

[36] J. Eustice. Experiments on stream-line motion in curved pipes. *Proc. R. Soc. Lond. A Math. Phys. Sci.*, 85(576):119–131, 1911.

[37] V. N. Kalashnikov and M. G. Tsiklauri. Ordered three-dimensional structures resulting from instability of two-dimensional flow in crossed channels. *Fluid Dyn.*, 26(2):161–165, 1991. doi: 10.1007/bf01050133.

[38] V. N. Kalashnikov and M. G. Tsiklauri. Effect of polymer additives on ordered three-dimensional structures arising in cross-slot flow. *J. Non-Newtonian Fluid Mech.*, 48(3):215–223, 1993. doi: 10.1016/0377-0257(93)87021-g.

[39] C. Lee and L. Fu. Recent advances and applications of micromixers. *Sens. Actuators, B*, 259:677–702, 2018. doi: 10.1016/j.snb.2017.12.034.

[40] W. M. Abed, A. F. Domingues, R. J. Poole, and D. J. C. Dennis. Heat transfer enhancement in a cross-slot micro-geometry. *Int. J. Therm. Sci.*, 121:249–265, 2017. doi: 10.1016/j.ijthermalsci.2017.07.017.

[41] V. V. Ramanan, K. A. Kumar, and M. D. Graham. Stability of viscoelastic shear flows subjected to steady or oscillatory transverse flow. *J. Fluid Mech.*, 379: 255–277, 1999. doi: 10.1017/s002211209800322x.

[42] K. A. Kumar and M. D. Graham. Buckling instabilities in models of viscoelastic free surface flows. *J. Non-Newtonian Fluid Mech.*, 89(3):337–351, 2000. doi: 10.1016/s0377-0257(99)00040-3.

[43] W. R. Dean. The stream-line motion of fluid in a curved pipe. *Lond. Edinb. Dubl. Phil. Mag.*, 5(30):673–695, 1928. doi: 10.1080/14786440408564513.

[44] S. A. Berger, L. Talbot, and L. S. Yao. Flow in curved pipes. *Annu. Rev. Fluid Mech.*, 15(1):461–512, 1983. doi: 10.1146/annurev.fl.15.010183.002333.

[45] H. Fellouah, C. Castelain, A. Ould El Moctar, and H. Peerhossaini. A criterion for detection of the onset of Dean instability in Newtonian fluids. *Eur. J. Mech. B Fluids*, 25(4):505–531, 2006. doi: 10.1016/j.euromechflu.2005.11.002.

[46] S. I. Bernad, A. Totorean, A. Bosioc, R. Stanciu, and E. S. Bernad. Numerical investigation of Dean vortices in a curved pipe. In *AIP Conference Proceedings*, volume 1558, pages 172–175. AIP, 2013. doi: 10.1063/1.4825448.

[47] S. Sugiyama, T. Hayashi, and K. Yamazaki. Flow characteristics in the curved rectangular channels: visualization of secondary flow. *JSMEB*, 26(216):964–969, 1983. doi: 10.1299/jsme1958.26.964.

[48] W. M. Abed, R. D. Whalley, D. J. C. Dennis, and R. J. Poole. Numerical and experimental investigation of heat transfer and fluid flow characteristics in a micro-scale serpentine channel. *Int. J. Heat Mass Transfer*, 88:790–802, 2015. doi: 10.1016/j.ijheatmasstransfer.2015.04.062.

[49] W. M. Abed, R. D. Whalley, D. J. C. Dennis, and R. J. Poole. Experimental investigation of the impact of elastic turbulence on heat transfer in a serpentine channel. *J. Non-Newtonian Fluid Mech.*, 231:68–78, 2016. doi: 10.1016/j.jnnfm.2016.03.003.

[50] N. Zaidon, A. N. Nordin, A. F. Ismail, and M. W. Cheung. *Symposium on design, test, integration and packaging of MEMS-MOEMS (DTIP)*, pages 1–5. IEEE, 2016.

[51] S. H. Wong, M. C. L. Ward, and C. W. Wharton. Micro T-mixer as a rapid mixing micromixer. *Sens. Actuators, B*, 100(3):359–379, 2004. doi: 10.1016/j.snb.2004.02.008.

[52] S. Dreher, N. Kockmann, and P. Woias. Characterization of laminar transient flow regimes and mixing in T-shaped micromixers. *Heat Transfer Eng.*, 30(1-2):91–100, 2009. doi: 10.1080/01457630802293480.

[53] S. Thomas and T. A. Ameel. An experimental investigation of moderate Reynolds number flow in a T-channel. *Exp. Fluids*, 49(6):1231–1245, 2010. doi: 10.1007/s00348-010-0863-7.

[54] M. Hoffmann, M. Schluter, and N. Rabiger. *Micro and macro mixing: analysis, simulation and numerical calculation*, pages 287–303. Springer-Verlag Berlin Heidelberg, Heat and Mass Transfer, 2010.

[55] R. J. Poole, M. Alfateh, and A. P. Gauntlett. Bifurcation in a T-channel junction: effects of aspect ratio and shear-thinning. *Chem. Eng. Sci.*, 104:839–848, 2013. doi: 10.1016/j.ces.2013.10.006.

[56] A. Fani, S. Camarri, and M. V. Salvetti. Investigation of the steady engulfment regime in a three-dimensional T-mixer. *Phys. Fluids*, 25(6):064102, 2013. doi: 10.1063/1.4809591.

[57] A. Fani, S. Camarri, and M. V. Salvetti. Unsteady asymmetric engulfment regime in a T-mixer. *Phys. Fluids*, 26(7):074101, 2014. doi: 10.1063/1.4885451.

[58] J. T. Ault, A. Fani, K. K. Chen, S. Shin, F. Gallaire, and H. A. Stone. Vortex-breakdown-induced particle capture in branching junctions. *Phys. Rev. Lett.*, 117 (8):084501, 2016. doi: 10.1103/physrevlett.117.084501.

[59] R. Govindarajan and K. C. Sahu. Instabilities in viscosity-stratified flow. *Annu. Rev. Fluid Mech.*, 46:331–353, 2014. doi: 10.1146/annurev-fluid-010313-141351.

[60] S. Sarkar, K. K. Singh, V. Shankar, and K. T. Shenoy. Numerical simulation of mixing at 1-1 and 1-2 microfluidic junctions. *Chem. Eng. Process. Process Intensif.*, 85:227–240, 2014. doi: 10.1016/j.cep.2014.08.010.

[61] S. J. Haward, M. S. N. Oliveira, M. A. Alves, and G. H. McKinley. Optimized cross-slot flow geometry for microfluidic extensional rheometry. *Phys. Rev. Lett.*, 109(12), 2012. doi: 10.1103/PhysRevLett.109.128301.

[62] F. J. Galindo-Rosales, M. A. Alves, and M. S. N. Oliveira. Microdevices for extensional rheometry of low viscosity elastic liquids: a review. *Microfluid. Nanofluid.*, 14(1-2):1–19, 2013.

[63] K. Zografos, N. Burshtein, A. Q. Shen, S. J. Haward, and R. J. Poole. Elastic modifications of an inertial instability in a 3D cross-slot. *J. Non-Newtonian Fluid Mech.*, 2018. doi: 10.1016/j.jnnfm.2018.02.002.

[64] Y. A. Aryshev, V. A. Golovin, and S. A. Ershin. Stability of colliding flows. *Fluid Dyn.*, 16(5):755–759, 1981. doi: 10.1007/bf01089591.

[65] S. H. Wong, P. Bryant, M. Ward, and C. Wharton. Investigation of mixing in a cross-shaped micromixer with static mixing elements for reaction kinetics studies. *Sens. Actuators, B*, 95(1-3):414–424, 2003. doi: 10.1016/s0925-4005(03)00447-7.

[66] T. R. Shih and C. Chung. A high-efficiency planar micromixer with convection and diffusion mixing over a wide Reynolds number range. *Microfluid. Nanofluid.*, 5(2):175–183, 2008.

[67] C. Srisamran and S. Devahastin. Numerical simulation of flow and mixing behavior of impinging streams of shear-thinning fluids. *Chem. Eng. Sci.*, 61(15): 4884–4892, 2006. doi: 10.1016/j.ces.2006.03.031.

[68] M. S. N. Oliveira, F. T. Pinho, and M. A. Alves. Divergent streamlines and free vortices in Newtonian fluid flows in microfluidic flow-focusing devices. *J. Fluid Mech.*, 711:171–191, 2012. doi: 10.1017/jfm.2012.386.

[69] T. Cochrane, K. Walters, and M. F. Webster. On newtonian and non-newtonian flow in complex geometries. *Philos. Trans. A Math. Phys. Eng. Sci.*, 301(1460): 163–181, 1981. doi: 10.1098/rsta.1981.0103.

[70] K. Walters and M. F. Webster. On dominating elastico-viscous response in some complex flows. *Philos. Trans. A Math. Phys. Eng. Sci.*, 308(1502):199–218, 1982. doi: 10.1098/rsta.1982.0159.

[71] J. A. C. Humphrey and S. Li. Tilting, stretching, pairing and collapse of vortex structures in confined counter-current flow. *J. Fluid Eng-T ASME*, 103(3):466–470, 1981. doi: 10.1115/1.3240817.

[72] J. A. C. Humphrey, J. L. Rosales, L. A. Legendre, J. P. LeDuc, and J. P. Landers. Vortex dynamics in confined counter-current shearing flows with applications to mixing. *Int. J. Heat Fluid Flow*, 29(4):1089–1102, 2008. doi: 10.1016/j.ijheatfluidflow.2008.02.005.

[73] E. Kumacheva and P. Garstecki. *Microfluidic reactors for polymer particles*. John Wiley & Sons, 2011. doi: 10.1002/9780470979228.

[74] H. Haddadi and D. Di Carlo. Inertial flow of a dilute suspension over cavities in a microchannel. *J. Fluid Mech.*, 811:436–467, 2017. doi: 10.1017/jfm.2016.709.

[75] H. Haddadi, H. Naghsh-Nilchi, and D. Di Carlo. Separation of cancer cells using vortical microfluidic flows. *Biomicrofluidics*, 12(1):014112, 2018. doi: 10.1063/1.5009037.

[76] R. Arshady, B. Corain, M. Zecca, A. Jayakrishnan, and D. Horak. Amphiphilic functional microgels. *MML Series*, 4:203–252, 2002.

[77] S. Chakraborty. *Microfluidics and microscale transport processes*. CRC Press, 2012. doi: 10.1201/b12976.

[78] I. Lashgari, O. Tammisola, V. Citro, M. P. Juniper, and L. Brandt. The planar X-junction flow: stability analysis and control. *J. Fluid Mech.*, 753:1–28, 2014. doi: 10.1017/jfm.2014.364.

[79] F. Huchet, J. Havlica, P. Legentilhomme, A. Montillet, J. Comiti, and J. Tihon. Use of electrochemical microsensors for hydrodynamics study in crossing microchannels. *Microfluid. Nanofluid.*, 5(1):55–64, 2008.

[80] F. P. Incropera, D. P. DeWitt, T. L. Bergman, and A. S. Lavine. *Introduction to heat transfer*, volume 5$^{\text{th}}$ edition. John Wiley and Sons, 2005.

[81] F. A. Morrison. *Understanding rheology*. New York : Oxford University Press, 2001, 2001.

[82] A. Groisman and S. R. Quake. A microfluidic rectifier: anisotropic flow resistance at low Reynolds numbers. *Phys. Rev. Lett.*, 92(9):094501, 2004. doi: 10.1103/physrevlett.92.094501.

[83] A. Groisman, M. Enzelberger, and S. R. Quake. Microfluidic memory and control devices. *Science*, 300(5621):955–958, 2003. doi: 10.1126/science.1083694[doi].

[84] A. Groisman and V. Steinberg. Efficient mixing at low Reynolds numbers using polymer additives. *Nature*, 410(6831):905, 2001. doi: 10.1038/35073524.

[85] R. J. Poole. The deborah and weissenberg numbers. *British Soc. Rheol. Rheol. Bull*, 53:32–39, 2012.

[86] P. C. Sousa, F. T. Pinho, and M. A. Alves. Purely-elastic flow instabilities and elastic turbulence in microfluidic cross-slot devices. *Soft Matter*, 14(8):1344–1354, 2018. doi: 10.1039/C7SM01106G.

[87] D. V. Boger. A highly elastic constant-viscosity fluid. *J. Non-Newtonian Fluid Mech.*, 3(1):87–91, 1977. doi: 10.1016/0377-0257(77)80014-1.

[88] R. J. Poole, M. A. Alves, and P. J. Oliveira. Purely elastic flow asymmetries. *Phys. Rev. Lett.*, 99(16):164503, 2007. doi: 10.1103/physrevlett.99.164503.

[89] P. Pakdel and G. H. McKinley. Elastic instability and curved streamlines. *Phys. Rev. Lett.*, 77:2459–2462, 1996. doi: 10.1103/PhysRevLett.77.2459.

[90] W. Saric. Görtler vortices. *Annu. Rev. Fluid Mech.*, 26:379–409, 1994.

[91] R. G. Larson, E. S. G. Shaqfeh, and S. J. Muller. A purely elastic instability in Taylor–Couette flow. *J. Fluid Mech.*, 218:573–600, 1990. doi: 10.1017/s0022112090001124.

[92] Y. L. Joo and E. S. G. Shaqfeh. Observations of purely elastic instabilities in the Taylor-Dean flow of a Boger fluid. *J. Fluid Mech.*, 262:27–73, 1994. doi: 10.1017/s002211209400042x.

[93] J. J. Magda and R. G. Larson. A transition occurring in ideal elastic liquids during shear flow. *J. Non-Newtonian Fluid Mech.*, 30(1):1–19, 1988. doi: 10.1016/0377-0257(88)80014-4.

[94] T. Burghelea, E. Segre, I. Bar-Joseph, A. Groisman, and V. Steinberg. Chaotic flow and efficient mixing in a microchannel with a polymer solution. *Phys. Rev. E*, 69(6):066305, 2004. doi: 10.1103/physreve.69.066305.

[95] A. J. Muller, J. A. Odell, and A. Keller. Elongational flow and rheology of monodisperse polymers in solution. *J. Non-Newtonian Fluid Mech.*, 30(2-3):99–118, 1988. doi: 10.1016/0377-0257(88)85018-3.

[96] R. C. Y. Ng and L. G. Leal. Concentration effects on birefringence and flow modification of semidilute polymer solutions in extensional flows. *J. Rheol.*, 37 (3):443–468, 1993. doi: 10.1122/1.550453.

[97] J. M. Broadbent, D. C. Pountney, and K. Walters. Experimental and theoretical aspects of the two-roll mill problem. *J. Non-Newtonian Fluid Mech.*, 3(4):359–378, 1978. doi: 10.1016/0377-0257(78)87014-1.

[98] B. Puangkird, F. Belblidia, and M. F. Webster. Numerical simulation of viscoelastic fluids in cross-slot devices. *J. Non-Newtonian Fluid Mech.*, 162(1-3): 1–20, 2009. doi: 10.1016/j.jnnfm.2009.05.001.

[99] F. A. Cruz, R. J. Poole, A. M. Afonso, F. T. Pinho, P. J. Oliveira, and M. A. Alves. A new viscoelastic benchmark flow: stationary bifurcation in a cross-slot. *J. Non-Newtonian Fluid Mech.*, 214:57–68, 2014. doi: 10.1016/j.jnnfm.2014.09.015.

[100] F. A. Cruz, R. J. Poole, A. M. Afonso, F. T. Pinho, P. J. Oliveira, and M. A. Alves. Influence of channel aspect ratio on the onset of purely-elastic flow instabilities in three-dimensional planar cross-slots. *J. Non-Newtonian Fluid Mech.*, 227:65–79, 2016. doi: 10.1016/j.jnnfm.2015.11.008.

[101] A. Baloch, P. Townsend, and M. F. Webster. On the simulation of highly elastic complex flows. *J. Non-Newtonian Fluid Mech.*, 59(2?3):111–128, 1995. doi: 10.1016/0377-0257(95)01369-7.

[102] S. O. S. Echendu, F. Belblidia, H. R. Tamaddon-Jahromi, and M. F. Webster. Modelling with viscous and viscoplastic materials under combining and separating flow configurations. *Mech. Time-Depend. Mat.*, 15(4):407–428, 2011. doi: 10.1007/s11043-011-9161-x.

[103] A. I. P. Miranda, P. J. Oliveira, and F. T. Pinho. Steady and unsteady laminar flows of Newtonian and generalized Newtonian fluids in a planar T-junction. *Int. J. Numer. Methods Fluids*, 57(3):295–328, 2008. doi: 10.1002/fld.1626.

[104] H. M. Matos and P. J. Oliveira. Steady and unsteady non-Newtonian inelastic flows in a planar T-junction. *Int. J. Heat Fluid Flow*, 39:102–126, 2013. doi: 10.1016/j.ijheatfluidflow.2012.11.005.

[105] H. M. Matos, M. A. Alves, and P. J. Oliveira. New formulation for stress calculation: application to viscoelastic flow in a T-junction. *Numer. Heat Tr. B-Fund.*, 56(5):351–371, 2010. doi: 10.1080/10407790903507972.

[106] H. M. Matos and P. J. Oliveira. Steady flows of constant-viscosity viscoelastic fluids in a planar T-junction, 2014.

[107] S. J. Haward, A. Jaishankar, M. S. N. Oliveira, M. A. Alves, and G. H. McKinley. Extensional flow of hyaluronic acid solutions in an optimized microfluidic cross-slot device. *Biomicrofluidics*, 7(4):044108, 2013. doi: 10.1063/1.4816708.

[108] S. J. Haward and G. H. McKinley. Stagnation point flow of wormlike micellar solutions in a microfluidic cross-slot device: effects of surfactant concentration and ionic environment. *Phys. Rev. E*, 85(3):031502, 2012. doi: 10.1103/physreve.85.031502.

[109] S. J. Haward and G. H. McKinley. Instabilities in stagnation point flows of polymer solutions. *Phys. Fluids*, 25(8):083104, 2013. doi: 10.1063/1.4818151.

[110] S. J. Haward, T. J. Ober, M. S. N. Oliveira, M. A. Alves, and G. H. McKinley. Extensional rheology and elastic instabilities of a wormlike micellar solution in a microfluidic cross-slot device. *Soft Matter*, 8(2):536–555, 2012. doi: 10.1039/c1sm06494k.

[111] S. J. Haward, J. A. Odell, Z. Li, and X. Yuan. Extensional rheology of dilute polymer solutions in oscillatory cross-slot flow: the transient behaviour of birefringent strands. *Rheol. Acta*, 49(6):633–645, 2010. doi: 10.1007/s00397-009-0420-6.

[112] G. G. Guilbault. *Practical fluorescence*, volume 3. CRC Press, 1990.

[113] W. T. Manson. *Fluorescent and luminescent probes for biological activity: a practical guide to technology for quantitative real-time analysis*. Academic Press, 1993.

[114] D. Sinton. Microscale flow visualization. *Microfluid. Nanofluid.*, 1(1):2–21, 2004. doi: 10.1007/s10404-004-0009-4.

[115] D. Ross, M. Gaitan, and L. E. Locascio. Temperature measurement in microfluidic systems using a temperature-dependent fluorescent dye. *Anal. Chem.*, 73 (17):4117–4123, 2001. doi: 10.1021/ac010370l.

[116] D. Ross and L. E. Locascio. Microfluidic temperature gradient focusing. *Anal. Chem.*, 74(11):2556–2564, 2002. doi: 10.1021/ac025528w.

[117] N. Nguyen and S. T. Wereley. *Fundamentals and applications of microfluidics. [electronic book]*. Boston, Artech House: 2 edition, 2006.

[118] F. E. H. Tay. *Microfluidics and BioMEMS applications*. Springer, 2002.

[119] C. Tropea and A. L. Yarin. *Springer handbook of experimental fluid mechanics*, volume 1. Springer Science & Business Media, 2007.

[120] F. Durst, S. Ray, B. Unsal, and O. A. Bayoumi. The development lengths of laminar pipe and channel flows. *J. Fluid Eng-T ASME*, 127(6):1154–1160, 2005. doi: 10.1115/1.2063088.

[121] J. Judy, D. Maynes, and B. W. Webb. Characterization of frictional pressure drop for liquid flows through microchannels. *Int. J. Heat Mass Transfer*, 45(17): 3477–3489, 2002. doi: 10.1016/s0017-9310(02)00076-5.

[122] M. E. Steinke and S. G. Kandlikar. Single-phase liquid friction factors in microchannels. *Int. J. Therm. Sci.*, 45(11):1073–1083, 2006. doi: 10.1016/j.ijthermalsci.2006.01.016.

[123] C. Huang, C. Li, H. Wang, and T. Liou. The application of temperature-sensitive paints for surface and fluid temperature measurements in both thermal developing and fully developed regions of a microchannel. *J. Micromech. Microeng.*, 23(3): 037001, 2013. doi: 10.1088/0960-1317/23/3/037001.

[124] C.-Y. Huang, C.-A. Li, B.-H. Huang, and T.-M. Liou. The study of temperature rise in a 90-degree sharp bend microchannel flow under constant wall temperature condition. *J. Mech.*, 30(6):661–666, 2014. doi: 10.1017/jmech.2014.60.

[125] R. K. Shah and A. L. London. *Laminar flow forced convection in ducts*. Academic press, 2014.

[126] L. E. Rodd, T. P. Scott, J. J. Cooper-White, and G. H. McKinley. Capillary break-up rheometry of low-viscosity elastic fluids. *Appl. Rheol.*, 15(1), 2005.

[127] H. A. Barnes, J. F. Hutton, and K. Walters. *An introduction to rheology*. Amsterdam: Elsevier, 1989. doi: 10.1007/978-94-007-6395-1_1.

[128] V. M. Entov and E. J. Hinch. Effect of a spectrum of relaxation times on the capillary thinning of a filament of elastic liquid. *J. Non-Newtonian Fluid Mech.*, 72(1):31–53, 1997. doi: 10.1016/s0377-0257(97)00022-0.

[129] ASME. Performance test codes, PTC 19.1-1998. Technical report, American Society of Mechanical Engineers, 1998.

[130] B. N. Taylor and C. E. Kuyatt. Guidelines for evaluating and expressing the uncertainty of NIST measurement results. Technical report, National Institute of Standards and Technology Gaithersburg, MD, 1994.

[131] ANSYS. *ANSYS Fluent user's guide*, 2011.

[132] J. H. Ferziger and M. Peric. *Computational methods for fluid dynamics*. Berlin : Springer, 2002; 3rd, rev. ed, 2002. doi: 10.1007/978-3-642-56026-2.

[133] S. V. Patankar and D. B. Spalding. A calculation procedure for heat, mass and momentum transfer in three-dimensional parabolic flows. *Int. J. Heat Mass Transfer*, 15(10):1787–1806, 1972. doi: 10.1016/0017-9310(72)90054-3.

[134] B. Cantwell. *Introduction to symmetry analysis*, volume 29. Cambridge University Press, paperback edition, 2002. doi: 10.1115/1.1641778.

[135] J. Zhou, R. J. Adrian, S. Balachandar, and T. M. Kendall. Mechanisms for generating coherent packets of hairpin vortices in channel flow. *J. Fluid Mech.*, 387:353–396, 1999. doi: 10.1017/S002211209900467X.

[136] S. V. Patankar, C. H. Liu, and E. M. Sparrow. Fully developed flow and heat transfer in ducts having streamwise-periodic variations of cross-sectional area. *J. Heat Transfer*, 99 Ser C(2):180–186, 1977. doi: 10.1115/1.3450666.

[137] A. R. Chandrupatla and V. M. K. Sastri. Laminar forced convection heat transfer of a non-newtonian fluid in a square duct. *Int. J. Heat Mass Transfer*, 20(12): 1315–1323, 1977. doi: 10.1016/0017-9310(77)90027-8.

[138] N. Burshtein, K. Zografos, A. Q. Shen, R. J. Poole, and S. J. Haward. Inertioelastic flow instability at a stagnation point. *Phys. Rev. X*, 7(4):041039, 2017. doi: 10.1103/physrevx.7.041039.

[139] M. D. Smith, Y. L. Joo, R. C. Armstrong, and R. A. Brown. Linear stability analysis of flow of an Oldroyd-B fluid through a linear array of cylinders. *J. Non-Newtonian Fluid Mech.*, 109(1):13–50, 2003. doi: 10.1016/s0377-0257(02)00162-3.

[140] L. Xi and M. D. Graham. A mechanism for oscillatory instability in viscoelastic cross-slot flow. *J. Fluid Mech.*, 622:145–165, 2009. doi: 10.1017/s0022112008005119.

[141] J. Guckenheimer and P. Holmes. Local bifurcations. In *Nonlinear oscillations, dynamical systems, and bifurcations of vector fields*, pages 117–165. Springer, 1983. doi: 10.1007/978-1-4612-1140-2_3.

[142] M. P. Escudier, I. W. Gouldson, A. S. Pereira, F. T. Pinho, and R. J. Poole. On the reproducibility of the rheology of shear-thinning liquids. *J. Non-Newtonian Fluid Mech.*, 97(2-3):99–124, 2001. doi: 10.1016/s0377-0257(00)00178-6.

[143] Glycerine Producers' Association. *Physical properties of glycerine and its solutions*. Glycerine Producers' Association, 1963.